



HAL
open science

Design and analysis of tensegrity-inspired manipulators

Vimalesh Muralidharan

► **To cite this version:**

Vimalesh Muralidharan. Design and analysis of tensegrity-inspired manipulators. Automatic. École centrale de Nantes, 2023. English. NNT : 2023ECDN0032 . tel-04520768

HAL Id: tel-04520768

<https://theses.hal.science/tel-04520768v1>

Submitted on 25 Mar 2024

HAL is a multi-disciplinary open access archive for the deposit and dissemination of scientific research documents, whether they are published or not. The documents may come from teaching and research institutions in France or abroad, or from public or private research centers.

L'archive ouverte pluridisciplinaire **HAL**, est destinée au dépôt et à la diffusion de documents scientifiques de niveau recherche, publiés ou non, émanant des établissements d'enseignement et de recherche français ou étrangers, des laboratoires publics ou privés.

MEMOIRE DE DOCTORAT DE

L'ÉCOLE CENTRALE DE NANTES

ÉCOLE DOCTORALE N° 602

Sciences de l'Ingénierie et des Systèmes
Spécialité : *Robotique*

Par

Vimalesh MURALIDHARAN

Design and analysis of tensegrity-inspired manipulators

Projet de recherche doctoral présenté et soutenu à École Centrale de Nantes,
le 06 Décembre 2023

Unité de recherche : UMR 6004, Laboratoire des Sciences du Numérique de Nantes (LS2N)

Rapporteurs avant soutenance :

Clément GOSSELIN Full Professor, Université Laval, Canada
Marc GOUTTEFARDE Directeur de recherche CNRS, Université de Montpellier

Composition du Jury :

Président :	Pierre RENAUD	Professeur des universités, Institut national des sciences appliquées de Strasbourg
Examineurs :	Clément GOSSELIN Marc GOUTTEFARDE	Full Professor, Université Laval, Canada Directeur de recherche CNRS, Université de Montpellier
	Quentin BOEHLER	Senior scientist, Eidgenössische Technische Hochschule (ETH) Zürich, Suisse
	Christine CHEVALLEREAU	Directrice de recherche CNRS, École Centrale de Nantes
Directeur de recherches doctorales :	Philippe WENGER	Directeur de recherche CNRS, École Centrale de Nantes

Dedicated to my great grandparents

{ Chinnathambi, Amaravathi, Alamelu from Vaniyambadi
Ganapathy, Sornammal from Tirupathur
Rathinam, Pattammal from Gudiyatham
Kandhasamy, Rathinammal from Gudiyatham

and all relatives

ABSTRACT

This thesis studies tensegrity-inspired joints and manipulators equipped with springs and redundantly actuated by antagonistic cables. The actuation redundancy is leveraged to modulate their stiffness at a given configuration. The condition to achieve a positive correlation between actuation forces and stiffness is derived for a general single-degree-of-freedom (1-DoF) joint. This phenomenon is called coactivation in biological joints, which leads to energy efficiency. Among the revolute joint (R-joint) and symmetric four-bar mechanisms, the anti-parallelogram (X-joint) offers the maximum range of movement with coactivation. Hence, a planar 2-DoF manipulator with two X-joints is conceived. Two actuation schemes with four and three cables, respectively, are examined for this manipulator. The workspace, velocity, force, and stiffness performances are compared for the two schemes. The design considerations for such manipulators, namely, the joint limits, mechanical feasibility of springs, and safety of bars, are addressed. Design optimization and comparison of 2-X and 2-R manipulators are performed with identical payload and workspace specifications. Finally, a modified X-joint is developed with only spherical joints, and a spatial 3-X tensegrity-inspired manipulator is constructed and studied.

Keywords: Tensegrity, bio-inspired design, anti-parallelogram, antagonistic actuation, workspace, optimal design

ACKNOWLEDGEMENT

Firstly, I thank my supervisors, Dr. Philippe Wenger and Dr. Christine Chevallereau, for providing me with an opportunity to work on an exciting topic in the growing field of human-robot interaction. I sincerely appreciate the time, attention, and support they provided me during the development of this thesis through numerous stimulating discussions, freedom to explore on my own, quick reviews of the papers/reports, etc. Working under their supervision has taught me countless professional and academic lessons I will carry forward in my career.

An important source of inspiration for me, which also applies to all researchers in this field, is the subject of robotics and mechanisms itself. The beautiful way it is, its evolution over the past decades, and the interesting problems it offers to date are astonishing. I thank all the researchers and teachers who have contributed to robotics and mechanisms, the professional body International Federation for the Promotion of Mechanism and Machine Science (IFTToMM), dedicated journals, and conferences in this field.

I am indebted to the reviewers of this thesis, Dr. Clément Gosselin, Dr. Marc Gouttefarde, Dr. Pierre Renaud, and Dr. Quentin Boehler, for their invaluable comments and timely reviews. I also thank the members of my annual monitoring committee, Prof. Sébastien Briot and Prof. Pierre Renaud, for the interesting suggestions they offered at the end of the first and second years of this thesis, which motivated the consideration of four-bar mechanisms in Chapter 2 and the detailed model of springs in Chapter 5.

I pleasantly acknowledge the discussion with Dr. Volkert van der Wijk and Dr. Gökhan Kiper on the term “tensegrity manipulator” at the ARK 2022 conference. It allowed us to develop the term “tensegrity-inspired manipulator”, which is more appropriate for the systems considered in this thesis.

I am grateful to our Robotique et Vivant (ReV) team at LS2N for organizing seminars and promoting scientific discussions regularly. I express my gratitude to the secretaries of LS2N, Ecole Centrale de Nantes, and Maison des Chercheurs Étrangers for their help with all the administrative documents. In the same spirit, I thank all the supporting staff at the S-building of ECN for taking extraordinary measures during COVID-19 to ensure that we have a hygienic workplace.

I acknowledge the help of Mathieu (IMT Atlantique) and all research engineers (LS2N) Denis, Philippe, Stéphane, Marceau, and Mamadou in prototyping and setting up the hardware for experimentation. I thankfully recall the numerous scientific and technical exchanges with my present and past colleagues: Nicolas, Durgesh, Isaac, Matthieu, Benjamin, Guillaume, Parag, Karol, and Barath.

I express my sincere gratitude to Dr. Sandipan Bandyopadhyay and his team at IIT Madras for employing me during 2016-2018 as a Project Associate and helping me develop the skills needed to pursue a career in robotics. I also fondly recall the robotics club (RMI) of NIT Trichy, which initiated me into robotics.

On the personal front, I am thankful to all my friends who are/were at Nantes during my tenure: Subiksha, Vijayalakshmi aunty, Sevugarayan, Varun, Krushna, Tharun, Krithish, Praveen, Puviarasu, Shivaraj, Irfan, and Jathursan. I am grateful to my family members, cousins,

Acknowledgement

and brother from Vaniyambadi, Gudiyatham, Thirupathur, and other places for their immense confidence and unwavering support throughout my stay in France. Finally, I attribute any degree of honesty and sincerity found in this work to my parents.

Nantes, France
January 2024

Vimallesh Muralidharan

TABLE OF CONTENTS

Abstract	5
Acknowledgement	7
Nomenclature	13
Introduction	23
1 State of the art	25
1.1 Introduction	26
1.2 Conventional tensegrity systems: their properties and applications	27
1.3 Tensegrity-based mechanisms and robots in literature	29
1.3.1 Property a : Isolated rigid bodies	30
1.3.2 Property b : Positive stiffness	32
1.3.3 Property c : Prestress or self-stress	32
1.3.4 Property d : Tensioned and compressed components	34
1.3.5 Property e : Rigid bodies are never in tension	35
1.4 Scope of this thesis	35
1.5 Conclusions	36
2 Antagonistically actuated tensegrity-inspired joints	39
2.1 Introduction	40
2.2 General single-degree-of-freedom joint antagonistically actuated by cables	41
2.2.1 Joint description	41
2.2.2 Joint limits and symmetry	42
2.2.3 Static model and stiffness modulation	44
2.3 Stiffness of a general joint antagonistically actuated with in-series linear springs	45
2.4 Some joints and cable arrangements with no stiffness modulation	47
2.5 Revolute joint	50
2.5.1 Congruent triangles	50
2.5.2 Experimental validation	51
2.5.3 Non-congruent triangles	53
2.5.4 Elliptical pulley-based actuation [CWA23]	55
2.6 Four-bar mechanisms with symmetric limbs as joints	57
2.6.1 Description	57
2.6.2 Kinematic model of the four-bar mechanism	59
2.6.3 Anti-parallelogram mechanism	59
2.6.4 Parallelogram mechanism	60
2.6.5 General four-bar mechanisms with unequal base and top bars	62
2.6.6 Experimental validation	64

2.6.7	Alternate cable attachments for coactivation in parallelogram mechanism	66
2.6.8	Alternate cable attachments for coactivation in a general four-bar mechanism with non-crossed limbs	70
2.7	Classification of the joints and possible applications	71
2.8	Conclusions	73
3	2-X manipulator: cable actuation and workspace	75
3.1	Introduction	76
3.2	Description of the 2-X manipulator	77
3.3	Actuation with four cables and three cables	78
3.4	Kinematic model of the 2-X manipulator	80
3.5	Static model for the 4-cable and 3-cable schemes	81
3.5.1	4-cable scheme	81
3.5.2	3-cable scheme	85
3.6	Stable wrench-feasible joint space (SWFJ) for the 4-cable and 3-cable schemes .	87
3.6.1	General algorithm	88
3.6.2	Numerical example	89
3.7	Stable wrench-feasible workspace (SWFW) for the 4-cable and 3-cable schemes .	94
3.8	Extension to n -X manipulator for $2n$ -cable and $(n + 1)$ -cable schemes	95
3.9	Conclusions	98
4	2-X manipulator: velocity, force, and stiffness performances	99
4.1	Introduction	100
4.2	Velocity performance	101
4.2.1	Kinematic sensitivity	103
4.3	Force performance	103
4.4	Stiffness performance	105
4.4.1	Cartesian stiffness matrix	105
4.4.2	Stiffness ellipse	105
4.4.3	Stiffness along x and y directions	107
4.5	Global performance in the workspace	107
4.5.1	Performance at chosen points in the workspace	109
4.5.2	Performance indices and their contours in the workspace	110
4.6	Conclusions	115
5	Design considerations for 2-X and 2-R manipulators	117
5.1	Introduction	118
5.2	Mechanical feasibility of springs	119
5.2.1	Assumptions in spring design	119
5.2.2	Governing conditions in spring design	120
5.3	Safety of a bar from buckling	122
5.4	Design considerations for the 2-X manipulator	122
5.4.1	Joint limits	123
5.4.2	Design space for the springs	125
5.4.3	Cross-sections and masses of the bars of 2-X manipulator	127

5.4.4	Consolidation of all design conditions and a numerical example for 2-X manipulator	131
5.5	Design considerations for the 2-R manipulator	134
5.5.1	Joint limits	135
5.5.2	Design space for the springs	136
5.5.3	Cross-sections and masses of the bars of 2-R manipulator	137
5.5.4	Static model of 2-R manipulator	140
5.5.5	Kinematic model of 2-R manipulator	141
5.5.6	Stable wrench-feasible workspace of 2-R manipulator with a numerical example	141
5.6	Conclusions	143
6	Optimal design and comparison of 2-X and 2-R manipulators	145
6.1	Introduction	146
6.2	Template of the SWFJ and SWFW for the two manipulators	147
6.3	Design variables and their bounds	148
6.4	Workspace optimization for a given payload	150
6.4.1	Problem formulation	150
6.4.2	Genetic algorithm based solver: NSGA-II	150
6.4.3	Results and discussion	151
6.5	Force, mass, and size optimization for a given payload and SWFW disk	152
6.5.1	Formulation and resolution of the design problem	152
6.5.2	Solution method and the Pareto optimal front	153
6.5.3	Extremal designs on the Pareto front	154
6.5.4	Exploration of the Pareto front	160
6.6	Effect of changing the payload and desired SWFW disk radius specifications	164
6.7	Possible applications and extensions	166
6.8	Conclusions	167
7	Spatial 3-X manipulator	169
7.1	Introduction	170
7.2	Modified X-joint for spatial tensegrity systems	171
7.3	Kinematic model of 3-X manipulator	174
7.4	Inverse kinematic model	175
7.4.1	First sub-problem	175
7.4.2	Second sub-problem	177
7.4.3	Numerical example	177
7.5	Singularity analysis	180
7.6	Workspace of 3-X manipulator	182
7.6.1	Construction of the workspace	182
7.6.2	Cross-sections of the workspace	185
7.7	Proof of concept and practical issues	190
7.8	Conclusions	193
	Conclusion	195

Relevant personal publications	200
A Derivation of equivalent polynomial equations for ${}^4f_1 = 0$	201
A.1 Polynomial in $t_1 = \tan(\alpha_1/4)$	201
A.2 Polynomial in $t_2 = \tan(\alpha_2/4)$	203
B Illustrations on the categorization of the force coefficients in the design of bars of 2-X manipulator	205
C Computation of actual compressive loads in the bars and validation of 2-X and 2-R designs	207
D Size of the 2-R manipulator relative to the maximal inscribed disk	211
E Designs on the Pareto fronts of the 2-X and 2-R manipulators	213
F Optimal designs of 2-X manipulator for different scenarios	217
Bibliography	218

NOMENCLATURE

DoF	Degree-of-freedom
SWFJ	Stable wrench-feasible joint space of a manipulator
SWFW	Stable wrench-feasible workspace of a manipulator
R	Revolute joint
X	Anti-parallelogram joint
α	Orientation of the top-bar relative to the base
F_1, F_2	Antagonistic cable forces actuating a 1-DoF joint/mechanism
K	Stiffness of the 1-DoF joint/mechanism
γ_1, γ_2	Force coefficients in the expression of stiffness for 1-DoF joint/mechanism
l, b	Lengths of bars in the X-joint
r, h	Semi-base length, height of the congruent triangles in the R-joint
a	Length of the link offsets in a manipulator
$\mathbf{f} = [f_x, f_y]^\top$	Force applied by the end-effector of a 2-DoF planar manipulator
$\mathcal{M}_v, \mathcal{M}_f$	Velocity, force manipulability indices
κ_v, κ_f	Velocity, force inverse condition indices
$\mathbf{K}_\alpha, \mathbf{K}_c$	Articular, Cartesian stiffness matrix
K_x, K_y	Stiffness along the principal x, y directions
${}^4(\cdot), {}^3(\cdot)$	Performance measure for 4-cable, 3-cable scheme
α_i	Orientation of the top-bar of i^{th} joint w.r.t. its base
θ_i	Orientation of the line joining the mid-points of the top and base bars of the i^{th} X-joint w.r.t. a line perpendicular to its base
$\overline{\alpha_{\max}}$	Upper bound for α_i due to geometry of the joint and cable actuation
σ_α	Fraction $\in]0, 1[$ used to set safe joint limits
$\overline{\alpha_{\max}}$	$(\sigma_\alpha \overline{\alpha_{\max}})$ safe upper bound for α_i inside the limits due to geometry and actuation
k_i, σ_{k_i}	Stiffness, selection parameter for the springs in installed in i^{th} joint
d, D, N_a	Wire diameter, coil diameter, number of active coils of a spring
$l_{0_i}, l_{\max_i}, m_{k_i}$	Free length, maximum operating length, mass of the springs installed in i^{th} joint
α_{\max_i}	$(\leq \overline{\alpha_{\max}})$ actual upper bound for α_i considering the spring free length (l_{0_i})
l_{b_j}, r_{b_j}, m_j	Length, cross-section radius, mass of the j^{th} bar in a manipulator
F_{l_i}, F_{r_i}	Forces imposed by the left, right cables on the i^{th} joint
F_{\min}, F_{\max}	Minimum, maximum bounds on the cable forces
m_p, F_p	Mass, weight of the point mass payload at end-effector
$\mathcal{D}(r_d)$	Disk of radius r_d that must be inscribed inside the SWFW
π_1, π_2	Two orthogonal planes in space containing the X-joints of the spatial 3-X manipulator

LIST OF FIGURES

1.1	A uniform circular cylinder of cross-section radius r_e and length l_e subjected to a load F in axial and transverse directions.	26
1.2	Robot manipulators with links loaded in axial (left) and transverse (right) directions.	27
1.3	Early tensegrity structures.	27
1.4	Examples of tensegrity sculptures.	28
1.5	Examples of tensegrity structures applied in civil and architectural engineering.	28
1.6	Examples tensegrity structures applied beyond art and architecture.	28
1.7	SUPERBall tensegrity robot with no contact between rigid bodies (Source: [Sab+15]).	30
1.8	Spatial tensegrity mechanism with contacting rigid bodies (Source: [AG08]).	31
1.9	Planar tensegrity mechanisms with contacting rigid bodies.	31
1.10	Variable stiffness tensegrity mechanism (Source: [Ars11]).	33
1.11	Antagonistically actuated tensegrity mechanisms with variable stiffness.	33
1.12	Applications of tensegrity mechanisms for achieving variable stiffness in bio-inspired systems.	33
1.13	Tensegrity systems with curved links.	34
1.14	General schematics of the tensegrity systems considered in this work.	37
2.1	Schematic of a general 1-DoF joint actuated antagonistically by two cables.	42
2.2	Illustration of limit of movement due to uncertainty configuration or constraint singularity in the anti-parallelogram mechanism.	42
2.3	Illustration of antagonism, non-antagonism, and limit of antagonism in cable actuation of a revolute joint.	43
2.4	Schematic of a general 1-DoF joint actuated antagonistically by two cables with in-series springs.	45
2.5	Joints and cable attachments that do not permit modulation of stiffness.	48
2.6	Schematic of an R-joint with congruent triangular trusses actuated antagonistically by two cables (dashed lines).	50
2.7	Experimental setup of an R-joint with congruent triangles.	52
2.8	External force required to produce the same displacement in the R-joint for different antagonistic actuation forces $F_1 = F_2 = F_{\text{ant}}$	52
2.9	Schematic of an R-joint with non-congruent triangular trusses actuated antagonistically by two cables (dashed lines).	53
2.10	Feasible region for the cable attachment point B_1 to achieve coactivation at the configuration $\alpha = 0$ rad in the R-joint (non-congruent triangles) with $r = 1, h = 1/2$	55
2.11	R-joint with $r = 1, h = 1/2$ whose left (resp. right) cable is attached to $B_{1\alpha} = (-2, -1)$ (resp. $B_{2\alpha} = (2, -1)$) at the base. The plot of force coefficients within its limits of movement $\pm\alpha_{\text{max}} = \pm 0.93$ rad. The force coefficient γ_1 (resp. γ_2) tends to infinity asymptotically as α approaches the limit $-\alpha_{\text{max}}$ (resp. α_{max}).	56

2.12	R-joint with $r = 1, h = 1/2$ whose left (resp. right) cable is attached to $B_{1b} = (-1, 2)$ (resp. $B_{2b} = (1, 2)$) at the base. The plot of force coefficients within its limits of movement $\pm\alpha_{\max} = \pm 0.64$ rad. The force coefficient γ_1 (resp. γ_2) tends to infinity asymptotically as α approaches the limit α_{\max} (resp. $-\alpha_{\max}$).	56
2.13	Schematic of a fixed center joint actuated antagonistically by two cables (blue and red) wound around an elliptical pulley (Source: [CWA23]).	57
2.14	Schematic diagram of four-bar mechanisms with symmetric limbs that are crossed when $b_0 < 0$ (left) and non-crossed when $b_0 > 0$ (right). The two actuating cables are shown in dashed lines.	58
2.15	Schematic of an anti-parallelogram mechanism actuated antagonistically by two cables (dashed lines).	60
2.16	Schematic of a parallelogram mechanism actuated antagonistically by two cables (dashed lines).	61
2.17	Stiffness of the mechanisms when $\theta \in]-\frac{\pi}{2}, \frac{\pi}{2}[$ for different actuation forces.	62
2.18	Experimental setup of different symmetric four-bar mechanisms.	64
2.19	External force required to produce the same displacement in a mechanism for different antagonistic actuation forces $F_1 = F_2 = F_{\text{ant}}$	65
2.20	Parallelogram mechanism with cables attached at points D_1 and D_2 in the base.	67
2.21	Feasible region for the cable attachment point D_1 to achieve coactivation at the configuration $\theta = 0$ rad in the parallelogram mechanism with $l = 1, b = 2$	68
2.22	Parallelogram mechanism with $l = 1, b = 2$, whose left (resp. right) cable is attached to $D_{1a} = (-1, 2)$ (resp. $D_{2a} = (3, 2)$) at the base. The plot of force coefficients within its limits of movement $\pm\theta_{\max} = \pm 0.46$ rad. The force coefficient γ_1 (resp. γ_2) tends to infinity asymptotically as θ approaches the limit $-\theta_{\max}$ (resp. θ_{\max}).	69
2.23	Parallelogram mechanism with $l = 1, b = 2$ whose left (resp. right) cable is attached to $D_{1b} = (-2/5, 2/5)$ (resp. $D_{2b} = (12/5, 2/5)$) at the base. The plot of force coefficients within its limits of movement $\pm\theta_{\max} = \pm 0.79$ rad. The force coefficient γ_1 (resp. γ_2) tends to infinity asymptotically as θ approaches the limit $-\theta_{\max}$ (resp. θ_{\max}).	69
2.24	Feasible region for the cable attachment point D_1 to achieve coactivation at the configuration $\alpha = 0$ rad in a four-bar mechanism with non-crossed limbs of geometry $l = 1, b = 1, b_0 = 1/2$	70
2.25	Four-bar mechanism with $l = 1, b = 1, b_0 = 1/2$ whose left (resp. right) cable is attached to $D_1^* = (1, 3)$ (resp. $D_2^* = (-1/2, 3)$) at the base. The plot of force coefficients within its limits of movement $\pm\alpha_{\max} = \pm 0.31$ rad. The force coefficient γ_1 (resp. γ_2) tends to infinity asymptotically as α approaches the limit α_{\max} (resp. $-\alpha_{\max}$).	71
3.1	Schematic of the 2-X manipulator.	78
3.2	Arrangement of bars in parallel planes (Source: [Fas+20]).	79
3.3	Actuation with four cables (left) and three cables (right).	79
3.4	Labels for the bars of the 2-X manipulator.	82

3.5	Feasible interval of α_1 for a given $\alpha_2 = 0$ (left), boundary points obtained while scanning α_2 (middle), and all the boundary points obtained by scanning both α_1 and α_2 (right).	90
3.6	Algorithm to find a cyclic ordering of planar points (α_1, α_2) on the boundary of the SWFJ.	92
3.7	Classification of boundary points into different groups (left), joining the points within groups (middle), and joining ends of the groups to form a cyclic ordering (right).	93
3.8	Stable wrench-feasible joint space (SWFJ) obtained for 4-cable (left) and 3-cable (right) schemes. The curves lying in the region where $\det(\mathbf{J}_x) > 0$ are shown in opaque style while those in the region $\det(\mathbf{J}_x) < 0$ are shown in transparent style.	93
3.9	Stable wrench-feasible workspace (SWFW) obtained for the 4-cable (left) and 3-cable (right) schemes. The opaque and transparent curves represent the two workspace components corresponding to configurations where $\det(\mathbf{J}_x) > 0$ and $\det(\mathbf{J}_x) < 0$, respectively.	95
3.10	Algorithm to compute the boundary points of SWFJ for the n -X manipulator.	96
4.1	2-X manipulator: workspace for actuation with four cables (left) and three cables (right) corresponding to the data presented in Table 3.1. In both cases, the manipulator is plotted in the configuration $(\alpha_1, \alpha_2) = (-0.63, -1.44)$ rad.	100
4.2	Joint velocity polytope and task velocity polytope for the 4-cable (red continuous) and 3-cable (black dashed) schemes at $(\alpha_1, \alpha_2) = (-0.63, -1.44)$ rad.	102
4.3	Force polytopes and associated constraints of the 4-cable (red continuous) and 3-cable (black dashed) schemes at $(\alpha_1, \alpha_2) = (-0.63, -1.44)$ rad.	104
4.4	Stiffness ellipse corresponding to different force combinations at $(\alpha_1, \alpha_2) = (-0.63, -1.44)$ rad for the 4-cable scheme.	106
4.5	Region of tunable stiffness for the 4-cable (red) and 3-cable (black) schemes at $(\alpha_1, \alpha_2) = (-0.63, -1.44)$ rad.	107
4.6	Four common points chosen in the workspace of 4-cable and 3-cable schemes.	109
4.7	Contours of velocity manipulability in the workspace of the two actuation schemes.	111
4.8	Contours of velocity inverse condition index in the workspace of the two actuation schemes.	111
4.9	Contours of force manipulability in the workspace of the two actuation schemes.	112
4.10	Contours of force inverse condition index in the workspace of the two actuation schemes.	112
4.11	Contours of maximum stiffness in x -direction in the workspace of the two actuation schemes.	113
4.12	Contours of maximum stiffness in y -direction in the workspace of the two actuation schemes.	114
4.13	Range of stiffness achievable in x -direction in the workspace of the two actuation schemes.	114
4.14	Range of stiffness achievable in y -direction in the workspace of the two actuation schemes.	115
5.1	Schematics of the manipulators under study: 2-X (left) and 2-R (right).	118
5.2	Schematic of a helical extension spring.	119

5.3	Sequence of treating the design considerations for the 2-X manipulator.	123
5.4	Joint limits of an X-joint depending on the spring free length and bar lengths. . .	124
5.5	Parametrization of the feasible spring space with $\sigma_{k_i} \in [0, 1]$ when $k_i = 3000$ N/m for an X-joint with $b = 0.2$ m and $l = 0.4$ m, and $\overline{\alpha_{\max}} = 5\pi/6$ rad.	126
5.6	Reaction forces at the ends of the bars.	127
5.7	Computational scheme for the determination of SWFW for the 2-X manipulator that accounts for all of its design considerations discussed in Section 5.4.	132
5.8	Stable wrench-feasible joint space (SWFJ) and stable wrench-feasible workspace (SWFW) for the 2-X manipulator with: $b = 0.2$ m, $l = 0.4$ m, $a = 0.5$ m, $\overline{\alpha_{\max}} = 5\pi/6$ rad, $k_1 = 3000$ N/m, $l_{0_1} = 0.2430$ m, $m_{k_1} = 1.0195$ kg, $k_2 = 1000$ N/m, $l_{0_2} = 0.2629$ m, $m_{k_2} = 0.8433$ kg, $F_{\max} = 200$ N. In SWFJ, the curves lying in the region where $\det(\mathbf{J}_x) > 0$ are shown in opaque style while those in $\det(\mathbf{J}_x) < 0$ region are shown in transparent style. The images of these curves in the task space are also shown in the same style for the sake of clarity.	134
5.9	Bar labels (left) and cable routing scheme (right) for the 2-R manipulator.	135
5.10	Joint limits of an R-joint depending on the spring free length (l_{0_i}) and bar lengths.	136
5.11	Reaction forces at the ends of the bars.	137
5.12	The stable wrench-feasible joint space (SWFJ) and stable wrench-feasible workspace (SWFW) for the 2-R manipulator with: $r = 0.1$ m, $h = 0.1732$ m, $a = 0.5$ m, $\sigma_\alpha = (9/10)$, $k_1 = 5000$ N/m, $l_{0_1} = 0.3250$ m, $m_{k_1} = 1.1008$ kg, $k_2 = 2000$ N/m, $l_{0_2} = 0.3120$ m, $m_{k_2} = 1.1311$ kg, $F_{\max} = 200$ N/m. In the joint space (α_1, α_2), the curves lying in the region ($\alpha_2 > 0$) are shown in opaque style while those in the region ($\alpha_2 < 0$) are shown in transparent style. The images of these curves in the task space are also shown in the same style for the sake of clarity.	143
6.1	Template of the stable wrench-feasible joint space (SWFJ) and stable-wrench feasible workspace (SWFW) for the 2-X and 2-R manipulators. In SWFJ (shaded portion), the curves lying above the singularity curve are shown in opaque style while those below are shown in transparent style. The images of these curves in the task space are also shown in the same style for the sake of clarity.	148
6.2	Maximum SWFW disk radius for different payload at the end-effector.	152
6.3	Pareto fronts for the two manipulators obtained for a payload mass (m_p) of 2 kg and desired SWFW disk radius (r_d) of 0.15 m.	153
6.4	Minimum force designs for the two manipulators.	157
6.5	Minimum mass designs.	158
6.6	Minimum size designs.	158
6.7	Pareto front and six optimal designs (X_I, \dots, X_{VI}) of the 2-X manipulator obtained for a payload mass (m_p) of 2 kg and SWFW disk radius (r_d) of 0.15 m. The range of the objectives are $F_{\max} \in [56.4474, 498.0113]$ N, mass $\in [1.5544, 50.8691]$ kg, and size $\in [0.7648, 7.6679]$ m. The minimum force design and a few points closer to it have been deleted to present a better view of the major part of the front. . .	161
6.8	Pareto front and six optimal designs (R_I, \dots, R_{VI}) of the 2-R manipulator obtained for a payload mass (m_p) of 2 kg and SWFW disk radius (r_d) of 0.15 m. The range of objectives are $F_{\max} \in [38.5137, 275.1206]$ N, mass $\in [4.5659, 10.0591]$ kg, size $\in [2.4306, 2.9799]$ m.	162

6.9	Minimum F_{\max} values for different payload and disk specifications for the 2-X and 2-R manipulators.	164
6.10	Minimum moving mass values for different payload and disk specifications for the 2-X and 2-R manipulators.	165
6.11	Minimum size values for different payload and disk specifications for the 2-X and 2-R manipulators.	165
7.1	A spatial manipulator with three X-joints arranged in two perpendicular planes.	170
7.2	Choosing attachment points for the bars on the fixed and moving platforms while designing the modified X-joint.	171
7.3	Constraint wrenches (red) and twists (blue) between the fixed and moving platforms connected by four bars.	172
7.4	Modified X-joint with five bars and spherical joints.	173
7.5	Construction of the spatial tensegrity-inspired 3-X manipulator with modified X-joints.	173
7.6	Kinematic diagram of the spatial 3-X manipulator.	174
7.7	First sub-problem in inverse kinematics.	176
7.8	Second sub-problem in inverse kinematics.	177
7.9	Four feasible configurations of the first joint ($\theta_1 = \{2.86, -1.38, -0.68, 0.82\}$ rad) for a manipulator with geometry $b = 1, l = 2, a = 6$, when the end-effector is located at $(x, y, z) = (3/2, 1, 3/2)$	178
7.10	Thirty-two inverse kinematic solutions of the manipulator (separated into four groups) with geometry $b = 1, l = 2, a = 6$, when the end-effector is located at $(x, y, z) = (3/2, 1, 3/2)$	179
7.11	Plot of all thirty-two inverse kinematic solutions of the manipulator together. The geometry of the manipulator is $b = 1, l = 2, a = 6$, and the end-effector is located at $(x, y, z) = (3/2, 1, 3/2)$	179
7.12	Singular configuration of the 3-X manipulator with geometry $b = 1, l = 2, a = 2$, at $(\theta_1, \theta_2, \theta_3) = (0.5, 1.45, -0.26)$ rad corresponding to $\sigma_1(\theta_2, \theta_3) = 0$	181
7.13	Singular configurations of the 3-X manipulator with geometry $b = 1, l = 2, a = 2$, corresponding to $\sigma_2(\theta_1, \theta_2, \theta_3) = 0$	181
7.14	Singularity surfaces ($\sigma_1 = 0, \sigma_2 = 0$) and joint limits ($\theta_1, \theta_2, \theta_3 = \pm \frac{\pi}{2}$) of a manipulator with geometry $b = 1, l = 2, a = 2$	182
7.15	Image of the singularity surface $\sigma_1(\theta_2, \theta_3) = 0$ for the manipulator $b = 1, l = 2, a = 2$.	183
7.16	Image of the singularity surface $\sigma_2(\theta_1, \theta_2, \theta_3) = 0$ for the manipulator $b = 1, l = 2, a = 2$	183
7.17	Image of the joint limits $\theta_1 = \pm \frac{\pi}{2}$ for the manipulator $b = 1, l = 2, a = 2$	184
7.18	Image of the joint limits $\theta_2 = \pm \frac{\pi}{2}$ for the manipulator $b = 1, l = 2, a = 2$	184
7.19	Image of the joint limits $\theta_3 = \pm \frac{\pi}{2}$ for the manipulator $b = 1, l = 2, a = 2$	184
7.20	Workspace boundaries of the 3-X manipulator with geometry $b = 1, l = 2, a = 2$, and joint limits $\theta_i = \pm \frac{\pi}{2}, i = 1, 2, 3$	185
7.21	Section of the workspace at $x = 0$ for the manipulator $b = 1, l = 2, a = 2$	186
7.22	Sections of the workspace at $x \in [0, 1.95]$ for the manipulator $b = 1, l = 2, a = 2$	187
7.23	Sections of the workspace at $x \in [2, 3]$ for the manipulator $b = 1, l = 2, a = 2$	188
7.24	Sections of the workspace at $x \in [3.5, 10.5]$ for the manipulator $b = 1, l = 2, a = 2$	189

7.25	Plastic prototypes of modified X-joint (left) and rigid offset (right).	191
7.26	Plastic prototypes of the 3-X spatial manipulator with planar X-joints (left) and modified X-joints (right).	191
7.27	Commercially available rod-end bearing (Source: [Reb]).	192
C.1	Computation of the buckling load in the bar j subjected to forces F'_j and F''_j at the two ends.	207
D.1	Simplified sketch of the 2-R manipulator and one half of its workspace in the presence of joint limits $\alpha_1, \alpha_2 \in]-\pi/2, \pi/2[$	211
F.1	Wrench-feasible workspace without stability: Pareto front and some optimal designs (X_I, \dots, X_{VI}) of the 2-X manipulator obtained for a payload (m_p) of 2 kg and WFW disk radius (r_d) of 0.15 m. The range of the objectives are $F_{\max} \in [7.6763, 499.0914]$ N, mass $\in [0.2964, 4.5853]$ kg, size $\in [0.4017, 3.7679]$ m.	219
F.2	Manipulator suspended along gravity: Pareto front and some optimal designs (X_I, \dots, X_{VI}) of the 2-X manipulator obtained for a payload (m_p) of 2 kg and SWFW disk radius (r_d) of 0.15 m. The range of the objectives are $F_{\max} \in [39.9668, 499.8568]$ N, mass $\in [0.4385, 5.8606]$ kg, size $\in [0.6348, 5.4645]$ m.	220
F.3	Optimal designs of 2-X manipulator chosen from the Pareto fronts obtained for different design scenarios.	221

LIST OF TABLES

1.1	General properties of conventional tensegrity structures and their equivalence/consequence in mechanics [Ful62],[Sne65],[Emm64],[Mot03].	29
2.1	Effect of antagonistic forces on the stiffness of general symmetric four-bar mechanisms.	63
2.2	Classification of the antagonistically actuated joints (except prismatic) based on their stiffness modulation ability. The range of movement is given by $\theta \in] -\theta_{\max}, \theta_{\max}[$ (limb orientation) for the parallelogram mechanism and $\alpha \in]-\alpha_{\max}, \alpha_{\max}[$ (top bar orientation) for the others. A limit on the upper bound of movement is presented in “{” below the mechanism.	72
3.1	Example design of the 2-X manipulator with a payload $m_p = 2$ kg at the end-effector.	89
4.1	Comparison of velocity, force, and stiffness performances of 4-cable and 3-cable actuation schemes at identical configurations configurations. The polytopes obtained for the 4-cable (resp. 3-cable) scheme are shown in red continuous (resp. black dashed) boundary.	108
5.1	Classification of the coefficients in Eq. (5.21) and computation of their bounds.	130
5.2	2-X manipulator: Range of estimated buckling loads and the resulting safe cross-section radii for the bars along with their masses.	133
5.3	Classification of the coefficients in Eq. (5.29) and computation of their bounds.	139
5.4	2-R manipulator: Range of estimated buckling loads and the resulting safe cross-section radii for the bars along with their masses.	142
6.1	Design variables and their bounds for the 2-X and 2-R manipulators.	148
6.2	Internal parameters of the optimization solver NSGA-II along with their recommended and assumed values.	151
6.3	Force, mass, and size optimal designs for the 2-X manipulator for carrying a payload of mass 2 kg and inscribing an SWFW disk of radius 0.15 m.	155
6.4	Force, mass, and size optimal designs for the 2-R manipulator for carrying a payload of mass 2 kg and inscribing an SWFW disk of radius 0.15 m.	156
7.1	Thirty-two inverse kinematic solutions for the 3-X manipulator with geometry $b = 1, l = 2, a = 6$ and the end-effector positioned at $(x, y, z) = (3/2, 1, 3/2)$. All the angular measures are presented in radians.	178
C.1	Ranges of the estimated load and the actual load in the bars of the 2-X manipulator. The positive sign indicates compressive loading while the negative sign indicates tensile loading.	208

LIST OF TABLES

C.2	Ranges of the estimated load and the actual load in the bars of the 2-R manipulator. The positive sign indicates compressive loading while the negative sign indicates tensile loading.	209
E.1	Optimal designs on the Pareto front of the 2-X manipulator for carrying a payload of mass 2 kg and inscribing an SWFW disk of radius 0.15 m.	214
E.2	Optimal designs on the Pareto front of the 2-R manipulator for carrying a payload of mass 2 kg and inscribing an SWFW disk of radius 0.15 m.	215
F.1	Optimal designs of the 2-X manipulator for carrying a payload of mass 2 kg and inscribing an SWFW disk of radius 0.15 m in different scenarios.	218

INTRODUCTION

This thesis is devoted to the design and analysis of tensegrity-inspired systems in the context of human-robot interaction. The motivation for studying these manipulators and the structure of this thesis are presented in the following.

Motivation

Ever since robots were introduced in the industries for simple loading/unloading operations in the 1950s, their scope and performance have been expanding continuously [GS19]. Today, robots can perform several tasks such as machining and palletizing, with accuracy and repeatability that cannot be matched by humans. However, there are certain other tasks that the robots are not well-equipped to carry out, e.g., picking a ruler from the table, which a human can perform without any training. Hence, to obtain the best of both worlds, several researches have been directed towards realizing a work cell with humans and robots collaborating to achieve a task [Ake+99],[Wil+16],[Bar+19],[LLD22]. This setting can redesign the assembly lines for improved industrial productivity and open new applications for robots in assisting humans, e.g., rehabilitation [Moh20]. Despite their promising benefits, we must address critical safety issues before implementation. Several studies in this direction have emphasized that collaborative robots (or cobots) must fundamentally have the following properties:

- (i) low mass/inertia
- (ii) low stiffness

to enable safe interaction with humans [Had+08],[HZ03]. The property (i) can be addressed only through the mechanical design of the robot, while property (ii) can be addressed through its mechanical design (e.g., with soft skin covering [Pan+21]) or the actuation/control scheme (e.g., with series-elastic actuators [Yu+15]).

Evidently, the conventional serial robots in the industries are not suitable for collaborative tasks due to their large moving masses primarily contributed by the actuators. Hence, alternate architectures such as parallel/hybrid robots with all the actuators placed at the base have been proposed for human-robot interaction in [Bad+18],[Wen+21]. Other researchers have considered continuum robots with flexible links for this application [DN19].

This thesis proposes tensegrity-inspired robots composed of only tensile and compression elements for collaboration with humans. Unlike the cobots mentioned above, they retain the conventional serial architecture with rigid links and joints arranged in succession. But, they are designed with a low moving mass by fixing the actuators on the ground and using cables as transmission elements, as considered in [RZZ19]. Additionally, the rigid links are designed as trusses with bars of simple cross-sections to further reduce the moving mass of the system. In order to manage the unilateral nature of cable actuation, these robots are actuated antagonistically with a number of cables more than their degree-of-freedom (DoF). They are also equipped with springs, as in other tensegrity systems, to induce the desired stiffness, and their actuation redundancy is leveraged to modulate this stiffness as and when required. Hence, in principle, these robots can be designed with a low stiffness to enable collaboration with humans, and their

stiffness can be increased through actuation only while performing tasks like machining, which require good accuracy. This feature makes them energy efficient and functionally similar to a limb in vertebrate animals that is actuated by muscles, e.g., a human arm. The bars, cables, and springs play the roles of bones, muscles, and ligaments, respectively. Thus, the proposed tensegrity-inspired robot also qualifies as a bio-inspired system.

This thesis addresses the design and analysis problems associated with tensegrity-inspired robots, otherwise referred to as tensegrity-inspired manipulators. The following section presents the organization of this thesis.

Organization of this thesis

This thesis contains seven chapters whose contents are briefly described in the following:

- Chapter 1 reviews the literature on tensegrity systems. It presents a brief history of these systems, their fundamental properties, and their diverse adoptions in robotics. Finally, it specifies the kind of tensegrity systems that will be studied in this thesis.
- Chapter 2 considers several single-DoF tensegrity-inspired joints antagonistically actuated by two cables and evaluates their stiffness modulation properties. Among these, it shows that the anti-parallelogram mechanism (X-joint) with cables attached between the unconnected pivot pairs offers the largest orientation range of movement while offering a positive correlation between the stiffness and actuation forces, as observed in biological systems.
- Chapter 3 studies a planar manipulator composed of two X-joints, designated as the 2-X manipulator. Two actuation schemes with four and three cables, respectively, are considered. An automatic method to compute and evaluate the stable wrench-feasible workspace (SWFW) of this manipulator is proposed and illustrated with a numerical example.
- Chapter 4 studies the instantaneous velocity, force, and stiffness characteristics of the 2-X manipulator for the 4-cable and 3-cable schemes. These performances are compared at various points in the mutual workspace of the two actuation schemes.
- Chapter 5 addresses the design issues associated with planar tensegrity-inspired manipulators, considering 2-X and 2-R manipulators as illustrative examples. These include joint limits due to free length of springs, mechanical feasibility of the springs used, and safety of the constituent bars from buckling failure.
- Chapter 6 conducts design optimization of 2-X and 2-R manipulators minimizing their maximal actuation force, moving mass, and size, while they are constrained to possess a desired workspace with a point mass payload at the end-effector. Pareto optimal fronts are presented for the two manipulators and optimal designs are compared between them.
- Chapter 7 presents a modified design of the X-joint using spherical joints instead of pivots. Three modified X-joints have been arranged in two perpendicular planes to construct a spatial 3-DoF tensegrity-inspired positioning manipulator, whose kinematics and workspace are studied in detail.

Finally, the conclusions of this study and future work are presented in the last chapter.

STATE OF THE ART

Abstract

This chapter begins by highlighting the advantage of using components loaded in tension-compression modes instead of those loaded in bending. This discussion leads to the tensegrity systems, which comprise compressed components suspended in a network of continuous tension. A historical review of tensegrity systems and their applications are presented. Then, five fundamental properties of the stationary tensegrity structures are identified from the original inventions and the associated literature. These are: (a) isolated rigid bodies, (b) positive stiffness, (c) prestress, (d) tensioned and compressed components, (e) rigid bodies free from tensile loading. Subsequently, we illustrate that some properties are partially or completely compromised while tensegrity systems are adopted into robotics for various applications. Finally, we specify the type of tensegrity systems that will be studied in the rest of this thesis and the properties they satisfy, namely, (b, c, d).

Contents

1.1	Introduction	26
1.2	Conventional tensegrity systems: their properties and applications	27
1.3	Tensegrity-based mechanisms and robots in literature	29
1.3.1	Property a: Isolated rigid bodies	30
1.3.2	Property b: Positive stiffness	32
1.3.3	Property c: Prestress or self-stress	32
1.3.4	Property d: Tensioned and compressed components	34
1.3.5	Property e: Rigid bodies are never in tension	35
1.4	Scope of this thesis	35
1.5	Conclusions	36

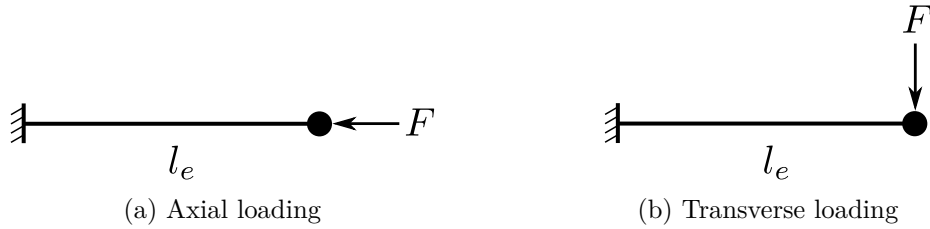


Figure 1.1 – A uniform circular cylinder of cross-section radius r_e and length l_e subjected to a load F in axial and transverse directions.

1.1 Introduction

It is well-known from the mechanics of materials that a body exhibits better resistance to deformation when loaded axially than transversally. As a simple illustration, consider a uniform circular cylinder with a cross-section radius r_e and length l_e subjected to the same load F in axial and transverse directions as shown in Figs. 1.1a and 1.1b, respectively. The former causes compression of the body, while the latter induces bending. Assuming that the loading is within the elastic limits, the deflection (δ_a) due to axial loading and the deflection (δ_t) due to transverse loading can be expressed as follows (see, e.g., [Ban09], p. 6 and p. 572):

$$\text{Axial} \implies \delta_a = \frac{Fl_e}{EA} \qquad \text{Transverse} \implies \delta_t = \frac{Fl_e^3}{3EI} \quad (1.1)$$

where E is the Young's modulus of the material, $A = \pi r_e^2$ is the cross-section area, and $I = \frac{\pi r_e^4}{4}$ is the second moment of area. Computing the ratio (δ_t/δ_a) leads to:

$$\delta_t = \frac{4}{3} \left(\frac{l_e}{r_e} \right)^2 \delta_a \quad (1.2)$$

Assuming that the length of the cylinder is ten times longer than its cross-section radius, we find that δ_t is approximately 133 times larger than δ_a . This computation clearly shows that the cylinder is more efficient in supporting loads in the axial direction than in the transverse direction. In fact, when the cylinder is loaded in compression, its maximum feasible load is only limited by buckling. This phenomenon will be considered in Chapter 5.

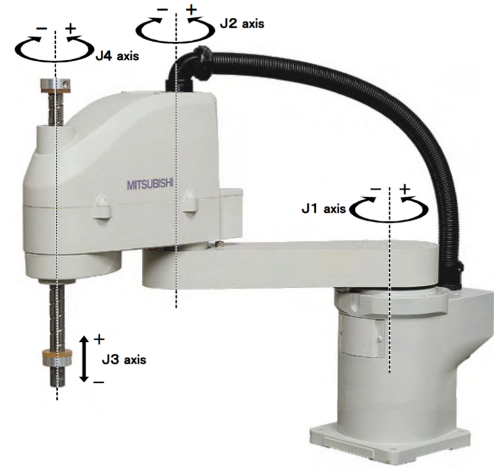
The efficient load-bearing capacity of a body in compression has been used to design robots for handling heavy payloads. For instance, the Gough-Stewart platform shown in Fig. 1.2a supports a payload of hundreds of kilograms with slender limbs loaded axially. In contrast, the SCARA (Selective Compliance Assembly Robot Arm) manipulator shown in Fig. 1.2b handles a significantly lower payload with thick cross-sections to cope with transverse loading.

This illustration shows that designing robot manipulators with links loaded axially leads to small cross-sections and low moving mass, as desired in human-robot interaction. Hence, further study in this chapter is devoted to systems primarily comprising tensile and compressive elements, also known as tensegrity systems.

The rest of this chapter is organized as follows: Section 1.2 presents a brief history of conventional tensegrity systems and their properties. Section 1.3 reviews various mechanisms and robots inspired by the tensegrity concept. Section 1.4 states the type of tensegrity-inspired mechanisms that will be considered in this thesis. Finally, Section 1.5 presents the conclusions of this chapter.



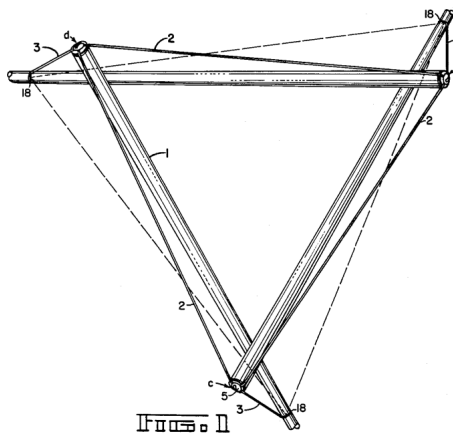
(a) Gough-Stewart platform as flight simulator (Source: [Hex])



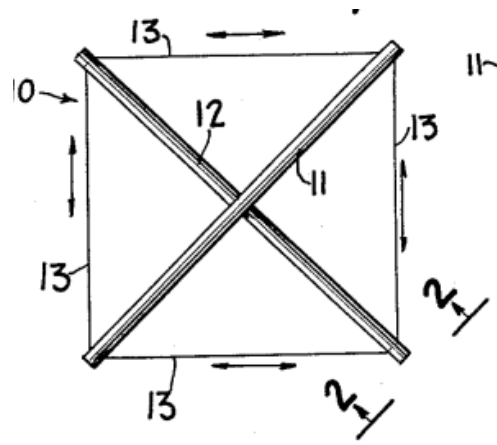
(b) SCARA robot for pick-and-place application (Source: [Sca])

Figure 1.2 – Robot manipulators with links loaded in axial (left) and transverse (right) directions.

1.2 Conventional tensegrity systems: their properties and applications



(a) Earliest patent on tensegrity structure (Source: [Ful62])



(b) Snelson X-shaped tensegrity unit (Source: [Sne65])

Figure 1.3 – Early tensegrity structures.

The term “tensegrity” was introduced by Fuller as a combination of two words “tensile” and “integrity” [Ful62] in 1962. The concept of tensegrity originated in the field of architecture and structural mechanics, with the creation of artistic structures containing isolated rigid bodies in space held together by tensioned cables [Sul09]. The earliest tensegrity structures were proposed by inventors Fuller and Snelson in 1962 and 1965, respectively. Fuller’s model contained a spatial unit with three bars connected by cables, as shown in Fig. 1.3a, while Snelson’s model contained

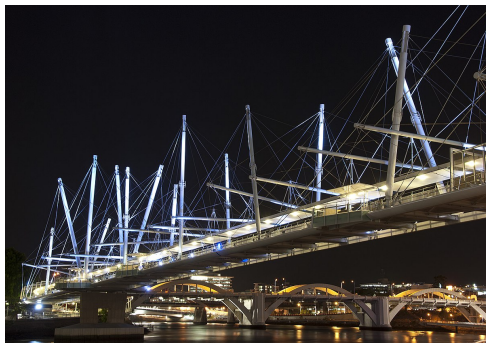


(a) Rainbow arch (Source: [SH13])



(b) Three-legged tensegrity structure (Source: [Pie+17])

Figure 1.4 – Examples of tensegrity sculptures.

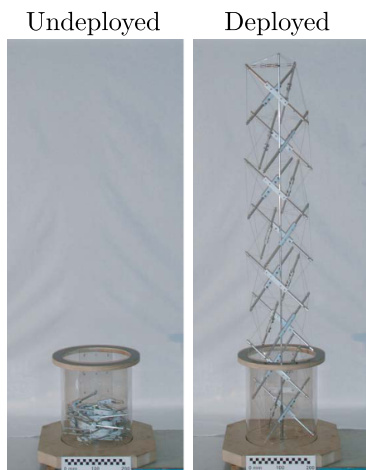


(a) Kurilpa bridge in Brisbane, Australia (Source: [Kur])

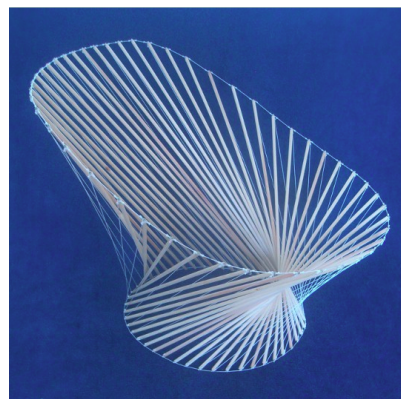


(b) Roof of a stadium in Plata, Argentina (Source: [Pla])

Figure 1.5 – Examples of tensegrity structures applied in civil and architectural engineering.



(a) Tensegrity-based deployable mast for space applications (Source: [Tib02])



(b) Tensegrity-based chair (Source: [Par])

Figure 1.6 – Examples tensegrity structures applied beyond art and architecture.

a planar unit with just two bars arranged in an X-shape with cables on the four sides, as shown in Fig. 1.3b. Snelson provides a detailed account of the invention of tensegrity in [Sne96] and clarifies that he was the original inventor of tensegrity.

At that time, the descriptions of tensegrity structures were very general, e.g., “islands of compressions in a sea of tension elements” by Fuller [Ful62], “discontinuous compression in continuous tension” by Snelson [Sne65], and “réseaux autotendants” (self-tensioning networks) by Emmerich [Emm64].

Later, in 2006, a complete definition was provided by Motro [Mot03], which states: “Tensegrity system is a system in a stable self-equilibrated state comprising a discontinuous set of compressed components inside a continuum of tensioned components.” Based on this definition and the previous descriptions, a list of important properties of conventional tensegrity structures is presented in Table 1.1.

Table 1.1 – General properties of conventional tensegrity structures and their equivalence/consequence in mechanics [Ful62],[Sne65],[Emm64],[Mot03].

Label	Property	Mechanics
a	Isolated rigid bodies	No kinematic constraints; configuration is determined only by static equilibrium equations
b	Positive stiffness	Reversible deformation upon external loading in any direction
c	Prestress or self-stress	Forces induced in the components before any external loading
d	Tensioned and compressed components	Tension: cables, springs Compression: bars/struts
e	Rigid bodies are never loaded in tension	If they are loaded in tension, they will be replaced by cables/springs

Ever since the invention of tensegrity in the 1960s, several artistic sculptures have been created, as illustrated in Fig. 1.4. They have also found applications in civil and architectural engineering with bridges and large stadium roofs constructed with bars and cables, as shown in Fig. 1.5. Furthermore, their lightweight and inherent compliance have promoted their use as deployable masts for potential space applications, as illustrated in Fig. 1.6a. The tensegrity concept can also find potential in building furniture for domestic use, like a chair shown in Fig. 1.6b. Many more examples of the applications of tensegrity systems can be found in [MPG22].

The following section reviews the adoption of tensegrity systems in robotics.

1.3 Tensegrity-based mechanisms and robots in literature

The lightweight, compliance, and deployability properties of tensegrity systems make them interesting candidates in robotics, especially in the context of human-robot interaction. A tensegrity structure is converted into a tensegrity mechanism by actuating one or more components contained in it [Ars01],[Liu+22]. Due to the actuation and other design requirements of the application, the tensegrity mechanism loses one or more properties mentioned in Table 1.1, par-

tially or entirely. Several examples from the literature are presented in the following to illustrate this fact.

1.3.1 Property α : Isolated rigid bodies

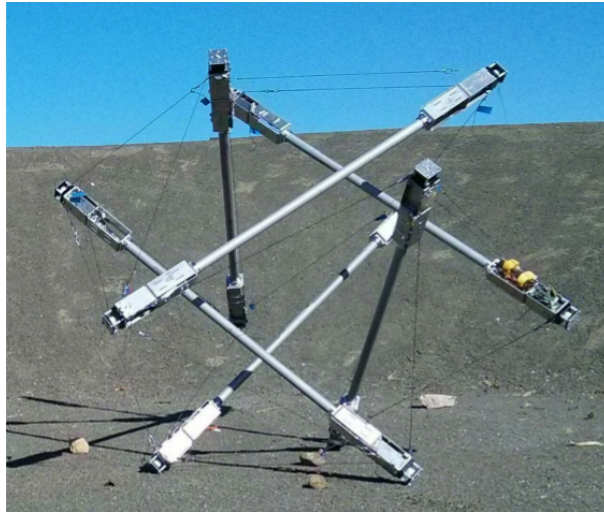


Figure 1.7 – SUPERBall tensegrity robot with no contact between rigid bodies (Source: [Sab+15]).

The SUPERball tensegrity robot shown in Fig. 1.7 contains six rigid bodies in the form of struts held together by a network of elastic cables [Sab+15]. Since the struts are isolated, each of them retain six freedoms, leading to a 36-DoF system. It is actuated by changing the cable lengths with 12 motors placed inside the ends of each strut. NASA developed this robot as a locomotory device for space exploration. More such robots used for locomotion have been reviewed in [Liu+22].

In contrast to the above application, the tensegrity robots developed for manipulation tasks have rigid bodies in contact, as shown in Figs. 1.8 and 1.9. In [SO09], such tensegrity systems are classified into different classes depending on the number of contacting rigid bodies. Practically, this contact is established to introduce kinematic constraints and limit the degree-of-freedom (DoF) of the system to what is required for the task. Such constraints also help reduce the number of equations in their static/dynamic models, thereby simplifying their analysis.

Figure 1.8a shows a spatial tensegrity module composed of six bars attached to their neighbors with spherical joints. Each module has six bars connected to their neighbors with spherical joints [AG08]. Further, the attachment points, or nodes, (A_i, B_i, C_i) (resp. $(A_{i+1}, B_{i+1}, C_{i+1})$) are constrained to be coplanar by using three sliders as shown in Fig. 1.8b. These constraints limit the DoF of the module to 6. Several such modules are stacked to form a tensegrity manipulator with a large reach, as shown in Fig. 1.8c.

There are also planar tensegrity modules, as shown in Fig. 1.9 whose movements are limited to a plane. In these mechanisms, the bars are connected by pivots instead of spherical joints to respect the planar constraint. Figure 1.9a shows a planar tensegrity mechanism with two crossed bars, inspired by Snelson’s X-shaped module (see Fig. 1.3b) [AG06]. It is a 3-DoF system that

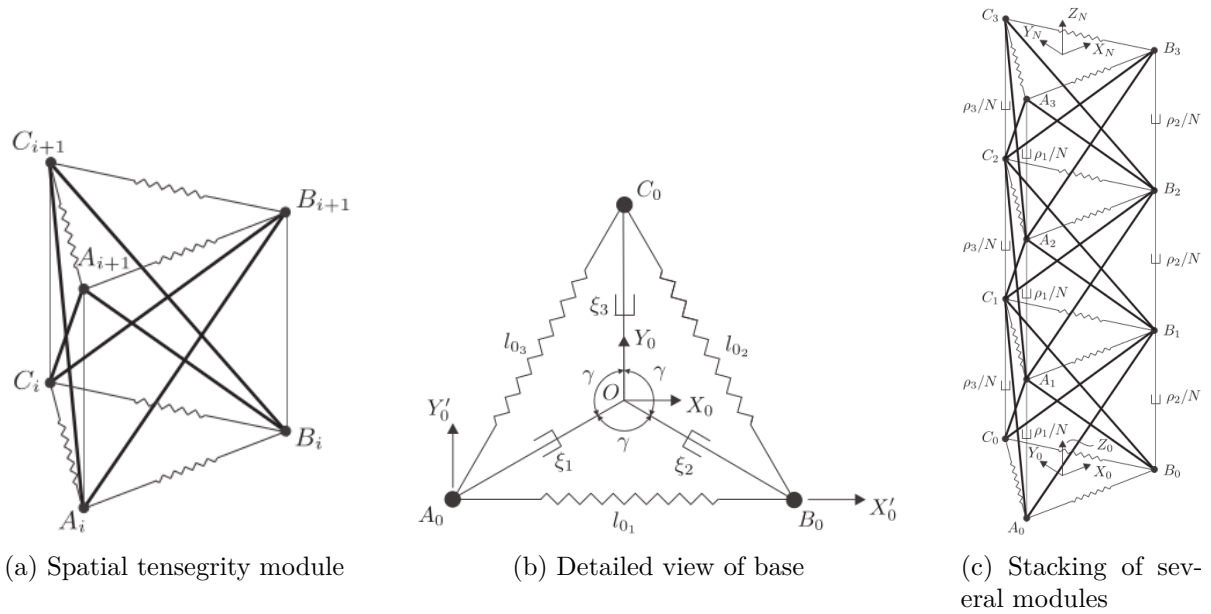


Figure 1.8 – Spatial tensegrity mechanism with contacting rigid bodies (Source: [AG08]).

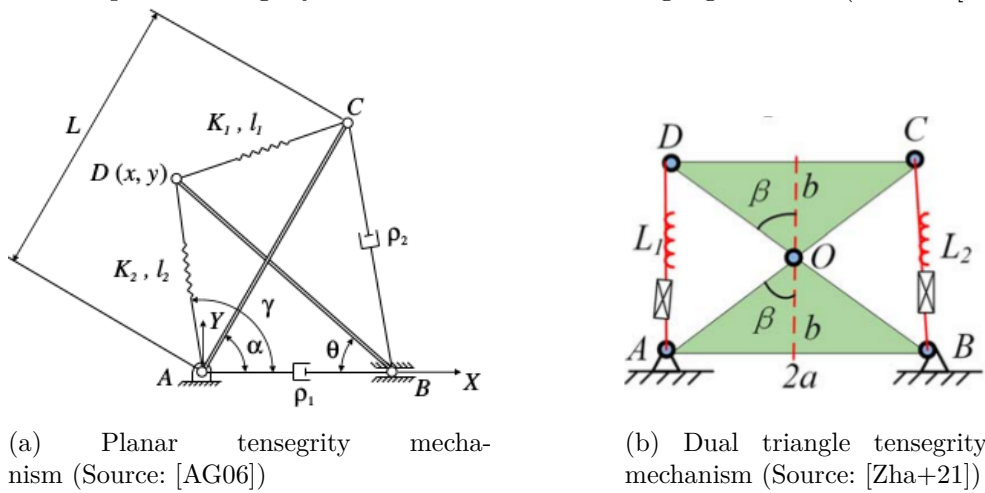


Figure 1.9 – Planar tensegrity mechanisms with contacting rigid bodies.

is actuated by the two prismatic joints labeled as ρ_1 and ρ_2 to control the position of the end-effector point D. Note that the authors of [AG06] refer to this mechanism as a 2-DoF system since two actuators are present. However, in this thesis, we use the term DoF to denote the number of independent coordinates required to define the configuration of the system completely, which is 3 for this example.

The tensegrity mechanism shown in Fig. 1.9b contains two rigid triangles connected by a revolute joint at O. It is a 1-DoF system that only permits a pure rotation about the fixed point O. It is actuated with two prismatic joints in series with springs on the two sides to control the orientation of the moving triangle.

These are examples of tensegrity mechanisms used for manipulation tasks that do not respect property (a) specified in Table 1.1.

1.3.2 Property b: Positive stiffness

Another notable property of conventional tensegrity systems is their positive stiffness and compliance. More precisely, the constituent rigid bodies exhibit compliance in all directions (three translations and three orientations). However, when it comes to tensegrity mechanisms, this feature is limited to the directions of feasible movement. For instance, the planar tensegrity mechanism in Fig. 1.9a exhibits compliance only in its plane of movement and remains rigid while it is pushed out of the plane. Indeed, this is due to the kinematic constraints imposed by the pivots which connect the rigid bodies.

Furthermore, even in the feasible directions of movement, the mechanism may not be stable at all the configurations, see, e.g., [AG06]. Hence, only the stable configurations of a tensegrity mechanism, also referred to as “tensegrity configuration” in [SO09], p. 1, must be considered in their analysis.

1.3.3 Property c: Prestress or self-stress

A unique property of conventional tensegrity systems is the prestress that can be induced in their components for stability. Additionally, this prestress can be modified by stretching or relaxing the elastic components, which in turn changes the stiffness of the structure [Gue10]. In a tensegrity mechanism, this change in prestress can be carried out implicitly using the actuators, thereby producing different stiffnesses at a given configuration. This feature will be of great interest to robots used in collaborative tasks.

The stiffness properties of the tensegrity mechanism shown in Fig. 1.10 was studied in [Ars11]. It has two crossed bars, a cable on the top, and actuators on the other three sides. The actuators on the left and right sides are used to fix the distance between the respective nodes they connect, while the actuator at the base changes the prestress of the mechanism by applying different forces. It was reported that the stiffness due to the prestress was insignificant compared to the contribution due to the axial stiffness of the bars and cables. However, in that study springs were not considered. We expect the effect of prestress to be more pronounced with the use of springs, as seen in the following examples.

Another possibility to achieve variable stiffness in a tensegrity mechanism is through antagonistic actuation, as shown in Fig. 1.11. The first example in Fig. 1.11a shows a parallelogram mechanism that is actuated by two motors in the base with springs and cables assembled in series [Boe+17a]. At a given configuration θ , the actuators change the position of the distal ends

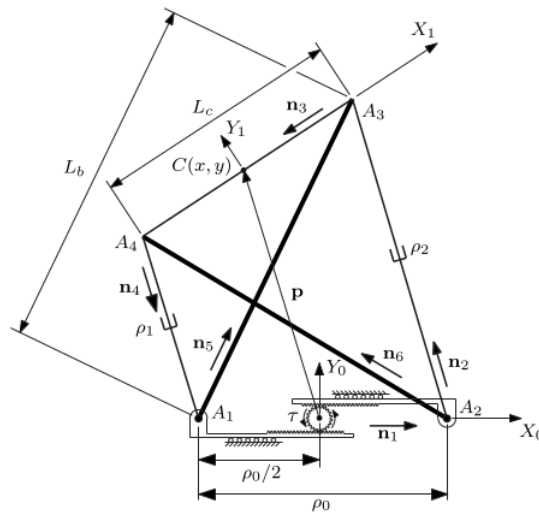
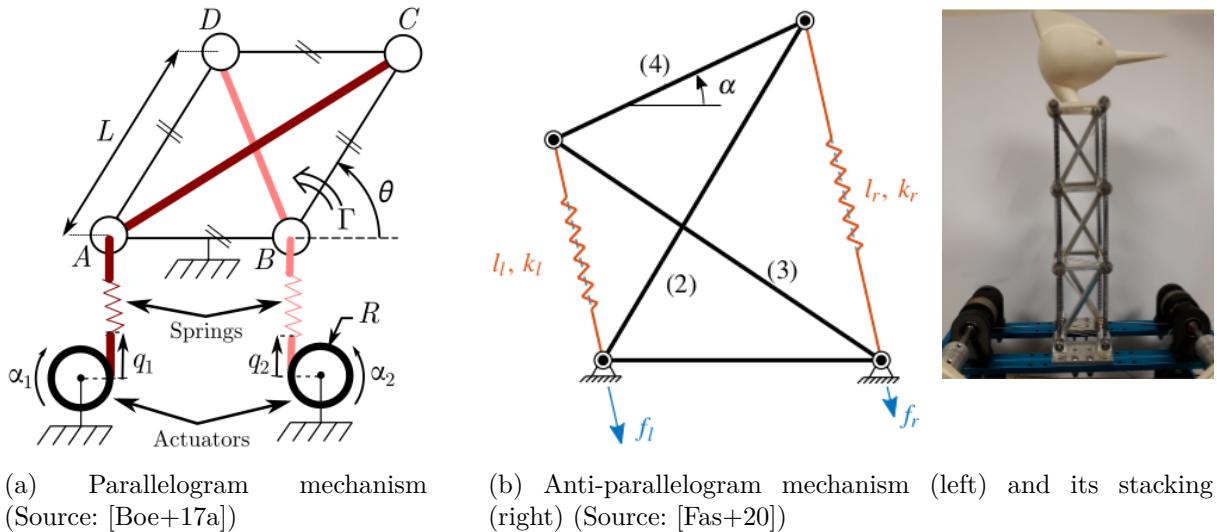


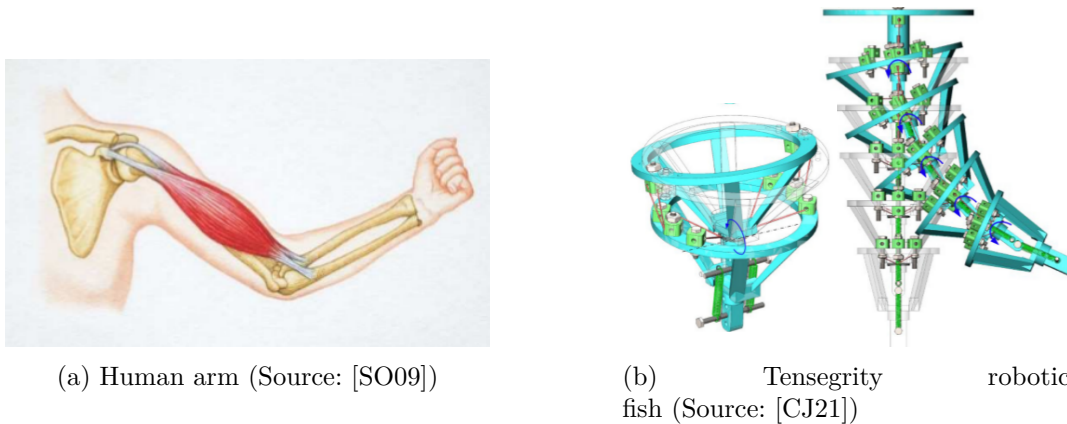
Figure 1.10 – Variable stiffness tensegrity mechanism (Source: [Ars11]).



(a) Parallelogram mechanism (Source: [Boe+17a])

(b) Anti-parallelogram mechanism (left) and its stacking (right) (Source: [Fas+20])

Figure 1.11 – Antagonistically actuated tensegrity mechanisms with variable stiffness.



(a) Human arm (Source: [SO09])

(b) Tensegrity robotic fish (Source: [CJ21])

Figure 1.12 – Applications of tensegrity mechanisms for achieving variable stiffness in bio-inspired systems.

of the springs appropriately such that the internal forces in the system change without altering its configuration, thereby varying its stiffness. This mechanism was proposed for medical applications.

A slightly different implementation of the antagonistic actuation scheme can be found in Fig. 1.11b where an anti-parallelogram is actuated by cables on the two sides with springs in parallel [Fas+20]. In contrast to the previous implementation, springs are not part of this actuation scheme, as the cables pass through them to connect to the nodes of the mechanism. Additionally, the actuators are not used as a position source but to set the tension in the cables in an open-loop scheme. Due to the antagonistic nature of the cables, there is an infinite combination of tensions that balance one another at any given configuration. This feature is used to achieve variable stiffness in the anti-parallelogram mechanism. Further, this mechanism has been stacked in series to create a manipulator inspired by a bird's neck [Fas+20].

The antagonistic arrangement of cables and stiffness modulation through tension variation is analogous to the arrangement of muscles and coactivation found in the musculoskeletal systems of animals [Lat18]. This similarity can be appreciated by comparing the anatomy of a human arm shown Fig. 1.12a ([SO09], p.8) with the tensegrity systems in Fig. 1.11. More details on this topic are provided in Chapter 2, which is devoted to studying coactivation in tensegrity systems.

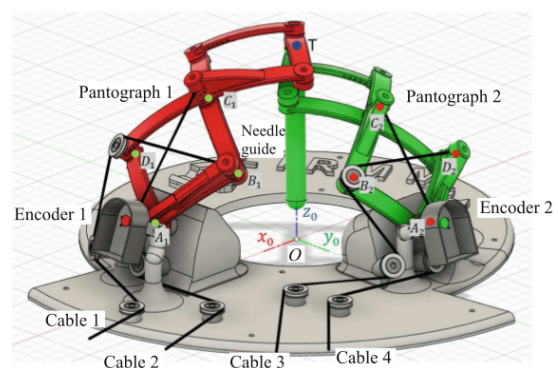
Figure 1.12b shows a tensegrity mechanism and its stacked arrangement proposed in [CJ21] for modeling the vertebrae of a fish. However, in their mechanism, the modulation of stiffness is achieved with a different principle, using a variable stiffness actuator introduced in [Ham+07].

1.3.4 Property ϑ : Tensioned and compressed components

All the tensile components, such as springs and cables, always remain in tension in all the tensegrity systems due to their unilateral force-withstanding capability. However, the rigid bodies in tensegrity systems can be subjected to different loading depending on their shape and contact with neighboring elements. For instance, the rigid bodies in Fig. 1.12b have a complex shape to cater to the attachments of various cables, which produces a complex loading pattern in them.



(a) Tensegrity-based spherical mobile robot (Source: [Böh+17])



(b) Spherical parallel tensegrity system (Source: [EJ+22])

Figure 1.13 – Tensegrity systems with curved links.

Contrary to this example, some tensegrity systems in the literature deliberately use curved links in their design motivated by specific applications. Two examples are presented in Fig. 1.13. The system considered in Fig. 1.13a is designed for a locomotion application similar to the SUPERBall tensegrity robot presented in Fig. 1.7. The rigid bodies are modeled as curved links to achieve a continuous rolling locomotion [Böh+17], which is not possible with straight links. The second example presented in Fig. 1.13b concerns the development of a device for realizing a spherical remote center of motion [EJ+22]. The authors have considered spherical pantographs, which require the axes of the revolute joints to intersect at a point and, consequently, the links to be curved. Clearly, the rigid bodies are not loaded in tension in these examples.

1.3.5 Property ϵ : Rigid bodies are never in tension

In conventional tensegrity structures, the rigid bodies are not allowed to be loaded in tension since their potential replacement with a lighter tensile element (cable/spring) is possible. However, the same does not apply to a tensegrity mechanism since the loading pattern of the bars can change from compression to tension with the configuration of the mechanism, especially while considering gravity. Hence, in general this property will not be respected by tensegrity mechanisms. For instance, the top bar in the anti-parallelogram mechanism shown in Fig. 1.11b will be loaded in tension at the presented configuration.

1.4 Scope of this thesis

Following the above discussion on tensegrity systems, this section defines the scope of this thesis. We consider 1-DoF modular tensegrity units, or joints, that can be stacked to form manipulators with two or more DoF as shown in Fig. 1.14. The details of their composition and actuation are presented in the following:

- **1-DoF joint** (Fig. 1.14a):

We consider a simple revolute joint (see Fig. 1.9b) and planar four-bar mechanisms (see Figs. 1.11a, 1.11b) as 1-DoF tensegrity joints. They are modeled as planar systems composed of bars connected by pivots, thereby avoiding bending.

These joints are actuated antagonistically with two cables whose tensions are set by the actuators fixed on the base. Hence, the control scheme is open-loop, and the joint remains compliant under external influence even while it is actuated. Indeed, this is true only when the actuators are backdrivable. We assume that direct-drive type actuators, i.e., motors without a gearbox, are used in this study. Such actuators enable backdrivability of the system and result in a low reflected inertia at the output shaft, making them suitable for interactive applications.

The tensions in the two cables are modified appropriately to achieve variable stiffness in these joints at a given configuration, as explained in Section 1.3.3 with the example of anti-parallelogram mechanism [Fas+20]. Several such joints are studied in Chapter 2.

One of the advantages of actuating the joint directly with cables, i.e., without springs in series (see Fig. 1.11a) is that, it is possible to switch to position/velocity control of the cables, if necessary, without making any changes in the hardware. Indeed, this leads to the loss of inherent compliance of the system and the variable stiffness character. But, the possibility to reconfigure the joint at the controller level makes it versatile for several

applications.

The joint is also equipped with springs in parallel to cables to ensure its stability even in the absence of actuation forces. No elasticity in the bars and cables are considered.

— **2-DoF manipulator** (Fig. 1.14b):

A 2-DoF planar manipulator can be constructed by stacking two tensegrity joints in series with rigid offsets as shown in Fig. 1.14b. The offsets are modeled as trusses with bars and pivots to ensure that they remain loaded in tension or compression modes only.

An interesting challenge in such manipulators with stacked joints is to find a suitable cable actuation scheme for them. This issue is addressed in Chapters 3 and 4 of this thesis by comparing two schemes with four cables and three cables, respectively.

Another challenge is finding good designs of these manipulators to carry a given payload over the desired workspace, while accounting for their springs and cable tensions. This problem is addressed in Chapters 5 and 6.

— **3-DoF manipulator** (Fig. 1.14c):

A 3-DoF manipulator can be constructed by arranging three tensegrity joints in two perpendicular planes as shown in Fig. 1.14c. However, since the original joints were designed with pivots in a plane, they must be redesigned with spherical joints to avoid any transmission of bending loads. The same applies to the offsets as well. These modifications are incorporated and the kinematics of the resulting 3-DoF manipulator is studied in Chapter 7. The cable actuation scheme and static model of this system is left for the future.

The joint and manipulators proposed above respect three properties (**b**, **c**, **d**) out of the five listed in Table 1.1. Hence, they will be referred to as tensegrity-inspired systems in this thesis without any discrepancy.

1.5 Conclusions

This chapter motivated the discussion on the tensegrity system with a simple example. It presented a historical review of tensegrity structures and their five fundamental properties. These properties are: (**a**) isolated rigid bodies, (**b**) positive stiffness, (**c**) prestress, (**d**) tensioned and compressed components, (**e**) rigid bodies free from tensile loading. We showed that adopting tensegrity structures into robotics and mechanisms by actuating one or more components leads to a partial or complete loss of some of its properties. Several illustrative examples from the literature were presented to demonstrate this fact. Finally, the type of tensegrity systems that will be studied in this thesis and the properties they satisfy, namely, (**b**, **c**, **d**) were stated.

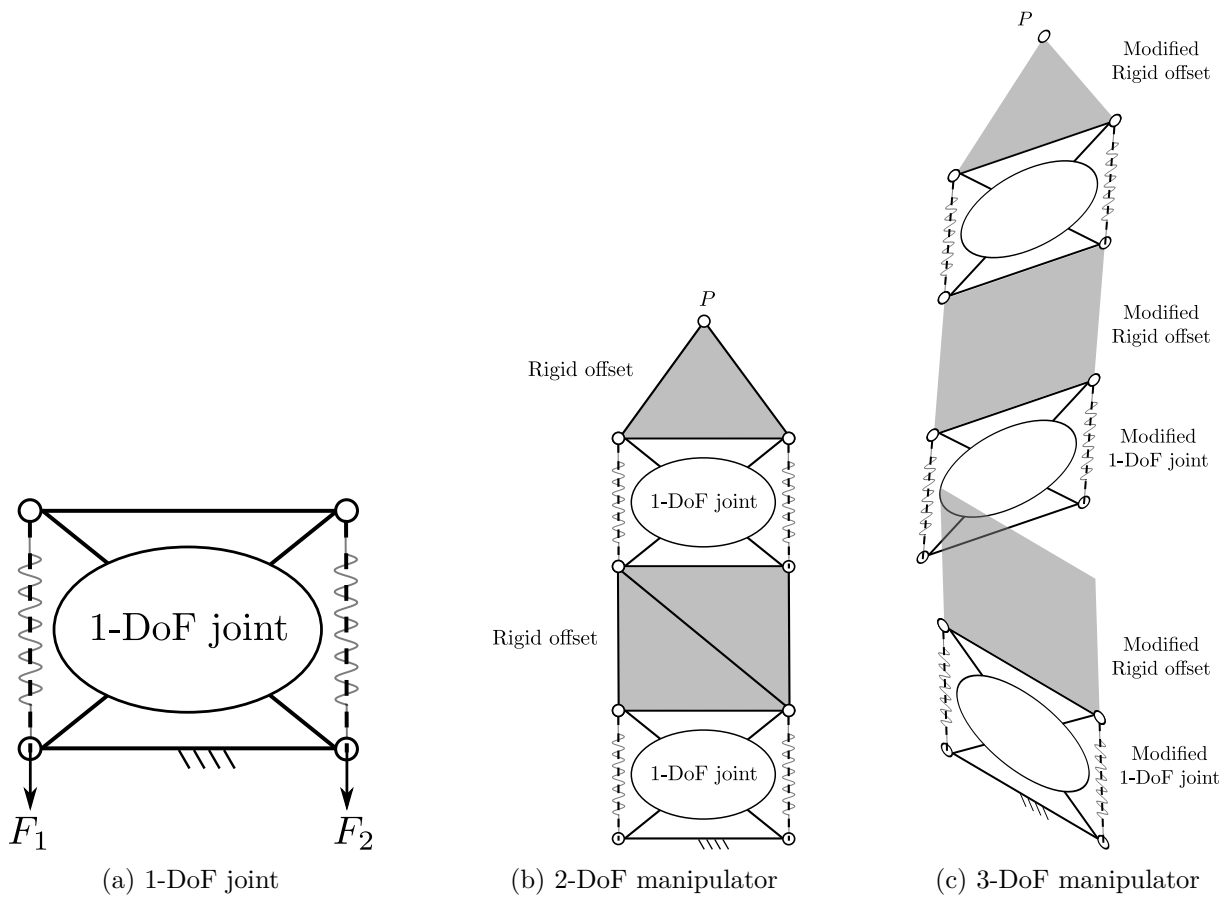


Figure 1.14 – General schematics of the tensegrity systems considered in this work.

ANTAGONISTICALLY ACTUATED TENSEGRITY-INSPIRED JOINTS

Abstract

This chapter studies single-degree-of-freedom (1-DoF) joints that are actuated antagonistically with two cables. The existence of two cables introduces an actuation redundancy of order one, which can be leveraged to tune the stiffness of the joint at a given equilibrium configuration. This work characterizes the nature of stiffness modulation in a joint based on the coefficients of actuation forces (>0) in the stiffness expression. If the coefficients are positive (resp. negative), then the stiffness of the joint can be increased (resp. decreased) by increasing the actuation forces. Joints with a positive correlation between forces and stiffness resemble the coactivation in muscles of biological joints where antagonistic muscles contract simultaneously to improve joint stiffness as and when required. This energy-efficient scheme can be used to develop bio-inspired robots suitable for low-stiffness and high-stiffness tasks. In this regard, several antagonistically actuated 1-DoF tensegrity-inspired joints, namely, revolute joint (R-joint) and symmetric four-bar mechanisms, are studied for their stiffness modulation capability. The R-joint comprises two congruent triangular trusses pivoted at a vertex and cables connecting the remaining pairs of vertices. In a four-bar mechanism, cables connect the unconnected pivot pairs. We show that the R-joint and four-bar mechanisms with non-crossed limbs have negative force coefficients within their range of movement. On the contrary, four-bar mechanisms with crossed limbs have positive force coefficients and exhibit coactivation. We present experimental validation for these results. We show through numerical examples that it is possible to achieve coactivation in the R-joint and four-bar mechanisms with non-crossed limbs by suitably modifying their cable attachments. Among all the joints discussed in this work, the anti-parallelogram mechanism offers the largest orientation range of $]-\pi, \pi[$ for the top bar w.r.t. its base while providing coactivation and is thus the best choice.

Contents

2.1	Introduction	40
2.2	General single-degree-of-freedom joint antagonistically actuated by cables	41
2.2.1	Joint description	41
2.2.2	Joint limits and symmetry	42
2.2.3	Static model and stiffness modulation	44
2.3	Stiffness of a general joint antagonistically actuated with in-series linear springs	45
2.4	Some joints and cable arrangements with no stiffness modulation	47

2.5	Revolute joint	50
2.5.1	Congruent triangles	50
2.5.2	Experimental validation	51
2.5.3	Non-congruent triangles	53
2.5.4	Elliptical pulley-based actuation [CWA23]	55
2.6	Four-bar mechanisms with symmetric limbs as joints	57
2.6.1	Description	57
2.6.2	Kinematic model of the four-bar mechanism	59
2.6.3	Anti-parallelogram mechanism	59
2.6.4	Parallelogram mechanism	60
2.6.5	General four-bar mechanisms with unequal base and top bars	62
2.6.6	Experimental validation	64
2.6.7	Alternate cable attachments for coactivation in parallelogram mechanism	66
2.6.8	Alternate cable attachments for coactivation in a general four-bar mechanism with non-crossed limbs	70
2.7	Classification of the joints and possible applications	71
2.8	Conclusions	73

2.1 Introduction

Recently, research on robotic arms with more sophisticated capabilities, such as stiffness modulation, deployability, and safe interaction with the environment, has been gaining prominence [BLG21],[PMM22]. An important source of inspiration for developing such robots stems from the nature/biological systems, e.g., human arm in [Liu+19a], giraffe’s neck in [Nii+22], bird’s neck in [Fur+22], elephant’s trunk in [Liu+19b].

One of the key differences between conventional robots and biological systems lies in their joints. While most of the robots are made up of revolute or prismatic joints, the biological systems hardly contain any of them. Instead, their joints are composed of complex surfaces in contact with one another. Some works have been dedicated exclusively to the study of kinematics of such joints, e.g., human knee in [PCS13],[HAC14]. The significance of closed kinematic chains in modeling biological movements is presented in [LSS17]. A review of the animal joints and their approximation with linkage mechanisms can be found in [Bur21].

Another interesting feature of biological joints is their actuation. Unlike conventional robots with linear or rotary actuators, they are actuated antagonistically by muscles. Typically, one set of muscle(s) contract while their antagonistic counterparts relax and vice versa to achieve the desired joint movement. However, under exceptional circumstances, both sets of muscles contract simultaneously to increase the stiffness of the joint. This phenomenon is called the coactivation of muscles in biological systems [Lat18]. This natural actuation scheme keeps the energy consumption at a minimum during regular operations and increases it through coactivation only while performing high-stiffness tasks. Inspired by this efficient scheme, variable stiffness actuators have been developed in [Van+13],[Li+22], where cables, along with non-linear springs, act as muscles to antagonistically actuate a pulley joint. The two cables are pulled (resp. released) simultaneously to increase (resp. decrease) the stiffness of this joint. However, it must be emphasized that this is possible for the pulley joint only in the presence of non-linear springs [Van+13]. There are also other designs of variable stiffness actuators that use separate motors for modulating

the effective stiffness of the springs to produce variable stiffness at the end-effector [Wol+16]. However, the scope of this study is limited to joints that use antagonistic actuators, as in the muscle actuation of a biological joint.

In this chapter, we present a different strategy to modulate the stiffness of a joint without involving springs and cams. We show that the stiffness of a joint (except the pulley joint) can be modulated at a given configuration simply by changing the tension in the antagonistic cables. In this case, the nature of modulation can be understood purely from the coefficients of forces (referred to as force coefficients) in the expression of joint stiffness. When these coefficients are positive, there is a positive correlation between the actuation forces and stiffness, as in muscle coactivation. But, if they are negative, then the joint stiffness decreases with increasing actuation forces. Interestingly, this coefficient is a kinematic quantity that depends only on the first- and second-order derivatives of the cable lengths w.r.t. a generalized coordinate. Hence, the study of stiffness modulation depends only on the kinematics of the joint and the choice of cable attachment points.

We study several joints with fixed and varying instant centers of rotation and several actuation schemes for them by modifying the attachment points of the cable to understand how their stiffness modulation ability changes. We show that this study is also relevant for joints that are actuated antagonistically with in-series linear springs, as the associated expressions contain the same coefficients (multiplied by spring stiffness) as in the other case. Using this equivalence, we corroborate some existing results in the literature on the revolute joint [CCJ18] and parallelogram mechanism [Boe+17b]. We also present experimental validation of many theoretical results.

This chapter has evolved from the following papers [MW21],[Mur+23a],[Mur+23b],[MCW23] co-written by the author. Its remaining contents are organized as follows: Section 2.2 presents the limits of movement and derives the force coefficients for a general joint antagonistically actuated by cables. Section 2.3 shows that the same force coefficients appear while using linear springs in series with the actuating cables. Section 2.4 presents some joints where no stiffness modulation can be achieved. Section 2.5 studies the revolute joint and the possibility of achieving coactivation in it. Section 2.6 deals with the four-bar mechanisms with symmetric limbs and studies their force coefficients. Section 2.7 classifies all the joints presented in this chapter based on their stiffness modulation property. Finally, Section 2.8 presents the conclusions of this work.

2.2 General single-degree-of-freedom joint antagonistically actuated by cables

A general 1-DoF joint is considered in this section. A description of its kinematic properties and cable actuation is presented in Section 2.2.1. The limits of movement of this joint is studied in Section 2.2.2, and its static model is presented in Section 2.2.3.

2.2.1 Joint description

The schematic of a general 1-DoF joint/mechanism¹ is shown in Fig. 2.1. It has a grounded base link and an end-effector whose movement is of interest to the designer. There can be several

1. In this chapter, the term “joint” is used in a generalized sense that includes 1-DoF mechanisms.

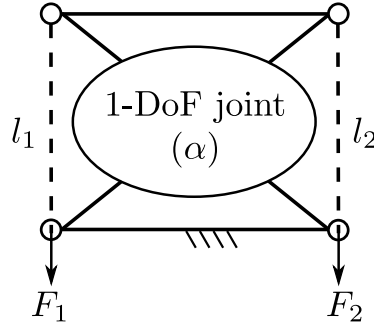


Figure 2.1 – Schematic of a general 1-DoF joint actuated antagonistically by two cables.

intermediate links between them, as in the case of four-bar and six-bar mechanisms [UPS04], but their arrangement should ensure that there is only 1-DoF between the end-effector and the fixed base at a regular configuration. The orientation of the end-effector relative to the base, denoted by α , will be used as the generalized coordinate in this study. For other joints with no change in the end-effector’s orientation, such as the prismatic joint, α will be suitably replaced by a length coordinate or another meaningful orientation coordinate.

This joint is actuated with two cables on the two sides, as indicated by dashed lines. The lengths of these cables are denoted by l_1 and l_2 , while the forces imparted by them are denoted by F_1 and F_2 , respectively. The actuation forces satisfy the condition $F_1, F_2 > 0$, respecting the unilateral actuation property of the cables. In principle, the cables are arranged such that the wrench produced by them oppose each other and can be mutually balanced. Hence, this scheme is referred to as “antagonistic” actuation by cables. It is noted that the cables are assumed to be massless and inelastic in this study.

The following sections present the limits of movement and the static model for this joint.

2.2.2 Joint limits and symmetry

The limits of movement for an antagonistically actuated joint can be due to two factors. Firstly, the degeneracy of the kinematic chain forming the joint, and secondly, the degeneracy of antagonism in cable actuation. These are explained in the following with an example.

Degeneracy of the kinematic chain

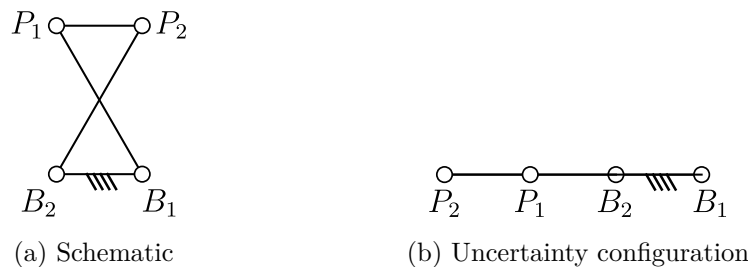


Figure 2.2 – Illustration of limit of movement due to uncertainty configuration or constraint singularity in the anti-parallelogram mechanism.

The kinematic chain forming the joint might reach an uncertainty configuration (see, e.g., [Hun78], pp. 37-39), also called a constraint singularity [ZBG02] during operation. For instance, in the case of an anti-parallelogram mechanism shown in Fig. 2.2a, the limit of movement is reached when it folds flat, i.e., when all the four pivots align (see Fig. 2.2b). When the joint reaches this configuration, it is no longer possible to determine whether it will assume the anti-parallelogram mode or the parallelogram mode. Hence, the range of movement must be limited inside such configurations. This degeneracy is only due to the kinematic chain and not related to the actuation scheme.

Degeneracy of antagonism in cable actuation

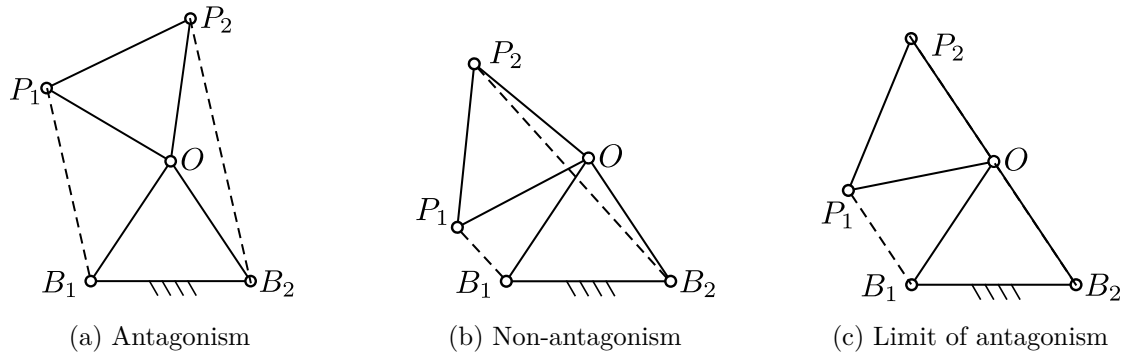


Figure 2.3 – Illustration of antagonism, non-antagonism, and limit of antagonism in cable actuation of a revolute joint.

An antagonistic arrangement of cables is illustrated for a simple revolute joint in Fig. 2.3a. However, as the joint moves, it can reach a configuration where this antagonism no longer holds (see Fig. 2.3b). In such a configuration, both cables impose wrenches in the same direction, and it is impossible to balance an arbitrary external wrench on the end-effector. Hence, the joint must not be allowed to cross the limiting configuration (see Fig. 2.3c), where the force imposed by one of the cables passes through the instant center of rotation of the joint. This configuration is referred to as the force-closure singularity [DML08]. Unlike the previous case, this singularity can change with the attachment points of the cables.

In summary, the feasible range of movement for the joint must respect the condition of antagonism in the cables and be free from degeneracies of the kinematic chain.

Symmetry

In order to simplify the analysis, we limit our study to joints with symmetric architectures and cable attachments. This consideration allows the specification of the feasible range of movement as $\alpha \in] -\alpha_{\max}, \alpha_{\max}[$, about a home configuration $\alpha = 0$. Further, it suffices to study the joint properties in just one half of its range of movement and generalize it to the other half.

2.2.3 Static model and stiffness modulation

The static model of the joint shown in Fig. 2.1 can be developed starting from its potential energy:

$$U = U_g + F_1 l_1 + F_2 l_2 \quad (2.1)$$

where U_g represents the contribution of gravity and springs (if any), $F_i l_i$ with $i = 1, 2$, represents the work done by the actuating cables. Treating α as the generalized coordinate in this study, differentiating U w.r.t. α and setting it to zero yields the static equilibrium equation:

$$\frac{dU}{d\alpha} := \frac{dU_g}{d\alpha} + F_1 \frac{dl_1}{d\alpha} + F_2 \frac{dl_2}{d\alpha} = 0 \quad (2.2)$$

Further differentiation w.r.t. α yields the stiffness (K) of the joint:

$$K := \frac{d^2 U_g}{d\alpha^2} + F_1 \frac{d^2 l_1}{d\alpha^2} + F_2 \frac{d^2 l_2}{d\alpha^2} \quad (2.3)$$

Since there are two actuation forces in a 1-DoF joint, there is an actuation redundancy of order 1. This redundancy allows an ∞ combination of equilibrating forces (F_1, F_2) to maintain equilibrium at a given configuration α . Due to the antagonistic arrangement of cables, as the joint moves within its limits $\alpha \in] -\alpha_{\max}, \alpha_{\max}[$, the length of one of the cables increases while the other decreases and vice versa. Thus, their first-order derivatives w.r.t. α , namely $\frac{dl_1}{d\alpha}$ and $\frac{dl_2}{d\alpha}$ have opposite signs inside these limits. Since these derivatives form the coefficients of the two actuation forces in the equilibrium equation, they confirm that the two forces are antagonistic. The formula also indicates that physically, $\left| \frac{dl_1}{d\alpha} \right|$, $\left| \frac{dl_2}{d\alpha} \right|$ represent the lengths of the lever arm associated with the respective cables about the instantaneous center of rotation.

The antagonistic nature of the forces requires that they increase or decrease simultaneously to maintain the equilibrium of the joint at a given configuration (α). While this change in forces preserves the joint configuration, it modifies the joint stiffness (K) at that configuration. In order to understand the evolution of stiffness with the change in actuation forces at a given configuration, one can solve for F_2 from Eq. (2.2) and substitute into Eq. (2.3) to obtain:

$$K = \gamma_1 F_1 + K_g \quad (2.4)$$

where $\gamma_1 F_1$ represents the contribution by actuation forces and K_g (devoid of actuation forces) denotes the contribution by gravity and springs (if any). The expression of γ_1 is given by:

$$\gamma_1 = \left(\frac{d^2 l_1}{d\alpha^2} + \left(\frac{-dl_1/d\alpha}{dl_2/d\alpha} \right) \frac{d^2 l_2}{d\alpha^2} \right) \quad (2.5)$$

Similarly, it is also possible to solve for F_2 from Eq. (2.2) and substitute in Eq. (2.3) to obtain the coefficient of F_2 in K as:

$$\gamma_2 = \left(\frac{d^2 l_2}{d\alpha^2} + \left(\frac{-dl_2/d\alpha}{dl_1/d\alpha} \right) \frac{d^2 l_1}{d\alpha^2} \right) \quad (2.6)$$

Due to the assumption of symmetry in the joint architecture and cable connections, l_1 and l_2 will be mutually symmetric about $\alpha = 0$, i.e., $l_1 = -l_2(\alpha)$. As a consequence, the force coefficients γ_1 and γ_2 will also satisfy $\gamma_2 = \gamma_1(-\alpha)$.

The effect of actuation forces on stiffness can be studied based on the force coefficients γ_1 and γ_2 . If $\gamma_1 > 0$ (resp. $\gamma_2 > 0$), it implies that F_1 (resp. F_2) has a positive influence on the stiffness, and the antagonistic forces exhibit coactivation in the joint. Similarly, if they are negative, then the forces negatively influence the stiffness, and there is no coactivation.

Joints with positive γ_1, γ_2 , are quite interesting because even when they become unstable due to external factors such as an addition of payload when it is placed vertically upward against gravity, they can be stabilized by simply increasing the actuation forces. This fundamental property makes them ideal candidates for mimicking muscle-actuated joints in biological systems, e.g., the elbow joint of a human arm, where its increased stability can be felt by simultaneous contraction of the associated muscles.

Interestingly, the force coefficients (γ_1, γ_2) depend only on the first- and second-order derivatives of the cable lengths w.r.t. a generalized coordinate. This property shows that the coactivation ability of the joint for a given cable actuation scheme is independent of other factors, such as gravity, springs, etc., although they influence the equilibrium configuration and the value of stiffness.

It will be shown in the next section that the study of stiffness modulation through the coefficients (γ_1, γ_2) also extends to other systems that use linear elongation springs in series with the actuators, e.g., series elastic actuators [PW95].

2.3 Stiffness of a general joint antagonistically actuated with in-series linear springs

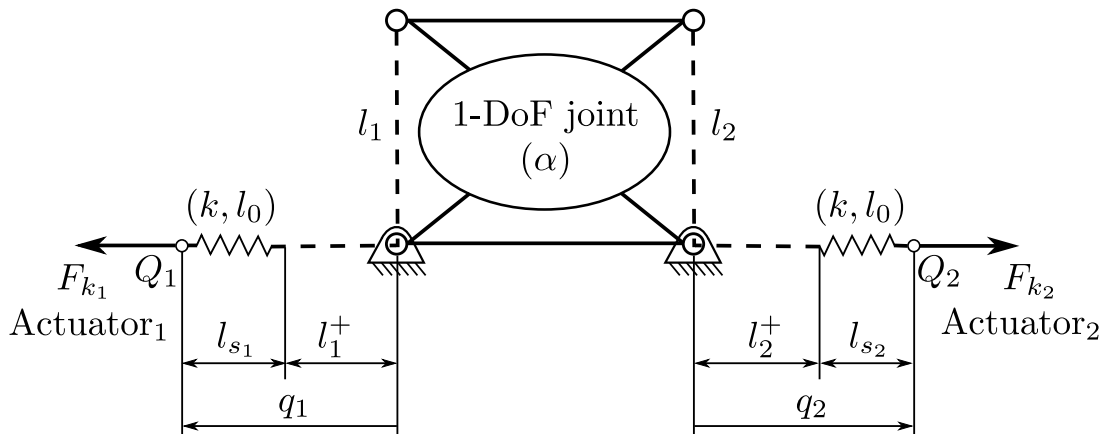


Figure 2.4 – Schematic of a general 1-DoF joint actuated antagonistically by two cables with in-series springs.

The schematic of a general 1-DoF joint that is antagonistically actuated by two motors with in-series cables and linear springs is shown in Fig. 2.4. The two springs have the same stiffness k and free length l_0 . The lengths of the cables inside the joint are denoted by l_1 and l_2 , respectively,

while those that extend outside and connect to the springs are denoted by l_1^+ and l_2^+ , respectively. However, the sum $l_i + l_i^+$, for $i = 1, 2$, remains a constant, say l_c . The motors fix the position of the nodes Q_1, Q_2 , indicated by the coordinates q_1, q_2 , respectively. For a given position of the motor coordinates, the joint reaches an equilibrium configuration (α) and exhibits stiffness due to the two springs.

Contrary to the system described in Section 2.2, where the actuators impose tension in the cables, in this one, the actuators fix/set the position of the latter ends of the springs. Consequently, the stiffness of the joint is only due to the springs. In order to modulate stiffness, the actuators modify the position of the spring ends such that the equilibrium of the joint remains intact while the elongation in the springs and the internal forces change [Wol+16].

These relations can be computed starting from the potential energy of the system (neglecting gravity):

$$U = \frac{1}{2}k(l_{s_1} - l_0)^2 + \frac{1}{2}k(l_{s_2} - l_0)^2 \quad (2.7)$$

Differentiating w.r.t. α and setting it to zero yields the static equilibrium equation:

$$\frac{dU}{d\alpha} := k(l_{s_1} - l_0)\frac{dl_{s_1}}{d\alpha} + k(l_{s_2} - l_0)\frac{dl_{s_2}}{d\alpha} = 0 \quad (2.8)$$

From Fig. 2.4, it is apparent that

$$l_{s_i} = q_i - l_i^+ = q_i + l_i - l_c \quad (2.9)$$

for $i = 1, 2$. Hence, its derivatives w.r.t. α reduce to:

$$\begin{cases} \frac{dl_{s_i}}{d\alpha} = \frac{dl_i}{d\alpha} \\ \frac{d^2l_{s_i}}{d\alpha^2} = \frac{d^2l_i}{d\alpha^2} \end{cases} \quad (2.10)$$

Substituting these in Eq. (2.8), and also replacing the term $k_i(l_{s_i} - l_0)$ by F_{k_i} , which represents the force in the springs, one obtains:

$$\frac{dU}{d\alpha} := F_{k_1}\frac{dl_1}{d\alpha} + F_{k_2}\frac{dl_2}{d\alpha} = 0 \quad (2.11)$$

The above equation is similar to the one in Eq. (2.2). Further differentiation w.r.t. α yields the stiffness expression:

$$K := F_{k_1}\frac{d^2l_1}{d\alpha^2} + F_{k_2}\frac{d^2l_2}{d\alpha^2} + \frac{dF_{k_1}}{d\alpha}\frac{dl_1}{d\alpha} + \frac{dF_{k_2}}{d\alpha}\frac{dl_2}{d\alpha} \quad (2.12)$$

When the springs are linear, i.e., $F_{k_i} = k(l_{s_i} - l_0)$, the derivatives of F_{k_i} in the last two terms simplify to:

$$\frac{dF_{k_i}}{d\alpha} = k\frac{dl_{s_i}}{d\alpha} = k\frac{dl_i}{d\alpha} \quad (2.13)$$

Substitution in Eq. (2.12) results in:

$$K = F_{k_1}\frac{d^2l_1}{d\alpha^2} + F_{k_2}\frac{d^2l_2}{d\alpha^2} + k\left(\frac{dl_1}{d\alpha}\right)^2 + k\left(\frac{dl_2}{d\alpha}\right)^2 \quad (2.14)$$

Solving for the actuation input q_2 (or equivalently F_{k_2}) from Eq. (2.8) and substituting in the above expression of stiffness leads to:

$$K = \gamma_1 F_{k_1} + k \left(\frac{dl_1}{d\alpha} \right)^2 + k \left(\frac{dl_2}{d\alpha} \right)^2 \quad (2.15)$$

where $\gamma_1 = \frac{d^2 l_1}{d\alpha^2} + \left(\frac{-dl_1/d\alpha}{dl_2/d\alpha} \right) \frac{d^2 l_2}{d\alpha^2}$ is same force coefficient that was presented in Eq. (2.5). Upon substituting for the expression of $F_{k_1} = k(q_1 + l_1 - l_c - l_0)$, one obtains:

$$K = k\gamma_1 q_1 + \text{other terms} \quad (2.16)$$

The above equation shows that the effect of redundant actuation input q_1 is characterized by the coefficient $k\gamma_1$, which is nothing but the force coefficient (derived in the previous section) amplified by the spring stiffness. Hence, the nature (increase/decrease) of stiffness modulation with q_1 remains equivalent to the modulation obtained by simply imposing tension in the cables without any springs.

However, it should be noted that the above equivalence holds only for linear springs in series with the actuator. If the springs are non-linear, then the term $\left(\frac{dF_{k_i}}{d\alpha} \right)$ will not reduce to a function of α as presented in Eq. (2.13). Instead, it will contain the actuation input q_i and introduce new terms that modulate stiffness in Eq. (2.16).

Since most of the existing tensegrity-inspired systems in the literature use in-series linear springs with the actuator [Boe+17b],[Zha+21][CCJ18], this study establishes the relevance of coefficients (γ_1, γ_2) in their designs as well.

In the subsequent sections, the nature of γ_1, γ_2 is studied for various joints.

2.4 Some joints and cable arrangements with no stiffness modulation

A set of joints and cable arrangements are shown in Fig. 2.5. The first one is a prismatic joint (see Fig. 2.5a) connected to cables on the two sides parallel to the sliding direction. The second one termed the circle-circle joint, represents the pure rolling of one circle over another with the same geometry, actuated by cables connected at their diametric ends. The third one represents a pulley joint, a simple revolute joint actuated with a circular pulley to maintain a constant lever arm for the cables. The fourth one, the pulley-2 joint, is also a pulley joint, but the cables are attached at different distances from the center. Among all the joints discussed in this work, the pulley-2 joint is the only one that features an asymmetric attachment of cables. Though such joints are out of the scope of this work, we present this one to illustrate the special nature of this joint.

The limits of movement of each of these joints and their stiffness modulation capabilities are studied by deriving their force coefficients (γ_1, γ_2) (see Eqs. (2.5),(2.6)) in the following:

- **Prismatic joint** [Fig. 2.5a]: From the schematic, it is observed that the antagonism of the system is preserved only when the block remains between the cable attachment points on the base. Hence, when we limit the block to this range, the sum of the cable

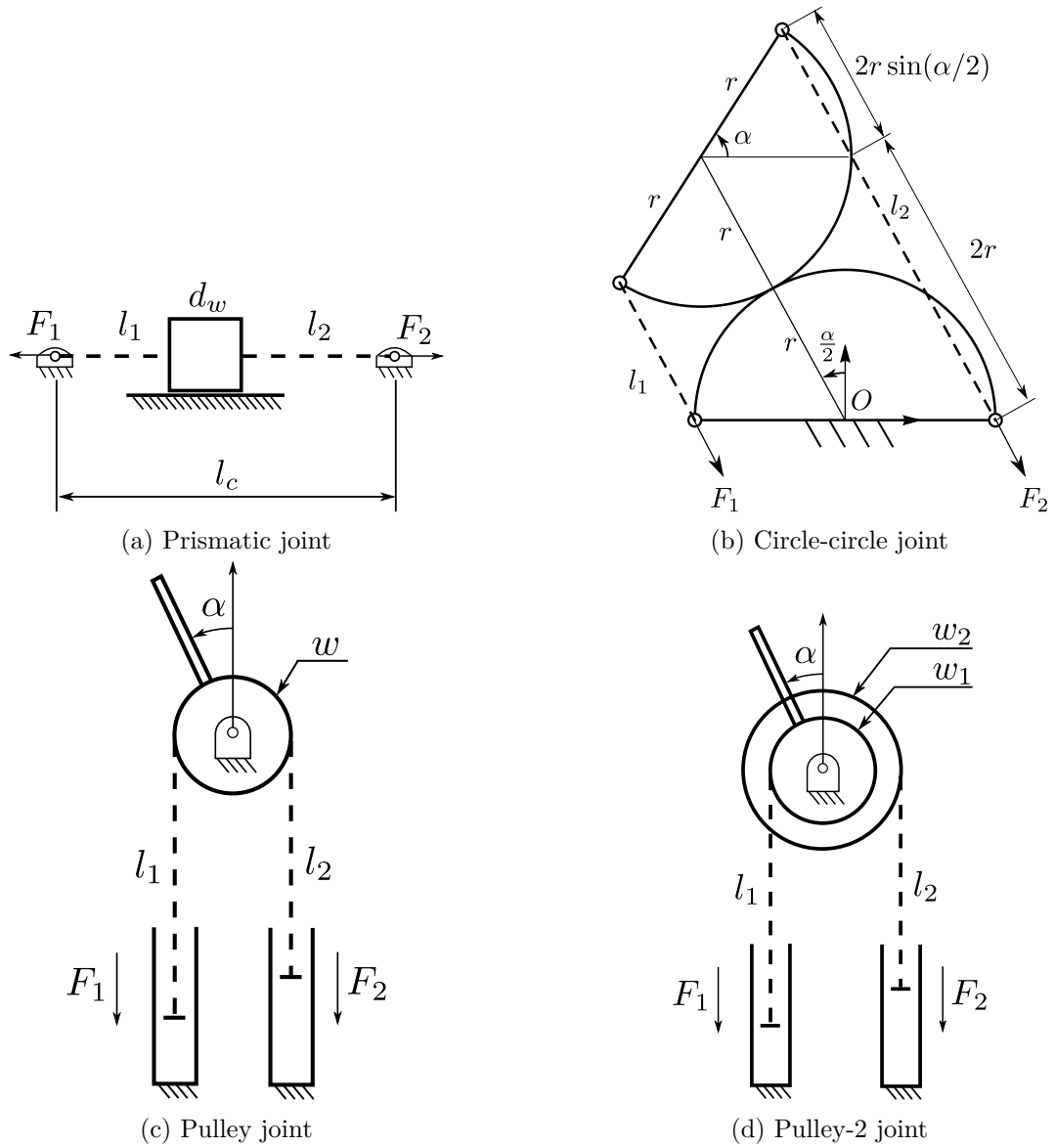


Figure 2.5 – Joints and cable attachments that do not permit modulation of stiffness.

lengths $(l_1 + l_2) = (l_c - d_w)$ remains constant. When we consider l_1 to be the generalized coordinate for this joint, the cable lengths and force coefficients are derived as follows:

$$\begin{cases} l_1 := l_1 \\ l_2 := l_c - d_w - l_1 \end{cases} \implies \begin{cases} \frac{dl_1}{d\alpha} = 1 \\ \frac{dl_2}{d\alpha} = -1 \end{cases} \implies \begin{cases} \frac{d^2 l_1}{d\alpha^2} = 0 \\ \frac{d^2 l_2}{d\alpha^2} = 0 \end{cases} \implies \begin{cases} \gamma_1 = 0 \\ \gamma_2 = 0 \end{cases} \quad (2.17)$$

- **Circle-circle joint** [Fig. 2.5b]: From the schematic, it is evident that the movement of this joint is limited by the vanishing of a cable length, which results in a feasible range of $\alpha \in] - \pi, \pi[$. The cable lengths and the force coefficients can be computed as follows:

$$\begin{cases} l_1 := 2r(1 + \sin(\alpha/2)) \\ l_2 := 2r(1 - \sin(\alpha/2)) \end{cases} \implies \begin{cases} \frac{dl_1}{d\alpha} = r \cos(\alpha/2) \\ \frac{dl_2}{d\alpha} = -r \cos(\alpha/2) \end{cases} \implies \begin{cases} \frac{d^2 l_1}{d\alpha^2} = -(r/2) \sin(\alpha/2) \\ \frac{d^2 l_2}{d\alpha^2} = (r/2) \sin(\alpha/2) \end{cases} \\ \implies \begin{cases} \gamma_1 = 0 \\ \gamma_2 = 0 \end{cases} \quad (2.18)$$

- **Pulley joint** [Fig. 2.5c]: The range of movement for this joint is unlimited, as one could wind the cables around the pulley any number of times. Assuming that the cable lengths at $\alpha = 0$ are l^0 , further computations can be made as follows:

$$\begin{cases} l_1 := l^0 + w\alpha \\ l_2 := l^0 - w\alpha \end{cases} \implies \begin{cases} \frac{dl_1}{d\alpha} = w \\ \frac{dl_2}{d\alpha} = -w \end{cases} \implies \begin{cases} \frac{d^2 l_1}{d\alpha^2} = 0 \\ \frac{d^2 l_2}{d\alpha^2} = 0 \end{cases} \implies \begin{cases} \gamma_1 = 0 \\ \gamma_2 = 0 \end{cases} \quad (2.19)$$

- **Pulley-2 joint** [Fig. 2.5d]: The only difference from the previous case is that cables are attached to pulleys of different radii, which leads to:

$$\begin{cases} l_1 := l^0 + w_1\alpha \\ l_2 := l^0 - w_2\alpha \end{cases} \implies \begin{cases} \frac{dl_1}{d\alpha} = w_1 \\ \frac{dl_2}{d\alpha} = -w_2 \end{cases} \implies \begin{cases} \frac{d^2 l_1}{d\alpha^2} = 0 \\ \frac{d^2 l_2}{d\alpha^2} = 0 \end{cases} \implies \begin{cases} \gamma_1 = 0 \\ \gamma_2 = 0 \end{cases} \quad (2.20)$$

Since the force coefficients are zero for all the joints in Fig. 2.5, it is impossible to modulate their stiffness by changing the tension in the cables. Hence, the redundancy in cable actuation does not allow stiffness tuning. In these scenarios, the proposed actuation scheme is not reasonable unless alternate means justify the use of redundant cables and actuators.

Interestingly, a single motor can actuate three of these joints (prismatic, circle-circle, pulley). This feature is evident from the expression of their cable lengths l_1 and l_2 , which sum up to a constant. Hence, the two cables can be connected on either side of a prismatic/rotary actuator to provide a remote actuation of the joint without any redundancy. However, this does not apply to the pulley-2 joint shown in Fig. 2.5d, as the sum of cable lengths vary with α .

We stress that the above observations on stiffness modulation hold only for this specific cable arrangement. If one changes the attachment points of the cables, the results could vary. For instance, in the case of the prismatic joint, we can show that shifting the attachment points in the direction perpendicular to the joint movement allows for stiffness tuning as the cable lengths become non-linear functions of the movement parameter. Similarly, the circle-circle joint with cables attached vertically above (resp. below) the diametric ends of the moving (resp. fixed) circles

results in negative values for γ_1, γ_2 , indicating a negative correlation between forces and stiffness [Mur+23b]. However, unlike these joints, no possible arrangement of cables can modulate the stiffness of the pulley and pulley-2 joints. This feature is attributed to the tangential connection of the cables and the resulting linear relationship between cable lengths and α (see Eq. (2.19), (2.20)). However, it is the most commonly used joint in the variable stiffness/impedance actuators with in-series springs [Van+13]. Due to its zero force coefficients, the designers are forced to introduce quadratic springs to modulate stiffness in that joint [ER99],[GT15], or construct complex mechanisms/cam systems with linear springs to produce non-linear stiffness behavior [Xio+22].

Based on the above study, we have two necessary conditions on cable lengths for a joint to allow for variable stiffness:

- The sum of the cable lengths must not be a constant.
- The cable lengths must not be an affine function of the generalized coordinate (α).

The following sections study tensegrity-inspired joints that allow for stiffness modulation.

2.5 Revolute joint

A classical revolute joint (R-joint), which offers rotation about a fixed center, is considered. Since the previous section showed that using a pulley-based actuation does not allow for stiffness modulation, we investigate an alternate arrangement of cables in the following.

2.5.1 Congruent triangles

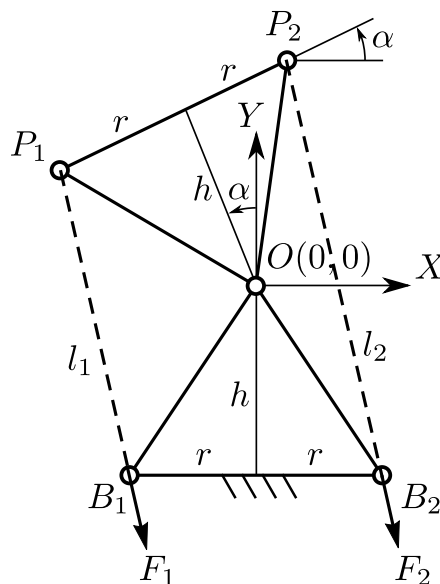


Figure 2.6 – Schematic of an R-joint with congruent triangular trusses actuated antagonistically by two cables (dashed lines).

The schematic of an R-joint composed of bars is shown in Fig. 2.6. It comprises two congruent

isosceles triangles (each consisting of three bars joined by pivots²), one inverted on top of the other. The semi-base length r and height h specify the geometry of these triangles. This study considers the orientation (α) of the top bar relative to its base as the generalized coordinate. At $\alpha = 0$, the top and base bars are parallel to each other and the joint is at a symmetric home configuration. From this configuration, it can rotate by an amplitude of α_{\max} in the clockwise and counterclockwise directions, limited by the force-closure singularities at the two extremes.

The amplitude of movement varies with the geometry of the joint as [MW21]:

$$\alpha_{\max} = \begin{cases} 2 \arctan(h/r), & \text{if } r > h \\ 2 \arctan(r/h), & \text{if } r < h \\ \frac{\pi}{2}, & \text{if } r = h \end{cases} \quad (2.21)$$

The study of stiffness modulation requires the computation of the cable lengths. From Fig. 2.6, these are found to be:

$$\begin{cases} l_1 = 2(h \cos(\frac{\alpha}{2}) - r \sin(\frac{\alpha}{2})) \\ l_2 = 2(h \cos(\frac{\alpha}{2}) + r \sin(\frac{\alpha}{2})) \end{cases} \quad (2.22)$$

Computing their derivatives w.r.t. α and finding the force coefficients (γ_1, γ_2) using Eqs. (2.5),(2.6), results in:

$$\begin{cases} \gamma_1 = \frac{-hr}{r \cos(\frac{\alpha}{2}) - h \sin(\frac{\alpha}{2})} \\ \gamma_2 = \frac{-hr}{r \cos(\frac{\alpha}{2}) + h \sin(\frac{\alpha}{2})} \end{cases} \quad (2.23)$$

It can be shown that the denominators in both expressions are positive, while $\alpha \in]-\alpha_{\max}, \alpha_{\max}[$, with α_{\max} in Eq. (2.21). Hence, both γ_1 and γ_2 are negative, implying a negative correlation between the actuation forces and the stiffness for all geometries of this joint. This property indicates that the R-joint with congruent triangles is suitable for stiffness modulation, but it does not offer coactivation as might be required for building bio-inspired joints/manipulators. This result is interesting and non-intuitive. But, it is consistent with the findings in [CCJ18] (case 8 in Table 2 of [CCJ18]), where the authors provide an example of R-joint with similar architecture driven by actuators with in-series linear springs on the two sides.

We conduct experiments to verify this result in the next section.

2.5.2 Experimental validation

This section presents experiments on an R-joint with congruent triangles to confirm the negative correlation between actuation forces and stiffness. The experimental setup can be found in Fig. 2.7. The congruent trusses are in the form of equilateral triangles with side 0.05 m, resulting in $r = 0.025$ m and $h = 0.043$ m. The joint is equipped with a spring of stiffness 500 N/m on each side with external supports (see Fig. 2.7) to ensure stability in the absence of actuation forces.

The variation of stiffness due to actuation forces is studied at the zero orientation shown in Fig. 2.7, by applying equal forces on the two cables $F_1 = F_2 = F_{\text{ant}}$. Three experiments are

2. In this thesis, the term pivot represents the connection between two neighboring elements (bars/springs), while the term revolute joint (R-joint) refers to the complete joint module inclusive of the two triangles.

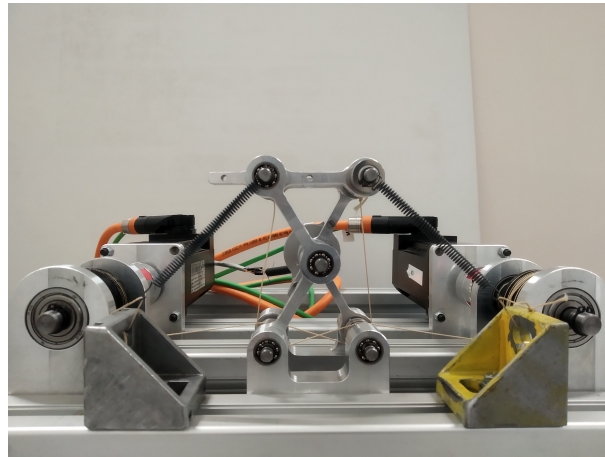


Figure 2.7 – Experimental setup of an R-joint with congruent triangles.

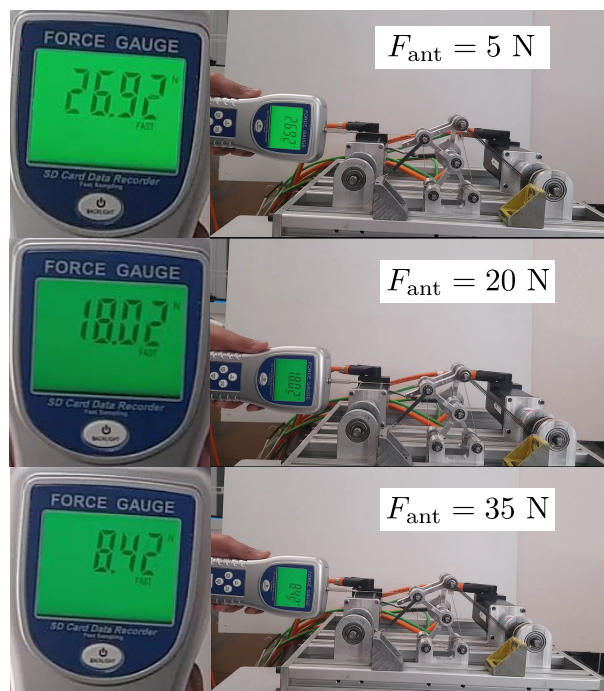


Figure 2.8 – External force required to produce the same displacement in the R-joint for different antagonistic actuation forces $F_1 = F_2 = F_{ant}$.

conducted on the joint by setting different values of $F_{\text{ant}} = 5, 20, 35$ N. In each case, the stiffness of the joint is studied by applying an external force with a dynamo-meter, as shown in Fig. 2.8. In order to enable a comparison between the results of the three experiments, the external force is regulated to produce the same displacement in the joint as observed in Fig. 2.8. From the readings of the dynamo-meter on the left part of the figures, it is apparent that the external force required decreases with the increase in actuation force F_{ant} . These results confirm that the antagonistic forces decrease the stiffness of the R-joint with congruent triangles.

To further illustrate the loss of stiffness in the R-joint, another experiment is conducted. In this case, the stiffer springs are replaced by ones with 100 N/m so that the joint has a low stiffness at zero orientation. The goal is to demonstrate the collapse of the joint by increasing the actuation forces $F_1 = F_2 = F_{\text{ant}}$ linearly with time, while no external forces are imposed. It was found that the joint loses stability and falls off when F_{ant} reaches 37.3 N. A video recording of this experiment can be found in the following link³.

The following section investigates the possibility of achieving coactivation in the R-joint using triangles of different geometry.

2.5.3 Non-congruent triangles

Since it has been shown that the coactivation property depends only on the first- and second-order derivatives of the cable lengths, this section studies different cable attachments for the R-joint to enable coactivation in it.

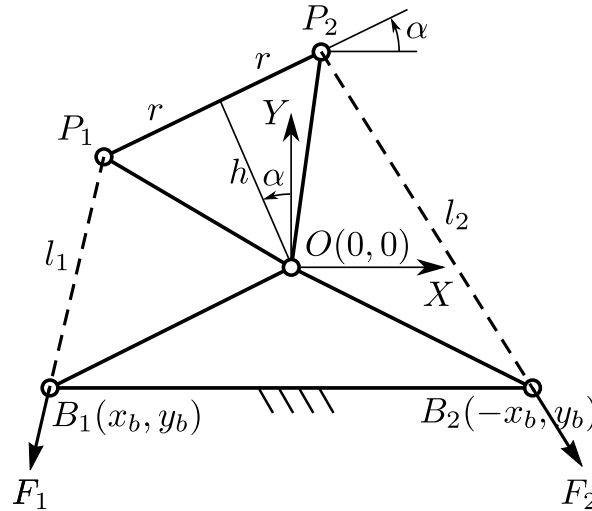


Figure 2.9 – Schematic of an R-joint with non-congruent triangular trusses actuated antagonistically by two cables (dashed lines).

The schematic of the R-joint composed of non-congruent triangular trusses is shown in Fig. 2.9. The geometry of the base triangle is parametrized by (x_b, y_b) . The cable attachment points B_1 and B_2 are placed symmetrically w.r.t. the Y-axis to preserve the symmetry of the joint about the home configuration $\alpha = 0$.

3. <https://youtu.be/itU7fgHq4ro?si=lHZskDNI2ijuH1yI>

Note that modifying the base triangle modifies the limits of movement of the joint as well. The formula presented in Eq. (2.21) is no longer valid. The new limits ($\pm\alpha_{\max}$) can be found from the collinearity of the cable attachment points with the center of rotation O .

The new cable lengths are found to be:

$$\begin{cases} l_1 := \|P_1 B_1\| = \sqrt{h^2 + 2(hx_b + ry_b) \sin \alpha + 2(rx_b - hy_b) \cos \alpha + r^2 + x_b^2 + y_b^2} \\ l_2 := \|P_2 B_2\| = \sqrt{h^2 - 2(hx_b + ry_b) \sin \alpha + 2(rx_b - hy_b) \cos \alpha + r^2 + x_b^2 + y_b^2} \end{cases} \quad (2.24)$$

The force coefficients γ_1, γ_2 can be obtained from Eqs. (2.5),(2.6). However, their expressions are not presented here due to their large size. But, they satisfy the symmetry condition due to configuration: $\gamma_1(x_b, y_b, \alpha) = \gamma_2(x_b, y_b, -\alpha)$. Additionally, for every attachment point $B_1(x_b, y_b)$ and its mirror image $B'_1(x'_b, y'_b)$ about the line $OP_1(\alpha = 0)$, the force coefficients satisfy the relation: $\gamma_1(x_b, y_b, \alpha) = \gamma_2(x'_b, y'_b, \alpha)$. It is also apparent that the limits of movement remain the same while the cables are attached at (B_1, B_2) or (B'_1, B'_2) , as the joint must rotate by the same amplitude to reach the force-closure singularity (see Fig. 2.10 and attachment point B_1 and B'_1 for the left cable). The only difference between these two scenarios is that the direction of the moment imposed by the respective cable is reversed.

In order to achieve coactivation in the above joint, the force coefficients must be positive. However, since their expressions are difficult to analyze analytically, we consider γ_1 at the home configuration ($\alpha = 0$) (similar to [CCJ18]):

$$\gamma_1(\alpha = 0) = -\frac{2(h^2 - hy_b + r(r + x_b))(-hy_b + x_b(r + x_b) + y_b^2)}{((h - y_b)^2 + (r + x_b)^2)^{3/2}} \quad (2.25)$$

It is apparent that the denominator is always positive. But, there are two non-trivial factors in the numerator along with a negative sign. Hence, for $\gamma_1(\alpha = 0) > 0$ to be satisfied, they should differ in their signs. After some manipulations, the two factors can be written as follows:

$$\mathcal{L} := rx_b - hy_b + r^2 + h^2 \quad (2.26)$$

$$\mathcal{C} := \left(x_b - \left(\frac{-r}{2}\right)\right)^2 + \left(y_b - \frac{h}{2}\right)^2 - \left(\frac{\sqrt{r^2 + h^2}}{2}\right)^2 \quad (2.27)$$

Evidently, in terms of the coordinates of B_1 , the factor $\mathcal{L} = 0$ describes a straight line, and $\mathcal{C} = 0$ describes a circle (see Fig. 2.10). From the expressions, it is clear that the circle $\mathcal{C} = 0$ has its center at $(-r/2, h/2)$ and has a radius of $\sqrt{r^2 + h^2}/2$, which makes it passes through the origin and point P_1 at $\alpha = 0$. It can also be shown that the straight line $\mathcal{L} = 0$ is tangential to the circle at point P_1 when $\alpha = 0$. Hence, the condition to achieve coactivation with the R-joint comprising non-congruent triangles at $\alpha = 0$ can be written as follows:

$$\gamma_1(\alpha = 0) > 0 \implies \begin{cases} \text{Always,} & \text{when } (\mathcal{L} < 0) \\ \mathcal{C} < 0, & \text{when } (\mathcal{L} > 0) \end{cases} \quad (2.28)$$

It is possible to show that these conditions are equivalent to the ones derived by the authors in [CCJ18]. However, after deriving these conditions, they imposed geometric conditions on the joint equivalent of $x_b < -r$ and $y_b < 0$ for the ease of analysis. These conditions ensured $\mathcal{C} > 0$ by default, leaving them with the only condition $\mathcal{L} < 0$ in further steps.

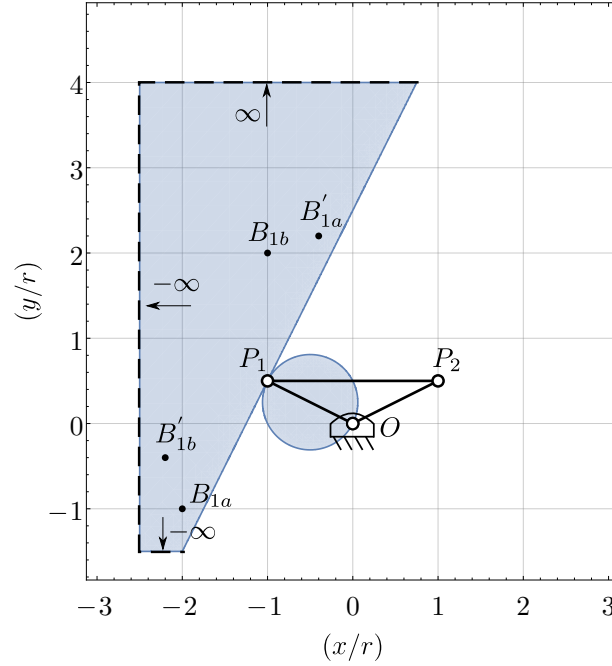


Figure 2.10 – Feasible region for the cable attachment point B_1 to achieve coactivation at the configuration $\alpha = 0$ rad in the R-joint (non-congruent triangles) with $r = 1, h = 1/2$.

As an illustration, the feasible region for the attachment point B_1 is shown along with the joint for parameters $r = 1, h = 1/2$ in Fig. 2.10. Note that the scale of the joint has been normalized w.r.t. r without any loss of generality. It is observed that the feasible region is symmetric about the line $OP_1(\alpha = 0)$, which is to be expected due to the symmetry relation $\gamma_1(x_b, y_b, \alpha) = \gamma_2(x'_b, y'_b, \alpha)$. Since the symmetric attachment points B_1 and B'_1 offer the same joint limits and force coefficients, the choice between them can be made based on secondary factors such as compactness or ease of motor placement.

For further study, we choose two points $B_{1a} = (-2, -1)$ and $B_{1b} = (-1, 2)$ inside the feasible region as shown in Fig. 2.10. The schematic of the resulting joints with cable attachment points and the plots of γ_1, γ_2 inside their respective joint limits are presented for B_{1a} in Fig. 2.11 and for B_{1b} in Fig. 2.12. In both cases, we observe that the force coefficients remain positive inside their entire joint limits, indicating that both attachment points offer coactivation at all feasible configurations of the R-joint. Since the attachment point B_{1a} is closer to the limiting boundary than B_{1b} (see Fig. 2.10), the associated value of force coefficients are smaller near $\alpha = 0$ (see Figs. 2.11b and 2.12b). However, as a compromise, the attachment at B_{1a} offers a larger range of movement than its counterpart. Hence, the designer must choose the attachment points appropriately depending on which feature is more significant for the task.

2.5.4 Elliptical pulley-based actuation [CWA23]

In [CWA23], the authors propose another interesting arrangement of cables that can modulate the stiffness of a revolute joint. They use elliptical pulley (with semi-major axis b and semi-minor axis a) constructed around a fixed center and consider symmetric cable attachments

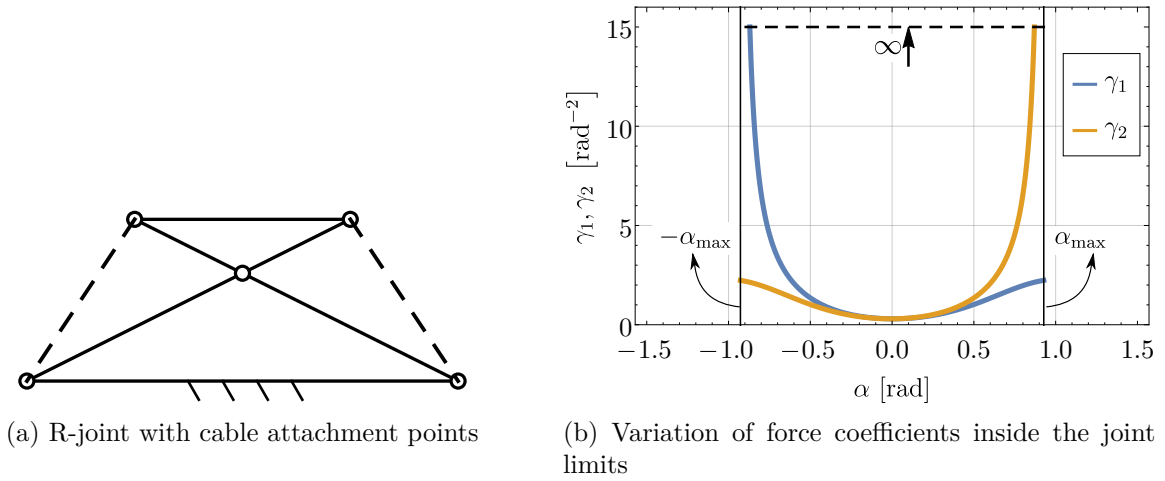


Figure 2.11 – R-joint with $r = 1, h = 1/2$ whose left (resp. right) cable is attached to $B_{1a} = (-2, -1)$ (resp. $B_{2a} = (2, -1)$) at the base. The plot of force coefficients within its limits of movement $\pm\alpha_{\max} = \pm 0.93$ rad. The force coefficient γ_1 (resp. γ_2) tends to infinity asymptotically as α approaches the limit $-\alpha_{\max}$ (resp. α_{\max}).

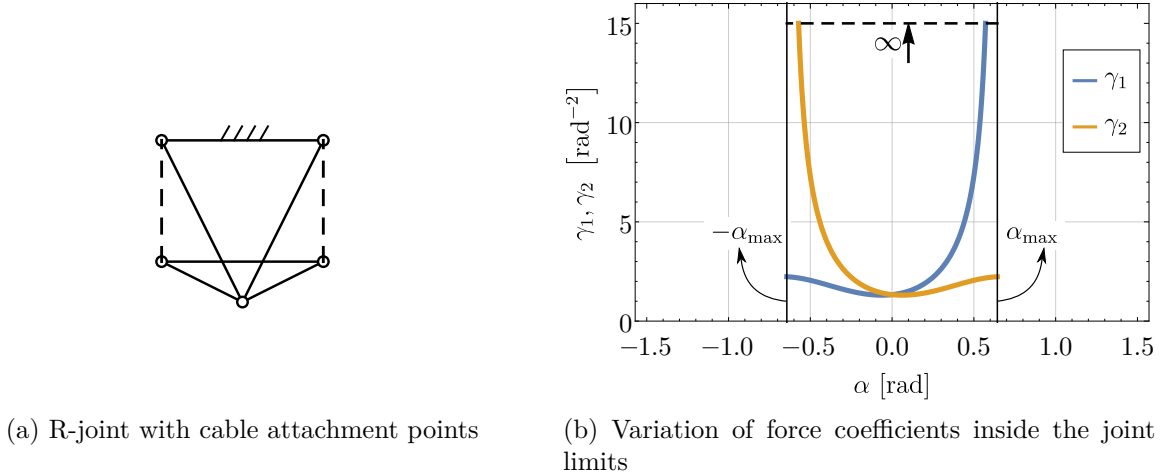


Figure 2.12 – R-joint with $r = 1, h = 1/2$ whose left (resp. right) cable is attached to $B_{1b} = (-1, 2)$ (resp. $B_{2b} = (1, 2)$) at the base. The plot of force coefficients within its limits of movement $\pm\alpha_{\max} = \pm 0.64$ rad. The force coefficient γ_1 (resp. γ_2) tends to infinity asymptotically as α approaches the limit α_{\max} (resp. $-\alpha_{\max}$).

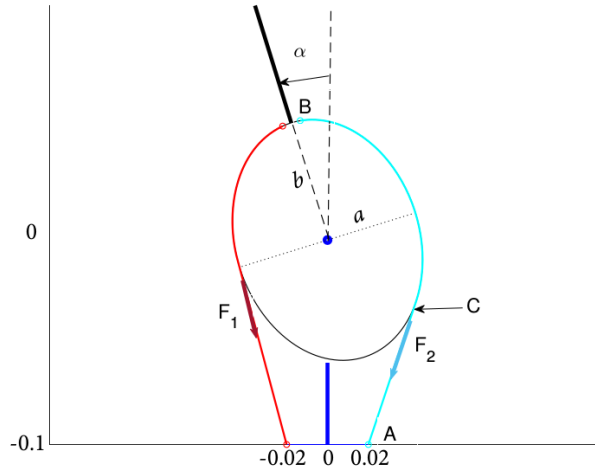


Figure 2.13 – Schematic of a fixed center joint actuated antagonistically by two cables (blue and red) wound around an elliptical pulley (Source: [CWA23]).

on the two sides as shown in Fig. 2.13. They show that this joint exhibits coactivation around at $\alpha = 0$ only when ($b > a$) and not otherwise. They also provide examples to show that the distance between the attachment points of the cables on the selected horizontal line must be less than the length of the minor axis to achieve coactivation.

Finally, a notable feature of this joint that is different from the others in the chapter is that there is a range of α around the home configuration where γ_i is positive (i.e., coactivation occurs), but beyond that γ_i becomes negative. This range is referred to as the coactivation range in [CWA23].

2.6 Four-bar mechanisms with symmetric limbs as joints

In this section, the simplest 1-DoF mechanism, namely, the four-bar mechanism, is studied for its ability to modulate stiffness while actuated by antagonistic cables. Section 2.6.1 describes the geometry of the mechanism and cable attachments considered. Section 2.6.2 presents the kinematics of this mechanism where the cable lengths are derived. Sections 2.6.3 and 2.6.4 study the anti-parallelogram and parallelogram mechanisms, respectively. Section 2.6.5 considers the general four-bar mechanisms with symmetric limbs. Section 2.6.6 presents experiments that validate the theoretical results. Finally, Sections 2.6.7 and 2.6.8 consider alternate cable attachments for mechanisms that do not exhibit coactivation.

2.6.1 Description

The schematics of four-bar mechanisms with symmetric limbs of length l and a top bar of length b are shown in Fig. 2.14. The two pivots fixed to the ground are set at locations $B_1(0, 0)$ and $B_2(b_0, 0)$, where b_0 is a parameter that can be varied to produce different four-bar mechanisms. Notably, $b_0 < 0$ produces mechanisms with crossed limbs, while $b_0 > 0$ produces mechanisms with non-crossed limbs as illustrated in Figs. 2.14a and 2.14b, respectively. The special

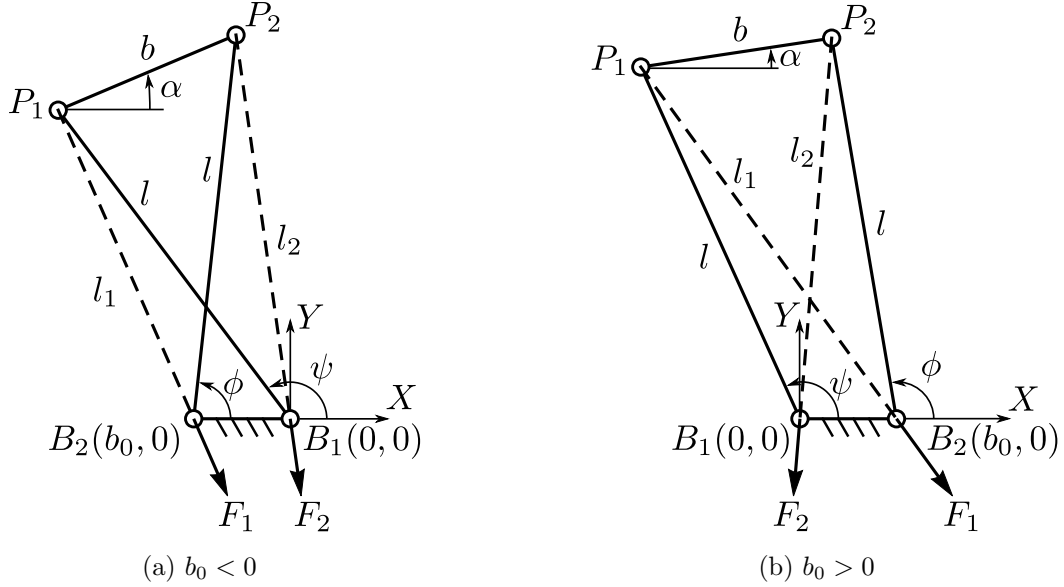


Figure 2.14 – Schematic diagram of four-bar mechanisms with symmetric limbs that are crossed when $b_0 < 0$ (left) and non-crossed when $b_0 > 0$ (right). The two actuating cables are shown in dashed lines.

cases of anti-parallelogram and parallelogram mechanisms are obtained when $b_0 = -b$ and $b_0 = b$, respectively. However, the case $b_0 = 0$ degenerates the four-bar mechanism to a revolute joint and will not be considered in this work. For all the mechanisms, it is necessary that the geometric condition $(l > \frac{|b-b_0|}{2})$ be satisfied for its assembly. Note that in the limiting assembly condition, all pivots of the mechanism align, and it has no finite range of movement.

This mechanism is actuated antagonistically with two cables C_1 and C_2 , connected between the pivots (P_1, B_2) and (P_2, B_1) , respectively, as indicated by dashed lines in Fig. 2.14. The force imparted by the cable C_i is given by $F_i \geq 0$, and its varying length in the mechanism is denoted by l_i , for $i = 1, 2$.

The orientation of the top bar w.r.t. the base is denoted by α , while those of the two limbs w.r.t. the base are given by ϕ, ψ , respectively (see Fig. 2.14). The coordinate α is used to measure the range of movement of the mechanism. The upper bound for α , denoted by α_{\max} , can be found by rotating the top bar from $\alpha = 0$ in the counterclockwise direction until any of the three pivots (B_1, B_2, P_1, P_2) become collinear. Thus, the feasible range of movement for this mechanism is given by $\alpha \in] -\alpha_{\max}, \alpha_{\max}[$, owing to the symmetry in architecture and actuation scheme about $\alpha = 0$.

However, the above representation is not valid for the parallelogram mechanism ($b_0 = b$) since α remains zero at all the configurations. This case will be treated separately in Section 2.6.4. But, for all other cases, further study will be conducted inside $\alpha \in] -\alpha_{\max}, \alpha_{\max}[$.

2.6.2 Kinematic model of the four-bar mechanism

The loop-closure equation for the four-bar mechanism can be written as follows (see Fig. 2.14):

$$\overrightarrow{B_1P_1} + \overrightarrow{P_1P_2} - \overrightarrow{B_2P_2} - \overrightarrow{B_1B_2} = \vec{0} \quad (2.29)$$

This can be expanded into:

$$l \begin{pmatrix} \cos \psi \\ \sin \psi \end{pmatrix} + b \begin{pmatrix} \cos \alpha \\ \sin \alpha \end{pmatrix} - l \begin{pmatrix} \cos \phi \\ \sin \phi \end{pmatrix} - \begin{pmatrix} b_0 \\ 0 \end{pmatrix} = \begin{pmatrix} 0 \\ 0 \end{pmatrix} \quad (2.30)$$

Since the above equations are homogeneous in terms of the length parameter, they can be normalized by setting $b = 1$ without any loss of generality. Considering α as the known input, it is possible to find the trigonometric ratios of the remaining angles (ϕ, ψ) as a function of α using the above equations (see, e.g., [MS10], pp. 411-412). There are two possible solutions $(\phi, \psi)_1$ and $(\phi, \psi)_2$, as presented below:

$$(\phi, \psi)_1 := \begin{cases} \cos \phi = \frac{\mu \sin \alpha + \cos \alpha - b_0}{2l} \\ \sin \phi = \frac{\sin \alpha + \mu(b_0 - \cos \alpha)}{2l} \\ \cos \psi = \frac{\mu \sin \alpha - \cos \alpha + b_0}{2l} \\ \sin \psi = \frac{\mu(b_0 - \cos \alpha) - \sin \alpha}{2l} \end{cases} \quad (\phi, \psi)_2 := \begin{cases} \cos \phi = -\frac{\mu \sin \alpha - \cos \alpha + b_0}{2l} \\ \sin \phi = -\frac{\mu(b_0 - \cos \alpha) - \sin \alpha}{2l} \\ \cos \psi = -\frac{\mu \sin \alpha + \cos \alpha - b_0}{2l} \\ \sin \psi = -\frac{\sin \alpha + \mu(b_0 - \cos \alpha)}{2l} \end{cases} \quad (2.31)$$

where $\mu = \sqrt{\frac{4l^2 - b_0^2 - 1 + 2b_0 \cos \alpha}{b_0^2 + 1 - 2b_0 \cos \alpha}}$. For a given $\alpha \in]-\alpha_{\max}, \alpha_{\max}[$, one of the above solutions corresponds to the top bar P_1P_2 being above the base B_1B_2 , while the other corresponds to the top bar being below the base. In this study, only the former solution is of interest. Note that the specified joint limits $\alpha \in]-\alpha_{\max}, \alpha_{\max}[$ preclude the case where one end of the top bar is above, while the other one is below.

By setting $\alpha = 0$ in Eq. (2.31), it can be deduced from the resulting expressions that the desired solution branch is given by $(\phi, \psi)_2$ when $(b_0 < 1)$ and by $(\phi, \psi)_1$ when $(b_0 > 1)$. Revoking the normalization w.r.t. b , the above conditions translate into $(b_0 < b)$ and $(b_0 > b)$ in the two cases, respectively.

From Fig. 2.14, the cable lengths (in all cases) can be written as follows:

$$\begin{cases} \text{Length of cable } C_1 \implies l_1 := \|P_1B_2\| = \sqrt{l^2 + b_0^2 - 2lb_0 \cos \psi} \\ \text{Length of cable } C_2 \implies l_2 := \|P_2B_1\| = \sqrt{l^2 + b_0^2 + 2lb_0 \cos \phi} \end{cases} \quad (2.32)$$

The lengths l_1, l_2 can be obtained as functions of α by substituting for $\cos \psi$ and $\cos \phi$ from Eq. (2.31), appropriately.

2.6.3 Anti-parallelogram mechanism

Figure 2.15 shows the schematic of the anti-parallelogram mechanism (also referred to as the X-joint) that is obtained by setting $b_0 = -b$. It is well known that the relative movement between the top and base bars is equivalent to an ellipse pure rolling over another one [Hua+22]. The top bar undergoes two rotations, i.e., $\alpha \in]-2\pi, 2\pi[$, as the mechanism goes through a complete

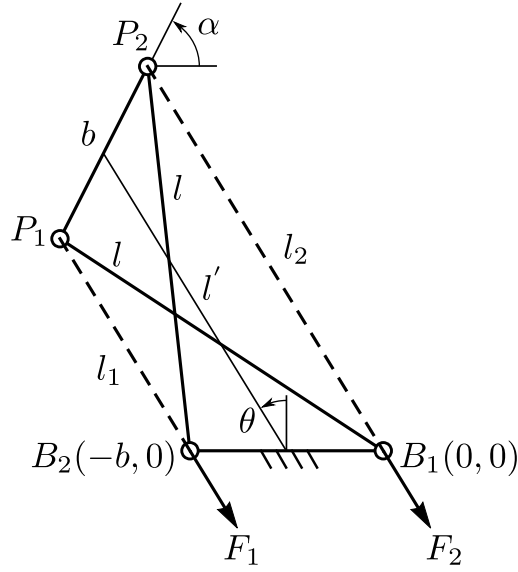


Figure 2.15 – Schematic of an anti-parallelogram mechanism actuated antagonistically by two cables (dashed lines).

cycle. However, in practice, the movement is limited to $\alpha \in]-\pi, \pi[$ owing to the flat-singularities or the uncertainty configurations at $\alpha = \pm\pi$, as explained in Section 2.2.2.

From Fig. 2.15, it can be shown that the line joining the centers of the base and top bars makes an angle of $\theta = (\alpha/2)$ w.r.t. the vertical [FW19]. Additionally, the length of this segment can be computed as: $l' = \sqrt{l^2 - b^2 \cos^2(\theta)}$. Thus, the cable lengths are found to be:

$$\begin{cases} l_1 = -b \cos \theta + \sqrt{l^2 - b^2 \cos^2(\theta)} \\ l_2 = b \cos \theta + \sqrt{l^2 - b^2 \cos^2(\theta)} \end{cases} \quad (2.33)$$

In order to avoid the fractional argument $(\alpha/2)$, the angle θ is used as the independent coordinate in this study. Following the procedure in Section 2.2.3 with θ in place of α , the expressions for force coefficients are found to be:

$$\begin{cases} \gamma_1 = \frac{2b \cos^2(\theta) (\sqrt{\lambda^2 - \cos^2(\theta)} - \sin \theta)}{\lambda^2 - \cos^2(\theta)} \\ \gamma_2 = \frac{2b \cos^2(\theta) (\sqrt{\lambda^2 - \cos^2(\theta)} + \sin \theta)}{\lambda^2 - \cos^2(\theta)} \end{cases} \quad (2.34)$$

where $\lambda = (l/b)$. Note that $\lambda > 1$ is necessary for assembling the anti-parallelogram mechanism. Hence, it is apparent that γ_1, γ_2 are both positive while $\theta \in]-\frac{\pi}{2}, \frac{\pi}{2}[$, within the flat-singularities. It shows that the actuation forces have a positive impact on the stiffness, and the mechanism exhibits coactivation throughout its entire range of movement. Hence, using the anti-parallelogram mechanism as a remotely actuated joint is justified for mimicking contact between bones, e.g., intervertebral contact of a bird's neck [Abo+19].

2.6.4 Parallelogram mechanism

The parallelogram mechanism, shown in Fig. 2.16, is obtained by setting $b_0 = b$. Unlike other four-bar mechanisms, α remains zero at all configurations for this mechanism. Hence,

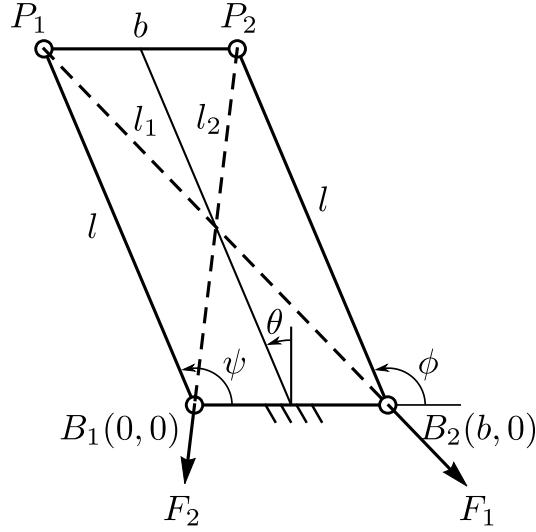


Figure 2.16 – Schematic of a parallelogram mechanism actuated antagonistically by two cables (dashed lines).

the orientation (θ) of the line joining mid-points of the top and base bars w.r.t. the vertical is used as the independent coordinate. The range of movement for this mechanism is limited by $\theta \in]-\frac{\pi}{2}, \frac{\pi}{2}[$, due to the flat-singularities.

From Fig. 2.16, it is apparent that $\phi = \psi = \frac{\pi}{2} + \theta$. Thus, from Eq. (2.32), the cable lengths are given by:

$$\begin{cases} l_1 = \sqrt{l^2 + b^2 + 2lb \sin \theta} \\ l_2 = \sqrt{l^2 + b^2 - 2lb \sin \theta} \end{cases} \quad (2.35)$$

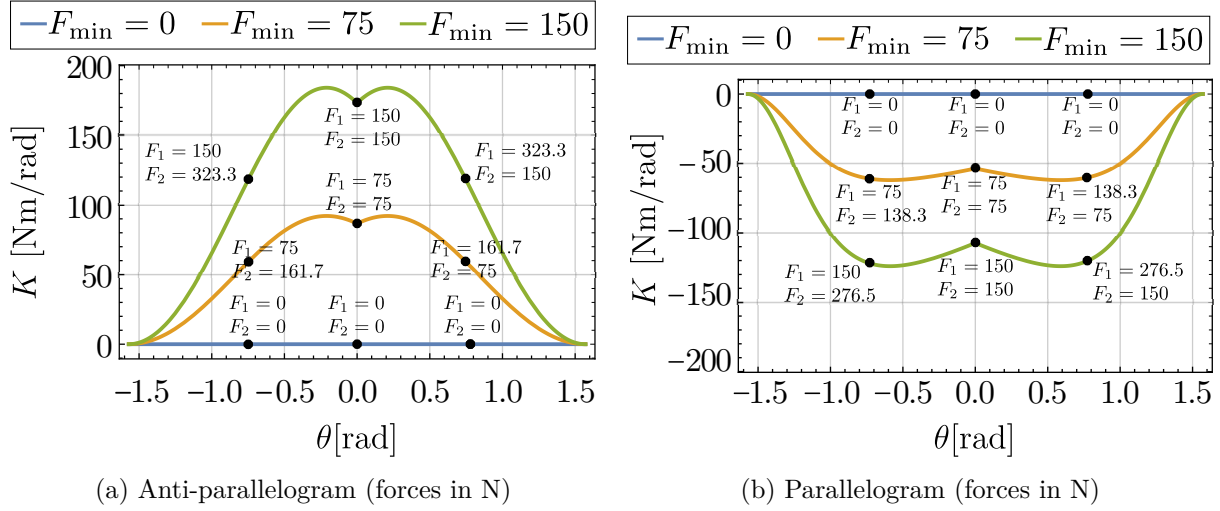
As in the previous section, one obtains γ_1, γ_2 for the parallelogram mechanism as:

$$\begin{cases} \gamma_1 = -\frac{2b\lambda^2(\lambda^2+1)\cos^2(\theta)}{(\lambda^2+1-2\lambda\sin\theta)(\lambda^2+1+2\lambda\sin\theta)^{3/2}} \\ \gamma_2 = -\frac{2b\lambda^2(\lambda^2+1)\cos^2(\theta)}{(\lambda^2+1-2\lambda\sin\theta)^{3/2}(\lambda^2+1+2\lambda\sin\theta)} \end{cases} \quad (2.36)$$

where $\lambda = (l/b)$. Except for the leading negative signs, all the factors in the numerators of γ_1 and γ_2 are positive. The two factors in the respective denominators are also positive since they are bounded inside $[(\lambda - 1)^2, (\lambda + 1)^2]$ for all real θ . Thus, it is clear that $\gamma_1, \gamma_2 < 0$, which shows that antagonistic forces have a negative impact on the stiffness of the parallelogram mechanism. This result is consistent with the experimental data presented in [Boe+17b], where the cable tensions were reduced to increase the stiffness of this mechanism. Note that the authors had considered linear springs in-series with the actuating cables in their work, but due to the equivalence proved in Section 2.3, we find the same stiffness behavior in the two systems.

As a numerical illustration consider parallelogram ($b_0 = b$) and anti-parallelogram ($b_0 = -b$) mechanisms with $b = 1$ m and $l = 2$ m each. For the sake of simplicity, the bar masses are neglected, and no springs are added to these mechanisms.

One of the ways to study the change in stiffness with increasing antagonistic forces is to specify a minimum value for the actuation forces, say F_{\min} . At a given configuration θ , one


 Figure 2.17 – Stiffness of the mechanisms when $\theta \in]-\frac{\pi}{2}, \frac{\pi}{2}[$ for different actuation forces.

could compute the balancing forces (F_1, F_2) from Eq. (2.2) (neglecting U_g) such that one of them is equal to F_{\min} while the other is greater than or equal to F_{\min} . These forces can be substituted in Eq. (2.3) to find the respective value of stiffness. This process has been carried out for different values of F_{\min} : 0 N, 75 N, and 150 N. The corresponding stiffness values are plotted for the anti-parallelogram and parallelogram mechanisms in Figs. 2.17b and 2.17a, respectively. The equilibrium forces are also represented in certain configurations. It is apparent that an increase in F_{\min} causes an increase (resp. decrease) in stiffness for the parallelogram (resp. anti-parallelogram) mechanism for all values of θ . It is a consequence of the positive (resp. negative) force coefficients γ_1, γ_2 for the anti-parallelogram (resp. parallelogram) mechanism. Hence, the anti-parallelogram mechanism can be a bio-inspired joint while the parallelogram mechanism cannot.

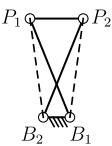
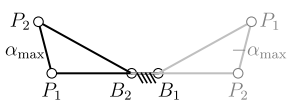
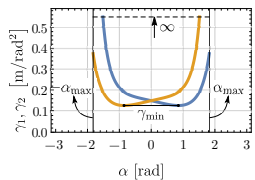
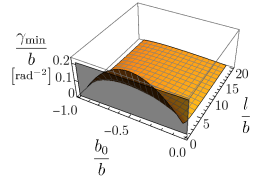
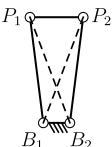
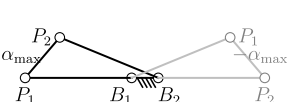
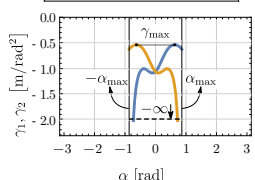
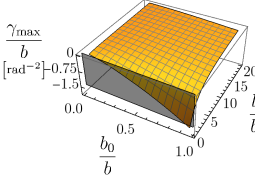
The coactivation properties of more general symmetric four-bar mechanisms are studied in the following section.

2.6.5 General four-bar mechanisms with unequal base and top bars

Unlike the anti-parallelogram and parallelogram mechanisms, it is very difficult to conduct analytical studies on γ_1, γ_2 for the general mechanisms ($b_0 \neq \pm b$) due to the emergence of nested square roots in expressions of l_1, l_2 (see Eqs. (2.31), (2.32)). Hence, the nature of γ_1, γ_2 will be studied through numerical examples for these mechanisms.

In the first version of this work [Mur+23a], we considered four distinct types of four-bar mechanisms apart from the parallelogram and anti-parallelogram architectures, depending on whether the base bar is longer/shorter than the top bar and the two limbs are crossed/non-crossed. However, the distinction based on the relative length of the base bar to the top bar is not necessary, as the relative kinematics and coactivation properties of a closed chain (i.e., the evolution of α and the cable lengths) remain invariant to the fixing of the longer or shorter bar. Indeed, this is because one mechanism is a kinematic inversion of the other (see, e.g., [GM98], pp. 12-14). Hence, in further study, the base bar is always set to be smaller than the top bar, i.e.,

Table 2.1 – Effect of antagonistic forces on the stiffness of general symmetric four-bar mechanisms.

Condition/ Schematic	Bounds on $\alpha \in] -\alpha_{\max}, \alpha_{\max}[$	Plot of γ_1 (—), γ_2 (---) for one design with $b = 1 \text{ m}, l = 2 \text{ m}$	(γ_{\min}/b) or (γ_{\max}/b) in design space $2l > (b - b_0) \ \& \ l \in$ $[0, 20b] \ \& \ b_0 \in [0, b]$
$-b < b_0 < 0$ 		$b_0 = -0.5 \text{ m}, \alpha_{\max} = 1.82 \text{ rad}$ 	
$0 < b_0 < b$ 		$b_0 = 0.5 \text{ m}, \alpha_{\max} = 0.86 \text{ rad}$ 	

$b_0 \in [-b, b]$, with $b > 0$. The two variants of general four-bar mechanisms that emerge depending on $b_0 < 0$ and $b_0 > 0$ are considered in the following. The coactivation properties are studied numerically in these cases, and experimental validations are provided for the same in the next section.

Table 2.1 presents the two variants of general four-bar mechanisms. In each case, the limiting configurations at $(\pm\alpha_{\max})$, plot of γ_1, γ_2 inside $\alpha \in] -\alpha_{\max}, \alpha_{\max}[$ for one candidate design, and the limiting value of γ_1, γ_2 inside the feasible design space, are presented in the successive columns of this table. The following observations are made from them:

- The maximum orientation (α_{\max}) of the top bar varies in $]0, \pi[$ when $b_0 < 0$, while it is limited to $]0, \frac{\pi}{2}[$ when $b_0 > 0$. Thus, mechanisms with crossed limbs must be preferred for applications requiring large α .
- From the plots of γ_1, γ_2 for one candidate design, it is observed that they remain positive (resp. negative) when $b_0 < 0$ (resp. $b_0 > 0$). The values of γ_1, γ_2 tend to $\pm\infty$ near the limits due to the vanishing of $\frac{dl_1}{d\alpha}$ or $\frac{dl_2}{d\alpha}$, present in the denominator of the respective expressions (see Eqs. (2.5),(2.6) and Sections 2.2.2, 2.2.3). However, this does not imply that the mechanism allows for infinite tuning of stiffness for a finite variation of actuation forces at the joint limits. It is rather indicative of the degeneracy of the wrench applied by one of the cables in that configuration. In the equilibrium equation (Eq. 2.2), the corresponding actuation force is no longer present due to the vanishing of its coefficient. Physically, the mechanism is not redundantly actuated at that configuration and will readily collapse when subjected to a disturbance that the remaining cable cannot balance.
- In order to verify if γ_1, γ_2 remain positive (resp. negative) for other designs when $b_0 < 0$ (resp. $b_0 > 0$), their minimum γ_{\min} (resp. maximum γ_{\max}) inside the range of movement is tested. Since the expressions of γ_1, γ_2 are homogeneous w.r.t. the derivatives of cable lengths, one of the length variables ($b \neq 0$) can be factored out as in Eqs. (2.34),(2.36).

This reduces the design space to just two variables $(\frac{l}{b}, \frac{b_0}{b})$. Firstly, a feasible design space satisfying the assembly condition $l > \frac{b-b_0}{2}$ and bounded by $0 < \frac{|b_0|}{b} < 1$ and $0 < \frac{l}{b} \leq 20$ is constructed. The values of $\frac{\gamma_{\min}}{b}$ and $\frac{\gamma_{\max}}{b}$ are computed for the feasible designs numerically to obtain the plots in the last column of the table. From these, it is clear that $\gamma_{\min} > 0$ when $b_0 < 0$ and $\gamma_{\max} < 0$ when $b_0 > 0$. This result illustrates that the antagonistic forces have a positive (resp. negative) influence on the stiffness of mechanisms with crossed (resp. non-crossed) limbs.

- For mechanisms with $b_0 < 0$, the value of γ_{\min} is large for designs close to the limiting assembly condition $2l = (b - b_0)$ (highlighted by gray plane in the last column of the table). Recalling that the mechanism has no finite range of movement (i.e., $\alpha_{\max} = 0$ rad) at the limiting assembly condition, we observe that there is a compromise between the range of movement and the minimum value of force coefficient (γ_{\min}) for designs in the category $b_0 < 0$.

Among the four-bar mechanisms that offer coactivation (i.e., $b_0 < 0$), the anti-parallelogram mechanism ($b_0 = -b$) has the largest range of movement $\alpha \in]-\pi, \pi[$ and is to be preferred in general. However, the other mechanisms with crossed bars might also be interesting for applications where a large orientation range may not be essential, e.g., joints in the hyper-redundant robots inspired by the elephant's trunk [Liu+19b].

2.6.6 Experimental validation

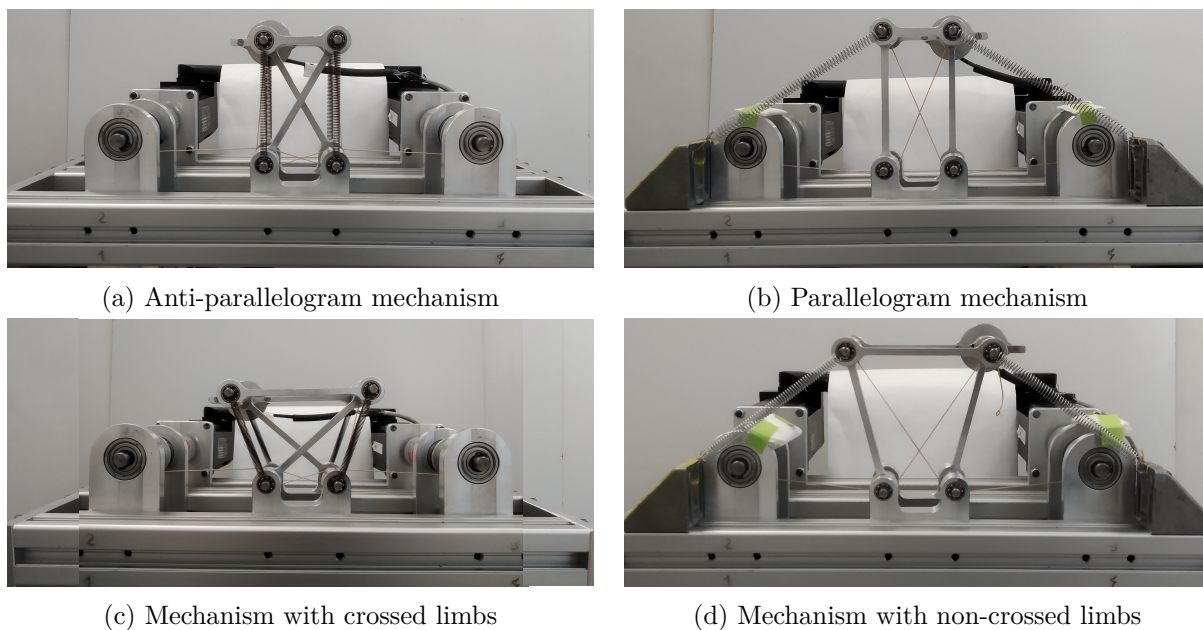


Figure 2.18 – Experimental setup of different symmetric four-bar mechanisms.

This section presents experiments on various four-bar mechanisms to confirm their ability/inability to produce coactivation. In this regard, four different mechanisms (anti-parallelogram, parallelogram, general crossed limbs, general non-crossed limbs) are considered as shown in Fig. 2.18. All the mechanisms have the same lengths for their base bars $|b_0| = 0.05$ m and



Figure 2.19 – External force required to produce the same displacement in a mechanism for different antagonistic actuation forces $F_1 = F_2 = F_{ant}$.

limbs $l = 0.1$ m, while the top bar lengths are fixed at $b = 0.05$ m for the mechanisms in Figs. 2.18a, 2.18b, and at $b = 0.1$ m for the mechanisms in Figs. 2.18c, 2.18d. Two actuating cables are attached between the unconnected pairs of pivots in all the mechanisms. They are equipped with springs on the two sides to ensure stability in the absence of actuation forces. For the mechanisms with crossed limbs shown in Figs. 2.18a and 2.18c, a pair of identical springs with stiffness 100 N/m is attached on each side in parallel to the actuating cables, thereby resulting in a total stiffness of 200 N/m on either side. On the other hand, for the mechanisms presented in Figs. 2.18b and 2.18d, just one spring of stiffness 100 N/m is attached on each side with external supports. The springs are not attached parallel to the cables like in the other mechanisms due to constraints on their maximum elongation lengths.

As in the case of R-joint with congruent triangles (see Section 2.5.2), the variation of stiffness due to actuation forces is studied at the zero orientation shown in Fig. 2.18, by applying equal forces on the two cables $F_1 = F_2 = F_{\text{ant}}$. Three experiments are conducted on each mechanism by setting different values of $F_{\text{ant}} = 10, 20, 30$ N. In each case, the stiffness of the mechanism is studied by applying an external force with a dynamo-meter, as shown in Fig. 2.19. In order to enable a comparison between the results of the three experiments, the external force is regulated to produce the same displacement in a mechanism as observed in Fig. 2.19. From the readings of the dynamo-meter on the left part of the figures, it is apparent that the external force required increases (resp. decreases) with the actuation force F_{ant} for mechanisms with crossed bars (resp. non-crossed bars). These results confirm that the antagonistic forces increase the stiffness of four-bar mechanisms when their limbs are crossed, while they decrease the stiffness when the limbs are non-crossed.

The loss of stiffness in the mechanisms with non-crossed limbs is further illustrated by another experiment where the actuation forces $F_1 = F_2 = F_{\text{ant}}$ are increased linearly with time. As expected, the mechanisms lose their stability and collapse once the force F_{ant} reaches a critical value (28.5 N for parallelogram and 55.5 N for general mechanism). The associated videos can be found in the following links for the parallelogram mechanism⁴ and the general mechanism⁵ with non-crossed limbs.

The next two sections investigate the possibility of coactivation in four-bar mechanisms with non-crossed limbs by changing their cable attachments.

2.6.7 Alternate cable attachments for coactivation in parallelogram mechanism

As in the R-joint with non-congruent triangles, this section studies different cable attachments for a parallelogram mechanism to enable coactivation.

The schematic of a parallelogram mechanism with the base cable attachment points parametrized by (x_d, y_d) is shown in Fig. 2.20. The attachment points D_1 and D_2 are placed symmetrically w.r.t. the base points B_1 and B_2 , respectively, such that the symmetry of the mechanism is preserved about the configuration $\theta = 0$. One obtains the actuation scheme presented in Fig. 2.16 by setting $(x_d, y_d) = (b, 0)$. However, in this study, we treat the coordinates (x_d, y_d) as design parameters that can be altered to obtain the desired coactivation behavior. Note that it is also possible to alter the cable attachment on the top bar from P_1 and P_2 to other points while

4. <https://youtu.be/iddUEDVTqJo>

5. https://youtu.be/Dx1eA_1-kSw

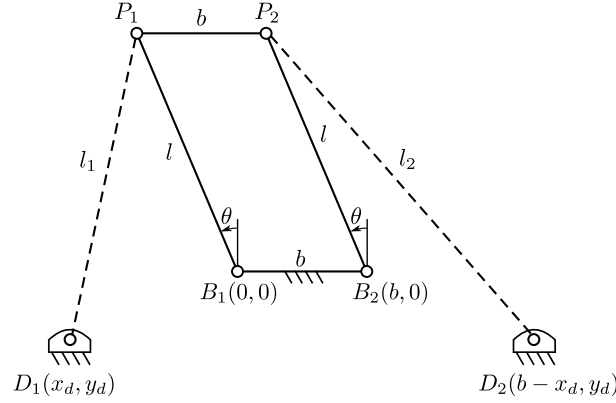


Figure 2.20 – Parallelogram mechanism with cables attached at points D_1 and D_2 in the base.

preserving the symmetry of the mechanism. But, we do not consider this change in this study for the sake of simplicity.

Introducing new cable attachment points introduces new limits to the movement of the mechanism due to the collinearity of points (D_i, B_i, P_i) , for $i = 1, 2$. Clearly, the parallelogram mechanism cannot achieve its original orientation range of $\theta \in]-\frac{\pi}{2}, \frac{\pi}{2}[$ unless $y_d = 0$ and $x_d \neq 0$. In all other cases, the feasible range of movement will be less than π . From Fig. 2.20, the coordinates of the points on the top bar are found to be $P_1 = l[-\sin \theta, \cos \theta]^\top$ and $P_2 = [b - l \sin \theta, l \cos \theta]^\top$. Thus, the cable lengths l_1, l_2 can be computed as follows:

$$\begin{cases} l_1 := \|P_1 D_1\| = \sqrt{l^2 + 2lx_d \sin \theta - 2ly_d \cos \theta + x_d^2 + y_d^2} \\ l_2 := \|P_2 D_2\| = \sqrt{l^2 - 2lx_d \sin \theta - 2ly_d \cos \theta + x_d^2 + y_d^2} \end{cases} \quad (2.37)$$

Note that the lengths of the cables are independent of b , indicating that the wrenches imposed by the cables, as well as the nature of coactivation, are independent of the width of the parallelogram. The force coefficients γ_1, γ_2 can be obtained from the formulae presented in Eqs. (2.5), (2.6). The expressions are not presented here due to their large sizes. But, they satisfy the symmetry condition due to configuration: $\gamma_1(x_d, y_d, -\theta) = \gamma_2(x_d, y_d, \theta)$.

Similar to the R-joint with non-congruent triangles (see Section 2.5.3), the force coefficients also satisfy a symmetry condition in attachment points: $\gamma_1(-x_d, y_d, \theta) = \gamma_2(x_d, y_d, \theta)$. This condition indicates that switching the attachment points of the cables from (D_1, D_2) to different points (D'_1, D'_2) that are mirror images about the vertical lines placed at B_1, B_2 , respectively, preserves the force coefficients in the stiffness. It can also be shown that the limits of movement remain the same while the cables are attached at (D_1, D_2) or (D'_1, D'_2) . The only difference is that the direction of the moment imposed by the respective cable changes between the two scenarios.

In order to achieve coactivation with the parallelogram mechanism, the force coefficients γ_1, γ_2 must be positive. However, since their expressions are difficult to analyze analytically, we consider γ_1 for one configuration ($\theta = 0$) of the mechanism as follows:

$$\gamma_1(\theta = 0) = \frac{2l(y_d - l)(y_d(y_d - l) + x_d^2)}{((l - y_d)^2 + x_d^2)^{3/2}} \quad (2.38)$$

It is apparent that the denominator is always positive. Hence, the condition to achieve coactivation at $\theta = 0$, i.e. $\gamma_1(\theta = 0) > 0$, can be written as:

$$\gamma_1(\theta = 0) > 0 \implies \begin{cases} \text{Always,} & \text{when } (y_d > l) \\ (x_d^2 + (y_d - (l/2))^2 - (l/2)^2) < 0, & \text{when } (y_d < l) \end{cases} \quad (2.39)$$

Thus, the limiting boundaries of attachment point $D_1(x_d, y_d)$ are formed by a circle and a

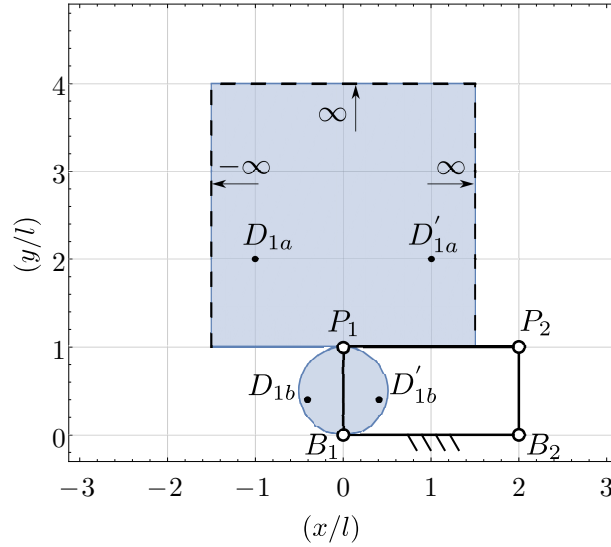
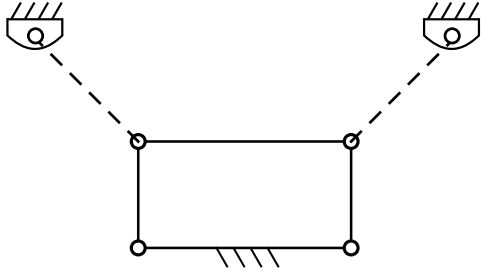


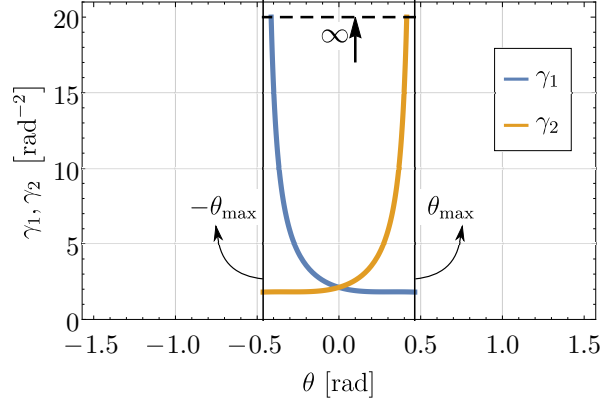
Figure 2.21 – Feasible region for the cable attachment point D_1 to achieve coactivation at the configuration $\theta = 0$ rad in the parallelogram mechanism with $l = 1, b = 2$.

straight line to achieve coactivation in a parallelogram mechanism, similar to the R-joint with non-congruent triangles (see Section 2.5.3). As an illustration, the feasible region for the attachment point D_1 is shown along with the mechanism for the parameters $l = 1, b = 2$, in Fig. 2.21. The scale of the mechanism has been normalized w.r.t. l without any loss of generality.

For further study, we choose two points $D_{1a} = (-1, 2)$ and $D_{1b} = (-2/5, 2/5)$ inside the feasible region as shown in Fig. 2.21. The schematic of the resulting mechanisms with cable attachment points and the plots of γ_1, γ_2 inside their respective joint limits are presented for D_{1a} in Fig. 2.22 and for D_{1b} in Fig. 2.23. In both cases, we observe that the force coefficients remain positive inside their joint limits, indicating that both attachment points offer coactivation at all feasible configurations of the parallelogram mechanism, similar to mechanisms with crossed limbs. Since the attachment point D_{1b} is closer to the limiting boundary than D_{1a} (see Fig. 2.21), the associated values of force coefficients are smaller near $\theta = 0$ (see Figs. 2.22b and 2.23b). However, as a compromise, the attachment at D_{1b} offers a larger range of movement for the mechanism, similar to what was observed for the R-joint with non-congruent triangles in Section 2.5.3.

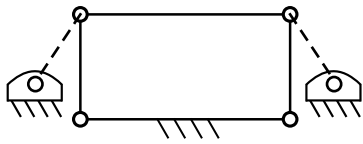


(a) Mechanism with cable attachment points

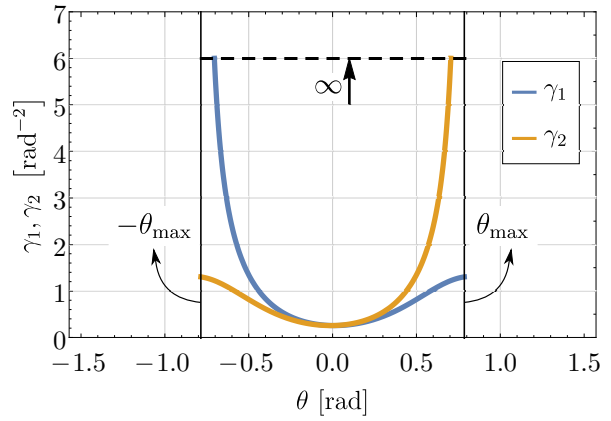


(b) Variation of force coefficients inside the joint limits

Figure 2.22 – Parallelogram mechanism with $l = 1, b = 2$, whose left (resp. right) cable is attached to $D_{1a} = (-1, 2)$ (resp. $D_{2a} = (3, 2)$) at the base. The plot of force coefficients within its limits of movement $\pm\theta_{\max} = \pm 0.46$ rad. The force coefficient γ_1 (resp. γ_2) tends to infinity asymptotically as θ approaches the limit $-\theta_{\max}$ (resp. θ_{\max}).



(a) Mechanism with cable attachment points



(b) Variation of force coefficients inside the joint limits

Figure 2.23 – Parallelogram mechanism with $l = 1, b = 2$ whose left (resp. right) cable is attached to $D_{1b} = (-2/5, 2/5)$ (resp. $D_{2b} = (12/5, 2/5)$) at the base. The plot of force coefficients within its limits of movement $\pm\theta_{\max} = \pm 0.79$ rad. The force coefficient γ_1 (resp. γ_2) tends to infinity asymptotically as θ approaches the limit $-\theta_{\max}$ (resp. θ_{\max}).

2.6.8 Alternate cable attachments for coactivation in a general four-bar mechanism with non-crossed limbs

This section considers a four-bar mechanism with non-crossed limbs with geometry $l = 1, b = 1, b_0 = 1/2$. As in the previous section, the cable attachment points at the base are parameterized by (x_d, y_d) coordinates while retaining the attachment points at P_1 and P_2 in the top bar. The lengths of the cables are computed to be:

$$\begin{cases} l_1 = \sqrt{l^2 - 2lx_d \cos \psi - 2ly_d \sin \psi + x_d^2 + y_d^2} \\ l_2 = \sqrt{l^2 + 2lx_d \cos \phi - 2ly_d \sin \phi + x_d^2 + y_d^2} \end{cases} \quad (2.40)$$

Unlike in the parallelogram mechanism, the presence of intermediate angles (ψ, ϕ) (see Fig. 2.14) ensures that all the bar lengths are involved in the expressions of cable lengths. Further, the force coefficients γ_1, γ_2 are computed using the formulae in Eqs. (2.5),(2.6). The symmetry due to configuration θ , i.e., $\gamma_1(x_d, y_d, \theta) = \gamma_2(x_d, y_d, -\theta)$ is respected, but there is no symmetry w.r.t. the sign of coordinate x_d as observed in the previous section.

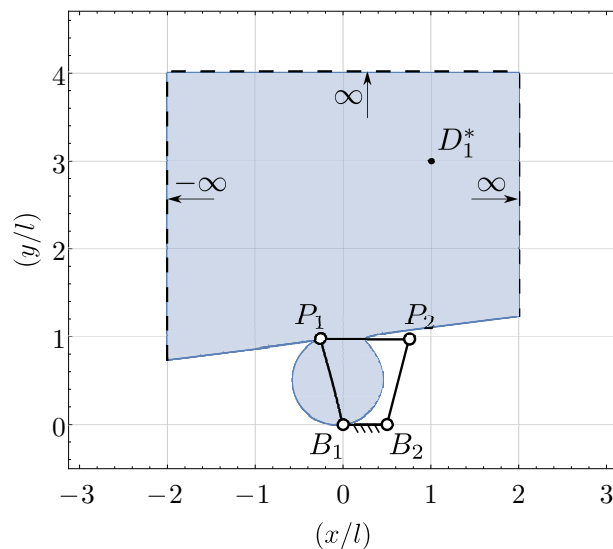


Figure 2.24 – Feasible region for the cable attachment point D_1 to achieve coactivation at the configuration $\alpha = 0$ rad in a four-bar mechanism with non-crossed limbs of geometry $l = 1, b = 1, b_0 = 1/2$.

For this mechanism, the condition for coactivation at one configuration $\alpha = 0$ is itself quite large to be analyzed. Hence, its geometry parameters $l = 1, b = 1, b_0 = 1/2$ are substituted to derive a simplified condition in terms of x_d and y_d as follows:

$$-\sqrt{15}x_d^3 + x_d^2(31y_d - 8\sqrt{15}) - x_d(\sqrt{15}y_d^2 - 8y_d + \sqrt{15}) + y_d(31(y_d^2 + 1) - 16\sqrt{15}y_d) > 0 \quad (2.41)$$

The above expression does not factor into simpler terms like in the previous case. Hence, the region satisfying the above condition (i.e., the feasible region for attachment point D_1) has been plotted as is, along with the mechanism in Fig. 2.24.

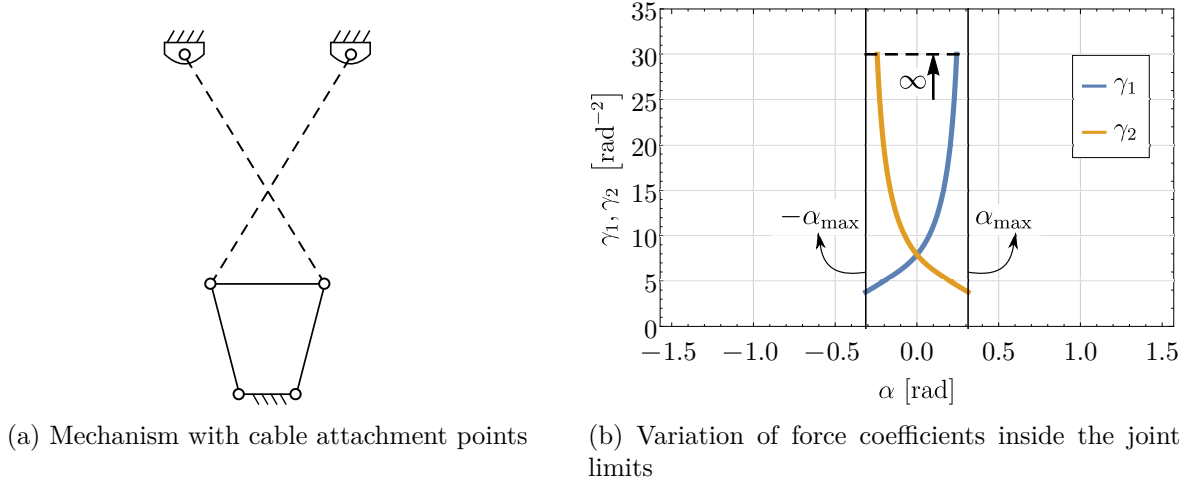


Figure 2.25 – Four-bar mechanism with $l = 1, b = 1, b_0 = 1/2$ whose left (resp. right) cable is attached to $D_1^* = (1, 3)$ (resp. $D_2^* = (-1/2, 3)$) at the base. The plot of force coefficients within its limits of movement $\pm\alpha_{\max} = \pm 0.31$ rad. The force coefficient γ_1 (resp. γ_2) tends to infinity asymptotically as α approaches the limit α_{\max} (resp. $-\alpha_{\max}$).

One feasible candidate $D_1^* = (1, 3)$ has been chosen for this mechanism. As explained in the previous section, additional limits of movement exist due to the collinearity of the points (D_i, B_i, P_i) . These limits are found to be $\alpha \in]-\alpha_{\max}, \alpha_{\max}[$ with $\alpha_{\max} = 0.31$ rad. The schematic of the mechanism with the chosen attachment points for the cables is shown in Fig. 2.25a, and the respective plot of the force coefficients within the joint limits is presented in Fig. 2.25b. It is observed that γ_1, γ_2 are both positive, indicating that the mechanism exhibits coactivation throughout the entire range of movement.

The above results show that it is possible to achieve coactivation in the parallelogram mechanism and general four-bar mechanisms with non-crossed limbs by selecting appropriate cable attachment points. However, there is a compromise on the range of movement permissible for the mechanism.

The following section summarizes all the results derived in this chapter.

2.7 Classification of the joints and possible applications

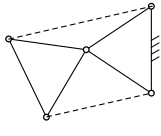
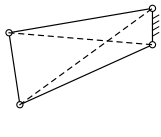
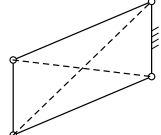
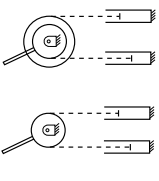
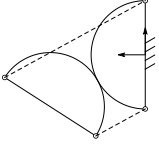
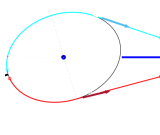
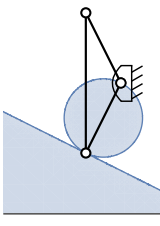
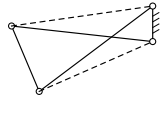
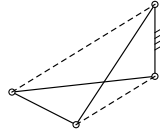
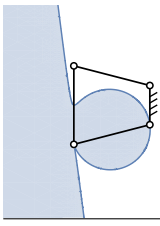
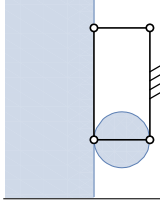
This section classifies all the joints and mechanisms studied in the previous sections based on their ability to modulate stiffness. The joints and their possible upper bounds of movement limits are presented in Table 2.2. Since the stiffness modulation capability of a joint depends on the attachment points of the cables, it is imperative to specify the assumed actuation scheme as shown in the schematics in Table 2.2. The results are likely to change for a different actuation scheme.

The following points can be made on the joints presented in Table 2.2:

- **Decreasing stiffness with increasing forces:**

The R-joint with congruent triangles, parallelogram mechanism, and general four-bar mechanism with non-crossed limbs, with the proposed actuation scheme, fall into this

Table 2.2 – Classification of the antagonistically actuated joints (except prismatic) based on their stiffness modulation ability. The range of movement is given by $\theta \in] - \theta_{\max}, \theta_{\max}[$ (limb orientation) for the parallelogram mechanism and $\alpha \in] - \alpha_{\max}, \alpha_{\max}[$ (top bar orientation) for the others. A limit on the upper bound of movement is presented in “{ }” below the mechanism.

Stiffness behavior	Pulley	R-joint	Four-bar with crossed limbs	Anti-parallelogram	Four-bar with non-crossed limbs	Parallelogram
Stiffness decreases with increasing actuation forces		 <p>R-joint (congruent) $\{\alpha_{\max} < (\pi/2)\}$</p>			 <p>Four-bar (non-crossed) $\{\alpha_{\max} < (\pi/2)\}$</p>	 <p>Parallelogram $\{\theta_{\max} = (\pi/2)\}$</p>
No stiffness modulation	 <p>Pulley/Pulley-2 $\{\alpha_{\max} \text{ unlimited}\}$</p>			 <p>Circle-circle $\{\alpha_{\max} = \pi\}$</p>		
Stiffness increases with increasing actuation forces (coactivation)	 <p>Elliptic pulley [CWA23] $\{\alpha_{\max} < (\pi/2)\}$</p>	 <p>R-joint (non-congruent) $\{\alpha_{\max} < (\pi/2)\}$</p>	 <p>Four-bar (crossed) $\{\alpha_{\max} < \pi\}$</p>	 <p>Anti-parallelogram $\{\alpha_{\max} = \pi\}$</p>	 <p>Four-bar (non-crossed) $\{\alpha_{\max} < (\pi/2)\}$</p>	 <p>Parallelogram $\{\theta_{\max} < (\pi/2)\}$</p>

category. The main disadvantage of its stiffness modulation is that the actuation forces must increase to reduce the stiffness of the joint, which in turn increases the energy consumption for low-stiffness tasks and decreases it for high-stiffness tasks. This behavior is unnatural; hence, these joints may not be efficient for variable stiffness applications. Yet, there could be possible uses for them when the natural state of a device should be very stiff (achieved with additional springs), and it becomes essential to reduce the stiffness during a task.

— **No stiffness modulation:**

The prismatic and circle-circle joints are part of this category for the specified cable attachments. But, exceptionally, the pulley joints can never exhibit stiffness modulation due to antagonistic forces for any cable attachment scheme. All of these joints (except pulley-2) can be remotely actuated with a single motor, which makes them interesting candidates for designing cable-driven lightweight wrists fixed on a moving platform, e.g., in cable-driven parallel robots.

— **Increasing stiffness with increasing forces:**

All the joints in the last row of Table 2.2 fall into this category. The ones with shading in the background represent the possible attachments for the left cable on the base to achieve coactivation. Indeed, the joint would belong to the first category if one chooses an attachment point outside this region. These joints exhibit coactivation like the muscle actuation in biological joints, which keeps the energy consumption at a minimum while performing low-stiffness tasks and increases it only on demand for high-stiffness tasks. They are suitable for developing devices for variable stiffness applications, e.g., multi-purpose manipulators for high-stiffness tasks (machining) and low-stiffness tasks (collaboration with workers). Notably, in this category, the anti-parallelogram mechanism offers the largest range of movement for the top bar relative to the base while ensuring coactivation. Hence, it is the most suitable for developing bio-inspired joints.

2.8 Conclusions

This chapter considered a general 1-DoF joint/mechanism actuated antagonistically with two cables. The joint geometry and the cable attachments are set such that the orientation range of a chosen end-effector remains symmetric w.r.t. a home configuration where the two cable lengths are equal. The singularities that limit the movement of such a joint were reported. The static model of this system was developed, and the ability of antagonistic cable forces (> 0) to modulate the joint stiffness was studied. This modulation is characterized by the coefficient of the redundant force in the stiffness expression. Interestingly, it was observed that this coefficient depends only on the first- and second-order derivatives of the two cable lengths w.r.t. a generalized coordinate, thereby placing the study of stiffness modulation inside the domain of kinematics. We have proved that this remains the case even while the joints are actuated by cables with in-series linear springs, as found in most of the tensegrity-inspired systems and series elastic actuators in the literature.

While the force coefficients in the stiffness are positive, the increase in actuation forces increases the joint stiffness, similar to coactivation in muscle actuation in biological systems. On the other hand, if the force coefficients are negative, then the joint stiffness decreases with increasing actuation forces, contrary to the behavior of biological systems. Finally, if the force coefficients

are zero, then the actuation forces cannot modulate the stiffness of the joint. Examples of joints exhibiting this particular behavior were presented.

Several joints were studied for their stiffness modulation property through their force coefficients. Tensegrity-inspired revolute joints (R-joint) constructed from congruent triangular trusses with cables arranged on the two sides have negative force coefficients. However, by relaxing the condition of congruence between the triangles, it is possible to achieve coactivation in this joint.

This study was extended to four-bar mechanisms with symmetric limbs actuated by cables attached between unconnected pivot pairs. We found that the mechanism exhibits coactivation only when the limbs are crossed and not otherwise. However, as in the R-joint, it is possible to change the attachment points of the cables and make the four-bar mechanisms with non-crossed limbs exhibit coactivation. But, this comes at the cost of a reduction in the range of movement. Several numerical examples have been presented to illustrate this fact.

Experiments were conducted on the R-joint and various four-bar mechanisms to confirm the theoretical results on the correlation between actuation forces and joint stiffness. The analysis of force coefficients could also explain some of the experiments reported in the literature. Among all the joints that exhibit coactivation, the anti-parallelogram mechanism (X-joint) offers the largest orientation range of movement for the top bar $]-\pi, \pi[$ relative to its base and is the best choice for developing bio-inspired systems.

In the future, it would be interesting to extend this study to multiple DoF joints that can more completely model the contact between bones in animals.

2-X MANIPULATOR: CABLE ACTUATION AND WORKSPACE

Abstract

This chapter introduces a planar two-degree-of-freedom (2-DoF) tensegrity-inspired manipulator composed of two anti-parallelogram (X) joints with springs and remotely actuated by cables. Two actuation schemes with four cables and three cables, respectively, are considered for this manipulator. A fast and automated method to compute the stable wrench-feasible joint space (SWFJ), followed by the stable wrench-feasible workspace (SWFW), is proposed for the two actuation schemes. It involves deriving the limiting conditions of wrench-feasibility and stability as univariate polynomials and their numerical resolution. The results show that the 4-cable scheme produces a larger and more symmetric SWFW than its counterpart. The proposed method is generic and can be used for computing the SWFJ of any n -DoF tensegrity-inspired manipulator that is fully actuated. However, additional challenges exist in the computation of SWFW for manipulators with kinematic redundancy.

Contents

3.1	Introduction	76
3.2	Description of the 2-X manipulator	77
3.3	Actuation with four cables and three cables	78
3.4	Kinematic model of the 2-X manipulator	80
3.5	Static model for the 4-cable and 3-cable schemes	81
3.5.1	4-cable scheme	81
3.5.2	3-cable scheme	85
3.6	Stable wrench-feasible joint space (SWFJ) for the 4-cable and 3-cable schemes	87
3.6.1	General algorithm	88
3.6.2	Numerical example	89
3.7	Stable wrench-feasible workspace (SWFW) for the 4-cable and 3-cable schemes	94
3.8	Extension to n-X manipulator for $2n$-cable and $(n + 1)$-cable schemes	95
3.9	Conclusions	98

3.1 Introduction

The most commonly found manipulators in the literature are of two types: serial and parallel. The serial manipulators contain links and motors arranged serially in a successive manner. They have a large workspace, but it comes at the cost of heavy moving masses and massive energy consumption due to the floating actuators. In contrast, the parallel manipulators contain a moving platform and a fixed base connected through several serial chains, each of which typically includes one actuator fixed to the ground. They have a smaller workspace but benefit from small moving mass and low energy requirements. This work considers a new class of manipulators, namely, tensegrity-inspired manipulators. They have a serial architecture but are actuated remotely by motors fixed to the base, as in the parallel manipulators, using cables (more number than DoF) as transmission elements. Hence, we expect them to retain the advantage of a large workspace while possessing a smaller moving mass. They are also equipped with springs for stability, and the redundant actuation by cables permits them to exhibit variable stiffness at a given configuration, simultaneously making them suitable for high-stiffness tasks (e.g., accurate trajectory tracking) and low-stiffness tasks (e.g., interaction with humans).

From Chapter 2 and [MW21], it is clear that the tensegrity-inspired anti-parallelogram (X) joint offers several interesting properties, such as coactivation and a large range of movement when compared to the others. Additionally, its kinematics is equivalent to the pure rolling of one ellipse over another, which approximates bone-bone contact in the biological systems more closely than the conventional revolute joint [HAC14]. Hence, motivated by these properties, a 2-DoF tensegrity-inspired/bio-inspired manipulator composed of two X-joints shown in Fig. 3.1 is considered for the study. Several challenges exist while moving from a single joint to two or more DoF cable-driven serial manipulators. The most important one concerns the choice of an actuation scheme [LOH13],[Ram+20].

In this work, two actuation schemes are considered for the 2-X manipulator. The first scheme uses four cables while the second uses three cables, the minimum required for a 2-DoF system [MA12]. An important measure to quantify the performance of such manipulators is their workspace. Since they are driven by cables that sustain only tensile forces, the reachable workspace is further qualified by the condition(s) of static equilibrium achievable with positive cable tensions. When bounds on the maximum cable forces are imposed, the resulting workspace is called the wrench-feasible workspace (WFW) for a cable-driven manipulator [BREU06]. For tensegrity-inspired manipulators, this workspace is further qualified by the stability condition as defined in [Boe+15]. In this thesis, we refer to this workspace as the stable wrench-feasible workspace (SWFW) to make a clear distinction from the WFW where stability is not imposed. The stability condition is helpful from the control perspective, as the inherent stiffness of the manipulator might be sufficient to mitigate the tracking errors and produce acceptable motions with simple open-loop control laws. This scheme also allows for soft interactions with humans/environment, making them suitable for collaborative tasks.

In the literature, continuation methods have been employed to compute the SWFW of a tensegrity mechanism [Boe+15]. However, the time taken for such computations have not been presented. A brute-force scanning technique has been followed in [FW19], where a two-dimensional (2-D) scanning was performed in the joint space of a 2-DoF manipulator to determine the wrench-feasible joint space (WFJ), followed by the WFW. The limitation of such a technique is that a high scanning resolution is required to obtain the boundary points with suf-

ficient accuracy, which is a computationally expensive task. Alternatively, it is possible to derive all the limiting conditions of wrench-feasibility, stability, and joint limits as implicit functions of the joint variables and plot their contours in the joint space as in [AG06]. But, after obtaining these plots, one needs to manually inspect one point inside each of the connected regions to find which ones are feasible and which are not. Though this is a viable method for analyzing a few designs, it is unsuitable for an automated design process.

This chapter proposes a computationally efficient method to determine the SWFW boundary of a kinematically non-redundant tensegrity manipulator with a good accuracy and in an automatic manner (i.e., without requiring human intervention). Such a method is beneficial for optimizing these manipulators, where several thousand designs will be explored. It combines the accuracy of resolving implicit equations with the simplicity of scanning to achieve the goal, which comes at the cost of some tedious symbolic precomputations. For an n -DoF manipulator, it involves $(n - 1)$ -D scanning of the joint space to be performed n times. At each grid point, the implicit equations are converted into univariate polynomials in the remaining joint angle and solved numerically to accurately determine the boundary points of the stable wrench-feasible joint space (SWFJ). Then, these points are mapped onto the task space along with the singularities to obtain the SWFW.

The rest of this chapter is organized as follows: a description of the 2-X manipulator is presented in Section 3.2. Two actuation schemes with four and three cables are proposed in Section 3.3. The kinematic and static models are developed in Sections 3.4 and 3.5, respectively. A method to compute the SWFJ is presented with an example in Section 3.6. The SWFW of the 4-cable and 3-cable schemes are plotted and compared in Section 3.7. The proposed method has been generalized to n -X manipulators in Section 3.8. Finally, the conclusions of this study are presented in Section 3.9.

3.2 Description of the 2-X manipulator

The schematic of the 2-X manipulator is shown in Fig. 3.1. It is a planar 2-DoF robotic system used to control the position of an end-effector point $P(x, y)$, containing a point payload of mass m_p .

The 2-X manipulator comprises two X-joints arranged in series with rigid offsets (highlighted in shading) as shown in Fig. 3.1. Each X-joint consists of a top bar and a base bar of length b , and two crossed bars of length l , satisfying the condition ($l > b$) for its assembly. All the bars are connected to their neighbors with pivots.

For joint i , the orientation of the top bar relative to its base is denoted by α_i , with $i = 1, 2$, as shown in Fig. 3.1. It is equipped with two identical extension springs of stiffness k_i and free length $l_{0,i}$, on either side to ensure that the manipulator remains in stable equilibrium at the home configuration $(\alpha_1, \alpha_2) = (0, 0)$ rad¹ when no external forces (other than the gravitational forces) are applied. There exist two rigid offsets (in the form of trusses) of length a between the two joints and between the second joint and the end-effector point P , as indicated by the shaded portions in Fig. 3.1. Note that the purpose of shading is only to differentiate between the offsets and joints, while both are composed of bars and pivots. All the bars and springs are arranged in parallel planes, as shown in Fig. 3.2 to avoid any interference between them. This arrangement

1. In this thesis, all the angular measurements are presented in radians unless specified otherwise.

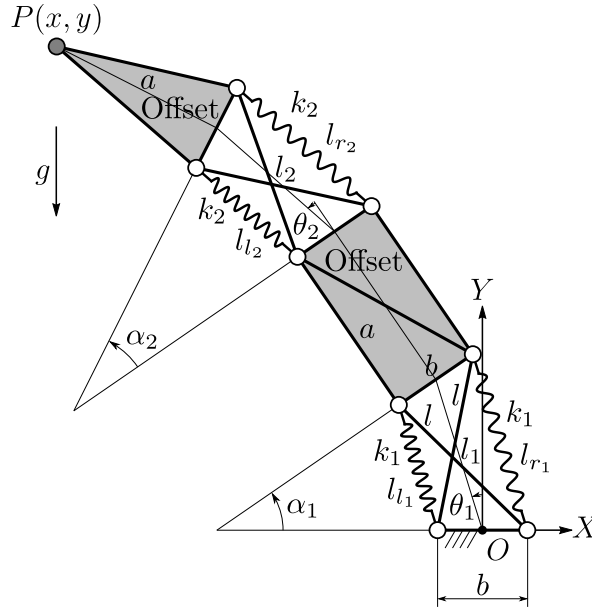


Figure 3.1 – Schematic of the 2-X manipulator.

also improves the rigidity of the manipulator in the direction normal to the plane of movement, as is necessary for its practical realization. All the bars are assumed to be inelastic and uniform circular cylinders in this study.

The 2-X manipulator is placed such that its plane of motion is parallel to the direction of gravity (see Fig. 3.1), unlike a conventional SCARA robot [HNP08]. This placement ensures that the moments induced due to the weight of bars/payload are parallel to the axes of the pivots, which they cannot transmit. Since pivots connect all the elements, there is only a transmission of axial forces between them. In order to preserve this property and keep the moving structure light, these manipulators will be actuated remotely by motors installed on the ground, using cables as transmission elements. The presence of only tension/compression elements and their arrangement with inherent mechanical stability makes the 2-X manipulator resemble a tensegrity system. Hence, it is classified as a tensegrity-inspired manipulator.

The following section explains the actuation scheme of the 2-X manipulator.

3.3 Actuation with four cables and three cables

Two actuation schemes with cables are considered for the 2-X manipulator, as shown in Fig. 3.3. The first one, referred to as the 4-cable scheme, involves four actuators/cables (see Fig. 3.3a), namely, C_{l_1} , C_{r_1} , C_{l_2} , C_{r_2} . The second one, referred to as the 3-cable scheme, involves only three cables (see Fig. 3.3b).

In the 4-cable scheme, the cables C_{l_1} and C_{r_1} actuate the first X-joint antagonistically, while the cables C_{l_2} and C_{r_2} actuate the second joint in a similar manner independently of the first one. In order to achieve this independence, the cables C_{l_2} , C_{r_2} have been routed along the bars of the first joint and the rigid offsets with pulleys, following the strut-routed scheme described

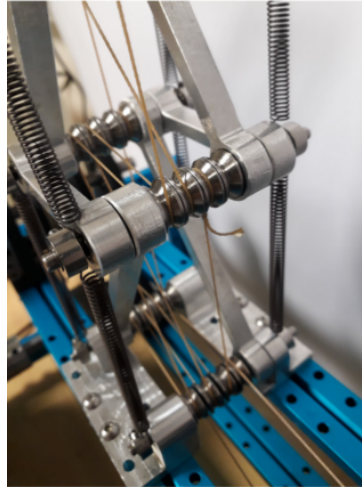


Figure 3.2 – Arrangement of bars in parallel planes (Source: [Fas+20]).

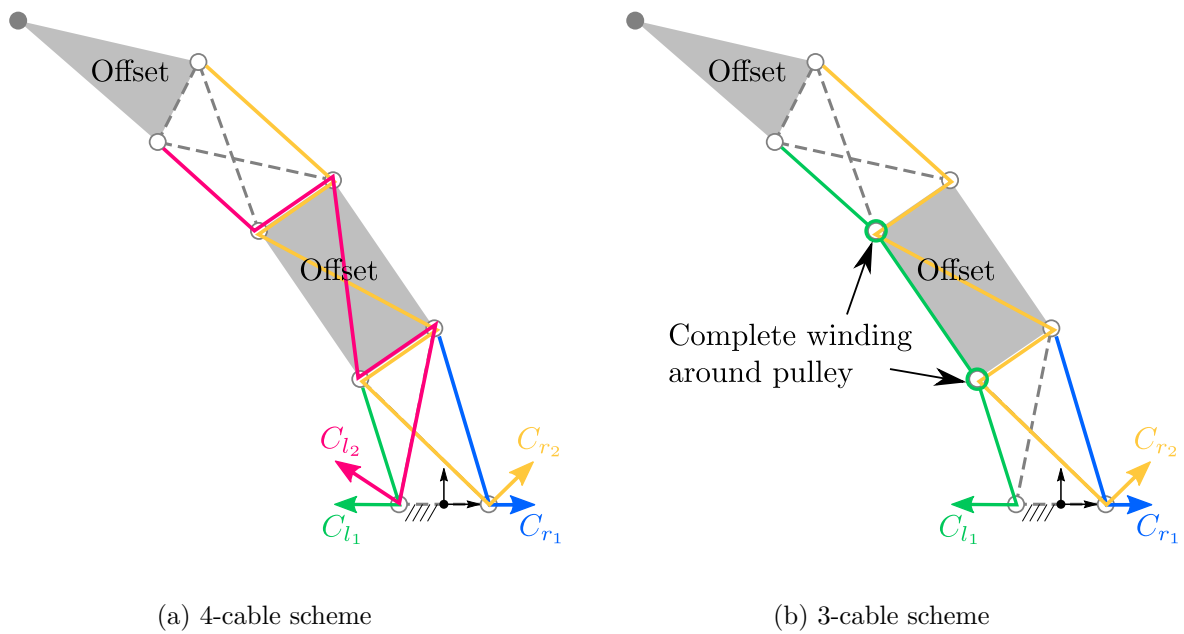


Figure 3.3 – Actuation with four cables (left) and three cables (right).

in [FW19]. They have been passed through the rigid offset multiple times in a zig-zag manner to avoid loss of contact with the pulleys. The advantage of this scheme is the independence in actuation of the two joints, but it uses one cable more than the minimum required [MA12].

On the other hand, the 3-cable scheme in Fig. 3.3b uses the minimum number of cables required for actuating the manipulator at hand. The cables C_{r_1} and C_{r_2} have the same connections as in the 4-cable scheme. In contrast, the cable C_l is routed along the left side of both the joints in a side-routed scheme [Fas+21]. It is wound completely around two pulleys (at the top left of the first joint and bottom left of the second joint) before being connected to the top left vertex of the second X-joint. This way, the cable C_l can control the movement of both joints, albeit in a dependent manner. This scheme is inspired from the muscle organization in a bird's neck [Fas+21].

This study assumes that the cables are massless and inextensible while the pulleys are massless points with zero radii. The forces imposed by the actuating cables are bounded below by F_{\min} and above by F_{\max} , with $F_{\min} = 0$ N for simplicity.

The kinematic model of the 2-X manipulator is presented in the next section. This is followed by the development of the static models for the two actuation schemes.

3.4 Kinematic model of the 2-X manipulator

From Section 2.6.3, it is recalled that the movement of each X-joint i is limited by the flat-singularities that occur at $\alpha_i = \pm\pi$. This limits the study of kinematics as well as statics of the manipulator to the range $\alpha_i \in]-\pi, \pi[$, for $i = 1, 2$. In this range, there exists a one-to-one map between the lengths of the cables (see Figs. 3.1 and 3.3) on the two sides and the joint angle (α_i). The expressions for cable lengths are recalled from Eq. (2.33) as follows:

$$\begin{cases} l_i(\alpha_i) = -b \sin(\alpha_i/2) + \sqrt{l^2 - b^2 \cos^2(\alpha_i/2)} \\ l_{r_i}(\alpha_i) = b \sin(\alpha_i/2) + \sqrt{l^2 - b^2 \cos^2(\alpha_i/2)} \end{cases} \quad (3.1)$$

The kinematic model of the 2-X manipulator involves expressing the end-effector coordinates (x, y) in terms of the joint angles (α_1, α_2) . Considering that $\alpha_i \in]-\pi, \pi[$, $i = 1, 2$, it is possible to present the direct kinematics of the manipulator (see Fig. 3.1) as follows (see [WF21] for more details):

$$\begin{cases} x = -l_1(\alpha_1) \sin(\alpha_1/2) - a(\sin \alpha_1 + \sin(\alpha_1 + \alpha_2)) - l_2(\alpha_2) \sin(\alpha_1 + \alpha_2/2) \\ y = l_1(\alpha_1) \cos(\alpha_1/2) + a(\cos \alpha_1 + \cos(\alpha_1 + \alpha_2)) + l_2(\alpha_2) \cos(\alpha_1 + \alpha_2/2) \\ \text{where } l_i(\alpha_i) = \sqrt{l^2 - b^2 \cos^2(\alpha_i/2)}, \quad i = 1, 2 \end{cases} \quad (3.2)$$

It has been shown in [WF21] that the inverse kinematic problem admits up to eight solutions without joint limits. But, in the presence of joint limits, we could find numerical examples with only up to four solutions, which occur when the offsets are given small values. However, we cannot definitively conclude the maximum number of inverse kinematic solutions when there are joint limits.

Differentiation w.r.t. time yields:

$$\begin{bmatrix} \dot{x} \\ \dot{y} \end{bmatrix} = \mathbf{J}_x \begin{bmatrix} \dot{\alpha}_1 \\ \dot{\alpha}_2 \end{bmatrix}, \text{ where } \mathbf{J}_x = \begin{bmatrix} J_{11} & J_{12} \\ J_{21} & J_{22} \end{bmatrix} = \begin{bmatrix} \frac{\partial x}{\partial \alpha_1} & \frac{\partial x}{\partial \alpha_2} \\ \frac{\partial y}{\partial \alpha_1} & \frac{\partial y}{\partial \alpha_2} \end{bmatrix}, \text{ is a Jacobian matrix.} \quad (3.3)$$

The singularity condition for the manipulator is obtained from the vanishing of the determinant of \mathbf{J}_x . After clearing the non-zero factors and the denominator of $\det(\mathbf{J}_x)$, the singularity condition can be expressed as [WF21]:

$$\begin{aligned}
 & 4a \sin \theta_2 \sqrt{l^2 - b^2 \cos^2 \theta_1} \left(l^2 - 2b^2 \cos^2 \theta_2 \right) + 2b^4 \cos \theta_1 \sin \theta_2 \cos^2 \theta_2 \\
 & + b^2 l^2 \left(\sin(\theta_1 - \theta_2) - 2 \cos^2 \theta_2 \sin(\theta_1 + \theta_2) \right) + l^4 \sin(\theta_1 + \theta_2) \\
 & + \sqrt{l^2 - b^2 \cos^2 \theta_2} \left(2a \left(\cos \theta_1 \sin \alpha_2 \left(l^2 - b^2 \right) - l^2 \sin \theta_1 \sin^2 \theta_2 + l^2 \sin \theta_1 \cos^2 \theta_2 \right) \right. \\
 & \left. - \left(b^2 - 4a^2 \right) \sin \alpha_2 \sqrt{l^2 - b^2 \cos^2 \theta_1} \right) = 0
 \end{aligned} \tag{3.4}$$

where $\theta_1 = (\alpha_1/2)$, $\theta_2 = (\alpha_2/2)$ (see Fig. 3.1). Such substitutions are made in this section and the next one to avoid presenting fractional arguments in the long equations. Note that $(\alpha_1, \alpha_2) = (0, 0)$ satisfies the singularity condition irrespective of the bar lengths.

The kinematic model presented above is independent of the cable actuation schemes. On the other hand, the static model varies with the actuation scheme and is described in the following section.

3.5 Static model for the 4-cable and 3-cable schemes

The static model of the 2-X manipulator actuated by the 4-cable scheme is discussed in detail in Section 3.5.1. The main differences that arise while using the 3-cable scheme are pointed out in Section 3.5.2.

3.5.1 4-cable scheme

The potential energy, equations of static equilibrium, and the stiffness matrix are derived for the 4-cable scheme in the following.

Potential energy

The total potential energy of the 2-X manipulator due to gravity, springs, and cable actuation is computed to be:

$$U_x = m_p g y_p + \sum_{j=1}^{12} m_j g y_j + \sum_{i=1}^2 \left(m_{k_i} g (y_{l_i} + y_{r_i}) + \frac{k_i}{2} \left((l_i - l_{0_i})^2 + (l_{r_i} - l_{0_i})^2 \right) + F_{l_i} l_i + F_{r_i} l_{r_i} \right) \tag{3.5}$$

where m_p is the mass of the point payload, y_p is its y -coordinate. The symbol m_j represents the mass of the j^{th} bar (see Fig. 3.4) and y_j is the y -coordinate of its geometric center. Similarly, m_{k_i} represents the mass of the springs in the i^{th} joint, and y_{l_i} (resp. y_{r_i}) is the y -coordinate of the mid-point of the attachment points of the left (resp. right) spring (see Fig. 3.1). In effect, the terms containing g ($= 9.8 \text{ m/s}^2$, the acceleration due to gravity) represent the contribution of gravity in the total potential energy (assuming the zero-potential reference along the x -axis). The remaining terms signify the contribution of spring stiffness and actuation forces to the total potential, respectively. The lengths l_i, l_{r_i} , shown in Fig. 3.1, can be expressed as functions of l, b, α_i (see Eq. (3.1)). The forces F_{l_i}, F_{r_i} are the actuation forces imposed by cables C_{l_i}, C_{r_i} (see Fig. 3.3a), respectively, for $i = 1, 2$.

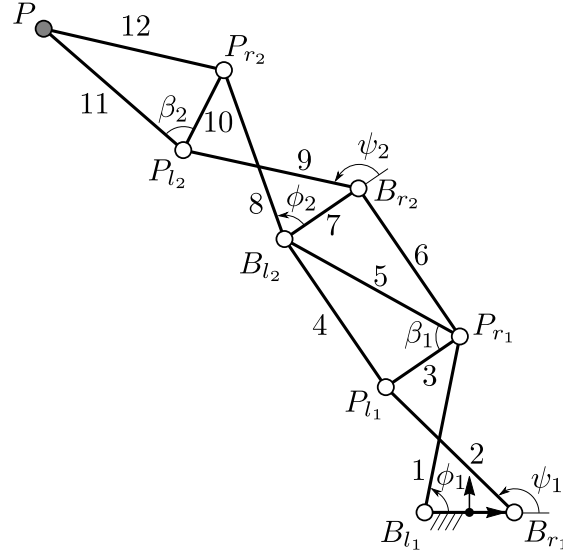


Figure 3.4 – Labels for the bars of the 2-X manipulator.

Static equilibrium equations

The static equilibrium equations can be obtained by setting the derivatives of U_x w.r.t. α_1 and α_2 , to zeros. This results in two equations, which can be written in the following form:

$$\begin{cases} G_1(k_1, g, \alpha_1, \alpha_2) = \Gamma_1(F_{l_1}, F_{r_1}, \alpha_1) \\ G_2(k_2, g, \alpha_1, \alpha_2) = \Gamma_2(F_{l_2}, F_{r_2}, \alpha_2) \end{cases} \quad (3.6)$$

where G_i represents the wrench due to springs and gravity, while Γ_i is the wrench due to the actuating cables on the i^{th} joint, with $i = 1, 2$. The expressions of G_i and Γ_i are given by:

$$\begin{cases} G_1 = -2C_{3x} \sin(\alpha_1 + \theta_2) \sqrt{l^2 - b^2 \cos^2(\theta_2)} + C_{1x} \sin \alpha_1 - C'_{3x} \sin(\alpha_1 + \alpha_2) \\ \quad + \frac{\sin(\theta_1) \left(-C''_{1x} (l^2 - 2b^2 \cos^2(\theta_1)) - C'_{1x} \cos(\theta_1) \right)}{\sqrt{l^2 - b^2 \cos^2(\theta_1)}} \\ G_2 = C_{2x} \sin \alpha_2 - C'_{3x} \sin(\alpha_1 + \alpha_2) \\ \quad + \frac{C_{3x} (b^2 \sin(\theta_2) \cos(\theta_2) \cos(\alpha_1 + \theta_2) + \sin(\alpha_1 + \theta_2) (b^2 \cos^2(\theta_2) - l^2)) - C'_{2x} \sin(\theta_2) \cos(\theta_2)}{\sqrt{l^2 - b^2 \cos^2(\theta_2)}} \\ \Gamma_1 = Z_{l_1} F_{l_1} + Z_{r_1} F_{r_1} \\ \Gamma_2 = Z_{l_2} F_{l_2} + Z_{r_2} F_{r_2} \end{cases} \quad (3.7)$$

where $\theta_1 = (\alpha_1/2), \theta_2 = (\alpha_2/2)$,

$$\begin{cases} C_{1x} = 2b^2k_1 - ag(2m_{10} + 4m_{11} + 2m_4 + m_5 + 2m_7 + 4m_8 + 4m_{k_2} + 2m_p) \\ C'_{1x} = 2b^2k_1l_{01} \\ C''_{1x} = g(m_1 + m_{10} + 2m_{11} + m_3 + 2m_4 + m_5 + m_7 + 2m_8 + m_{k_1} + 2m_{k_2} + m_p) \\ C_{2x} = 2b^2k_2 \\ C'_{2x} = 2b^2k_2l_{02} \\ C_{3x} = g(m_{10} + 2m_{11} + m_8 + m_{k_2} + m_p) \\ C'_{3x} = 2ag(m_{11} + m_p) \end{cases} \quad (3.8)$$

and

$$\begin{cases} Z_{l_i} = -\frac{dl_{i_i}}{d\alpha_i} = -b \cos(\theta_i) \left(\frac{b \sin(\theta_i)}{\sqrt{l^2 - b^2 \cos^2(\theta_i)}} - 1 \right) \\ Z_{r_i} = -\frac{dr_{i_i}}{d\alpha_i} = -b \cos(\theta_i) \left(\frac{b \sin(\theta_i)}{\sqrt{l^2 - b^2 \cos^2(\theta_i)}} + 1 \right) \end{cases} \quad (3.9)$$

for $i = 1, 2$.

The masses (m_2, m_6, m_9, m_{12}) have been replaced by (m_1, m_4, m_8, m_{11}) , respectively, to ensure mass symmetry of the manipulator (see Fig. 3.4) about the home configuration $(\alpha_1, \alpha_2) = (0, 0)$.

It can be shown that the coefficients of forces in the actuation wrench Γ_i have opposite signs, i.e., $Z_{l_i} > 0$ and $Z_{r_i} < 0$ when $\theta_i \in]-\frac{\pi}{2}, \frac{\pi}{2}[$, within the flat-singularities for $i = 1, 2$ (see [MW21]). This implies that F_{l_i} imposes a counterclockwise moment and F_{r_i} imposes a clockwise moment on the i^{th} joint, respectively. This feature is also evident from the cable routing shown in Fig. 3.3a. Thus, an increase in the force F_{r_i} means that F_{l_i} also increases to preserve the configuration of the manipulator. This simultaneous increase (or decrease) of the antagonistic forces allows the manipulator to achieve different stiffnesses at the same configuration, making them suitable for applications requiring variable stiffness.

Recall that the actuation forces imposed by cables are limited by: $F_{l_i}, F_{r_i} \in [F_{\min}, F_{\max}]$. Thus, at a given configuration (α_1, α_2) , the actuation wrench Γ_i is bounded below by $\underline{\Gamma}_i$ which occurs when $(F_{l_i} = F_{\min} \text{ and } F_{r_i} = F_{\max})$, and bounded above by $\overline{\Gamma}_i$ which occurs when $(F_{l_i} = F_{\max} \text{ and } F_{r_i} = F_{\min})$, for $i = 1, 2$. Consequently, the equilibrium equation given in Eq. (3.6) can be satisfied at (α_1, α_2) only when $G_i \in [\underline{\Gamma}_i, \overline{\Gamma}_i]$, which are known as the wrench-feasibility conditions. Hence, the limiting conditions of wrench-feasibility for the 4-cable scheme are given by: $G_1 = \underline{\Gamma}_1, G_1 = \overline{\Gamma}_1, G_2 = \underline{\Gamma}_2, G_2 = \overline{\Gamma}_2$.

Articular stiffness matrix

In general, the stability of an equilibrium configuration can be characterized by the positive definiteness of the associated stiffness matrix. For the 2-X manipulator actuated with the 4-cable scheme, the articular stiffness matrix (${}^4\mathbf{K}_\alpha$) can be computed as the Hessian of its potential energy w.r.t. $[\alpha_1, \alpha_2]^\top$, as follows:

$${}^4\mathbf{K}_\alpha = \begin{pmatrix} {}^4K_{11} & {}^4K_{12} \\ {}^4K_{12} & {}^4K_{22} \end{pmatrix} \text{ with } {}^4K_{11} = \frac{4({}^4K'_{11})}{(\lambda^2 - c_1^2)^{3/2}} \text{ and } {}^4K_{22} = \frac{4({}^4K'_{22})}{(\lambda^2 - c_2^2)^{3/2}} \quad (3.10)$$

where

$$\left\{ \begin{aligned}
 {}^4K'_{11} &= -4b^4c_{12}C_{3x}(\lambda^2 - c_1^2)^{3/2}\sqrt{\lambda^2 - c_2^2} - b^4c_1C''_{1x}\{2c_1^4 - c_1^2(3\lambda^2 + 2s_1^2) + \lambda^4 + 3\lambda^2s_1^2\} \\
 &\quad + b^2C'_{1x}(c_1^4 - c_1^2\lambda^2 + \lambda^2s_1^2) - 2b^3c'_{12}C'_{3x}(\lambda^2 - c_1^2)^{3/2} + 2b^3C_{1x}(\lambda^2 - c_1^2)^{3/2}(c_1^2 - s_1^2) \\
 &\quad - b^4F_{r_1}\left\{s_1(\lambda^2 - c_1^2)^{3/2} + (c_1^4 - c_1^2\lambda^2 + \lambda^2s_1^2)\right\} \\
 &\quad + b^4F_{l_1}\left\{s_1(\lambda^2 - c_1^2)^{3/2} - (c_1^4 - c_1^2\lambda^2 + \lambda^2s_1^2)\right\} \\
 {}^4K'_{22} &= -b^4C_{3x}\{c_{12}(2c_2^4 - 3c_2^2\lambda^2 + \lambda^4 + \lambda^2s_2^2) + 2c_2s_{12}s_2(\lambda^2 - c_2^2)\} \\
 &\quad - 2b^3c'_{12}C'_{3x}(\lambda^2 - c_2^2)^{3/2} + 2b^3C_{2x}(\lambda^2 - c_2^2)^{3/2}(c_2^2 - s_2^2) + b^2C'_{2x}(c_2^4 - c_2^2\lambda^2 + \lambda^2s_2^2) \\
 &\quad - b^4F_{r_2}\left\{s_2(\lambda^2 - c_2^2)^{3/2} + (c_2^4 - c_2^2\lambda^2 + \lambda^2s_2^2)\right\} \\
 &\quad + b^4F_{l_2}\left\{s_2(\lambda^2 - c_2^2)^{3/2} - (c_2^4 - c_2^2\lambda^2 + \lambda^2s_2^2)\right\} \\
 {}^4K_{12} &= -8C'_{3x}c'_{12} + \frac{4b}{\sqrt{\lambda^2 - c_2^2}}[C_{3x}\{c'_{12}c_2 - s'_{12}s_2 - (2\lambda^2 - 1)c_{12}\}]
 \end{aligned} \right. \quad (3.11)$$

in which $\lambda = (l/b)$, $c_1 = \cos(\theta_1)$, $s_1 = \sin(\theta_1)$, $c_2 = \cos(\theta_2)$, $s_2 = \sin(\theta_2)$, $s_{12} = \sin(2\theta_1 + \theta_2)$, $c_{12} = \cos(2\theta_1 + \theta_2)$, $c'_{12} = \cos(2(\theta_1 + \theta_2))$, $s'_{12} = \sin(2(\theta_1 + \theta_2))$.

Since the equilibrium equations in Eq. (3.6) must be satisfied while evaluating the stiffness, one could solve for two of the forces, say, (F_{l_1}, F_{l_2}) from the two equations and substitute in Eq. (3.11). This results in the stiffness matrix ${}^4\mathbf{K}_\alpha^{\text{rr}}$ which contains only the redundant actuation forces (F_{r_1}, F_{r_2}) :

$${}^4\mathbf{K}_\alpha^{\text{rr}} = \begin{pmatrix} {}^4K_{11}^{\text{rr}} & {}^4K_{12} \\ {}^4K_{12} & {}^4K_{22}^{\text{rr}} \end{pmatrix} \quad \text{with } {}^4K_{11}^{\text{rr}} = \frac{4({}^4K_{11}^{\text{rr}'})}{bc_1(\lambda^2 - c_1^2)} \quad \text{and } {}^4K_{22}^{\text{rr}} = \frac{4({}^4K_{22}^{\text{rr}'})}{bc_2(\lambda^2 - c_2^2)} \quad (3.12)$$

where

$$\left\{ \begin{aligned}
 {}^4K_{11}^{\text{rr}'} &= -2b^2C_{3x}\sqrt{\lambda^2 - c_2^2}\left(2c_1c_{12}(\lambda^2 - c_1^2) + c_1^2s_{12}\sqrt{\lambda^2 - c_1^2} + \lambda^2s_1s_{12}\right) \\
 &\quad + b^2C''_{1x}\left\{2c_1^4s_1 - c_1^2\lambda^2s_1 + \sqrt{\lambda^2 - c_1^2}(2c_1^4 - 2c_1^2s_1^2 - \lambda^2)\right\} \\
 &\quad + bC'_{3x}\left\{2c_1c'_{12}(c_1^2 - \lambda^2) - c_1^2s'_{12}\sqrt{\lambda^2 - c_1^2} - \lambda^2s_1s'_{12}\right\} \\
 &\quad + 2bc_1^3C_{1x}\left(s_1\sqrt{\lambda^2 - c_1^2} - c_1^2 + \lambda^2 + s_1^2\right) - c_1^3C'_{1x}\left(\sqrt{\lambda^2 - c_1^2} + s_1\right) \\
 &\quad + 2b^2c_1^3F_{r_1}\left(\sqrt{\lambda^2 - c_1^2} + s_1\right) \\
 {}^4K_{22}^{\text{rr}'} &= b^2C_{3x}\left[c_{12}c_2\left\{c_2^2\left(2\sqrt{\lambda^2 - c_2^2} + s_2\right) - \lambda^2\sqrt{\lambda^2 - c_2^2}\right\}\right. \\
 &\quad \left.+ s_{12}\left\{c_2^4 - c_2^2\left(2s_2\sqrt{\lambda^2 - c_2^2} + \lambda^2\right) - \lambda^2s_2\sqrt{\lambda^2 - c_2^2}\right\}\right] \\
 &\quad + C'_{3x}\left\{2bc'_{12}c_2(c_2^2 - \lambda^2) - bs'_{12}\left(c_2^2\sqrt{\lambda^2 - c_2^2} + \lambda^2s_2\right)\right\} \\
 &\quad + 2bc_2^3C_{2x}\left(s_2\sqrt{\lambda^2 - c_2^2} - c_2^2 + \lambda^2 + s_2^2\right) - c_2^3C'_{2x}\left(\sqrt{\lambda^2 - c_2^2} + s_2\right) \\
 &\quad + 2b^2c_2^3F_{r_2}\left(\sqrt{\lambda^2 - c_2^2} + s_2\right)
 \end{aligned} \right. \quad (3.13)$$

From the above expressions, one finds that the redundant force F_{r_i} is present only in the i^{th} diagonal term. Additionally, its coefficient $\frac{4\{2b^2c_i^3(\sqrt{\lambda^2-c_i^2+s_i})\}}{bc_i(\lambda^2-c_i^2)}$ is always positive since $\lambda > 1$ (assembly condition) and $\theta_i \in]-\frac{\pi}{2}, \frac{\pi}{2}[$ within the flat-singularities, for $i = 1, 2$. This shows that the antagonist forces positively correlate with the stiffness for the 2-X manipulator, similar to that of a single X-joint (see Section 2.6.3). Hence, maximum stiffness at a given configuration can be obtained by setting maximum forces in the cables such that all of them are within their bounds $[F_{\min}, F_{\max}]$. Since there are two redundant actuators in this manipulator, a pair of forces (F_{r_1}, F_{r_2}) or (F_{r_1}, F_{l_2}) or (F_{l_1}, F_{r_2}) or (F_{l_1}, F_{l_2}) can be set to F_{\max} to obtain maximum stiffness at any configuration.

Suppose a given configuration permits setting the forces (F_{r_1}, F_{r_2}) to F_{\max} , the stiffness matrix corresponding to maximum stiffness can be obtained as ${}^4\bar{\mathbf{K}}_{\alpha}^{\text{rr}} = {}^4\mathbf{K}_{\alpha}^{\text{rr}}(F_{r_1} = F_{\max}, F_{r_2} = F_{\max})$ from Eqs. (3.12),(3.13). If the resulting matrix is positive-definite, then that configuration is stable, or else it is not. However, while the configuration is not known a priori, the maximum stiffness could occur when any one of the four pairs of forces is at F_{\max} . Thus, the expressions for stiffness matrices corresponding to each force pair at F_{\max} are computed beforehand. They are denoted by $({}^4\bar{\mathbf{K}}_{\alpha}^{\text{rr}}, {}^4\bar{\mathbf{K}}_{\alpha}^{\text{rl}}, {}^4\bar{\mathbf{K}}_{\alpha}^{\text{lr}}, {}^4\bar{\mathbf{K}}_{\alpha}^{\text{ll}})$. Since the stiffness matrix $({}^4\mathbf{K}_{\alpha})$ was derived from the Hessian of the potential energy, it is a real symmetric matrix. Hence, it has two real eigenvalues (see [Str06], p. 330) and is positive-definite when both of them are positive. The limiting case of positive definiteness is obtained when the least of the eigenvalues becomes zero while the other one remains positive. However, obtaining explicit expressions for the eigenvalues and imposing conditions on them is difficult. Hence, we use the fact that the product of eigenvalues is equal to the determinant of the matrix (see [Str06], p. 266) and that the determinant vanishes when one/more eigenvalues vanish. Thus, the limiting condition(s) of positive definiteness/stability is contained in the conditions: $\det({}^4\bar{\mathbf{K}}_{\alpha}^{\text{rr}}) = 0, \det({}^4\bar{\mathbf{K}}_{\alpha}^{\text{rl}}) = 0, \det({}^4\bar{\mathbf{K}}_{\alpha}^{\text{lr}}) = 0, \det({}^4\bar{\mathbf{K}}_{\alpha}^{\text{ll}}) = 0$. These conditions include the vanishing of the least eigenvalue and the vanishing of the others as well. However, it is possible to filter the relevant solutions from the zeros by studying their neighborhood. This process will be illustrated with a numerical example in Section 3.6.2.

The zero-level sets of the above determinants can be plotted in the joint space to distinguish between the stable and unstable configurations of the manipulator. If a configuration (α_1, α_2) is identified as stable, then at least one combination of actuation forces can stabilize the manipulator at that configuration. The set of all (α_1, α_2) inside the joint limits, which respect the conditions of wrench-feasibility and stability, forms the stable wrench-feasible joint space (SWFJ) for this manipulator. A numerical example of its computation will be presented in Section 3.6.

In the next section, the static model is presented for the 3-cable scheme.

3.5.2 3-cable scheme

The limiting conditions of wrench-feasibility and stability are derived for the 3-cable scheme in the following.

Static equilibrium equations

In the 3-cable scheme, the side-routed cable C_l applies the same force F_l on the left side of both the joints (see Fig. 3.3b), while the cable C_{r_i} applies a force F_{r_i} only on the i^{th} joint.

Thus, the associated equilibrium equations are similar to the 4-cable scheme, but with F_{l_1} and F_{l_2} replaced by F_l . This can be written as:

$$\begin{cases} G_1 = Z_{l_1} F_l + Z_{r_1} F_{r_1} \\ G_2 = Z_{l_2} F_l + Z_{r_2} F_{r_2} \end{cases} \quad (3.14)$$

All the symbols have the same meaning as in Eqs. (3.7),(3.9). Recalling that $Z_{l_i} > 0$ and $Z_{r_i} < 0$, the minimum actuation wrenches are obtained when ($F_l = F_{\min}, F_{r_i} = F_{\min}$) and the maximum actuation wrenches are obtained when ($F_l = F_{\max}, F_{r_i} = F_{\min}$), for $i = 1, 2$. This results in the same limiting conditions for wrench-feasibility as in the 4-cable scheme: $G_1 = \underline{\Gamma}_1, G_1 = \overline{\Gamma}_1, G_2 = \underline{\Gamma}_2, G_2 = \overline{\Gamma}_2$. These are necessary for the 3-cable scheme but are not sufficient, as they do not account for the coupling in the two joints due to the side-routed cable on the left. The constraint due to this coupling can be obtained by first eliminating F_l from the two equilibrium equations to obtain the following equation:

$$G_3(k_1, k_2, \alpha_1, \alpha_2) = \Gamma_3(F_{r_2}, F_{r_1}, \alpha_1, \alpha_2) \quad (3.15)$$

where

$$\begin{cases} G_3 = G_1 - G_2(Z_{l_1}/Z_{l_2}) \\ \Gamma_3 = -Z_{r_2}(Z_{l_1}/Z_{l_2})F_{r_2} + Z_{r_1}F_{r_1} \end{cases} \quad (3.16)$$

Equation (3.15) must also be satisfied for the 3-cable scheme, in addition to the equations in Eq. (3.14) while $F_l, F_{r_1}, F_{r_2} \in [F_{\min}, F_{\max}]$. Since $Z_{l_i} > 0$ and $Z_{r_i} < 0$, it follows that the coefficient of F_{r_2} (resp. F_{r_1}) is positive (resp. negative). Thus, the actuation wrench Γ_3 is bounded below by $\underline{\Gamma}_3 = \Gamma_3(F_{r_1} = F_{\min}, F_{r_2} = F_{\max})$ and above by $\overline{\Gamma}_3 = \Gamma_3(F_{r_1} = F_{\max}, F_{r_2} = F_{\min})$. Thus, the additional limiting conditions for wrench-feasibility of the 3-cable scheme are formed by $G_3 = \underline{\Gamma}_3$ and $G_3 = \overline{\Gamma}_3$.

Articular stiffness matrix

For the 3-cable scheme, the articular stiffness matrix (${}^3\mathbf{K}_\alpha$) can be derived in the same manner as that of the 4-cable scheme. The resulting matrix is the same as in Eq. (3.10) and (3.11), with F_{l_1} and F_{l_2} replaced by F_l .

Since the two equilibrium equations in Eq. (3.14) must be satisfied, two of the forces (e.g., F_{r_1}, F_{r_2}) can be found in terms of the third one (e.g., F_l) and substituted into the stiffness matrix (${}^3\mathbf{K}_\alpha$). This results in the matrix ${}^3\mathbf{K}_\alpha^1$ with the redundant force F_l , expressed as follows:

$${}^3\mathbf{K}_\alpha^1 = \begin{pmatrix} {}^3K_{11}^1 & {}^3K_{12} \\ {}^3K_{12} & {}^3K_{22}^1 \end{pmatrix} \text{ with } {}^3K_{11}^1 = \frac{4({}^3K_{11}^{\prime})}{bc_1(\lambda^2 - c_1^2)} \text{ and } {}^3K_{22}^1 = \frac{4({}^3K_{22}^{\prime})}{bc_2(\lambda^2 - c_2^2)} \quad (3.17)$$

where ${}^3K_{12} = {}^4K_{12}$ (see Eq. (3.11)) and

$$\left\{ \begin{array}{l} {}^3K'_{11} = 2b^2C_{3x}\sqrt{\lambda^2 - c_2^2} \left(-2c_1c_{12}(\lambda^2 - c_1^2) + c_1^2s_{12}\sqrt{\lambda^2 - c_1^2} - \lambda^2s_1s_{12} \right) \\ \quad + b^2C''_{1x} \left\{ -2c_1^4s_1 + c_1^2\lambda^2s_1 + \sqrt{\lambda^2 - c_1^2} (2c_1^4 - 2c_1^2s_1^2 - \lambda^2) \right\} \\ \quad + bC'_{3x} \left\{ 2c_1c'_{12}(c_1^2 - \lambda^2) + c_1^2s'_{12}\sqrt{\lambda^2 - c_1^2} - \lambda^2s_1s'_{12} \right\} \\ \quad + 2bc_1^3C_{1x} \left(-s_1\sqrt{\lambda^2 - c_1^2} - c_1^2 + \lambda^2 + s_1^2 \right) - c_1^3C'_{1x} \left(\sqrt{\lambda^2 - c_1^2} - s_1 \right) \\ \quad + 2b^2c_1^3F_l \left(\sqrt{\lambda^2 - c_1^2} - s_1 \right) \\ {}^3K'_{22} = b^2C_{3x} \left[c_{12}c_2 \left\{ c_2^2 \left(2\sqrt{\lambda^2 - c_2^2} - s_2 \right) - \lambda^2\sqrt{\lambda^2 - c_2^2} \right\} \right. \\ \quad \left. - s_{12} \left\{ c_2^4 - c_2^2 \left(-2s_2\sqrt{\lambda^2 - c_2^2} + \lambda^2 \right) + \lambda^2s_2\sqrt{\lambda^2 - c_2^2} \right\} \right] \\ \quad + C'_{3x} \left\{ 2bc'_{12}c_2(c_2^2 - \lambda^2) + bs'_{12} \left(c_2^2\sqrt{\lambda^2 - c_2^2} - \lambda^2s_2 \right) \right\} \\ \quad + 2bc_2^3C_{2x} \left(-s_2\sqrt{\lambda^2 - c_2^2} - c_2^2 + \lambda^2 + s_2^2 \right) - c_2^3C'_{2x} \left(\sqrt{\lambda^2 - c_2^2} - s_2 \right) \\ \quad + 2b^2c_2^3F_l \left(\sqrt{\lambda^2 - c_2^2} - s_2 \right) \end{array} \right. \quad (3.18)$$

As in the 4-cable scheme, the coefficient of redundant force F_l is positive in both the diagonal terms of matrix ${}^3\mathbf{K}_\alpha^1$, indicating the positive correlation between the forces and stiffness. Similarly, the stiffness matrices corresponding to the other forces F_{r_1}, F_{r_2} can be derived as ${}^3\mathbf{K}_\alpha^{r1}, {}^3\mathbf{K}_\alpha^{r2}$, respectively. The stiffness matrices obtained by setting each redundant force to F_{\max} are denoted by $({}^3\bar{\mathbf{K}}_\alpha^1, {}^3\bar{\mathbf{K}}_\alpha^{r1}, {}^3\bar{\mathbf{K}}_\alpha^{r2})$. Thus, similar to the 4-cable scheme, the limiting condition(s) of stiffness are given by: $\det({}^3\bar{\mathbf{K}}_\alpha^1) = 0, \det({}^3\bar{\mathbf{K}}_\alpha^{r1}) = 0, \det({}^3\bar{\mathbf{K}}_\alpha^{r2}) = 0$.

The following section presents a method to compute the SWFJ for the 4-cable and 3-cable schemes.

3.6 Stable wrench-feasible joint space (SWFJ) for the 4-cable and 3-cable schemes

A general algorithm to obtain the boundary of the SWFJ is presented in Section 3.6.1. It is illustrated with a numerical example for the two schemes in Section 3.6.2.

3.6.1 General algorithm

As a first step in the determination of the SWFJ boundary, all the limiting conditions of wrench-feasibility and stability can be grouped for the 4-cable and 3-cable schemes as follows:

$${}^4\mathbf{f}(\alpha_1, \alpha_2) = \begin{cases} {}^4f_1 := G_1 - \underline{\Gamma}_1 = 0 \\ {}^4f_2 := -G_1 + \overline{\Gamma}_1 = 0 \\ {}^4f_3 := G_2 - \underline{\Gamma}_2 = 0 \\ {}^4f_4 := -G_2 + \overline{\Gamma}_2 = 0 \\ {}^4f_5 := \det({}^4\overline{\mathbf{K}}_\alpha^{\text{rr}}) = 0 \\ {}^4f_6 := \det({}^4\overline{\mathbf{K}}_\alpha^{\text{rl}}) = 0 \\ {}^4f_7 := \det({}^4\overline{\mathbf{K}}_\alpha^{\text{lr}}) = 0 \\ {}^4f_8 := \det({}^4\overline{\mathbf{K}}_\alpha^{\text{ll}}) = 0 \end{cases} \quad {}^3\mathbf{f}(\alpha_1, \alpha_2) = \begin{cases} {}^3f_1 := G_1 - \underline{\Gamma}_1 = 0 \\ {}^3f_2 := -G_1 + \overline{\Gamma}_1 = 0 \\ {}^3f_3 := G_2 - \underline{\Gamma}_2 = 0 \\ {}^3f_4 := -G_2 + \overline{\Gamma}_2 = 0 \\ {}^3f_5 := G_3 - \underline{\Gamma}_3 = 0 \\ {}^3f_6 := -G_3 + \overline{\Gamma}_3 = 0 \\ {}^3f_7 := \det({}^3\overline{\mathbf{K}}_\alpha^{\text{l1}}) = 0 \\ {}^3f_8 := \det({}^3\overline{\mathbf{K}}_\alpha^{\text{r1}}) = 0 \\ {}^3f_9 := \det({}^3\overline{\mathbf{K}}_\alpha^{\text{r2}}) = 0 \end{cases} \quad (3.19)$$

Since each of these equations is a function of (α_1, α_2) , it is possible to plot their contours in the joint space and determine the SWFJ by inspecting the feasibility of one point inside each connected region. However, this approach requires manual intervention and is unsuitable for a design process where several manipulator designs might be explored.

Hence, an alternate approach that allows for fast and automated computation of the SWFJ boundary is followed in this work. It involves the conversion of all the limiting conditions into univariate polynomials and their numerical resolution for obtaining bounding points of the SWFJ with good accuracy. The steps involved in this process are listed in the following:

1. All the limiting conditions of wrench-feasibility and stability, must be consolidated together into a vector $\mathbf{f}(\alpha_1, \alpha_2) = \mathbf{0}$.
2. These conditions must be rewritten as polynomials in $t_1 = \tan(\alpha_1/4)$ (resp. $t_2 = \tan(\alpha_2/4)$) by suppressing the variable α_2 (resp. α_1) inside its coefficients to obtain $\mathbf{f}_1(t_1) = \mathbf{0}$ (resp. $\mathbf{f}_2(t_2) = \mathbf{0}$).
3. The joint space (α_1, α_2) must be discretized into grid lines of α_1 and α_2 inside the joint limits.
4. On each grid line of α_1 (resp. α_2), the bounding values of the stable wrench-feasible intervals of α_2 (resp. α_1) can be determined by solving the univariate polynomials $\mathbf{f}_2(t_2) = \mathbf{0}$ (resp. $\mathbf{f}_1(t_1) = \mathbf{0}$). The spurious solutions (if any) must be eliminated.
5. Once the boundary points (α_1, α_2) of the SWFJ on all the grid lines are calculated, a linear interpolation must be performed between them to obtain polygon(s) approximating the actual SWFJ.

The above algorithm can be adapted to the 4-cable and 3-cable schemes by using the conditions ${}^4\mathbf{f}$ and ${}^3\mathbf{f}$, respectively, in place of \mathbf{f} . It is clarified that $t_i = \tan(\alpha_i/4)$ represents the tangent half-angle form of the angle $\theta_i = \alpha_i/2$ in all the limiting equations presented in Sections 3.5.1 and 3.5.2.

The derivation of polynomials in step 2 involves the elimination of the square roots and tedious symbolic manipulations. This process is illustrated for one condition (${}^4f_1 = 0$) in Appendix A. The other steps are illustrated with a numerical example in the following sections.

3.6.2 Numerical example

This section presents a numerical example to compute the SWFJ of a 2-X manipulator actuated by the 4-cable and 3-cable schemes.

Data

The SWFJ can be computed for any design parameters of the 2-X manipulator using the proposed method. However, it is very difficult to come up with a good set of parameters intuitively to obtain a reasonably large SWFJ while ensuring the mechanical feasibility of springs and safety for the bars from buckling failure. Thus, we choose a special set of parameters for the 2-X manipulator presented in Table 3.1 for further study. These parameters are adopted from the design X_{IV} in Table E.1 (see Appendix E). This design satisfies all the above requirements and was obtained through a design optimization process that will be explained in detail in Chapters 5 and 6. This manipulator also contains a payload of mass $m_p = 2$ kg at the end-effector.

Table 3.1 – Example design of the 2-X manipulator with a payload $m_p = 2$ kg at the end-effector.

No.	Parameters	Values
1	b [m]	0.15
2	λ (l/b) $\{l$ [m] $\}$	2 {0.30}
3	a [m]	0.27
4	Spring 1: k_1 [N/m] $\{d$ [mm], D [mm], N_a , l_{0_1} [m], l_{\max_1} [m], m_{k_1} [kg] $\}$	2550 {3.0, 17.8, 57.38, 0.20, 0.33, 0.19}
5	Spring 2: k_2 [N/m] $\{d$ [mm], D [mm], N_a , l_{0_2} [m], l_{\max_2} [m], m_{k_2} [kg] $\}$	750 {3.0, 32.5, 32.05, 0.16, 0.42, 0.20}
6	F_{\max} [N]	176
7	$\{\alpha_{\max_1}, \alpha_{\max_2}\}$ [rad]	{0.86, 2.14}
8	Bar cross-section radius r_{b_j} [mm] $j = 1, \dots, 12$	{7, 7, 5, 6, 6, 6, 5, 5, 5, 5, 5, 5}
9	Moving mass [kg]	1.62
10	Size [m]	1.06

In Table 3.1, the first three rows contain the geometry parameters of the 2-X manipulator. The fourth and fifth rows present the specifications of the springs used. In addition to the stiffness k_i , the wire diameter (d), coil diameter (D), number of active coils (N_a), free length (l_{0_i}), maximum operation length (l_{\max_i}), and mass (m_{k_i}) are also presented for the springs installed in joint i , for $i = 1, 2$. The sixth row presents the maximal actuation forces in the cables (F_{\max}).

Due to the flat-singularities at $\alpha_i = \pm\pi$ and the free length of the springs, the range of movement of each joint i is limited to $\alpha_i \in [-\alpha_{\max_i}, \alpha_{\max_i}]$. These limits are presented for the two joints in the seventh row.

In this study, all the bars are assumed to have a uniform circular cross-section, made of Aluminum material with volumetric density is $\rho = 2700 \text{ kg/m}^3$. The cross-section radii of the bars (see Fig. 3.4 for their labels) are presented in the eighth row.

The moving mass of the manipulator, which includes the masses of the moving bars and all the springs (without the payload), is presented in the ninth row.

Finally, the size of the manipulator, measured as its maximum vertical reach at the home configuration $(\alpha_1, \alpha_2) = (0, 0)$, is presented in the last row.

The computation of the SWFJ is illustrated for these parameters in the following.

Boundary points of the SWFJ

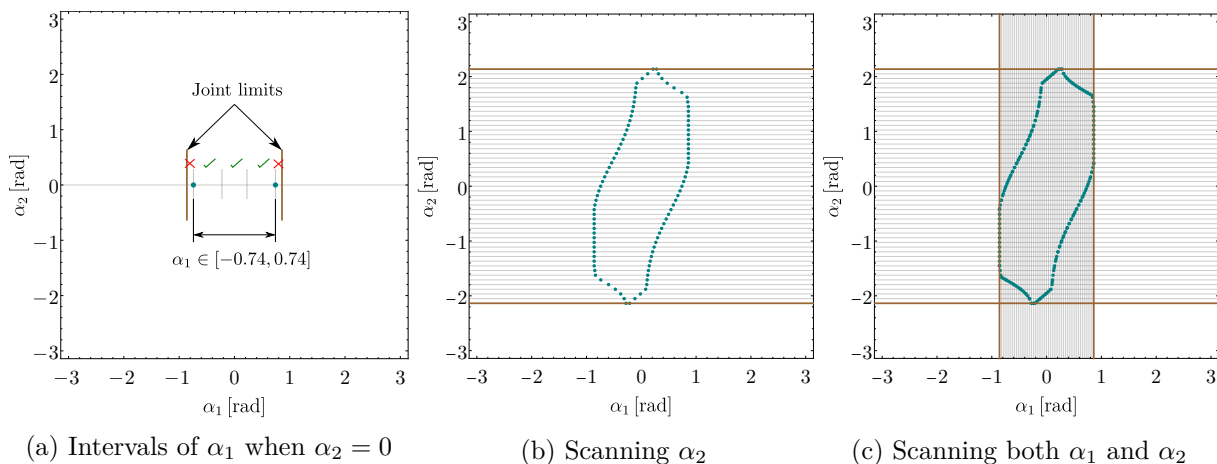


Figure 3.5 – Feasible interval of α_1 for a given $\alpha_2 = 0$ (left), boundary points obtained while scanning α_2 (middle), and all the boundary points obtained by scanning both α_1 and α_2 (right).

The steps 3-5 listed in Section 3.6.1 are illustrated for the 4-cable scheme for the above data. The joint axis α_i is discretized into 50 equally spaced points inside its joint limits $[-\alpha_{\max_i}, \alpha_{\max_i}]$ as shown in Fig. 3.5c. At a given grid line, e.g., $\alpha_2 = 0$, all the polynomial equations $\mathbf{f}_1(t_1) = \mathbf{0}$ are solved numerically. All the real roots within the joint limits $[-\alpha_{\max_1}, \alpha_{\max_1}]$ are collected as indicated by small vertical lines in Fig. 3.5a. The resulting intervals between two successive roots, and between the joint limits and their neighboring roots are inspected for wrench-feasibility and stability with one arbitrary point (α_1^*, α_2^*) inside them. If this point satisfies both conditions, then the entire interval is recognized as a feasible one. In this manner, all the intervals are classified into feasible and infeasible sets. This is indicated by a “tick” mark for a feasible set and a “cross” mark for an infeasible set in Fig. 3.5a. The union of all the feasible intervals forms the stable wrench-feasible values of α_1 when $\alpha_2 = 0$. For the example considered, the feasible range is found to be $\alpha_1 \in [-0.74, 0.74]$ rad. This process is repeated for all the grid lines of α_2 as shown in Fig. 3.5b.

Similarly, at the grid lines of α_1 , the polynomial equations $\mathbf{f}_2(t_2) = 0$ are resolved to obtain

the respective bounding values of α_2 . All the bounding points on the grid lines of α_2 and α_1 are shown together in Fig. 3.5c.

The proposed technique has the following advantages over the brute force 2-D scanning of the joint space. Firstly, the bounding points are obtained by solving polynomials, which does not miss out on any of them. Secondly, they are quite accurate with a very small residue (about 10^{-10} units) w.r.t. the original conditions.

The following section performs a linear interpolation between the bounding points to approximate the SWFJ as a polygon.

Polygonal approximation of the SWFJ

This section presents a method to connect the bounding points on the grid lines of the joint space with linear segments. Since several limiting conditions determine the SWFJ boundary, their contours have sharp turns at locations where the critical condition changes. Hence, a simple connection based on the smallest norm does not yield the desired interpolation. Thus, an enhanced interpolation scheme with prior classification of the points is followed in this work. The flowchart in Fig. 3.6 presents the complete algorithm.

The first step collects all the bounding points into a list. In step 2, each point is classified by defining four points around it, as illustrated with point A in Fig. 3.7a (magnified left bottom part). These points are tested for feasibility (wrench-feasibility and stability) in turns. Each could be feasible or infeasible, resulting in a total of $2^4 = 16$ combinations of results. But, since we disregard the cases where all the points are feasible or infeasible (see step 2 in Fig. 3.6), there are only 14 possible results. Thus, every boundary point can be classified into one of the 14 categories as indicated in the last block of step 2 in Fig. 3.6. For point A , only two of the four points (top and right) satisfy the feasibility conditions. This case is represented by the blue color, and so is point A (see Fig. 3.7a). Similarly, when the {(top, left), (bottom, right), (bottom, left)} points are feasible, the respective boundary points are shown in {orange, green, red} colors, respectively. Additionally, there are four groups along the four joint limits, which have three feasible neighbors. These points are shown in brown, violet, cyan, and olive colors.

The next step involves the definition of rules to connect two points. Note that every point lies on either an α_2 grid line (horizontal) or an α_1 grid line (vertical). Since we know that the boundary of SWFJ must be a continuous closed loop(s) inside the joint limits, it follows that for any given point, its neighbors must necessarily lie inside the box formed by the neighboring grid lines. More precisely, the neighbors must be on the bounding lines of this box or on the same grid line as the point inside the box. For instance, consider a point B from the α_2 grid line (magnified right bottom part of Fig. 3.7a), the box formed around it is highlighted by blue lines. There are two possible neighbors for this point, and they are said to be *proximal* to B . Similarly, for a point C on the α_1 grid line (top left magnified part of Fig. 3.7a), the box containing its neighbors has been defined, and there are two proximal points on it. Note that the shape of the boxes is different depending on the grid line to which the point belongs.

In step 3 (see Fig. 3.6), the proximal points within a group are connected starting from an open end, resulting in several interpolated groups as shown in Fig. 3.7b. At this stage, it is also possible to have “isolated” points that are not linked to any neighbors, as illustrated in [MWC22a]. Such points must be treated as groups with two identical ends. In the step 4, the ends of the groups are connected to one another based on the proximity check illustrated previously. This leads to a single closed loop, as shown in Fig. 3.7c. In other words, we have

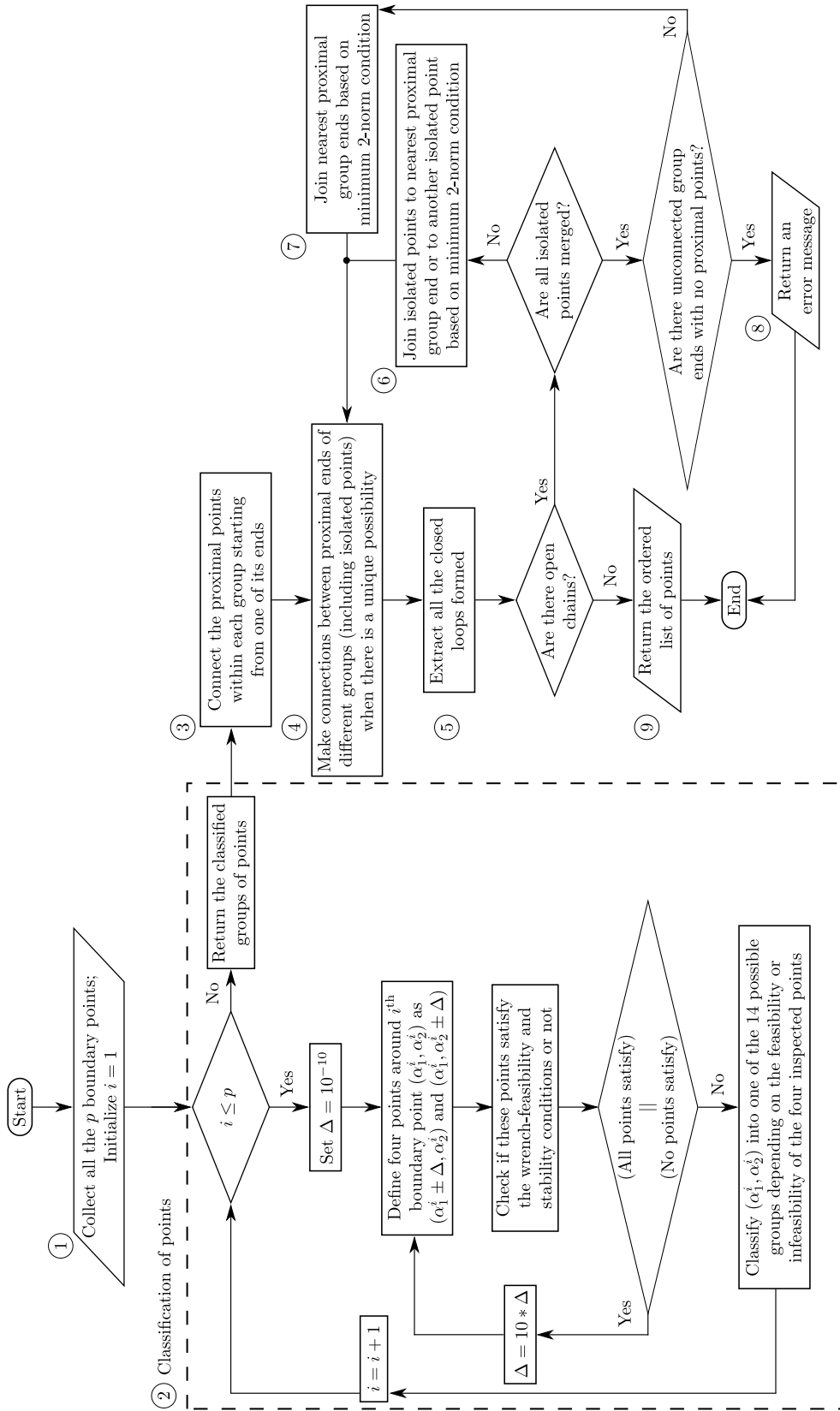


Figure 3.6 – Algorithm to find a cyclic ordering of planar points (α_1, α_2) on the boundary of the SWFJ.

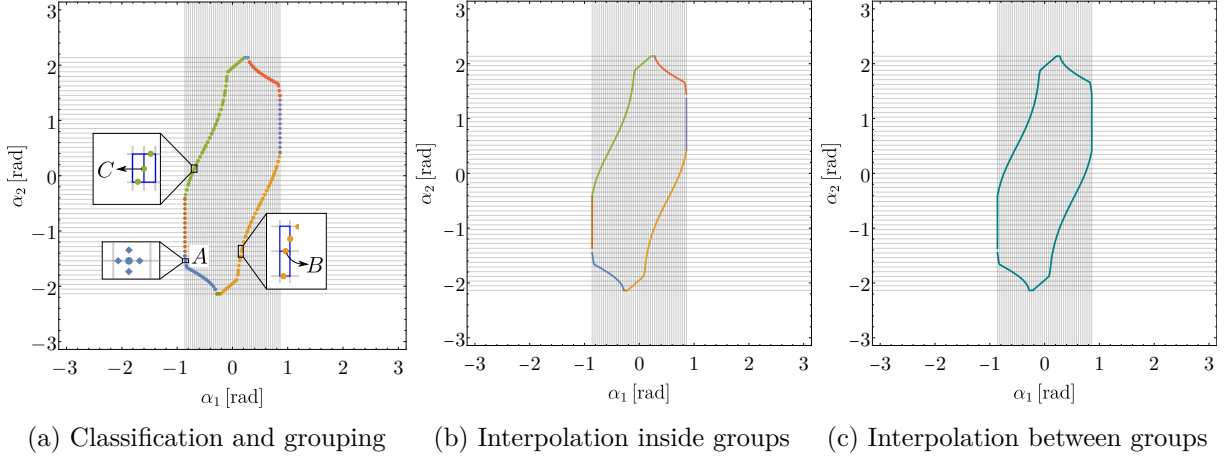


Figure 3.7 – Classification of boundary points into different groups (left), joining the points within groups (middle), and joining ends of the groups to form a cyclic ordering (right).

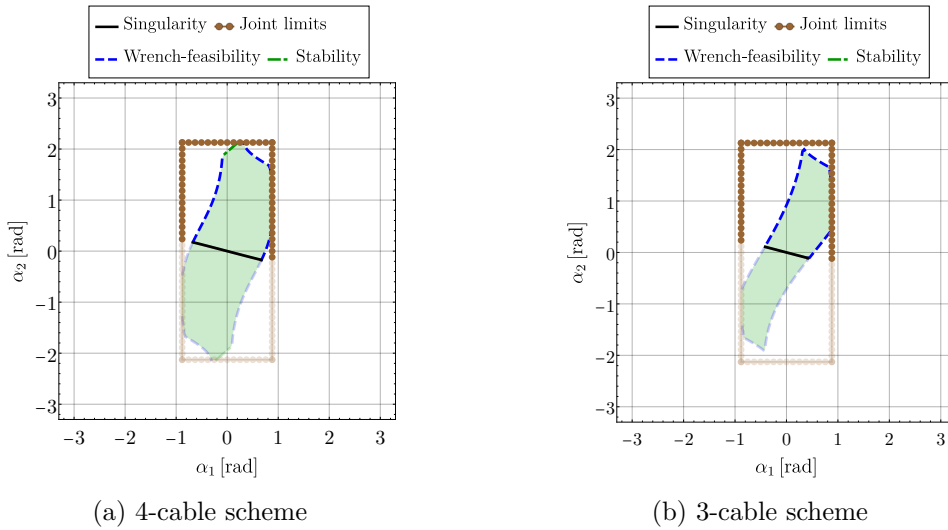


Figure 3.8 – Stable wrench-feasible joint space (SWFJ) obtained for 4-cable (left) and 3-cable (right) schemes. The curves lying in the region where $\det(\mathbf{J}_x) > 0$ are shown in opaque style while those in the region $\det(\mathbf{J}_x) < 0$ are shown in transparent style.

formed a polygon that well approximates the actual SWFJ. The maximum error due to the linear interpolation is limited above by the step size between two successive grid lines. One can improve the accuracy by increasing the number of grid lines.

Some other examples have been encountered where some group ends could not be connected in step 4 due to the existence of several proximal neighbors. In such cases, the points must be connected using the minimum 2-norm condition as mentioned in steps 6 and 7 of the algorithm in Fig. 3.6.

The plot of SWFJ boundaries for the 4-cable and 3-cable schemes are shown in Figs. 3.8a and 3.8b, respectively. The SWFJ is highlighted by shading, and its boundaries have been appropriately classified based on the associated limiting conditions, namely, joint limits, wrench-feasibility, and stability. It is clear that the SWFJ of the 3-cable scheme is a subset of the SWFJ obtained with the 4-cable scheme. Additionally, the 4-cable scheme has a symmetric SWFJ (i.e., (α_1, α_2) is equivalent to $(-\alpha_1, -\alpha_2)$) that is limited by the stability condition at the top and bottom ends. In contrast, no stability boundaries can be found for the 3-cable scheme.

In addition to the SWFJ boundary, the singularity curve ($\det(\mathbf{J}_x) = 0$) has also been plotted inside the SWFJ, which will be useful for constructing the workspaces in the two cases. The singularity condition was also treated in the same manner as the limiting equations in Eq. (3.19), by deriving equivalent polynomials, solving them at the grid lines in the joint space, and interpolating between the singular points. In Fig. 3.8, the limiting curves that lie in the region ($\det(\mathbf{J}_x) > 0$) are shown in opaque style and those in the region ($\det(\mathbf{J}_x) < 0$) are shown in transparent style. This distinction is made to show their overlapping images in the task space clearly.

The proposed method for ordering the boundary points is applicable to all planar problems with similar needs. It can also handle disconnected regions and voids inside a given region by treating them as separate loops. It has been tested for robustness with several designs of the 2-X manipulator for the 4-cable scheme.

The following section derives the stable wrench-feasible workspace from the SWFJ for the two actuation schemes.

3.7 Stable wrench-feasible workspace (SWFW) for the 4-cable and 3-cable schemes

The stable wrench-feasible workspace (SWFW) of the 2-X manipulator represents the set of all end-effector positions (x, y) in the task space where the manipulator can be held in a stable equilibrium for at least one combination of actuation forces inside their bounds. It can be computed by mapping the boundary of SWFJ and the singularities onto the task space using the direct kinematic model in Eq. (3.2). The images of the opaque and transparent curves in the SWFJ are shown in the task space with the same styles for the 4-cable scheme in Fig. 3.9a and the 3-cable scheme in Fig. 3.9b. In both cases, the SWFW is formed by two connected regions, which overlap over a small portion around the vertically straight configuration $(\alpha_1, \alpha_2) = (0, 0)$. There are two feasible configurations for the manipulator in the overlapping part, but just one in the others. It is observed that the 4-cable scheme has a larger SWFW that is also symmetric about the y -axis. On the other hand, the 3-cable scheme has a smaller and non-symmetric SWFW.

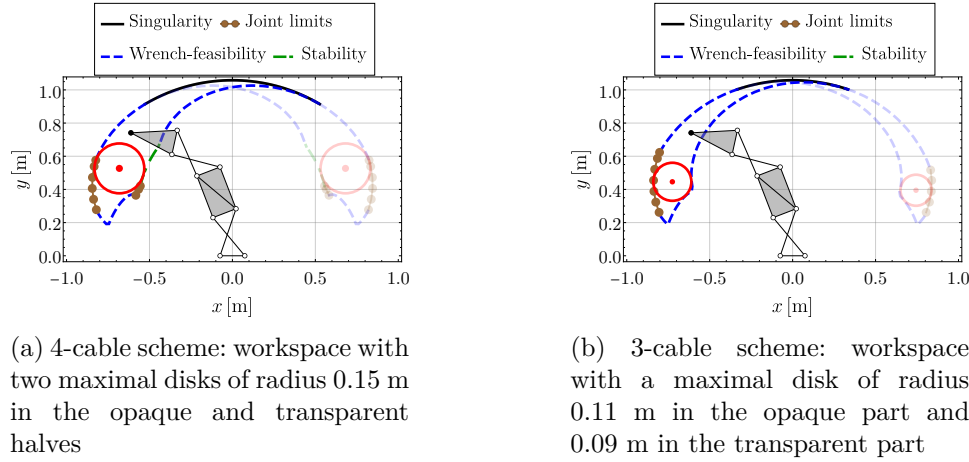


Figure 3.9 – Stable wrench-feasible workspace (SWFW) obtained for the 4-cable (left) and 3-cable (right) schemes. The opaque and transparent curves represent the two workspace components corresponding to configurations where $\det(\mathbf{J}_x) > 0$ and $\det(\mathbf{J}_x) < 0$, respectively.

Since the two parts of the SWFW are represented as polygons, it is possible to quantify them by fitting maximally inscribed disks inside each of them, as shown in Fig. 3.9. The `polylabel` library² in `c++` readily achieves this task with an ordered set of points. The SWFW of the 4-cable scheme contains two identical maximally inscribed disks of radius 0.15 m placed symmetrically in the two halves. Meanwhile, the SWFW of the 3-cable scheme contains maximally inscribed disks of different radii in the two parts (0.11 m in the opaque part and 0.09 m in the transparent part). The disks obtained with the 3-cable scheme are smaller than those obtained with the 4-cable scheme. The entire computation starting from the determination of boundary points to the fitting of disks takes about 43 ms (averaged over 100 runs³). This low time requirement makes the proposed method suitable for use in a design optimization tool, where several thousands of designs will be explored.

The possibility of extending the proposed algorithm to compute the SWFJ and SWFW boundary points for an n -X manipulator is discussed in the following section.

3.8 Extension to n -X manipulator for $2n$ -cable and $(n + 1)$ -cable schemes

This section extends the SWFJ and SWFW computation method discussed for the 2-X manipulator to an n -X serial manipulator for two actuation schemes, one with $2n$ cables (two cables per joint) and the other with $(n + 1)$ cables (one per joint and one connecting all the joints). The manipulator could be a planar or a spatial one.

Since there are n X-joints, the manipulator is an n -DoF system. Thus, there are n equations representing its static equilibrium. The general form of these equations is $G_i = \Gamma_i$, with $i = 1, \dots, n$. For the $2n$ -cable scheme, there are two limiting conditions from each equation, namely,

2. The associated code could be found at <https://github.com/mapbox/polylabel>.

3. All the computations reported in this thesis have been performed on a computer with an Intel® Core™ i7-6700 CPU running @ 3.40GHz processor, using a C++ code.

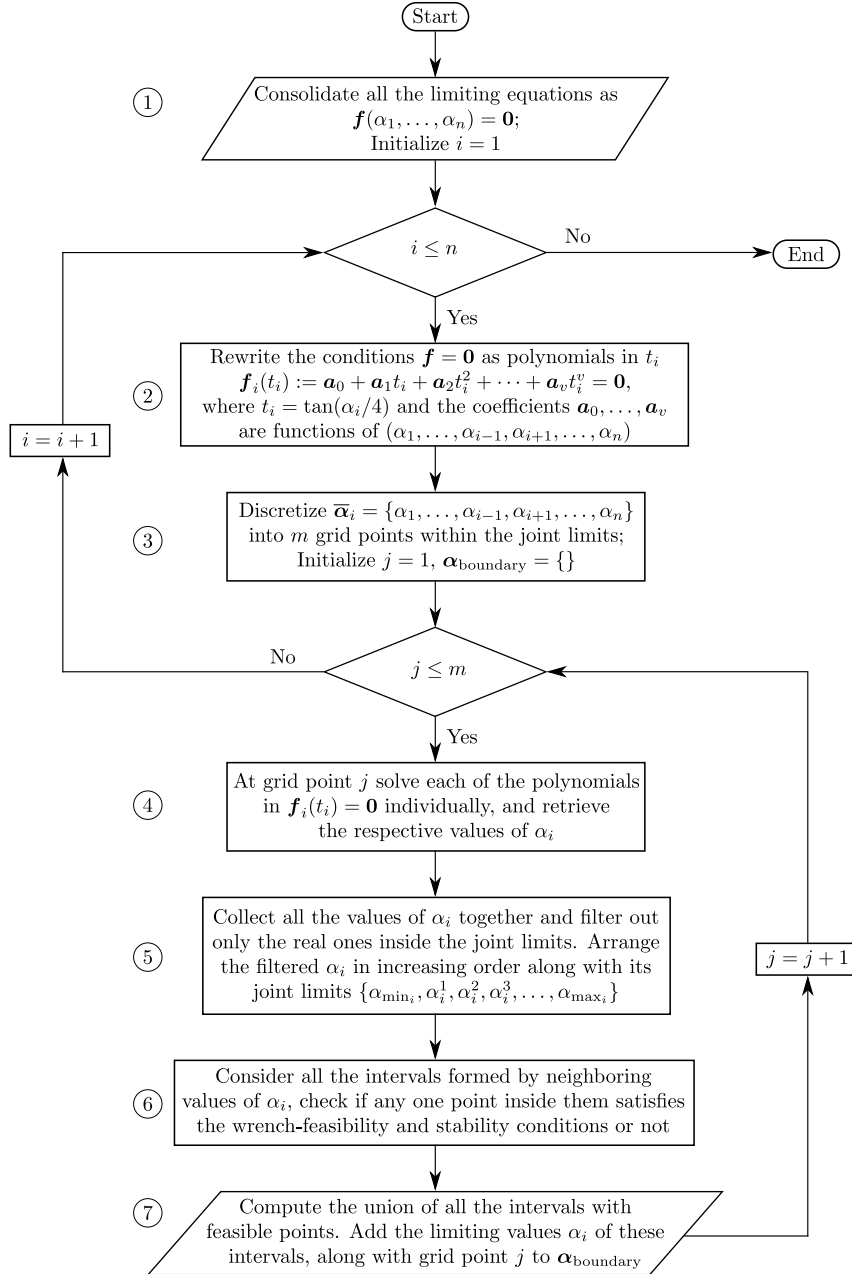


Figure 3.10 – Algorithm to compute the boundary points of SWFJ for the n -X manipulator.

$G_i = \underline{\Gamma}_i$ and $G_i = \overline{\Gamma}_i$, resulting in a total of $2n$ conditions. However, it should be noted that if the routing is such that one cable actuates more than one joint, additional conditions for wrench-feasibility will arise.

The articular stiffness matrix of n -X manipulator actuated by $2n$ -cable scheme will be an $(n \times n)$ real symmetric matrix, with actuation forces (F_{l_i}, F_{r_i}) appearing in the i^{th} diagonal term. Thus, it is possible to solve for one of the forces from the i^{th} equilibrium equation and obtain the stiffness matrix with one redundant force per diagonal term. Two possibilities exist for this redundant force in each term, resulting in a total of 2^n possible stiffness matrices. All of them must be derived, and the redundant forces must be set to F_{\max} to obtain the stiffness matrices corresponding to maximum stiffness. The limiting conditions of stability are obtained from the vanishing of the determinant of each of these matrices, thereby resulting in 2^n conditions. Hence, the $2n$ -cable scheme has a total of $(2n + 2^n)$ limiting conditions for constructing the SWFJ.

On the other hand, for the $(n + 1)$ -cable scheme, the $2n$ limiting conditions for wrench-feasibility mentioned above are applicable. Additionally, due to the coupling induced by the common cable, there are $n(n - 1)$ more equations, resulting in a total of $n(n + 1)$ equations for wrench-feasibility. Unlike in the $2n$ -cable scheme, there is only one redundant force in the $(n + 1)$ -cable scheme, which produces $(n + 1)$ possible stiffness matrices and the same number of limiting conditions. Thus, there are a total of $(n + 1)^2$ conditions to determine the boundary of SWFJ.

A generic algorithm for determining the SWFJ boundary points for the n -X manipulator is presented in Fig. 3.10. It involves the derivation of n polynomials out of each condition, resulting in a total of $n(2n + 2^n)$ conditions for the $2n$ -cable scheme and $n(n + 1)^2$ conditions for the $(n + 1)$ -cable scheme. When $n = \{2, 3, 4, 5, 6\}$, this amounts to $\{16, 42, 96, 210, 456\}$ polynomials for $2n$ -cable scheme and $\{18, 48, 100, 180, 294\}$ polynomials for $(n + 1)$ -cable scheme, respectively. Since the number of polynomials to be derived is very large for $n \geq 4$, the proposed method is more suitable for low ($n \leq 3$)-DoF manipulators.

Up to the computation of SWFJ boundary points, the algorithm is universally applicable to all types of manipulators, planar/spatial, kinematically non-redundant/redundant. However, the next step which involves computing the SWFW boundary points, poses difficulties for kinematically redundant manipulators. This is because the boundary in the joint space has a higher dimension than the boundary in the task space. Thus, while mapping all the SWFJ boundary points onto the task space, they will fill up workspace volumes rather than just remaining on the boundary. Thus, the shape of the SWFW cannot be well-identified for these manipulators. However, it must be noted that this challenge is inherent in the kinematically redundant systems and was not introduced by the proposed algorithm.

For kinematically non-redundant manipulators, the boundary points of SWFJ can be mapped onto the task space along with the singularities to obtain a cloud of points on the boundary of SWFW without any difficulties. However, finding a suitable interpolation between the points becomes more challenging in higher (≥ 3) dimensional spaces.

Chapter 7 uses this algorithm to compute the singularities of a 3-X spatial manipulator and, eventually, its workspace in the presence of joint limits. It uses small planes to interpolate between the points in the joint space and maps them onto the workspace to obtain an approximation of the workspace boundary. However, it does not consider the wrench-feasibility and stability conditions, which can also be accounted for using this method.

3.9 Conclusions

A planar tensegrity-inspired manipulator composed of two anti-parallelogram (*X*) joints arranged in series with offsets was introduced in this chapter. The manipulators are placed vertically against gravity, and each joint is equipped with springs for stability when no actuation forces are applied. Two actuation schemes with four cables and three cables, respectively, were proposed to actuate this manipulator. The 4-cable scheme actuates each joint with two cables independently of the other. In contrast, the 3-cable scheme uses one cable for each joint on the right side and a single shared cable for both joints on the left side.

The kinematic model of the 2-*X* manipulator, which applies to both actuation schemes, was presented. The static model of the manipulator for each of the actuation schemes was discussed. The limiting conditions of wrench-feasibility and stability were derived for the two actuation schemes, which were used to compute the bounding points of the stable wrench-feasible joint space (SWFJ). An algorithm was proposed to explore the joint space in terms of grid lines parallel to each axis. All the limiting conditions were converted to equivalent polynomials, which were resolved at these grid lines to find the bounding points of the SWFJ accurately. This accuracy comes at the cost of tedious symbolic precomputations of the equivalent polynomials and their numerical resolution.

Another algorithm was presented to find a cyclic ordering of these boundary points and interpolate between them with linear segments. This process resulted in a polygonal approximation of the SWFJ and the stable wrench-feasible workspace (SWFW). An existing `c++` library was used to inscribe maximal disk(s) inside the SWFW and evaluate its size. It was found through a numerical example of the 2-*X* manipulator that the 4-cable scheme produces a more symmetric and larger SWFJ, as well as SWFW, than the 3-cable scheme. It took only about 43 ms to compute the SWFW and the inscribed disk for the two schemes, making it suitable for exploring several designs in an optimization framework.

The proposed method for computing the SWFJ and SWFW was generalized to an n -*X* manipulator for actuation with $2n$ and $(n + 1)$ cables. It was observed that the number of polynomials to be derived increases drastically beyond $n = 3$. Hence, this method is suitable mainly for low ($n \leq 3$) DoF manipulators despite being applicable to other cases.

2-X MANIPULATOR: VELOCITY, FORCE, AND STIFFNESS PERFORMANCES

Abstract

This chapter studies the instantaneous velocity, force, and stiffness performances of the planar 2-X tensegrity-inspired manipulator remotely actuated by cables. We consider two actuation schemes with four cables and three cables, respectively. We impose realistic bounds on the cable velocities and actuation forces and study the effects on the end-effector velocities, force application capabilities, and stiffness performances. We show that the 4-cable scheme has better and more symmetric force and stiffness performances throughout the workspace when compared to its counterpart. In contrast, the 3-cable scheme achieves larger velocities in certain directions at some parts of the workspace. We present several numerical examples and the evolution of relevant indices inside the workspace to acquire a global understanding of the instantaneous performances.

Contents

4.1	Introduction	100
4.2	Velocity performance	101
3.5.1	4-cable scheme	103
4.3	Force performance	103
4.4	Stiffness performance	105
4.4.1	Cartesian stiffness matrix	105
4.4.2	Stiffness ellipse	105
4.4.3	Stiffness along x and y directions	107
4.5	Global performance in the workspace	107
4.5.1	Performance at chosen points in the workspace	109
4.5.2	Performance indices and their contours in the workspace	110
4.6	Conclusions	115

4.1 Introduction

In the previous chapter, we studied the workspace¹ (global performance measure) of the 2-X manipulator actuated by the 4-cable scheme and 3-cable scheme (see Fig. 4.1). Note that the workspace boundary due to joint limits, stability, and wrench-feasibility conditions (see Fig. 3.9) have been combined together as (α_{SWFW}) and denoted by the cyan curve, for the sake of simplicity. As a follow-up, in this chapter, we aim to study the local performances, namely, velocity, force application capabilities, and variable stiffness properties for the two actuation schemes, and compare them. One of the objectives of this study is to see the impact of reducing the number of actuators and, therefore, the cost of the associated robot. It might seem that reducing the number of actuators will reduce the performance of the robot, but we will show that it is not so direct.

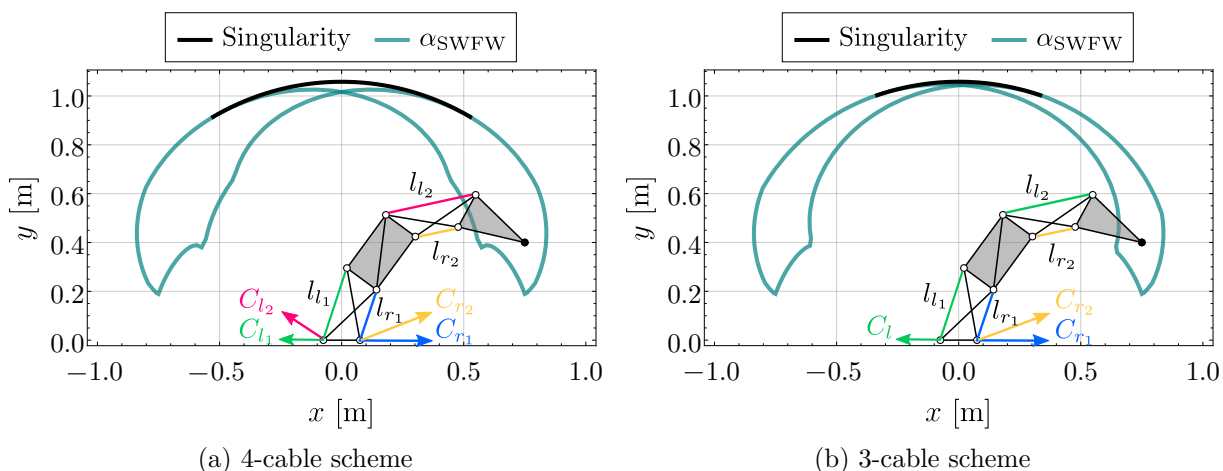


Figure 4.1 – 2-X manipulator: workspace for actuation with four cables (left) and three cables (right) corresponding to the data presented in Table 3.1. In both cases, the manipulator is plotted in the configuration $(\alpha_1, \alpha_2) = (-0.63, -1.44)$ rad.

Yoshikawa carried out one of the earliest works on the velocity capabilities of robot manipulators [Yos85]. He proposed to study the end-effector velocities by fixing the 2-norm of the joint velocities. He showed that this results in an ellipsoid in the task velocity space, representing relative ease of movement of the end-effector in different directions. Performance measures have been proposed based on the ellipsoid’s volume (manipulability) and eccentricity (condition number of the Jacobian matrix mapping the velocities in the two spaces). Despite its wide popularity and acceptance, this representation has shortcomings, as pointed out in [Lee97]. Principally, fixing the 2-norm of joint velocities does not represent the actual constraints on the actuators. Instead, the use of ∞ -norm is suggested. This results in polytopes in the joint and task velocity spaces [Lee97]. It has been shown that using ∞ -norm and polytopes can also handle actuation redundancies [KCP04], which is not possible in the other representation. Since cable-driven systems usually have more actuators than their DoF, they are redundantly actuated and can be best analyzed with polytopes. The twist capabilities of cable-driven parallel robots are studied

1. In this chapter, the term “workspace” refers to the stable wrench-feasible workspace (SWFW) of the manipulator.

with polytopes in [Les+18]. This work will also adopt the polytope representation to quantify the velocity performance of the 2-X manipulator actuated by the 4-cable and 3-cable schemes, shown in Fig. 4.1.

The actuation redundancy has caused the wrench capability analysis of cable-driven parallel robots to be conducted in terms of polytopes [BREU06],[BGM09]. This work will also use polytopes to study the force capabilities of the 2-X manipulator, albeit with the inclusion of the effects of gravity and springs.

In addition to velocity and force performances, it is also interesting to study the stiffness properties for tensegrity-inspired manipulators [Ars11]. Assuming that the tensions in the cables are imposed, the manipulator deforms when subjected to an external force. Thus, it would be interesting to study the force-deflection characteristics of the manipulator at different configurations. In addition to configuration, stiffness also varies with the redundant actuation forces imposed at a given configuration, making them suitable candidates for applications requiring variable stiffness properties, e.g., surgical assistance. Unlike velocity and force, the analysis of stiffness performance can be carried out in terms of ellipsoids since it represents the map between the end-effector deflections and the forces applied at that location, independent of the actuation redundancies in the system. It is interesting to note that apart from roboticists, the researchers from biomechanics also study the stiffness ellipse of manipulators actuated by elastic cables (approximating muscles) to simulate the range of stiffness achieved by a human arm for different synergies [IVC16]. Several other references can also be found on this interesting topic, e.g., [FMI90],[Bor+23]. This work presents the stiffness ellipse of the 2-X manipulator for the two actuation schemes at one configuration. Later, it switches to a different measure of stiffness owing to the computational complexities involved.

The rest of this chapter is organized as follows. The velocity performance of the 2-X manipulator actuated by the 4-cable and 3-cable schemes are presented in Section 4.2. The force performance of the manipulator is studied in Section 4.3, and the stiffness performance in section 4.4. This is followed by an extension of the local study to the entire workspace in Section 4.5. Finally, the conclusions of this work are presented in Section 4.6.

4.2 Velocity performance

In a cable-driven system, the peak speed of the cables is limited by the velocity limits of the actuators driving them. Let us assume that identical motors actuate all the cables. We use the motor and drum characteristics data specified in [Fas+21], which limits the maximum cable speed to $\dot{l}_{\max} = 0.42$ m/s. From Fig. 3.3, it is apparent that the velocities of the cables C_{l_i}, C_{r_i} , when they are wound, are equal to the negative time-derivatives of l_i, l_{r_i} , respectively. Recalling the notations $\left(Z_{l_i} = -\frac{dl_i}{d\alpha_i}, Z_{r_i} = -\frac{dl_{r_i}}{d\alpha_i} \right)$ from Eq. (3.9), the constraints on the cable velocities can be mapped to the joint velocities $(\dot{\alpha}_1, \dot{\alpha}_2)$ as follows:

$$\dot{C}_{l_i} \in [-\dot{l}_{\max}, \dot{l}_{\max}] \implies -\dot{l}_i \in [-\dot{l}_{\max}, \dot{l}_{\max}] \implies -\frac{\dot{l}_{\max}}{Z_{l_i}} \leq \dot{\alpha}_i \leq \frac{\dot{l}_{\max}}{Z_{l_i}} \quad (4.1)$$

$$\dot{C}_{r_i} \in [-\dot{l}_{\max}, \dot{l}_{\max}] \implies -\dot{l}_{r_i} \in [-\dot{l}_{\max}, \dot{l}_{\max}] \implies -\frac{\dot{l}_{\max}}{-Z_{r_i}} \leq \dot{\alpha}_i \leq \frac{\dot{l}_{\max}}{-Z_{r_i}} \quad (4.2)$$

for $i = 1, 2$. Unlike the other cables, the velocity of cable C_l (see Fig. 4.1b) is given by $-(\dot{l}_1 + \dot{l}_2)$, and the associated constraints involve both joint rates as follows:

$$\dot{C}_l \in [-\dot{l}_{\max}, \dot{l}_{\max}] \implies -\dot{l}_{\max} \leq (Z_{l_1}\dot{\alpha}_1 + Z_{l_2}\dot{\alpha}_2) \leq \dot{l}_{\max} \quad (4.3)$$

For the 4-cable actuation scheme, the constraints in Eqs. (4.1) and (4.2) apply simultaneously, resulting in a total of eight constraints. On the other hand, for the 3-cable scheme, only six constraints are defined by Eqs. (4.2) and (4.3).

As a numerical illustration, consider the data for the 2-X manipulator presented in Table 3.1. The joint velocity constraints are shown in Fig. 4.2a (resp. Fig. 4.2b) for the 4-cable (resp. 3-cable) scheme, when the manipulator is at the configuration $(\alpha_1, \alpha_2) = (-0.63, -1.44)$ rad (see Fig. 4.1). The region respecting the constraints imposed by the left cables (Eqs. (4.1), (4.3)) is shown in orange shade, while the one respecting the constraints imposed by the right cables (Eq. (4.2)) is shown in blue shade. The polytope that lies at the intersection of these two regions represents the set of feasible joint velocities and is referred to as the joint velocity polytope. This polytope is highlighted by a red continuous line for the 4-cable scheme and a black dashed line for the 3-cable scheme. This style is followed for the two schemes throughout this chapter.

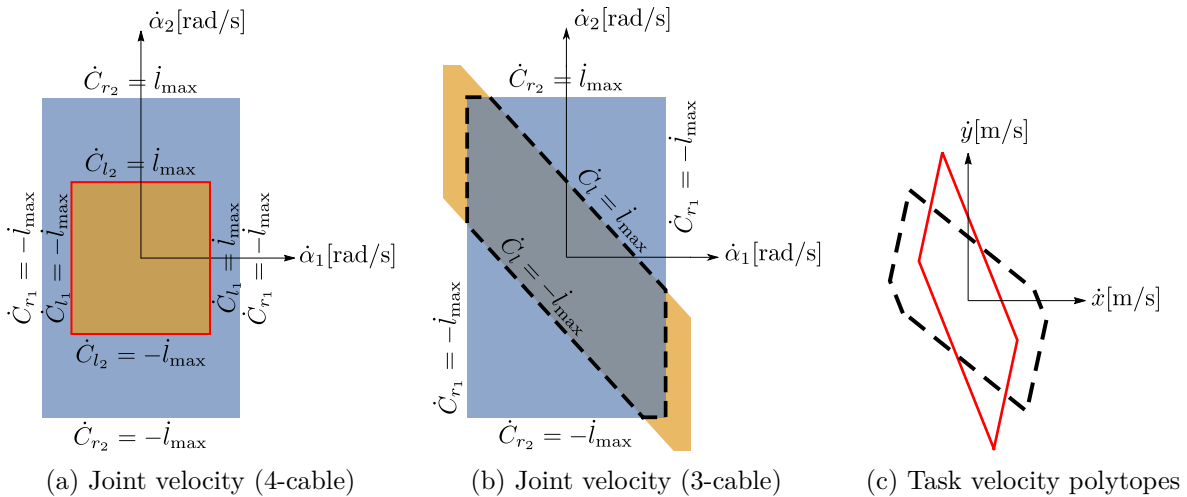


Figure 4.2 – Joint velocity polytope and task velocity polytope for the 4-cable (red continuous) and 3-cable (black dashed) schemes at $(\alpha_1, \alpha_2) = (-0.63, -1.44)$ rad.

The respective polytopes in the task velocity space (\dot{x}, \dot{y}) can be obtained by mapping the vertices of the joint velocity polytope using the Jacobian matrix in Eq. (3.3). The task velocity polytopes for the two actuation schemes are superimposed in Fig. 4.2c. Interestingly, the polytope of the 3-cable scheme extends beyond the one obtained with the 4-cable scheme, and its direction of maximum velocity is different from that of its counterpart.

The larger velocities obtained with the 3-cable scheme in certain directions can be attributed to the smaller number of constraints and the coupling in cable routing. Physically, in the 4-cable scheme, the velocities of cables C_{l_i}, C_{r_i} can only determine the velocity of joint i . But, in the 3-cable scheme, all three cables can influence the velocities of both the joints due to the coupling in cable routing. For instance, the cable C_{r_1} can induce a velocity in the second joint while the left cable C_l is blocked, which is impossible in the 4-cable scheme. This study shows that the

nature of cable routing, despite the number of cables, plays an important role in the velocity performance of the manipulator.

4.2.1 Kinematic sensitivity

The kinematic sensitivity of a manipulator at a given configuration measures the end-effector displacements due to small variations in the actuator positions [CBG10]. For a cable-driven manipulator such as the 2-X manipulator, these variations must be assumed on the cable lengths, e.g., $\delta l \in [-\delta l_{\max}, \delta l_{\max}]$. The map of these variations onto the task space should follow the same process illustrated above for velocity analysis. Thus, the shape of the resulting polytopes, representing equivalent end-effector displacements, will be identical to the velocity polytopes, with a difference in the units of measure. Hence, the analysis of kinematic sensitivity is also conducted implicitly through the velocity analysis.

In the following section, the force performance of the 2-X manipulator is studied for the two actuation schemes.

4.3 Force performance

This section aims at quantifying the force that the manipulator (end-effector) can apply on its environment at a given configuration while remaining in static equilibrium. The force capabilities are bounded due to the limits $[F_{\min}, F_{\max}]$ assumed on the cable forces.

Considering $\mathbf{f} = [f_x, f_y]^\top$ to be the force applied by the end-effector, the equilibrium equation of the manipulator presented in Eq. (3.6) changes as follows:

$$\mathbf{J}_x^\top \mathbf{f} + \mathbf{G} = \mathbf{\Gamma} \quad (4.4)$$

where \mathbf{J}_x is the Jacobian matrix defined in Eq. (3.3), $\mathbf{G} = [G_1, G_2]^\top$ denotes the wrench due to the springs and gravity, and $\mathbf{\Gamma} = [\Gamma_1, \Gamma_2]^\top$ is the wrench applied by the cables, which depends on the actuation scheme (see Eq. (3.7)).

For the 4-cable scheme, $\Gamma_i = Z_{l_i} F_{l_i} + Z_{r_i} F_{r_i}$, $i = 1, 2$ (see Eq. (3.7)). Thus, Eq. (4.4) can be written component-wise as follows:

$$\begin{bmatrix} J_{11} & J_{21} \\ J_{12} & J_{22} \end{bmatrix} \begin{bmatrix} f_x \\ f_y \end{bmatrix} + \begin{bmatrix} G_1 \\ G_2 \end{bmatrix} = \begin{bmatrix} Z_{l_1} F_{l_1} + Z_{r_1} F_{r_1} \\ Z_{l_2} F_{l_2} + Z_{r_2} F_{r_2} \end{bmatrix} \quad (4.5)$$

The limits on actuation forces shall be imposed as: $F_{l_i}, F_{r_i} \in [F_{\min}, F_{\max}]$ with numerical values $F_{\min} = 0$ N, $F_{\max} = 176$ N (see Table 3.1). From Section 3.5.1, recalling that $Z_{l_i} > 0$ and $Z_{r_i} < 0$, the lower (resp. upper) bound of the actuation wrench Γ_i occurs when $F_{l_i} = F_{\min}, F_{r_i} = F_{\max}$ (resp. $F_{l_i} = F_{\max}, F_{r_i} = F_{\min}$). Thus, from Eq. (4.5), the following inequalities must hold:

$$Z_{l_i} F_{\min} + Z_{r_i} F_{\max} - G_i \leq (J_{1i} f_x + J_{2i} f_y) \leq Z_{l_i} F_{\max} + Z_{r_i} F_{\min} - G_i \quad (4.6)$$

for $i = 1, 2$. The region in the task force space (f_x, f_y) that satisfies these four conditions represents the force polytope for the 4-cable scheme. It is shown by the red continuous boundary, at configuration $(\alpha_1, \alpha_2) = (-0.63, -1.44)$ rad in Fig. 4.3.

In the 3-cable scheme, the side-routed cable C_l applies the same force F_l on the left side of both the joints (see Fig. 4.1b, right), while the cable C_{r_i} applies a force F_{r_i} only on the i^{th}

joint. Thus, the actuation wrench components are given by $\Gamma_i = Z_{l_i}F_l + Z_{r_i}F_{r_i}$ (see Eq. (3.14)). The associated equilibrium equations resemble the one in Eq. (4.5), with F_{l_1}, F_{l_2} replaced by F_l . Thus, proceeding similarly, one obtains the same conditions in Eq. (4.6) for the 3-cable scheme as well. Additionally, one must also impose the constraints due to the coupling of the side-routed cable C_l . These are obtained by firstly eliminating F_l from the two equilibrium equations:

$$J'_{11}f_x + J'_{21}f_y + G' = Z'_{l_1}F_{r_2} + Z_{r_1}F_{r_1} \quad (4.7)$$

where $J'_{i1} = \left(J_{i1} - \frac{Z_{l_1}}{Z_{l_2}}J_{i2}\right)$, $i = 1, 2$, $G' = \left(G_1 - \frac{Z_{l_1}}{Z_{l_2}}G_2\right)$, $Z'_{l_1} = -\left(\frac{Z_{l_1}}{Z_{l_2}}Z_{r_2}\right)$. It can be shown that $Z'_{l_1} > 0$ in the above equation. Thus, the wrench bounds can be obtained as above, and the final conditions on (f_x, f_y) are:

$$Z'_{l_1}F_{\min} + Z_{r_1}F_{\max} - G' \leq J'_{11}f_x + J'_{21}f_y \leq Z'_{l_1}F_{\max} + Z_{r_1}F_{\min} - G' \quad (4.8)$$

The force polytope for the 3-cable scheme lies at the intersection of all the six conditions in Eqs. (4.6) and (4.8), as illustrated by the dashed boundary in Fig. 4.3.

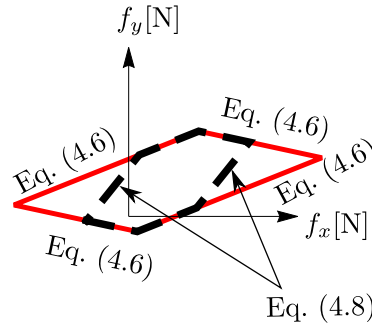


Figure 4.3 – Force polytopes and associated constraints of the 4-cable (red continuous) and 3-cable (black dashed) schemes at $(\alpha_1, \alpha_2) = (-0.63, -1.44)$ rad.

Evidently, the force polytope of the 3-cable scheme lies inside that of the 4-cable scheme, as it satisfies two additional conditions in Eq. (4.8). Thus, the 4-cable actuation scheme permits the end-effector to apply more forces than the 3-cable scheme. From Fig. 4.3, it is observed that the force polytopes are off-centered w.r.t. the origin. This shift is due to the terms (G_1, G_2) , which accounts for the springs and gravity.

Note that the above analysis does not consider the stability of the manipulator while computing the forces at the end-effector. Hence, it is possible that the manipulator becomes unstable and falls off while applying a force greater than a critical value. We can handle this issue in two different ways depending on the application of the manipulator. If the task (I) is a precise machining operation, we can use a closed-loop control law with position feedback for stabilizing the manipulator while applying the desired forces on the part. On the other hand, if the task (II) is to collaborate with human operators while applying a desired force, then an open-loop control that only specifies the tension in the cables (without position feedback) is recommended. However, in the latter task, it is necessary to ensure that the manipulator is inherently stable (i.e., positive-definiteness of the stiffness matrix) with desired stiffness while applying the forces. This feature will induce additional constraints on the end-effector forces and make the computation

of their boundaries much more challenging. In this context, we will assume that the manipulator is used for task I, with a closed-loop control for stability.

The following section discusses the stiffness performance of the manipulator for the 4-cable and 3-cable actuation schemes.

4.4 Stiffness performance

This section studies the stiffness of the manipulator in the task space for 4-cable and 3-cable schemes. A notable difference from the previous section is that we consider the manipulator to be controlled in an open-loop scheme where only tensions are imposed in the cables without any position feedback so that it is compliant. We disregard the compliance in the bars, pivots, and cables, in this study. The derivation of the Cartesian stiffness matrix and analysis of stiffness in different directions are presented in the following sections.

4.4.1 Cartesian stiffness matrix

The Cartesian stiffness matrix (\mathbf{K}_c) can be obtained from the articular stiffness matrix by a transformation using the Jacobian matrix \mathbf{J}_x as follows (see [Sal80],[QG08],[FW19]):

$$\mathbf{K}_c = \mathbf{J}_x^{-\top} \mathbf{K}_\alpha \mathbf{J}_x^{-1} \quad (4.9)$$

The matrix \mathbf{K}_c represents the mapping between the deflection of the end-effector and the force applied on it. From the above expression, it is clear that this matrix is defined only at a non-singular configuration of the manipulator. Since we obtained the matrix \mathbf{K}_c through a congruence transformation of the articular stiffness matrix (\mathbf{K}_α), the signs of their eigenvalues remain the same. This property indicates that while \mathbf{K}_α is positive-definite, \mathbf{K}_c is also positive-definite and vice versa, both signifying the stability of the manipulator.

The articular stiffness matrix (\mathbf{K}_α) can be replaced by the matrix ${}^4\mathbf{K}_\alpha^{\text{ll}}$ for the 4-cable scheme and by ${}^3\mathbf{K}_\alpha^{\text{l}}$ for the 3-cable scheme (see Sections 3.5.1 and 3.5.2). At a given configuration, the two (resp. one) redundant forces can be altered within their admissible bounds to vary the stiffness of the manipulator. This variable stiffness property makes them interesting candidates for tasks requiring high stiffness (e.g., machining) and low stiffness (e.g., collaboration). Since this study assumes an open-loop control of cable tensions, only the stable wrench-feasible configurations of the manipulator are considered for the two schemes.

The following sections quantify the stiffness performance of the manipulator for the two actuation schemes.

4.4.2 Stiffness ellipse

The linear relationship between an applied force ($\delta \mathbf{f}$) and the end-effector displacement ($\delta \mathbf{x}$) can be written as:

$$\delta \mathbf{f} = \mathbf{K}_c \delta \mathbf{x} \quad (4.10)$$

It is a common practice to normalize the displacement to a unit disk $\|\delta \mathbf{x}\| = 1$, and study the force required to produce this displacement [CDM09],[ATB17]. From Eq. (4.10) This leads to

the following condition:

$$(\delta \mathbf{f})^\top \mathbf{K}_c^{-\top} \mathbf{K}_c^{-1} (\delta \mathbf{f}) = 1 \quad (4.11)$$

This equation represents an ellipse in the stiffness space ($\delta \mathbf{f} / \|\delta \mathbf{x}\|$) whose semi-major and semi-minor axes lengths are given by the maximum and minimum singular values of \mathbf{K}_c , respectively, directed along the respective eigenvectors. Since \mathbf{K}_c is symmetric and positive-definite in stable configurations, the singular values are the same as its eigenvalues.

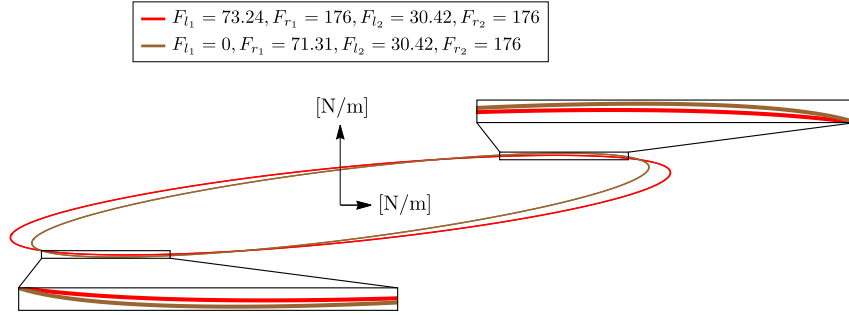


Figure 4.4 – Stiffness ellipse corresponding to different force combinations at $(\alpha_1, \alpha_2) = (-0.63, -1.44)$ rad for the 4-cable scheme.

For the 4-cable and 3-cable schemes, several force combinations are feasible at a given configuration, and each of them has a corresponding stiffness matrix and stiffness ellipse. For instance, at the configuration $(\alpha_1, \alpha_2) = (-0.63, -1.44)$ rad shown in Fig. 4.1, the feasible range of redundant forces for the two actuation schemes are computed to be:

$$\text{4-cable} \implies \begin{cases} F_{l_1} \in [0, 73.25] \text{ N} \\ F_{l_2} \in [0, 30.42] \text{ N} \end{cases} \quad (4.12)$$

$$\text{3-cable} \implies F_l \in [0, 30.42] \text{ N} \quad (4.13)$$

The presence of an additional cable on the left side allows the 4-cable scheme to have a larger force range at a given configuration. The stiffness ellipses corresponding to the maximum redundant forces (red) and a feasible combination of redundant forces (brown) for the 4-cable scheme are presented in Fig. 4.4. It is observed that the ellipse corresponding to maximum forces exhibits larger stiffness in most of the directions. However, a small portion exists on the top right and bottom left where the brown ellipse exceeds the boundary of its counterpart, implying a greater stiffness in those directions. It illustrates that the maximum actuation forces result in maximum stiffness only in certain directions, but stiffness obtained with lower forces can be greater in other directions.

Hence, to visualize the maximum stiffness of the manipulator in all directions, it is necessary to scan the redundant forces within their feasible ranges and plot all the stiffness ellipses together, as shown in Figs. 4.5a for the 4-cable scheme. The dense region that appears to be shaded in red represents the range of all stiffness values the manipulator can assume at the chosen configuration with the 4-cable scheme. Similarly, the stiffness ellipses for the 3-cable scheme can be obtained by scanning the only redundant force in its feasible range, as shown (in black) in Fig. 4.5b. The feasible stiffness regions of the two schemes are superimposed in Fig. 4.5c for comparison. It is

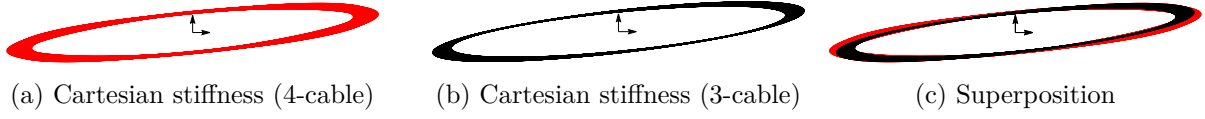


Figure 4.5 – Region of tunable stiffness for the 4-cable (red) and 3-cable (black) schemes at $(\alpha_1, \alpha_2) = (-0.63, -1.44)$ rad.

found that the stiffness range obtained with the 3-cable scheme is a subset of the one obtained with the 4-cable scheme, which corroborates with the smaller range of redundant forces for this scheme (see Eqs, (4.12),(4.13)).

The presentation of feasible regions in the stiffness space is helpful for appropriately positioning the parts for machining tasks (e.g., drilling) requiring a large stiffness. It also informs the designer of the minimum stiffness values that are relevant for collaborative tasks with human operators. Though the ellipses provide a complete picture of the stiffness performance of the manipulator in all directions, it is difficult to compute their outer and inner boundaries automatically. Hence, further study of stiffness will be carried out only along the principal directions (along x and y), as explained in the next section.

4.4.3 Stiffness along x and y directions

The diagonal terms of the Cartesian stiffness matrix (\mathbf{K}_c), denoted by K_x and K_y , can provide a reasonable estimation of the stiffness along x and y directions [FW19]. From Eq. (4.9), it can be shown that these terms attain their maximum and minimum values while the redundant forces are set to their maximum and minimum values, respectively. Thus, their bounds can be computed directly. For the 4-cable and 3-cable schemes, the stiffness ranges along x and y directions at the configuration $(\alpha_1, \alpha_2) = (-0.63, -1.44)$ rad (see Fig. 4.1) are found to be:

$$\text{4-cable} \implies \begin{cases} {}^4K_x \in [233.14, 269.62] \text{ N/m} \\ {}^4K_y \in [29.39, 33.17] \text{ N/m} \end{cases} \quad (4.14)$$

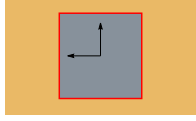
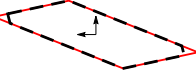
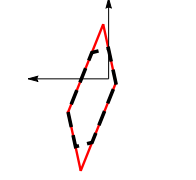
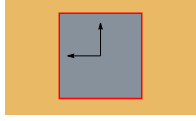
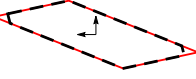
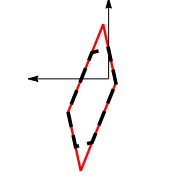
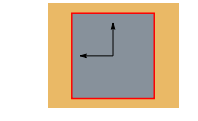
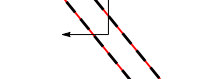
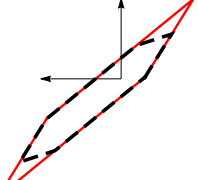
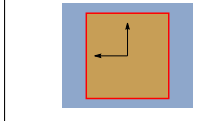

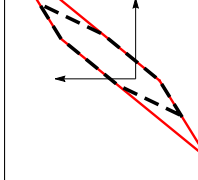
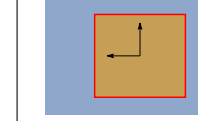
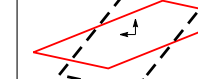
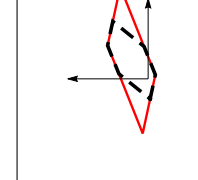
$$\text{3-cable} \implies \begin{cases} {}^3K_x \in [233.14, 259.06] \text{ N/m} \\ {}^3K_y \in [29.39, 32.68] \text{ N/m} \end{cases} \quad (4.15)$$

It is apparent that the 4-cable scheme allows for a larger and better tuning range of stiffness in both x and y directions when compared to the 3-cable scheme.

4.5 Global performance in the workspace

This section aims to study the velocity, force, and stiffness performance of the manipulator for the two actuation schemes at various points in their workspaces to acquire a global understanding of their distributions. The performances at discrete points in their common workspace are considered in Section 4.5.1. Several performance measures are defined, and their contours are visualized in Section 4.5.2.

Table 4.1 – Comparison of velocity, force, and stiffness performances of 4-cable and 3-cable actuation schemes at identical configurations configurations. The polytopes obtained for the 4-cable (resp. 3-cable) scheme are shown in red continuous (resp. black dashed) boundary.

Position [m]/ Configuration [rad]	Joint velocity polytopes $(\dot{\alpha}_1, \dot{\alpha}_2)$ [rad/s] (4-cable) 	Task velocity polytopes (\dot{x}, \dot{y}) [m/s] 	Task force polytopes (f_x, f_y) [N] 	Stiffness ranges in x and y directions K_x, K_y [N/m]
$P_1 =$ $(-0.75, 0.4);$ $(\alpha_1, \alpha_2) =$ $(0.63, 1.44)$				${}^4K_x \in [233.14, 269.62]$ ${}^4K_y \in [29.39, 33.17]$ ${}^3K_x \in [240.17, 269.62]$ ${}^3K_y \in [29.72, 33.17]$
$P_2 =$ $(-0.58, 0.8);$ $(\alpha_1, \alpha_2) =$ $(0.36, 0.83)$				${}^4K_x \in [422.73, 597.83]$ ${}^4K_y \in [384.43, 551.03]$ ${}^3K_x \in [453.83, 597.83]$ ${}^3K_y \in [388.68, 551.03]$
$P_3 =$ $(0.58, 0.8);$ $(\alpha_1, \alpha_2) =$ $(-0.36, -0.83)$				${}^4K_x \in [422.73, 597.83]$ ${}^4K_y \in [384.43, 551.03]$ ${}^3K_x \in [446.84, 574.30]$ ${}^3K_y \in [390.60, 542.01]$
$P_4 =$ $(0.75, 0.4);$ $(\alpha_1, \alpha_2) =$ $(-0.63, -1.44)$				${}^4K_x \in [233.14, 269.62]$ ${}^4K_y \in [29.39, 33.17]$ ${}^3K_x \in [233.14, 259.06]$ ${}^3K_y \in [29.39, 32.68]$

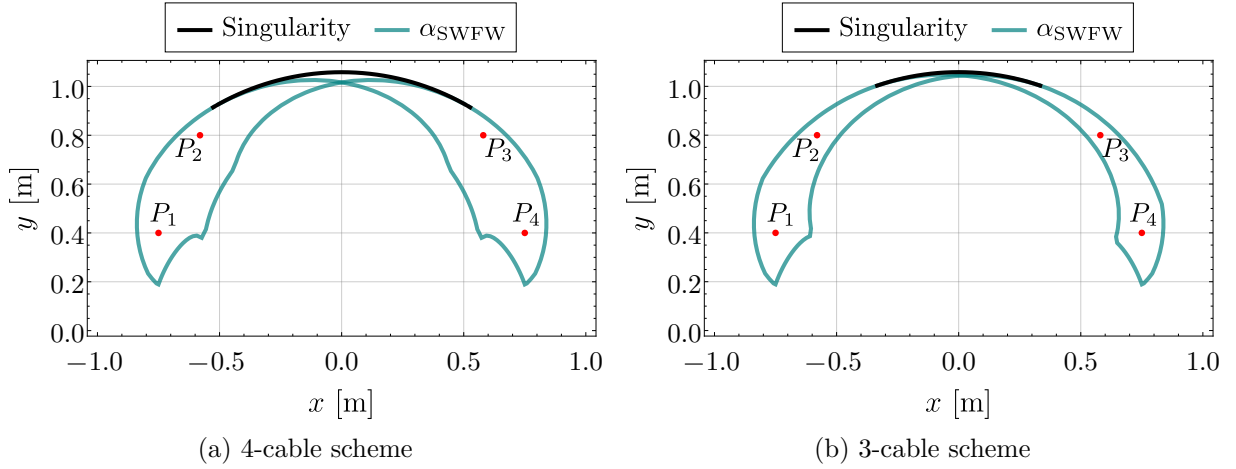


Figure 4.6 – Four common points chosen in the workspace of 4-cable and 3-cable schemes.

4.5.1 Performance at chosen points in the workspace

Four points (P_1, P_2, P_3, P_4) (see Fig. 4.6) that are common to the workspaces of 4-cable and 3-cable actuation schemes have been chosen to compare the velocity, force, and stiffness performances locally. The polytopes associated with velocities and forces and the stiffness ranges in x and y directions are shown in Table 4.1. The following observations can be made from these data:

- **Symmetry:** For the 4-cable scheme, it is observed that all the performances are symmetric at the points (P_1, P_4) and (P_2, P_3), where the task velocity and force polytopes are mirror images about their respective vertical axes and the stiffness ranges are identical. This result is justified since the manipulator and the actuation scheme are symmetric in the two parts of its workspace.
- **Velocity:** For the 4-cable scheme, the critical constraints in the joint velocity polytopes are formed by only the right (resp. left) cables at points P_1, P_2 (resp. P_3, P_4). In contrast, all three cables constrain the velocity polytopes in the 3-cable scheme. The polytopes of the two schemes are almost identical at points (P_1, P_2), with the 4-cable scheme having small additional parts at two ends. But, at points (P_3, P_4), the constraints imposed by the left cables become more significant, and thus, the polytopes have a significant difference in size as well as shape. There are some velocity states that can be achieved only in one of the schemes.
- **Force:** As expected, the force polytopes of the 3-cable scheme lie entirely inside the respective polytopes of the 4-cable scheme. However, the difference in their size and shape becomes more pronounced as one moves from P_1 to P_4 . Another interesting feature is that the direction of maximum force inside the force polytope is roughly orthogonal to the direction of maximum velocity inside the velocity polytope, which is similar to duality between the velocity and force ellipsoids [SR95].
- **Stiffness:** The value and range of stiffness are larger along both directions at points (P_2, P_3) when compared to those at (P_1, P_4). At all these points, we observe that the ranges of stiffness obtained with the 3-cable scheme remain inside those of the 4-cable scheme. Interestingly, the maximum (resp. minimum) stiffness value along both directions

matches for the two schemes at P_1, P_2 (resp. P_4). This occurrence can be explained based on the feasible range of forces at these configurations. At points P_1, P_2 (resp. P_4) the maximum feasible forces involve setting $F_{l_1} = F_{l_2} = F_{\max}$ (resp. F_{\min}) for the 4-cable scheme and $F_l = F_{\max}$ (resp. F_{\min}) for the 3-cable scheme. Clearly, these force settings are equivalent in the two actuation schemes despite the difference in the number of cables. Hence, they result in the same stiffness. However, the stiffness ranges offered by the 4-cable scheme is slightly greater ($\approx 1.01 - 1.5$ times) along both directions compared to its counterpart.

In summary, the 4-cable scheme offers a symmetric performance in the two parts of its workspace. It has better force and stiffness capabilities throughout the workspace when compared to those of the 3-cable scheme. It also has a better velocity performance in the left part of the workspace. But, the 3-cable scheme can achieve certain velocities on the right part that the 4-cable scheme cannot and vice-versa.

4.5.2 Performance indices and their contours in the workspace

In this section, the performance analysis presented at certain configurations will be extended to the entire workspace by adopting suitable measures from the literature. In order to quantify the size and shape of polytopes, two performance measures, namely, manipulability index (\mathcal{M}) and condition index, were proposed in [Lee97]. In this work, the inverse of the condition index (κ) will be used instead of the condition index, as it is a bounded measure. Geometrically, the manipulability index measures the surface area of the polytope, and the inverse condition index is the ratio of maximum performance (velocity/force) that can be achieved in *all* directions to the maximum performance inside the polytope.

These measures are applied to the velocity and forces polytopes, and their distributions are plotted in the workspace for the 4-cable and 3-cable schemes in the following. Subsequently, the maximum and tunable stiffness in the x and y directions are also presented as contours in their workspaces.

Velocity manipulability and inverse condition indices

The velocity manipulability (\mathcal{M}_v) and velocity inverse condition index (κ_v) are shown in Figs. 4.7 and 4.8, respectively, for the two actuation schemes. It is observed that these two measures have similar contours on the left part of the workspaces for the two schemes. In contrast, on the right part, especially at the bottom, there is a significant difference in the velocity performance between the two schemes. While the 4-cable scheme has a symmetric performance on the left and right parts of its workspace, the 3-cable scheme has a higher manipulability and inverse condition index on the right part. These results indicate that the 4-cable scheme will be suited for industrial tasks such as profile cutting, inspection, welding, etc., where a symmetric performance is beneficial. On the other hand, the 3-cable scheme will be suitable for building bio-inspired systems such as a bird's neck, which exhibits explosive velocities in regions farther from its body to catch its prey while remaining relatively slower in the other parts.

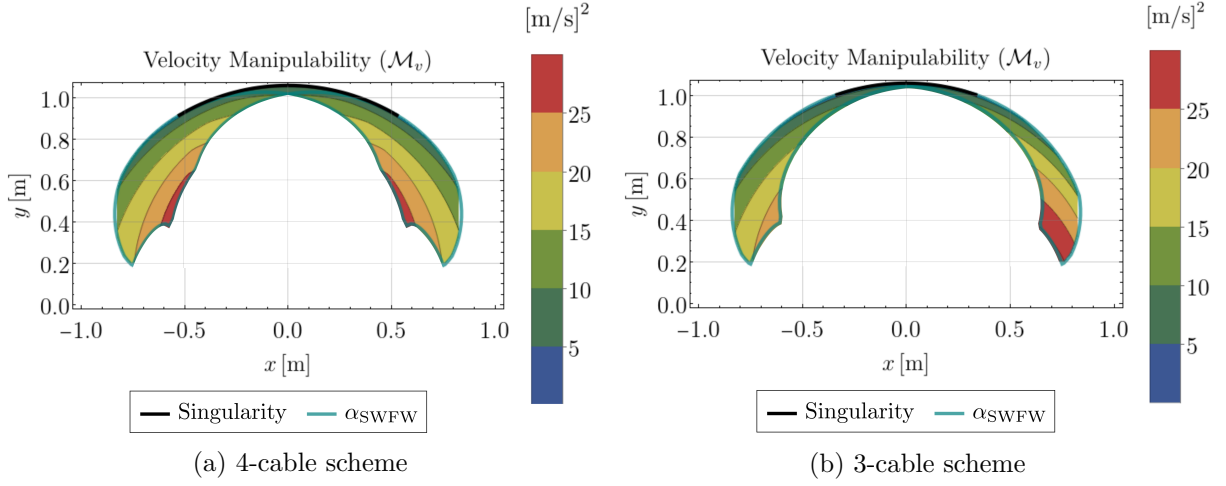


Figure 4.7 – Contours of velocity manipulability in the workspace of the two actuation schemes.

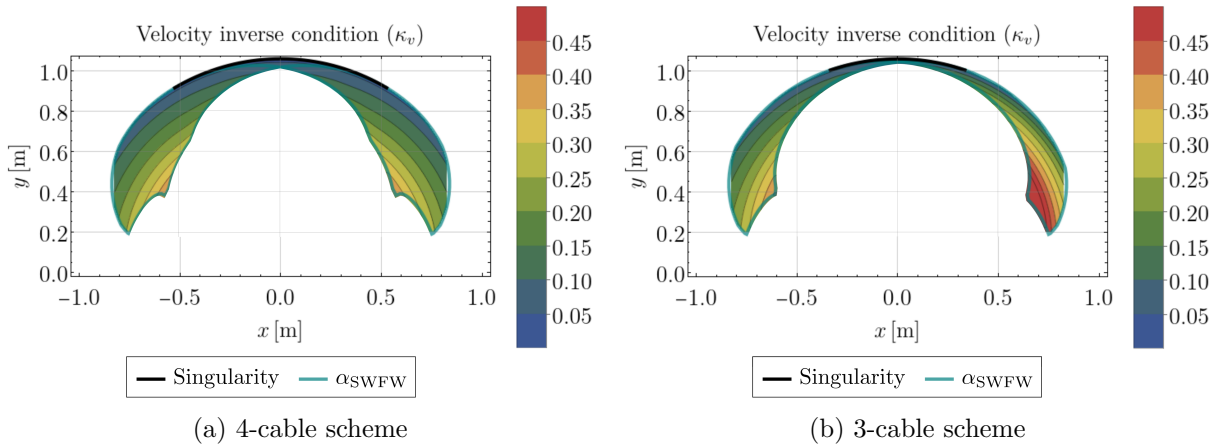


Figure 4.8 – Contours of velocity inverse condition index in the workspace of the two actuation schemes.

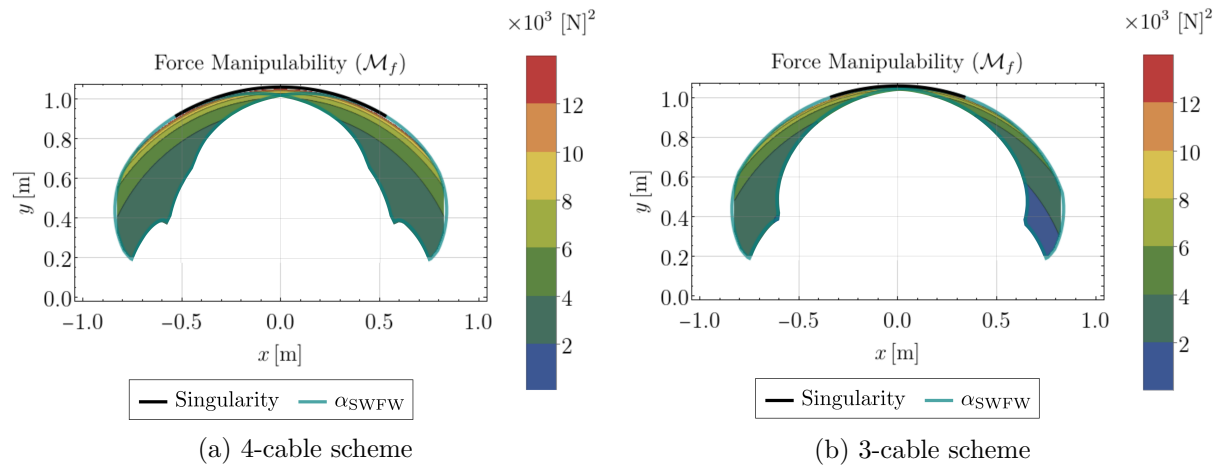


Figure 4.9 – Contours of force manipulability in the workspace of the two actuation schemes.

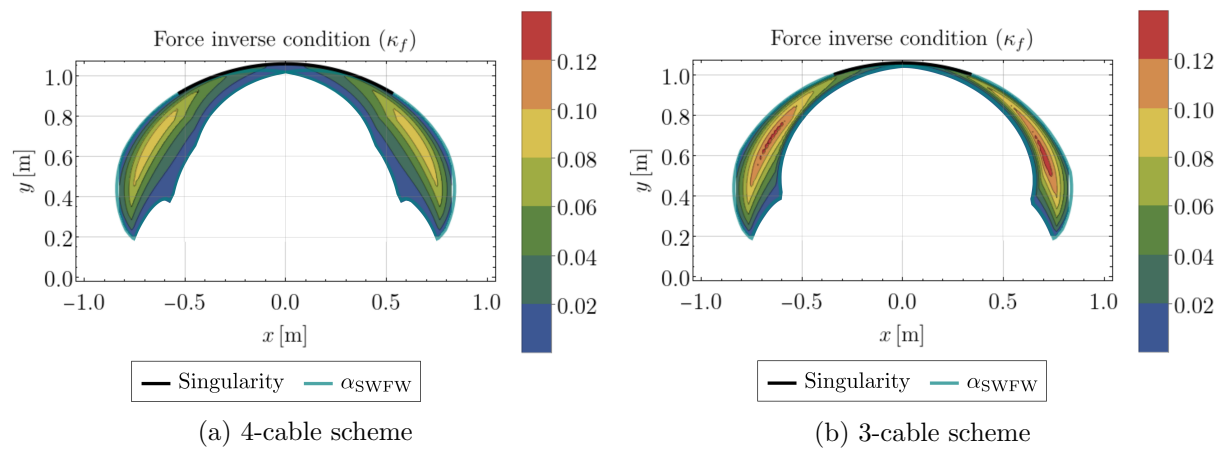


Figure 4.10 – Contours of force inverse condition index in the workspace of the two actuation schemes.

Force manipulability and inverse condition indices

The force manipulability (\mathcal{M}_f) and force inverse condition index (κ_f) are shown in Figs. 4.9 and 4.10, respectively, for the two actuation schemes. For the 4-cable scheme, the force performance is symmetric on the two halves of the workspace, similar to its velocity. The distributions of the force performance indices are similar on the left part of the workspaces for the two actuation schemes. But, on the bottom right, the 3-cable scheme has a lower force manipulability compared to its counterpart. This behavior contrasts with what was observed for velocity manipulability in Fig. 4.8b, which is reasonable.

The force inverse condition index is low, in general, for both the actuation schemes due to the off-centered position of the polytopes (see Fig. 4.3). There is only a small difference in its value between the two schemes.

Maximum stiffness and tunable range along x and y directions

The maximum stiffness along x and y directions, denoted by \overline{K}_x and \overline{K}_y , respectively, are presented in the workspaces of the two actuation schemes in Figs. 4.11 and 4.12. It is observed that the contours are similar for the two schemes throughout the workspace. When compared to \overline{K}_x , the value of \overline{K}_y increases drastically from the bottom of the workspace towards the top, close to the singularities. It is interesting to note that, unlike the velocity and force indices, the stiffness performance of the 3-cable scheme is comparable in the left and right parts of its workspace.

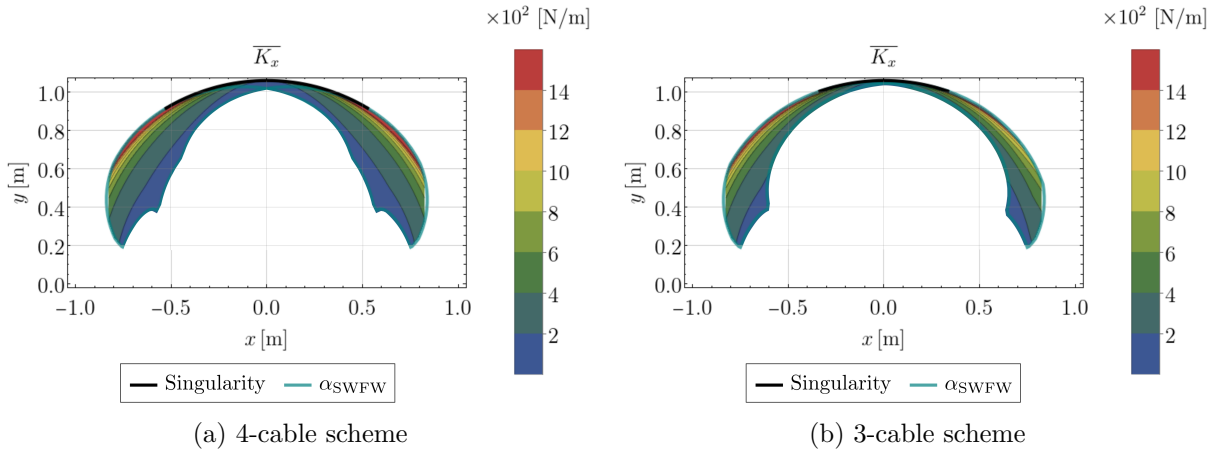


Figure 4.11 – Contours of maximum stiffness in x -direction in the workspace of the two actuation schemes.

The stiffness ranges achievable in x and y directions, denoted by ΔK_x and ΔK_y , respectively, are shown in Figs. 4.13 and 4.14. It is observed that the 4-cable scheme offers a slightly larger range of stiffness along both directions in several parts of the workspace. Similar to \overline{K}_y , the tuning range ΔK_y also increases drastically from the bottom of the workspace towards the top.

In summary, the velocity, force, and stiffness performances obtained with the two actuation schemes are comparable in the left part of their workspaces. However, on the right part, the

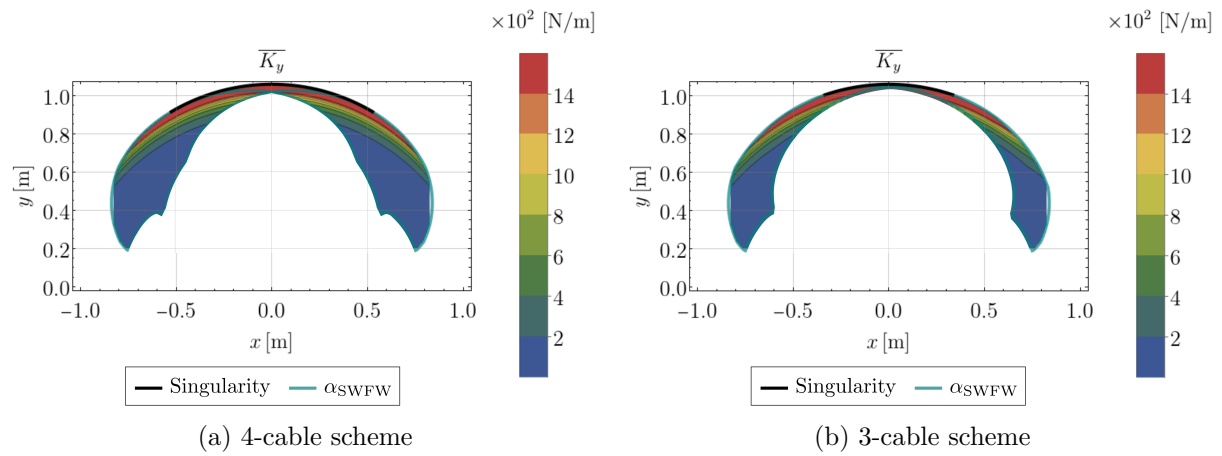


Figure 4.12 – Contours of maximum stiffness in y -direction in the workspace of the two actuation schemes.

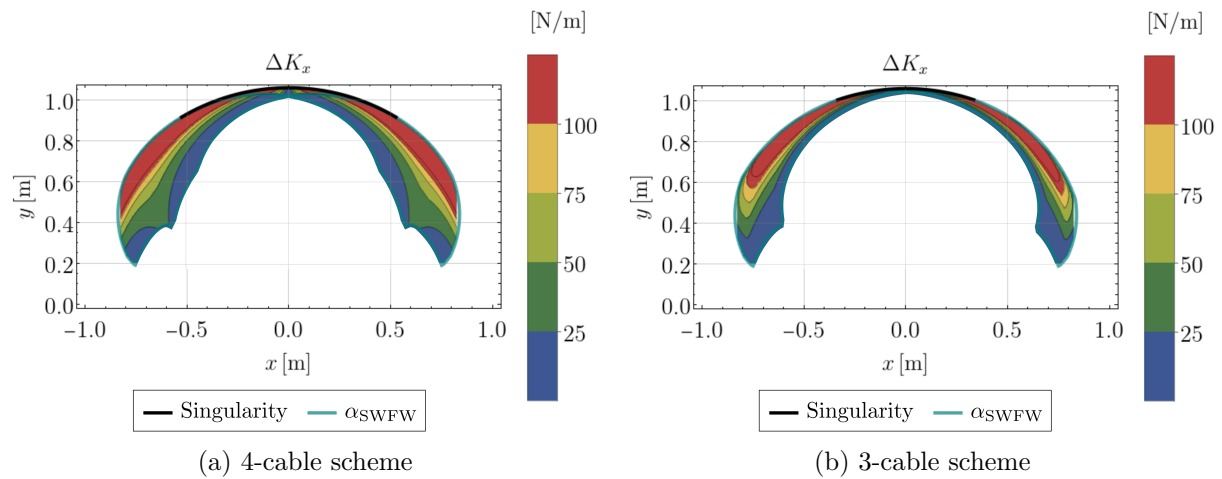


Figure 4.13 – Range of stiffness achievable in x -direction in the workspace of the two actuation schemes.

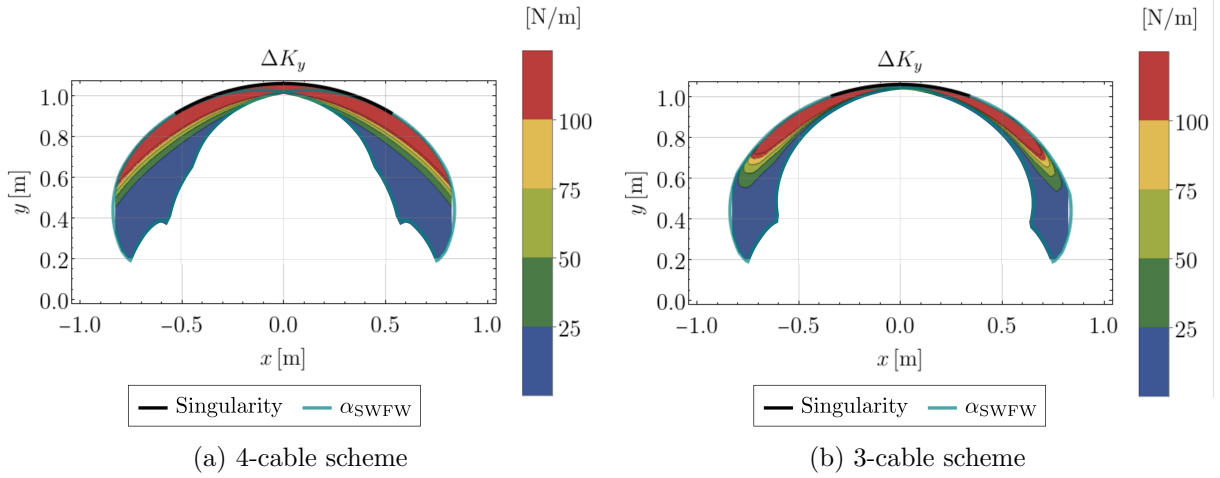


Figure 4.14 – Range of stiffness achievable in y -direction in the workspace of the two actuation schemes.

3-cable scheme has a better (resp. worse) velocity performance (resp. force performance). The evolution of maximum stiffness along the x and y directions are roughly the same for the two schemes, but the 4-cable scheme offers a better tuning range in several parts of its workspace.

4.6 Conclusions

The instantaneous velocity (equivalently kinematic sensitivity), static force, and stiffness properties were analyzed for the 2-X tensegrity-inspired manipulator for two cable actuation schemes. The first scheme involves four cables distributed as two per joint, while the second one involves only three, distributed as one per joint on the right side and one common cable for both joints on the left side. Practical limits were considered on the cable velocities and the actuation forces. The effect of these limits on the end-effector velocity, force application capabilities, and stiffness properties were studied for the two actuation schemes. The feasible end-effector velocities and forces could be represented as polytopes in the task velocity and task force spaces, respectively. On the other hand, the diagonal terms of the Cartesian stiffness matrix were used to characterize the stiffness along x and y directions.

While computing the velocity polytopes, the constraints on the cable velocities were mapped onto the joint space and then to the task space using the Jacobian matrix. It was shown that each cable imposes two constraints, leading to a total of eight constraints for the 4-cable scheme and six constraints for the 3-cable scheme. It was found that the polytopes obtained with the two schemes are similar on the left part of the workspace, while they differ considerably on the right part. The 3-cable scheme has a better velocity manipulability and inverse condition index on the right part of the workspace.

Unlike in velocity analysis, the number of constraints on the force polytopes is four for the 4-cable scheme and six for the 3-cable scheme. It was observed that the force polytope of the 3-cable scheme lies completely inside that of the 4-cable scheme at all configurations. Thus, the force manipulability is greater for the 4-cable scheme throughout the workspace. However, the

force inverse condition index has a small value (< 0.15) for both the actuation schemes due to the off-centered placement of the polytope owing to the effect of springs and gravity.

The stiffness analysis showed that redundant actuating cables allow for varying the equilibrium forces at a given configuration, thereby producing different stiffnesses at that configuration. For the 4-cable scheme, the presence of two redundant cables permits it to have a wider range of actuation forces and more stiffness variation when compared to its counterpart. However, contour plots of maximum stiffness and ranges of stiffness showed that the difference is not very significant between the two schemes, unlike in the velocity and force performances. Further, the stiffness performance is similar in both the left and right parts of the workspace for the 3-cable scheme, unlike in the case of velocities and forces.

In summary, the 3-cable scheme has a smaller stable wrench-feasible workspace and lesser force capabilities but larger velocity capabilities in some parts of the workspace. It can be suitable for developing bio-inspired systems such as a bird's neck where the velocity performance is better away from its body. On the other hand, the 4-cable scheme is best suited for all industrial tasks, such as welding, inspection, machining, etc., due to its symmetric workspace and performance capabilities.

DESIGN CONSIDERATIONS FOR 2-X AND 2-R MANIPULATORS

Abstract

This chapter considers two-degree-of-freedom planar tensegrity-inspired manipulators composed of anti-parallelogram (X) and revolute (R) joints containing springs and actuated remotely by four cables. The goal is to design the constituent elements of these manipulators while they carry a given payload in the presence of gravity. While this is a classical problem in serial and parallel manipulators with known approaches in the literature, their extension to tensegrity-inspired manipulators is challenging due to the presence of springs and actuation by cables. In this chapter, we address all these challenges in a sequence for the 2-X and 2-R manipulators. Firstly, we discuss the limits on joint movement due to the geometry and spring free length. Then, we find the set of all feasible springs that can be installed on these joints while respecting their mechanical constraints, e.g., maximum elongation. We estimate the axial loads in the bars to obtain cross-sections safe from buckling failure. Finally, we compute the stable wrench-feasible joint space (SWFJ) and stable wrench-feasible workspace (SWFW) for the two manipulators.

Contents

5.1	Introduction	118
5.2	Mechanical feasibility of springs	119
5.2.1	Assumptions in spring design	119
5.2.2	Governing conditions in spring design	120
5.3	Safety of a bar from buckling	122
5.4	Design considerations for the 2-X manipulator	122
5.4.1	Joint limits	123
5.4.2	Design space for the springs	125
5.4.3	Cross-sections and masses of the bars of 2-X manipulator	127
5.4.4	Consolidation of all design conditions and a numerical example for 2-X manipulator	131
5.5	Design considerations for the 2-R manipulator	134
5.5.1	Joint limits	135
5.5.2	Design space for the springs	136
5.5.3	Cross-sections and masses of the bars of 2-R manipulator	137
5.5.4	Static model of 2-R manipulator	140
5.5.5	Kinematic model of 2-R manipulator	141
5.5.6	Stable wrench-feasible workspace of 2-R manipulator with a numerical example	141

5.1 Introduction

This chapter addresses the design considerations of two planar tensegrity-inspired manipulators shown in Fig. 5.1. The first manipulator is the 2-X manipulator, which has been studied in the previous chapters. The second one is a 2-R manipulator that contains revolute joints with congruent triangles (see Section 2.5.1) in place of the X-joints. Two manipulators have been considered in this chapter to illustrate the generic nature of this study, which one can also extend to other planar tensegrity-inspired manipulators. The 4-cable scheme discussed in the previous chapters (see Fig. 3.3a) will be adopted for both manipulators due to the symmetric performance it offers.

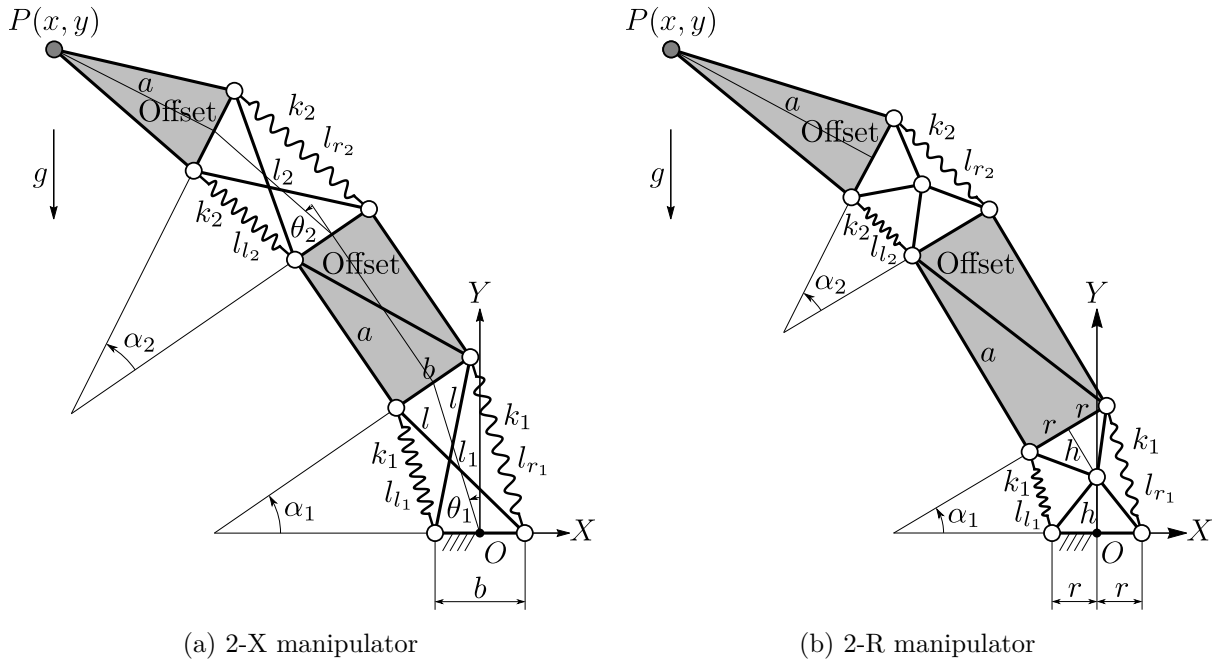


Figure 5.1 – Schematics of the manipulators under study: 2-X (left) and 2-R (right).

The objective of this work is to present the various factors to consider while designing tensegrity-inspired manipulators for carrying a payload, similar to those of serial and parallel manipulators [GG10],[YYL22], and eventually perform their design optimization. The design of tensegrity-inspired manipulators must also consider the springs, whose mechanical feasibility conditions are more challenging to incorporate inside the overall design of the manipulator. Secondly, the cross-sections of the bars must also be chosen appropriately based on the payload weight, forces due to springs, and cable routing to prevent buckling failure. Further, there could be limits on the joint movement due to the free length of the springs.

This chapter addresses the above design challenges for two planar tensegrity-inspired manipulators shown in Fig. 5.1. The significant contributions can be noted as follows:

- All the conditions of mechanical feasibility for the springs (with non-zero free lengths) are considered to derive the total feasible design space for them. A two-parameter representation of this space is presented to access all the springs.
- The limits of movement for each of the joints in the manipulator are studied systematically by considering their geometry, actuation scheme of cables, and free length of springs installed in them.
- A geometric method is proposed to estimate the axial forces in the bars conservatively within the permissible range of movement. This estimation is used to design sufficiently large cross-sections to avoid buckling failure.
- A computational scheme is presented to treat the above feasibility conditions in a sequence that accounts for the interactions between them.

The rest of this chapter is organized as follows: Section 5.2 presents the conditions of mechanical feasibility for a spring. Section 5.3 gives the buckling condition of a bar. Section 5.4 lists all the design considerations for the 2-X manipulator and presents a safe design for this manipulator. Section 5.5 performs the same analysis for the 2-R manipulator. Finally, Section 5.6 concludes this study.

5.2 Mechanical feasibility of springs

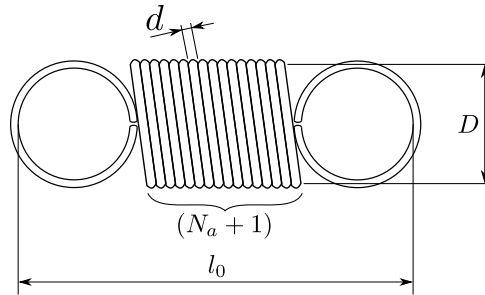


Figure 5.2 – Schematic of a helical extension spring.

The schematic of a helical extension spring in its unloaded state is shown in Fig. 5.2. It is fabricated by winding a steel wire of diameter d around a cylinder successively to form identical coils of nominal diameter D . The coils at the two ends have been bent out, as can be seen in the figure, to form hooks on either side of the spring for its attachment. The distance between the inner ends of hooks is the free length l_0 of the spring. The coils that deform while the spring ends are subjected to a tensile force are referred to as active coils. The number of such coils is denoted by N_a .

The following sections present the design assumptions and the governing conditions.

5.2.1 Assumptions in spring design

The assumptions and idealization made on the spring design are reported with appropriate literary reference in the following:

- **Active coils and hooks:**

For an extension spring, the number of active coils is usually assumed to be one less

than the total number of coils in the body (N), $N_a = N - 1$ (see, e.g., [Chi21], p. 357). The hooks of the spring are designed in several forms depending on the attachment requirements (see, e.g., [MM17], p. 378). In this report, the hooks will be assumed as loops with the same nominal diameter as that of the coil, as depicted in Fig. 5.2.

— **Material and associated properties:**

The helical springs are generally manufactured with various carbon steel wires [Chi21]. One of the commonly found materials in the catalog of spring manufacturers is EN 10720-1 (SH/DH) (or, equivalently, ASTM A228), which is also known as the music/piano wire. This material will be assumed for the springs in this report. The mechanical properties of this material can be found in the standard [Eur22]. Notably, the value of shear modulus (G_k) is 81.5 GPa, volumetric density is $\rho_k = 7850 \text{ Kg/m}^3$. The value of ultimate tensile strength (R_m) varies with the wire diameter (d), as tabulated in [Eur22]. The critical value of shear stress is calculated as $\tau_{\max}(d) = 0.45R_m$, as mentioned in [Chi21], p. 348.

Using Fig. 5.2, the mass of the spring inclusive of the two hooks can be computed as:

$$m_{k_i} = \frac{1}{4}\rho_k(\pi d)^2 D(N_a + 3) \quad (5.1)$$

— **Standard wire diameters:**

The wire diameter (d) is the most influential parameter in the spring design. Hence, it is customary to use wires of standard diameters manufactured with a good accuracy. It is possible to find catalogs of spring manufacturers such as Vanel¹, Federnshop², with prescribed wire diameters. Additionally, these manufacturers also permit the user to specify custom wire diameters to fabricate springs with desired properties. For the purpose of this study, the wire diameter (d) is assumed to be a discrete variable that takes the following values $\{0.2, 0.3, \dots, 6.0\}$ mm.

— **Zero initial tension:**

The force-deflection relationship of an extension spring is modeled as (see [Chi21], p. 355):

$$F = F_0 + k(l - l_0) \quad (5.2)$$

where F is the tensile force applied on the spring, F_0 its initial tension, k its stiffness, l its deformed length, and l_0 its free length. In extension springs, initial tension exists as a consequence of the twist in the coils that hold them closely together. However, it is said that the initial tension can be eliminated by using heat treatment methods after fabrication (see [SMBJ04], p. 6.31). Hence, to simplify this study, initial tension is assumed to be $F_0 = 0 \text{ N}$.

The next section presents the governing conditions of a spring.

5.2.2 Governing conditions in spring design

There are two equations that must be satisfied by a spring. The first one depicts the dependence of the spring stiffness on its geometry and material properties (see [Chi21], p. 355):

$$k = \frac{G_k d^4}{8N_a D^3} \implies N_a = \frac{G_k d^4}{8k D^3} \quad (5.3)$$

1. <https://www.vanel.com>

2. <https://www.federnshop.com>

The second condition represents the geometric relation between the free length and other spring parameters, as can be derived from Fig. 5.2:

$$l_0 = (N_a + 1)d + 2(D - d) \quad (5.4)$$

While the material is known, the parameters (d, D, k, l_0, N_a) completely define a spring. Given that the above two equalities must always be satisfied, it follows that three independent parameters are sufficient to define a spring. In this thesis, the parameters (k, d, D) will be treated as independent parameters, while (N_a, l_0) will be determined from Eqs. (5.3) and (5.4), respectively.

There are several inequalities which must also be respected by a spring. These are listed and derived in terms of the independent parameters in the following:

— **Strength condition:**

The shear stress induced in the spring coils during maximum elongation must be within the elastic limit (τ_{\max}) of the material to ensure its safety. This is given by (see [Chi21], p. 345):

$$\chi_1 := \tau_{\max}(d) - \nu K_w \frac{8F_{\max}^s D}{\pi d^3} \geq 0, \text{ where} \quad (5.5)$$

$$\begin{cases} \nu = 1.2 \\ K_w = \frac{4c-1}{4c-4} + \frac{0.615}{c}, \text{ with } c = \frac{D}{d} \\ F_{\max}^s = k\delta_{\max} \\ \delta_{\max} = (l_{\max} - l_0) \end{cases} \quad (5.6)$$

where $\tau_{\max}(d)$ is the limiting shear stress of the material computed from [Eur22] as explained above. A factor of safety $\nu = 1.2$ is considered to ensure the safe operation of the spring near its elongation limits. The factor K_w is a function of the spring index $c(= D/d)$, which accounts for the curvature of the spring [Wah44]. The factor F_{\max}^s is the force induced in the spring at its maximum deflection δ_{\max} . The maximum extension length and free length of the springs are denoted by l_{\max}, l_0 , respectively. At this stage, no information on l_0 or l_{\max} is known. Hence, this condition can be further treated only based on its application and the data (if any) on its attachment points.

— **Number of active coils:**

For cold coiled extension springs, the standard [Eur14] specifies the following condition:

$$\chi_2 := N_a - 3 \geq 0 \quad (5.7)$$

— **Spring index:**

The standard [Eur14] specifies the following conditions for the spring index $c(D/d)$:

$$\chi_3 := \begin{cases} c - 4 \geq 0 \\ 20 - c \geq 0 \end{cases} \quad (5.8)$$

— **Helix angle:**

The helix angle of the extension spring is defined as (see [Par01], p. 201):

$$\zeta = \arctan(p/\pi D) \quad (5.9)$$

where p is the pitch of the spring. At the unstretched configuration (Fig. 5.2), the pitch $p = d$. The formula presented in Eq. (5.5) holds exactly only when the helix angle is zero. But, in reality ζ is never exactly zero. Wahl in [Wah44], p.42, notes that Eq. (5.5) differs from the actual behavior by only less than 2% while the spring index is greater than 3 and ζ is small. Parades in [Par01], p. 58, presents a limit of 7.5° for ζ to use the above formulation. The maximum value of ζ occurs while the spring is at its maximum elongation. This value must be smaller than the specified limit:

$$\chi_4: = 7.5^\circ - \zeta_{\max} \geq 0 \quad (5.10)$$

$$\begin{cases} \zeta_{\max} = \arctan\left(\frac{d+\delta_{\max}^c}{\pi D}\right), \text{ where} \\ \delta_{\max}^c = \frac{\delta_{\max}}{N_a} = \frac{(l_{\max}-l_0)}{N_a} \end{cases} \quad (5.11)$$

Using Eqs. (5.3),(5.4), N_a and l_0 can be written in terms of the independent spring parameters (k, d, D) . Thus, the conditions in Eqs. (5.7), (5.8) can be obtained in terms of (k, d, D) . If one obtains a value for l_{\max} or formulates it in terms of the other geometric parameters, the inequalities in Eq. (5.5), (5.10) can also be written in terms of (k, d, D) .

In addition to the inequalities χ_1, \dots, χ_4 , new conditions on spring installations arising from specific applications can also be accommodated, if they could be expressed in terms of the independent spring parameters (k, d, D) .

5.3 Safety of a bar from buckling

Since it is known that the bars experience only axial loads in the tensegrity-inspired manipulators, they are most likely to fail in buckling. In this study, all the bars are assumed to be made of Aluminum with a uniform circular cross-section. Let l_b and r_b denote the length and cross-section radius of the bar, respectively. From [Ban09], p. 819, the critical buckling load of this bar is found to be:

$$F_{\text{critical}} = \frac{\pi^2 EI_b}{l_b^2} \quad (5.12)$$

where $E = 70$ GPa is the Young's modulus of Aluminum, $I_b = \frac{\pi r_b^4}{4}$ is the second moment of area of the bar about an axis lying in the cross-section. Substituting for I_b and rearranging the above equation, one obtains:

$$r_b = \left(\frac{4F_{\text{critical}} l_b^2}{E\pi^3} \right)^{1/4} \quad (5.13)$$

This value of r_b represents a limiting value of the cross-section radius for which the bar will just buckle when the applied load is equal to F_{critical} . Suppose one could overestimate the load experienced by this bar and assign it to F_{critical} in Eq. (5.13), a safe value for its cross-section radius can be obtained.

5.4 Design considerations for the 2-X manipulator

The various steps involved in the feasible design and workspace computation of a 2-X manipulator are summarized in Fig. 5.3 and are described in detail in the following sections. As a first

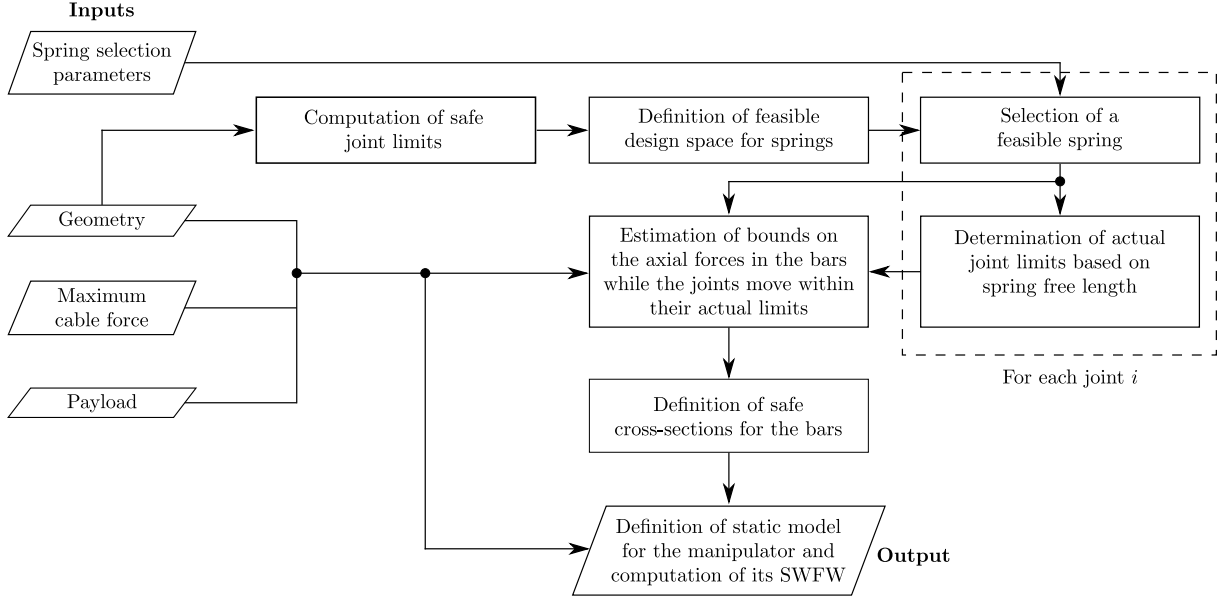


Figure 5.3 – Sequence of treating the design considerations for the 2-X manipulator.

step, safe limits for the movement of the joints are computed from the joint geometry and cable routing scheme in Section 5.4.1. These limits are used to define the complete feasible design space for the springs in Section 5.4.2. Inside this design space, the designer must independently choose springs for each joint. Then, the actual joint limits for each joint are determined based on the free length of the springs installed in it (discussed in Section 5.4.1). These data, along with the user-defined maximal actuation forces and payload, are used to estimate the axial forces in the bars and define safe cross-sections for them in Section 5.4.3. Finally, the entire process is illustrated with a numerical example in Section 5.4.4.

5.4.1 Joint limits

The range of movement of an X-joint is limited by the flat-singularities at $\alpha_i = \pm\pi$ where i denotes its position in the serial chain. A static analysis shows that the forces in the bars of the joint tend to infinity while it approaches these singularities (more details to follow in Section 5.4.3). Thus, it is necessary to set safe limits $[-\overline{\alpha}_{\max}, \overline{\alpha}_{\max}]$, such that $\overline{\alpha}_{\max} (< \pi)$ for all the joints to keep them far from flat-singularities.

In addition to the above limits, which apply identically to all the X-joints, the movement of the i^{th} X-joint in the serial chain could be further limited by the springs installed in it (see Fig. 5.4a). This limit arises because the extension springs cannot have a length smaller than their free length. The lengths of the springs (or, equivalently distance between their attachment points) on either side of the joint can be computed as (see 3.1):

$$l_i(\alpha_i) = -b \sin(\alpha_i/2) + \sqrt{l^2 - b^2 \cos^2(\alpha_i/2)} \quad l_{r_i}(\alpha_i) = b \sin(\alpha_i/2) + \sqrt{l^2 - b^2 \cos^2(\alpha_i/2)} \quad (5.14)$$

Since we use identical springs on the two sides, it is apparent that their free length must be

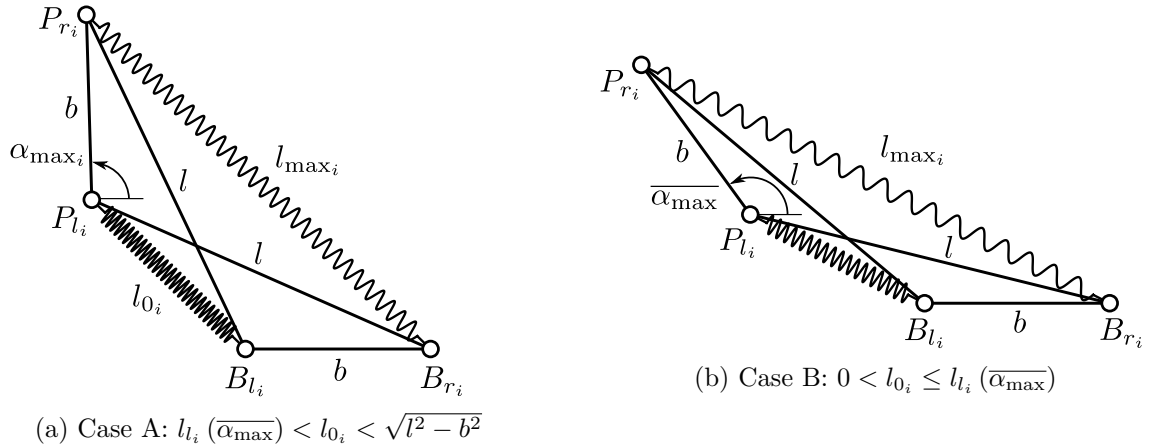


Figure 5.4 – Joint limits of an X-joint depending on the spring free length and bar lengths.

in the range $]0, \sqrt{l^2 - b^2}[$ for their installation. Further study of joint limits bifurcates into two cases depending on the free length (l_{0_i}) of the springs, as follows:

- **Case A** [$l_{0_i}(\overline{\alpha_{\max}}) < l_{0_i} < \sqrt{l^2 - b^2}$ in Fig. 5.4a]: In this case, the free length (l_{0_i}) of the springs in i^{th} joint happens to be more than the distance between the attachment points (P_{l_i}, B_{l_i}) at $\alpha_i = \overline{\alpha_{\max}}$. Thus, the actual amplitude of movement for i^{th} X-joint, denoted by $\alpha_{\max_i} (< \overline{\alpha_{\max}})$, will be attained when the left spring reaches its free length. Owing to the symmetry of this joint, the right spring reaches its maximum operating length (l_{\max_i}) at this configuration. Thus, from the geometry of the X-joint in Fig. 5.4a, α_{\max_i} and l_{\max_i} can be computed in terms of the free length (l_{0_i}) as follows:

$$\begin{cases} \alpha_{\max_i} = 2 \arcsin \left(\frac{l^2 - b^2 - l_{0_i}^2}{2bl_{0_i}} \right) \\ l_{\max_i} = \frac{l^2 - b^2}{l_{0_i}} \end{cases} \quad (5.15)$$

- **Case B** [$0 < l_{0_i} \leq l_{0_i}(\overline{\alpha_{\max}})$ in Fig. 5.4b]: In this case, the free length of the springs allows the joint to reach its safe limits $\pm \overline{\alpha_{\max}}$. The maximum operating length of the springs is given by the distance between the attachment points of the spring on the right side at $\overline{\alpha_{\max}}$ (see Fig. 5.4b) as:

$$\begin{cases} \alpha_{\max_i} = \overline{\alpha_{\max}} \\ l_{\max_i} = l_{r_i}(\overline{\alpha_{\max}}) \end{cases} \quad (5.16)$$

In summary, from Eqs. (5.15),(5.16), it is observed that the joint limits for the i^{th} X-joint depend on the geometry (b, l), designer-specified safe limit ($\overline{\alpha_{\max}}$), and the free length (l_{0_i}) of the springs. Though the designer can choose the values of ($b, l, \overline{\alpha_{\max}}$) rather arbitrarily, the choice of free length is not an obvious one. This is because the springs with stiffness required to stabilize the manipulator may not possess the chosen free length and vice versa. Hence, a more reasonable approach would be to find all the feasible springs that can be installed in the joint based on the ($b, l, \overline{\alpha_{\max}}$) parameters and let the designer choose a suitable one. Once this choice is made, the actual joint limits ($\pm \alpha_{\max_i}$) can be determined from Eq. (5.15) or Eq. (5.16) depending on whether the free length of the chosen spring belongs to case A or case B.

In order to compute all the feasible springs, the conditions on free length (l_{0_i}) and required operating length (l_{\max_i}) derived in cases A and B must be used along with other feasibility conditions for the springs. This process is carried out in the next section.

5.4.2 Design space for the springs

In this section, a method to compute the complete feasible design space for the springs for an X-joint with known geometry (b, l) and safe joint limits ($\pm\overline{\alpha_{\max}}$) is presented.

Firstly, the four inequalities governing a spring are recalled from Section 5.2.2, as follows:

$$\begin{cases} \chi_1: \text{coils must be strong enough to support the specified deflection} \\ \chi_2: \text{there should be more than three active coils} \\ \chi_3: \text{the spring index } (D/d) \text{ must be bounded inside } [4, 20] \\ \chi_4: \text{the helix angle must be less than } 7.5^\circ \end{cases} \quad (5.17)$$

Additionally, for incorporating the spring into an X-joint, the following conditions are specified:

$$\begin{cases} \chi_5: \text{the outer diameter } (D + d) \text{ must be less than one third the joint width } (b/3) \text{ for compactness} \\ \chi_6: \text{condition on } l_{0_i} \text{ in case A (denoted } \chi_{6a}) \text{ or case B (denoted } \chi_{6b}) \text{ as in Section 5.4.1} \end{cases} \quad (5.18)$$

Recalling that the conditions on l_{0_i} and the respective expressions of l_{\max_i} are different in cases A and B discussed above, we come up with two sets of feasibility conditions for the springs. The ones corresponding to case A are consolidated into χ_a and those corresponding to case B in χ_b , as follows:

$$\chi_a = \begin{cases} \chi_1 \left(l_{\max_i} = \frac{l^2 - b^2}{l_{0_i}} \right) \\ \chi_2 \\ \chi_3 \\ \chi_4 \left(l_{\max_i} = \frac{l^2 - b^2}{l_{0_i}} \right) \\ \chi_5 \\ \chi_{6a} := l_{0_i} \in]l_{i_i}(\overline{\alpha_{\max}}), \sqrt{l^2 - b^2}[\end{cases} \quad \chi_b = \begin{cases} \chi_1 (l_{\max_i} = l_{r_i}(\overline{\alpha_{\max}})) \\ \chi_2 \\ \chi_3 \\ \chi_4 (l_{\max_i} = l_{r_i}(\overline{\alpha_{\max}})) \\ \chi_5 \\ \chi_{6b} := l_{0_i} \in]0, l_{i_i}(\overline{\alpha_{\max}})] \end{cases} \quad (5.19)$$

Note that the conditions χ_1, χ_4 which depend on the desired maximum elongation (l_{\max}) have been substituted with the expression of l_{\max_i} from Eqs. (5.15),(5.16) in the two cases, respectively. Rewriting l_{0_i} using Eq. (5.4), all the above conditions can thus be formulated solely in terms of the independent spring parameters (k, d, D).

The set of all (k, d, D) values satisfying χ_a (resp. χ_b) form the feasible design space for springs belonging to case A (resp. B). The complete feasible design space for the springs is obtained from the union of the two sets $\chi_a \cup \chi_b$.

As a numerical illustration, consider the X-joint with geometry: $b = 0.2$ m, $l = 0.4$ m, and safe joint limit $\overline{\alpha_{\max}} = 5\pi/6$ rad. A slice of the spring space for $k_i = 3000$ N/m is shown in Fig. 5.5a. The vertical grid lines represent the chosen discrete values of d (see Section 5.2.1). For each value of d , D can vary inside an interval Δ_j to generate feasible spring designs. These feasible intervals on each grid line are shown in blue. In this example, all the feasible springs

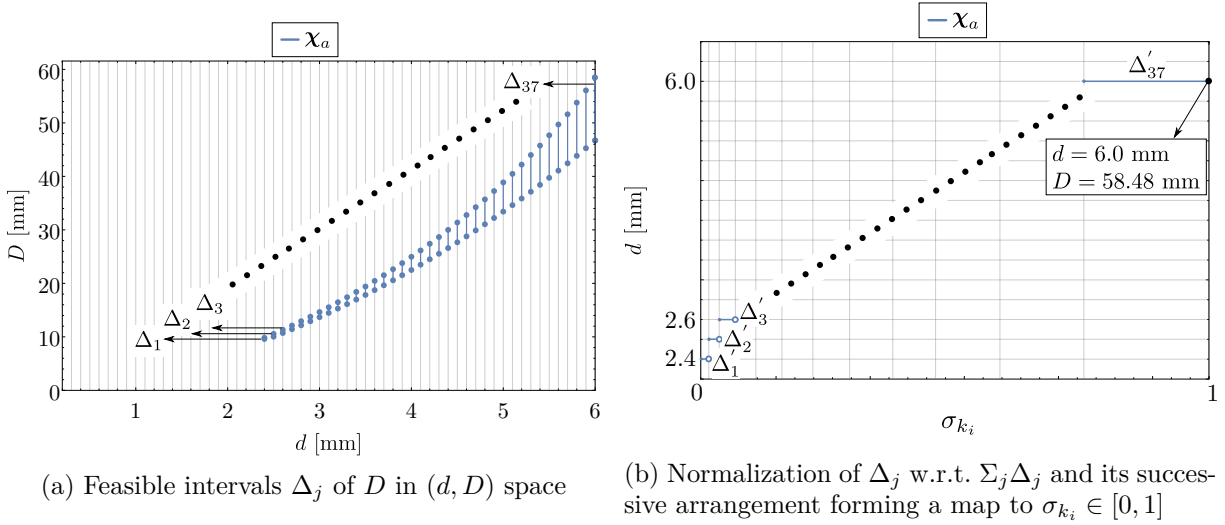


Figure 5.5 – Parametrization of the feasible spring space with $\sigma_{k_i} \in [0, 1]$ when $k_i = 3000$ N/m for an X-joint with $b = 0.2$ m and $l = 0.4$ m, and $\overline{\alpha_{\max}} = 5\pi/6$ rad.

belong to set χ_a . But, it is possible to have feasible springs from both sets for other values of geometry and spring stiffness, which is illustrated in the technical report [Mur22].

There are a total of 37 feasible intervals $\Delta_1, \Delta_2, \dots, \Delta_{37}$ of D for different values of d , as shown in Fig. 5.5a. These intervals can be normalized w.r.t. the sum of all the interval sizes $\sum_{j=1}^{37} \Delta_j$, to form Δ'_j . This permits one to arrange them successively as in Fig. 5.5b, to create a *bijective* map between the feasible intervals and a fraction $\sigma_{k_i} \in [0, 1]$. For instance, when $\sigma_{k_i} = 1.0$, the corresponding point in the feasible space is found to be $(d, D) = (6.0, 58.4844)$ mm, as depicted in Fig. 5.5b. In this manner, all the feasible points in (d, D) space can be accessed with just a single parameter σ_{k_i} .

It is noted that the map from σ_{k_i} to the intervals has several discontinuities as observed from Fig. 5.5b. At all such values of σ_{k_i} , the right-sided limit for $d(\sigma_{k_i})$ has been assigned arbitrarily. This leads to the loss of the upper bounding point in all the intervals, except the last one. However, the loss of a few discrete points in an ∞^1 space is an acceptable compromise to obtain a one-parameter (σ_{k_i}) representation of that space.

In summary, the complete feasible design space for the springs of an X-joint i , with known geometry (l, b) and safe joint limits ($\pm \overline{\alpha_{\max}}$), can be described with just two parameters (k_i, σ_{k_i}) with $\sigma_{k_i} \in [0, 1]$. The wire and coil diameters (d, D) of the springs can be found from the mapping illustrated in Fig. 5.5b. The remaining parameters, namely, number of active coils, free length, and mass, can be found using Eqs. (5.3),(5.4),(5.1), respectively. In the above example, when $k_i = 3000$ N/m, $\sigma_{k_i} = 1.0$, $(d, D) = (6.0, 58.4844)$ mm, the other parameters are found to be: $N_a = 22.0005$, $l_{0_i} = 0.2430$ m, $m_{k_i} = 1.0195$ kg. Further, from Eq. (5.15), the actual upper limit of movement for this joint is computed to be $\alpha_{\max_i} = 1.3561$ rad and the maximum operating length of this spring is $l_{\max_1} = 0.4939$ m.

In the next section, the data of springs and actual limits for all the joints will be used to estimate the forces in the bars and design safe cross-sections for them.

5.4.3 Cross-sections and masses of the bars of 2-X manipulator

This section presents a method to estimate an upper bound for compressive forces in the bars of the 2-X manipulator, whose bar lengths, springs, maximum cable forces, and payload mass are known. These forces are then substituted into Eq. (5.13), to determine safe cross-sections for each of them.

Safe estimation for axial load in the bars

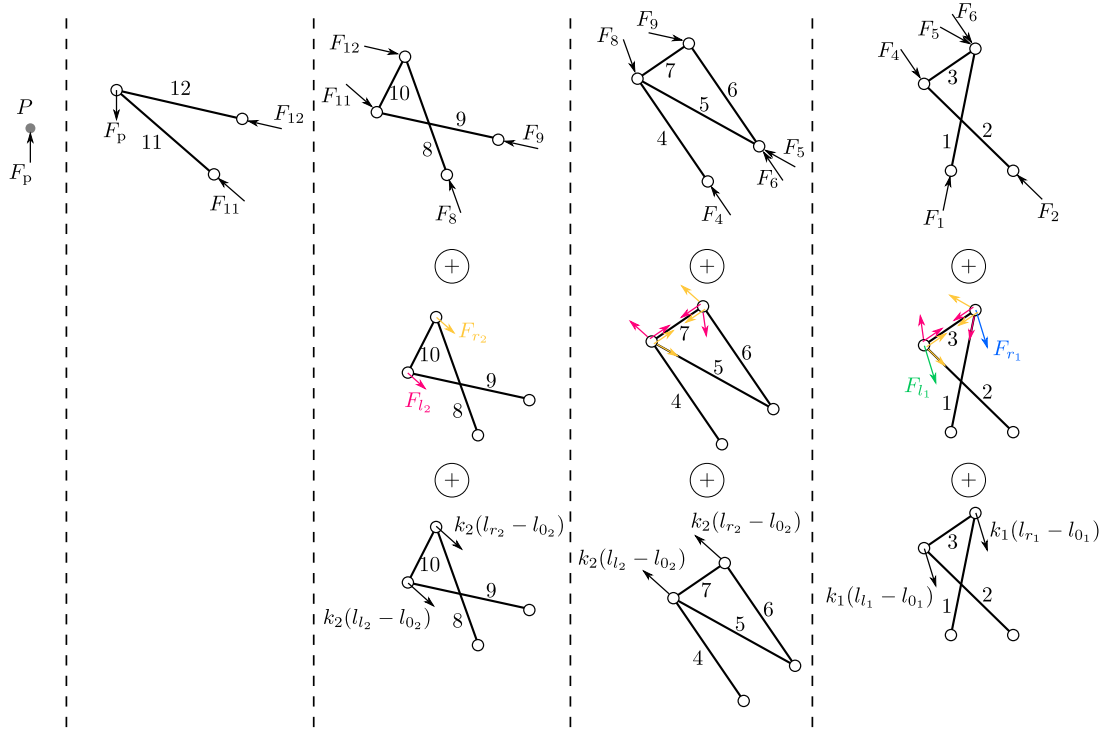


Figure 5.6 – Reaction forces at the ends of the bars.

This section aims to estimate the forces experienced by each of the bars while the manipulator is held in static equilibrium by the actuating cables. This estimation is challenging since the forces in the bars vary with the configuration and the redundant equilibrating cable forces at that configuration. Additionally, the masses of the bars and springs must also be considered for calculating these forces accurately. However, the cross-sections of the bars are not known to the designer a priori, which makes the accurate computation of the bar reactions extremely difficult. Hence, an alternate approach that provides a conservative estimation of these forces will be followed in this work.

In this approach, the masses of bars and springs are neglected since their contributions are expected to be lower than the others. Hence, the reaction forces F_j acting at the ends of each bar j must be directed along their respective longitudinal axes in opposite directions. As a convention, while the forces are compressive (i.e., directed towards the geometric center), they are considered positive. While they are tensile, they are considered negative. Some of these forces and their transmissions between the bars are visualized by splitting the manipulator into many

parts, as shown in the first row of Fig. 5.6. In addition to these, forces imposed by the cables (based on the routing shown in Fig. 3.3a) and the stiffness of springs are also considered at the various pivots, as shown in the second and third rows of Fig. 5.6, respectively.

The forces in each of the bars can be computed successively starting from the bars 12 and 11. From the second column in Fig. 5.6, it is apparent that forces induced in these two bars are only due to the payload weight F_p . Hence, the forces F_{12} and F_{11} can be computed by the vectorial resolution of this force along the directions of these bars. The resulting expressions are represented as: $F_{12} = \Omega_p^{12} F_p$ and $F_{11} = \Omega_p^{11} F_p$, where the coefficients of F_p are defined in Eq. (5.21).

Similarly, the net force at one end of all the bars are computed as in Eq. (5.20) and the expressions for force coefficients³ are presented in Eq. (5.21). While $(-\pi < \alpha_i < \pi)$, it can be shown that $\theta_i = \alpha_i/2$ [FW19]. The other intermediate angles (ϕ_i, ψ_i) shown in Fig. 3.4 can be obtained in terms of α_i using the loop-closure equations of the X-joint (see [Fur+19]). Finally, the constant angles (β_1, β_2) in offsets shown in Fig. 3.4, can be obtained from the lengths of the bars.

$$\left\{ \begin{array}{l}
 F_{12} = \Omega_p^{12} F_p \\
 F_{11} = \Omega_p^{11} F_p \\
 F_{10} = \Omega_{11}^{10} F_{11} + \Omega_{Fk_{l_2}}^{10} (F_{l_2} + k_2(l_{l_2} - l_{0_2})) \\
 F_9 = \Omega_{11}^9 F_{11} + \Omega_{Fk_{l_2}}^9 (F_{l_2} + k_2(l_{l_2} - l_{0_2})) \\
 F_8 = \Omega_{12}^8 F_{12} + \Omega_{Fk_{r_2}}^8 (F_{r_2} + k_2(l_{r_2} - l_{0_2})) \\
 F_7 = \Omega_9^7 F_9 + \Omega_{F_{l_2}}^7 F_{l_2} + \Omega_{F_{r_2}}^7 F_{r_2} + \Omega_{k_{r_2}}^7 k_2(l_{r_2} - l_{0_2}) \\
 F_6 = \Omega_9^6 F_9 + \Omega_{F_{l_2}}^6 F_{l_2} + \Omega_{Fk_{r_2}}^6 (F_{r_2} + k_2(l_{r_2} - l_{0_2})) \\
 F_5 = \Omega_8^5 F_8 + \Omega_7^5 F_7 + \Omega_{F_{l_2}}^5 F_{l_2} + \Omega_{F_{r_2}}^5 F_{r_2} + \Omega_{k_{l_2}}^5 k_2(l_{l_2} - l_{0_2}) \\
 F_4 = \Omega_8^4 F_8 + \Omega_7^4 F_7 + \Omega_{F_{l_2}}^4 F_{l_2} + \Omega_{F_{r_2}}^4 F_{r_2} + \Omega_{k_{l_2}}^4 k_2(l_{l_2} - l_{0_2}) \\
 F_3 = \Omega_4^3 F_4 + \Omega_{F_{l_2}}^3 F_{l_2} + \Omega_{F_{r_2}}^3 F_{r_2} + \Omega_{Fk_{l_1}}^3 (F_{l_1} + k_1(l_{l_1} - l_{0_1})) \\
 F_2 = \Omega_4^2 F_4 + \Omega_{F_{l_2}}^2 F_{l_2} + \Omega_{F_{r_2}}^2 F_{r_2} + \Omega_{Fk_{l_1}}^2 (F_{l_1} + k_1(l_{l_1} - l_{0_1})) \\
 F_1 = \Omega_6^1 F_6 + \Omega_5^1 F_5 + \Omega_{F_{l_2}}^1 F_{l_2} + \Omega_{F_{r_2}}^1 F_{r_2} + \Omega_{Fk_{r_1}}^1 (F_{r_1} + k_1(l_{r_1} - l_{0_1}))
 \end{array} \right. \quad (5.20)$$

3. Note that $\csc(\cdot) = 1/\sin(\cdot)$ and $\sec(\cdot) = 1/\cos(\cdot)$.

$$\left\{ \begin{array}{l}
 \Omega_p^{12} = \csc(2\beta_2) \cos(\beta_2 + (\alpha_1 + \alpha_2)); \Omega_p^{11} = \csc(2\beta_2) \cos(\beta_2 - (\alpha_1 + \alpha_2)); \\
 \Omega_{F_{l_2}}^{10} = \csc(\psi_2 - \alpha_2) \sin(\beta_2 + \alpha_2 - \psi_2); \Omega_{F_{k_{l_2}}}^{10} = \csc(\psi_2 - \alpha_2) \cos(\theta_2 - \psi_2); \\
 \Omega_{F_{l_2}}^9 = \csc(\psi_2 - \alpha_2) \sin(\beta_2); \Omega_{F_{k_{l_2}}}^9 = \csc(\psi_2 - \alpha_2) \cos(\theta_2); \\
 \Omega_{F_{r_2}}^8 = \csc(\phi_2 - \alpha_2) \sin(\beta_2); \Omega_{F_{k_{r_2}}}^8 = \csc(\phi_2 - \alpha_2) \cos(\theta_2); \\
 \Omega_{F_{l_2}}^7 = \cos(\psi_2); \Omega_{F_{l_2}}^7 = 1 + \cos(\beta_1); \Omega_{F_{r_2}}^7 = 1 + \sin(\theta_2); \Omega_{k_{r_2}}^7 = \sin(\theta_2); \\
 \Omega_{F_{l_2}}^6 = \sin(\psi_2); \Omega_{F_{l_2}}^6 = \sin(\beta_1); \Omega_{F_{k_{r_2}}}^6 = -\cos(\theta_2); \\
 \Omega_{F_{l_2}}^5 = -\sec(\beta_1) \cos(\phi_2); \Omega_{F_{l_2}}^5 = -\sec(\beta_1); \Omega_{F_{l_2}}^5 = \sec(\beta_1)(1 - \sin(\theta_2)); \\
 \Omega_{F_{r_2}}^5 = 1 + \sec(\beta_1); \Omega_{k_{l_2}}^5 = -\sec(\beta_1) \sin(\theta_2); \\
 \Omega_{F_{l_2}}^4 = \sec(\beta_1) \sin(\beta_1 + \phi_2); \Omega_{F_{l_2}}^4 = \tan(\beta_1); \\
 \Omega_{F_{l_2}}^4 = -\sec(\beta_1) \cos(\beta_1 + \theta_2) - \tan(\beta_1); \\
 \Omega_{F_{r_2}}^4 = -\tan(\beta_1); \Omega_{k_{l_2}}^4 = -\sec(\beta_1) \cos(\beta_1 + \theta_2); \\
 \Omega_{F_{l_2}}^3 = \cot(\psi_1 - \alpha_1); \Omega_{F_{l_2}}^3 = 1 + \csc(\alpha_1 - \psi_1) \sin(\beta_1 + \alpha_1 - \psi_1); \\
 \Omega_{F_{r_2}}^3 = 1; \Omega_{F_{k_{l_1}}}^3 = \cos(\theta_1 - \psi_1) \csc(\psi_1 - \alpha_1); \\
 \Omega_{F_{l_2}}^2 = \csc(\psi_1 - \alpha_1); \Omega_{F_{l_2}}^2 = \sin(\beta_1) \csc(\alpha_1 - \psi_1); \Omega_{F_{r_2}}^2 = 1; \\
 \Omega_{F_{k_{l_1}}}^2 = \cos(\theta_1) \csc(\psi_1 - \alpha_1); \\
 \Omega_{F_{l_2}}^1 = \csc(\phi_1 - \alpha_1); \Omega_{F_{l_2}}^1 = \sin(\beta_1) \csc(\phi_1 - \alpha_1); \Omega_{F_{l_2}}^1 = 1; \\
 \Omega_{F_{r_2}}^1 = \sin(\beta_1) \csc(\alpha_1 - \phi_1); \Omega_{F_{k_{r_1}}}^1 = \cos(\theta_1) \csc(\phi_1 - \alpha_1)
 \end{array} \right. \quad (5.21)$$

From the above expressions of force coefficients, it is clear that the ones containing $\csc(\psi_i - \alpha_i)$ and $\csc(\phi_i - \alpha_i)$ can tend to infinity while their respective arguments approach zero. Physically, this happens when the joint i is near its flat-singularities ($\alpha_i = \pm\pi$). Hence, to avoid unreasonably large forces in the bars, the designer must ensure that the joints operate within safe limits sufficiently far from these singular configurations, as detailed in Section 5.4.1.

The next step involves the computation of the bounds for the bar forces. From Eq. (5.20), it is observed that each term contains a product of a force and a force coefficient which depends on the configuration. A conservative estimation of the range of each of the terms can be obtained by firstly computing the bounds of the forces $[F, \bar{F}]$ and the respective coefficients $[\Omega, \bar{\Omega}]$. Then, the bounds of the product (ΩF) can be obtained as the minimum and maximum values of the set $\{\underline{\Omega} F, \underline{\Omega} \bar{F}, \bar{\Omega} F, \bar{\Omega} \bar{F}\}$. The range of forces and force coefficients are obtained as follows:

- Though the payload weight $F_p = m_p g$ (where $g = 9.8 \text{ m/s}^2$ is the acceleration due to gravity), is a known constant, its bounds are assumed to be $F_p \in [0, 2m_p g]$. The lower bound is set to 0 to ensure that the manipulator remains safe even when it is loaded with a lighter payload than the assumed one. The upper bound is set to twice the actual weight to compensate for the masses of the bars and springs that were neglected. This is also expected to account for the dynamic forces that might arise while moving the manipulator. The bounds of other forces due to cables and the stiffness of the springs are also listed in the following ($i = 1, 2$):

$$\left\{ \begin{array}{l}
 F_p \in [0, 2m_p g] \\
 \{F_{l_i}, F_{r_i}\} \in [F_{\min}, F_{\max}] \\
 \{k_i(l_{l_i} - l_{0_i}), k_i(l_{r_i} - l_{0_i})\} \in [0, k_i(l_{\max_i} - l_{0_i})]
 \end{array} \right. \quad (5.22)$$

- From Eq. (5.21), $\Omega_p^{12}, \Omega_p^{11}$ are functions of $(\alpha_1 + \alpha_2)$. Since $\alpha_i \in [-\alpha_{\max_i}, \alpha_{\max_i}]$, it follows that $(\alpha_1 + \alpha_2)$ must be bounded within $[-(\alpha_{\max_1} + \alpha_{\max_2}), (\alpha_{\max_1} + \alpha_{\max_2})]$. Hence, the bounding values of $\Omega_p^{12}, \Omega_p^{11}$ can be found by evaluating the respective cosine functions at the stationary points and the bounds. It is also apparent from Eq. (5.21) that one can reduce all the other force coefficients to functions of just one of the angles α_i . Thus, they can be classified into several categories as in Table 5.1, by studying them analytically (see Appendix B for illustrations). This classification aids in the computation of their bounding values. Note that while $\alpha_i = \alpha_{\max_i}$ (resp. $-\alpha_{\max_i}$), all the dependent angles $(\psi_i, \phi_i, \theta_i)$ in that joint attain their maximum (resp. minimum) values. Hence, the bounds of coefficients in categories II and III can be computed directly without rewriting them in terms of α_i .

Table 5.1 – Classification of the coefficients in Eq. (5.21) and computation of their bounds.

Category	Nature	Coefficients	Minimum	Maximum
I	Constant	$\Omega_{F_{l_2}}^7, \Omega_{F_{l_2}}^6, \Omega_{F_{l_2}}^5, \Omega_{F_{r_2}}^5, \Omega_{F_{l_2}}^4,$ $\Omega_{F_{r_2}}^4, \Omega_{F_{r_2}}^3, \Omega_{F_{r_2}}^2, \Omega_{F_{l_2}}^1$	Value of the constant	
II	Monotonic increase with $\alpha_i \in]-\pi, \pi[$	$\Omega_{F_{l_2}}^{10}, \Omega_{F_{k_{l_2}}}^{10}, \Omega_{F_{k_{r_2}}}^8, \Omega_{F_{r_2}}^7,$ $\Omega_{k_{r_2}}^7, \Omega_{F_{l_2}}^5, \Omega_{F_{l_2}}^3, \Omega_{F_{k_{l_1}}}^3, \Omega_{F_{k_{r_1}}}^1$	Maximum angles	Minimum angles
III	Monotonic decrease with $\alpha_i \in]-\pi, \pi[$	$\Omega_{F_{k_{l_2}}}^9, \Omega_{F_{l_2}}^7, \Omega_{F_{l_2}}^5, \Omega_{k_{l_2}}^5,$ $\Omega_{F_{l_2}}^3, \Omega_{F_{k_{l_1}}}^2$	Minimum angles	Maximum angles
IV	Possible extrema	$\Omega_p^{12}, \Omega_p^{11}, \Omega_{F_{l_2}}^9, \Omega_{F_{l_2}}^8, \Omega_{F_{l_2}}^6,$ $\Omega_{F_{k_{r_2}}}^6, \Omega_{F_{l_2}}^4, \Omega_{F_{l_2}}^4, \Omega_{k_{l_2}}^4, \Omega_{F_{l_2}}^2,$ $\Omega_{F_{l_2}}^2, \Omega_{F_{l_2}}^1, \Omega_{F_{l_2}}^1, \Omega_{F_{r_2}}^1$	Evaluate at stationary points, bounds; choose the minimum and maximum from them.	

- Once the bounds of distal bars F_{12}, F_{11} are found, they will be used successively for computing the bounds of F_{10}, F_9, F_8 , and so on. This causes the force estimations to be increasingly more conservative as one moves toward the base. This computational feature is acceptable since the effect of neglected bar masses also increases as one moves closer to the base.
- Finally, the upper bounds of the estimated bar forces, denoted by F_j^* , will be used in Eq. (5.13) to compute the safe cross-section radius for bar j , for $j = 1, \dots, 12$ (see Fig. 3.4).

Practical considerations and symmetry of the manipulator

Let r_{b_j} denote the cross-section radius of the j^{th} bar. The safe value for r_{b_j} determined by substituting $F_{\text{critical}} = F_j^*$ in Eq. (5.13) is given by $r_{b_j}^*$. Further, to avoid practical issues associated with the fabrication of small sections, a minimum cross-section radius $\underline{r_{b_j}} = 5$ mm is considered. Hence, a corrected cross-section radius is obtained as: $r_{b_j} = \max(\underline{r_{b_j}}, r_{b_j}^*)$, which is safe and viable.

Further, to preserve the mass symmetry of the manipulator about the configuration $(\alpha_1, \alpha_2) = (0, 0)$, it is necessary to have the same cross-sections for the following pairs of the bars (see Fig. 3.4): (1, 2), (4, 6), (8, 9), (11, 12). This requirement is satisfied by setting the largest of the

two cross-sections for both bars in each pair. Finally, the mass of j^{th} bar (m_j) can be computed as $m_j = \pi \rho r_{b_j}^2 l_{b_j}$, where $\rho = 2700 \text{ kg/m}^3$ is the volumetric density of Aluminum.

5.4.4 Consolidation of all design conditions and a numerical example for 2-X manipulator

In this section, all the design considerations discussed above for the 2-X manipulator are consolidated to determine its SWFW and a numerical example is presented.

Starting from a given design of the 2-X manipulator, i.e., with defined geometry (b, l, a), safe joint limits ($\overline{\alpha_{\max}}$), springs (k_i, σ_i) for $i = 1, 2$, and maximal actuation force (F_{\max}), the steps involved in the computation of its SWFW are presented in a flow chart in Fig. 5.7. As a numerical illustration, consider the following design of the 2-X manipulator: $b = 0.2 \text{ m}$, $l = 0.4 \text{ m}$, $a = 0.5 \text{ m}$, $\overline{\alpha_{\max}} = 5\pi/6 \text{ rad}$, $k_1 = 3000 \text{ N/m}$, $\sigma_{k_1} = 1.0$, $k_2 = 1000 \text{ N/m}$, $\sigma_{k_2} = 0.7$, $F_{\max} = 200 \text{ N}$. A payload of $m_p = 2 \text{ kg}$ is considered at the end-effector. The SWFJ and SWFW obtained for this design are presented in Figs. 5.8a and 5.8b, respectively. The steps involved are described in the following:

- **Section 5.4.2:** The first step involves the computation of the feasible design space for each of the springs and determining the dependent parameters. If the feasible design space is empty for any of the springs, then the design of that 2-X manipulator is deemed infeasible. The spring stiffnesses were chosen such that the manipulator is in stable equilibrium at $(\alpha_1, \alpha_2) = (0, 0)$ without actuation forces. For spring 1, $k_1 = 3000 \text{ N/m}$, $\sigma_{k_1} = 1.0$, the dependent parameters are found to be (see Fig. 5.5b and Eqs. (5.3),(5.4),(5.15),(5.1)): $d = 6.0 \text{ mm}$, $D = 58.4844 \text{ mm}$, $N_a = 22.0005$, $l_{0_1} = 0.2430 \text{ m}$, $l_{\max_1} = 0.4939 \text{ m}$, $m_{k_1} = 1.0195 \text{ kg}$. Similarly, for spring 2, $k_2 = 1000 \text{ N/m}$, $\sigma_{k_2} = 0.7$, the parameters are found to be: $d = 4.7 \text{ mm}$, $D = 52.3495 \text{ mm}$, $N_a = 34.6515$, $l_{0_2} = 0.2629 \text{ m}$, $l_{\max_2} = 0.4565 \text{ m}$, $m_{k_2} = 0.8433 \text{ kg}$. The total mass contributed by all the springs is found to be $2(m_{k_1} + m_{k_2}) = 3.7257 \text{ kg}$.
- **Section 5.4.1:** By substituting the spring free length data in Eq. (5.15), one obtains $\alpha_{\max_1} = 1.3561 \text{ rad}$ and $\alpha_{\max_2} = 1.0108 \text{ rad}$, i.e., the actual range of movement of the two joints are $\alpha_1 = [-1.3561, 1.3561] \text{ rad}$ and $\alpha_2 \in [-1.0108, 1.0108] \text{ rad}$, respectively.
- **Section 5.4.3:** The conservative bounds for bar forces are computed using the data of geometry, maximal actuation force F_{\max} , springs, and payload. The numerical values are presented in the second column of Table 5.2. The safe cross-section radii for the bars and their corrected values based on symmetry and assumed minimum $r_{b_j} = 5 \text{ mm}$ are presented in the subsequent columns. Further, the respective masses (m_j) for all the bars have also been presented. The total mass contributed by the moving bars is 1.4956 kg , which is much smaller than those of the springs (3.7257 kg). The total moving mass of the manipulator is found to be 5.2244 kg .
- **Chapter 3:** Using the static model and joint limits (α_{\max_i}) for all joints $i = 1, 2$, the SWFJ of the manipulator can be constructed as in Fig. 5.8a (shaded part). In this example, it is observed that the limiting boundaries of SWFJ are only formed by the wrench-feasibility and joint limits but not by stability. This indicates that the manipulator must possess good stiffness throughout the SWFJ. Further, the bounding points of SWFJ and singularities in the joint space have been mapped onto the task space using the direct kinematic map. The resulting plot of the SWFW of the manipulator is shown in Fig. 5.8b.

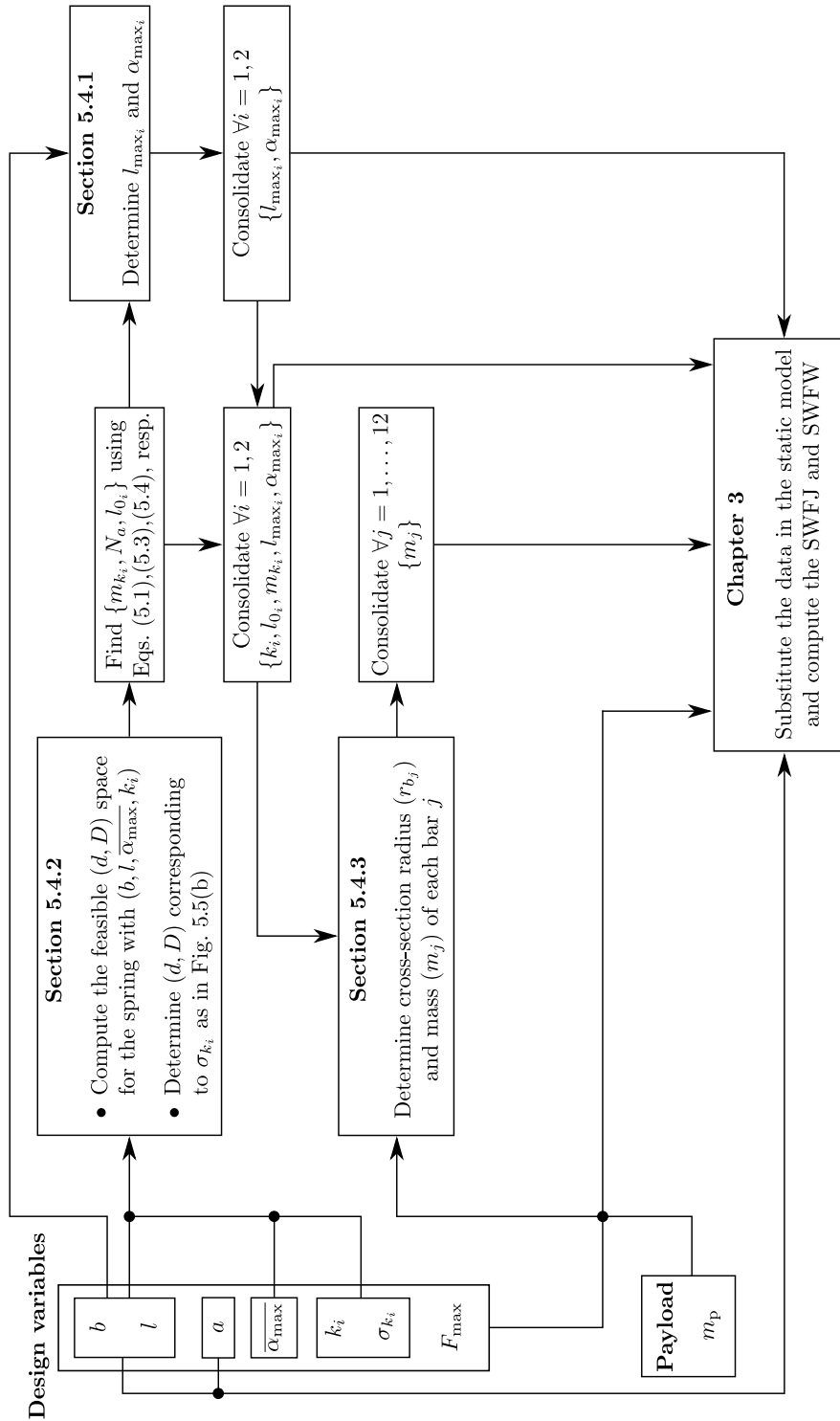


Figure 5.7 – Computational scheme for the determination of SWFW for the 2-X manipulator that accounts for all of its design considerations discussed in Section 5.4.

Table 5.2 – 2-X manipulator: Range of estimated buckling loads and the resulting safe cross-section radii for the bars along with their masses.

Bar index j	Estimated load [N]	Cross-section radius [mm]		Mass [kg] m_j
		Computed ($r_{b_j}^*$)	Corrected (r_{b_j})	
12	[-101.92, 101.92]	2.64	5.00	0.1081
11	[-101.92, 101.92]	2.64		
10	[-461.71, 162.19]	1.86	5.00	0.0424
9	[-173.81, 772.84]	3.89	5.00	0.0848
8	[-173.81, 772.84]	3.89		
7	[-726.05, 807.06]	2.78	5.00	0.0424
5	[-4128.03, 4128.03]	6.85	6.85	0.2146
6	[-567.46, 958.53]	4.58	6.60	0.1845
4	[-4091.47, 4107.72]	6.60		
3	[-8434.49, 8240.10]	4.96	5.00	0.0424
2	[-9041.49, 10451.80]	7.45	7.70	0.2010
1	[-9694.20, 11896.80]	7.70		
Total bar mass				1.4986
Mass of springs ($2(m_{k_1} + m_{k_2})$)				3.7257
Total moving mass of the manipulator				5.2244

In Fig. 5.8a, all the curves in the region ($\det(\mathbf{J}_x) > 0$) (resp. region ($\det(\mathbf{J}_x) < 0$)) are shown in opaque (resp. transparent) styles, to distinguish between the two symmetric halves in the joint space and display the overlapping regions in task space with clarity. As expected from the manipulator symmetry, the images of the two halves of SWFJ in the task space, are symmetric about the y -axis. The overlapping region around the y -axis has two feasible configurations, while those on the two farther sides have just one feasible configuration. The inscribed disks shown in Fig. 5.8b have a radius of 0.0736 m each. The maximal vertical reach (i.e., the y -coordinate of the end-effector while the joint angles are $(\alpha_1, \alpha_2) = (0, 0)$) of the manipulator is 1.6928 m, which is about 23 times the radius of the inscribed disk.

As a validation of the obtained design, it has been verified that the actual loads induced in the bars are less than the estimated ones at several configurations (α_1, α_2) inside the SWFJ and for several combinations of actuation forces $\in [F_{\min}, F_{\max}]$ in Appendix C. This study confirms that the design of the 2-X manipulator proposed is safe from buckling failure for manipulating a payload of 2 kg inside its SWFW. Note that the resulting mass of the bars and springs (5.2244 kg) is more than twice the payload mass assumed in the design process in Section 5.4.3. But, the actual forces induced in the bars are much smaller than the estimated ones. This difference can be attributed to the further overestimation in the scheme, where the worst combinations of all forces and the respective force coefficients were considered. It is observed that this difference also increases as one moves from the end-effector toward the base. This is due to the overestimation of forces at the distal bars and their recursive substitutions in the computation of forces in the proximal bars (see Eq. (5.20)). Nevertheless, the resulting cross-sections of the bars are not impacted severely due to this overestimation, as observed from Table 5.2, thanks to the

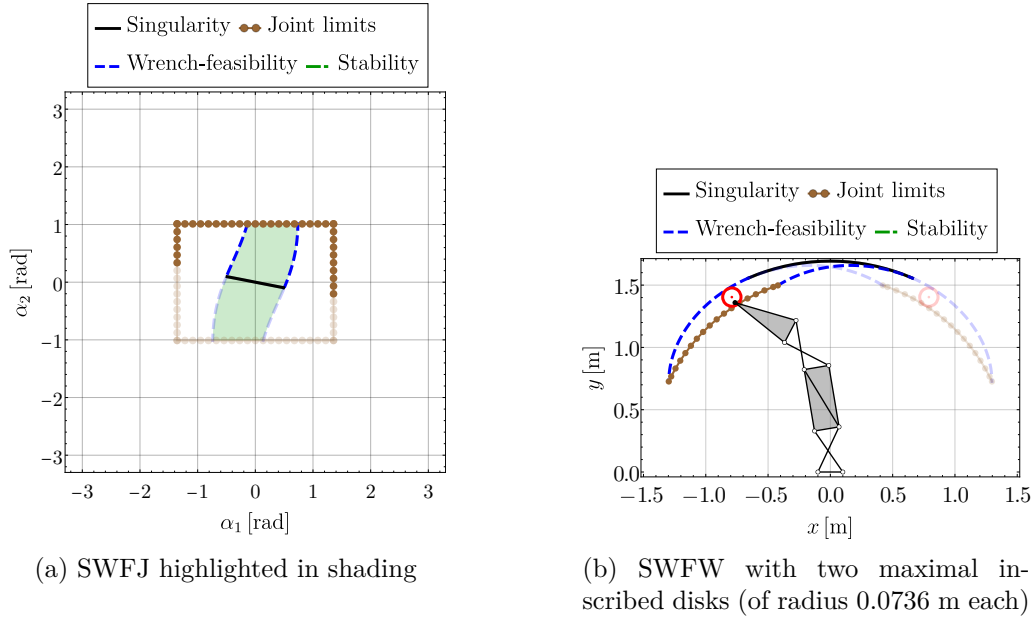


Figure 5.8 – Stable wrench-feasible joint space (SWFJ) and stable wrench-feasible workspace (SWFW) for the 2-X manipulator with: $b = 0.2$ m, $l = 0.4$ m, $a = 0.5$ m, $\overline{\alpha_{\max}} = 5\pi/6$ rad, $k_1 = 3000$ N/m, $l_{0_1} = 0.2430$ m, $m_{k_1} = 1.0195$ kg, $k_2 = 1000$ N/m, $l_{0_2} = 0.2629$ m, $m_{k_2} = 0.8433$ kg, $F_{\max} = 200$ N. In SWFJ, the curves lying in the region where $\det(\mathbf{J}_x) > 0$ are shown in opaque style while those in $\det(\mathbf{J}_x) < 0$ region are shown in transparent style. The images of these curves in the task space are also shown in the same style for the sake of clarity.

damping exponent (1/4) in Eq. (5.13). It was verified through several numerical examples that the resulting bar cross-sections are safe for the 2-X manipulator, thereby validating the proposed methodology.

The design considerations for the 2-R manipulator and the computation of its SWFW will be discussed in the following section.

5.5 Design considerations for the 2-R manipulator

The schematic of the 2-R manipulator with bar and pivot labels is shown in Fig. 5.9a. This manipulator is also *remotely* actuated with four motors using one cable each, as shown in Fig. 5.9b. The cables C_{l_i} and C_{r_i} actuate the i^{th} joint *independently*, for $i = 1, 2$, as explained in the case of 2-X manipulator (see Section 3.5.1).

In the following, we describe the different factors to be considered in the design of 2-R manipulator. The joint limits of an R-joint are explored in Section 5.5.1. The governing conditions for spring design are listed in Section 5.5.2. The estimation of buckling loads for the bars and the determination of their cross-section radii are carried out in Section 5.5.3. The static and kinematic models of the 2-R manipulator are developed in Sections 5.5.4 and 5.5.5, respectively. Finally, the SWFW computation is illustrated with an example in Section 5.5.6.

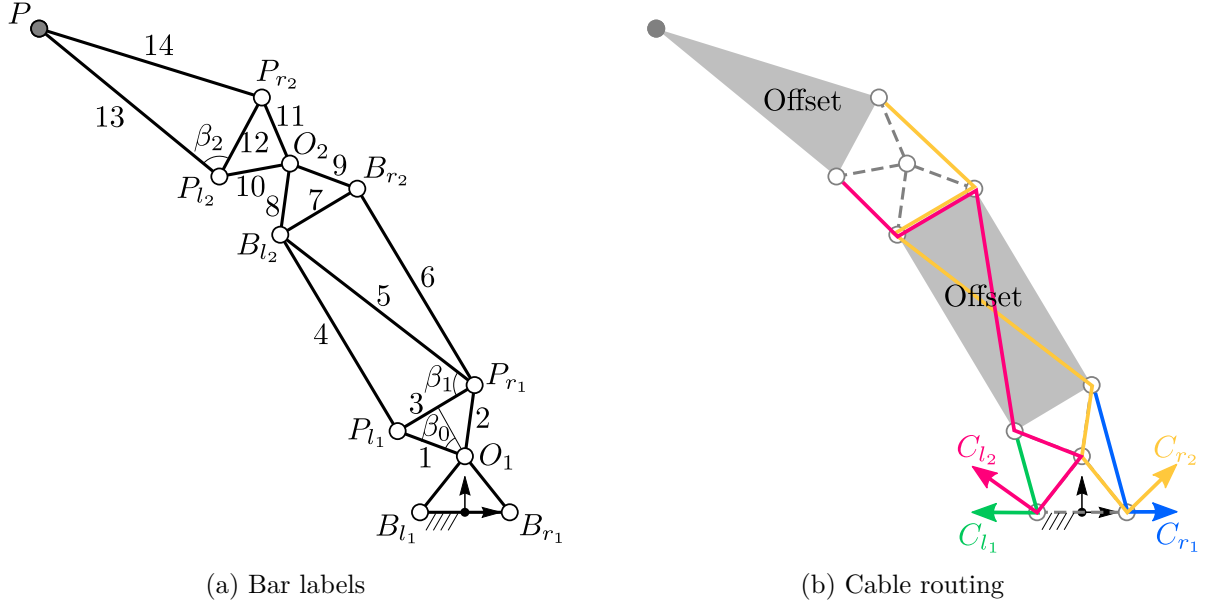


Figure 5.9 – Bar labels (left) and cable routing scheme (right) for the 2-R manipulator.

5.5.1 Joint limits

From Section 2.5.1 on R-joint, the upper bound of its joint limits, denoted by $\overline{\overline{\alpha_{\max}}}$, is recalled below:

$$\overline{\overline{\alpha_{\max}}} = \begin{cases} 2 \arctan(h/r), & \text{if } r > h \\ 2 \arctan(r/h), & \text{if } r < h \\ \frac{\pi}{2}, & \text{if } r = h \end{cases} \quad (5.23)$$

As in the case of X-joint, a safe amplitude of movement should be defined by the designer as $\overline{\alpha_{\max}}$ which is strictly less than $\overline{\overline{\alpha_{\max}}}$. However, unlike in the X-joint, the singularities occur at different joint angles depending on the geometry of the joint. Hence, it is more convenient to define the safe limits as a fraction of the bounds due to singularity, i.e., $\overline{\alpha_{\max}} = \sigma_{\alpha} \overline{\overline{\alpha_{\max}}}$, with $\sigma_{\alpha} \in]0, 1[$, such that it is valid for all joint geometries.

Further, for the i^{th} R-joint in the manipulator, the actual joint limits ($\pm\alpha_{\max_i}$) can differ from the safe joint limits ($\pm\overline{\alpha_{\max}}$) depending on the free length (l_{0_i}) of the springs installed in it (see Fig. 5.10). Since identical springs are used on the two sides of the joint, it is apparent that their free length must respect $l_{0_i} \in [0, 2h]$ for installation. The lengths of the springs on either side (i.e., the distance between their attachment points) are given by (see Eq. (2.22)):

$$l_l(\alpha_i) = 2 \left(h \cos\left(\frac{\alpha_i}{2}\right) - r \sin\left(\frac{\alpha_i}{2}\right) \right) \quad l_r(\alpha_i) = 2 \left(h \cos\left(\frac{\alpha_i}{2}\right) + r \sin\left(\frac{\alpha_i}{2}\right) \right) \quad (5.24)$$

The computation of actual joint limit (α_{\max_i}) and maximum operating length (l_{\max_i}) of the springs is carried out in a case-wise manner in the following:

- **Case A** [$(l_i(\overline{\alpha_{\max}}) < l_{0_i} < 2h)$ in Fig. 5.10a]: In this case, α_{\max_i} is attained when the left spring reaches its free length (l_{0_i}). At this configuration, the right spring attains its

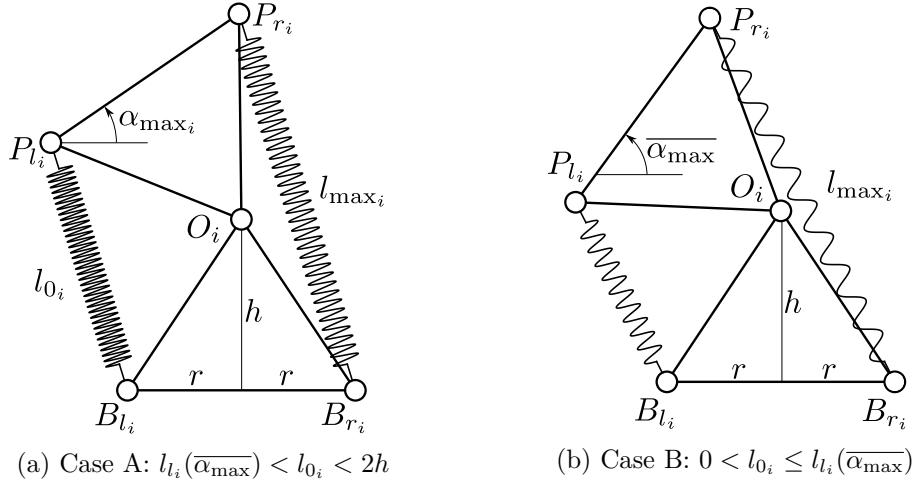


Figure 5.10 – Joint limits of an R-joint depending on the spring free length (l_{0i}) and bar lengths.

maximum operating length (l_{\max_i}). From the geometry of R-joint, α_{\max_i} and l_{\max_i} can be obtained in terms of l_{0i} as:

$$\begin{cases} \alpha_{\max_i} = 2 \left(\arccos \left(\frac{l_{0i}}{2\sqrt{h^2+r^2}} \right) - \arccos \left(\frac{h}{\sqrt{h^2+r^2}} \right) \right) \\ l_{\max_i} = \frac{2hr \sqrt{4(h^2+r^2) - l_{0i}^2} + l_{0i}(h^2-r^2)}{h^2+r^2} \end{cases} \quad (5.25)$$

- **Case B** [$0 < l_{0i} \leq l_i(\overline{\alpha_{\max}})$ in Fig. 5.10b]: In this case, the joint movement is limited by the safe limits, i.e., $\alpha_{\max_i} = \overline{\alpha_{\max}}$, irrespective of the spring free length. The maximum operating length of the springs is also attained at these limits, as computed by:

$$\begin{cases} \alpha_{\max_i} = \overline{\alpha_{\max}} \\ l_{\max_i} = l_{r_i}(\overline{\alpha_{\max}}) \end{cases} \quad (5.26)$$

In the next section, the feasible design space for the springs is derived using the aforementioned conditions and mechanical feasibility.

5.5.2 Design space for the springs

The design of springs for the R-joint is conducted like that of the X-joint in Section 5.4.2. For the R-joint, in Eq. (5.18), expression of one third the joint width ($b/3$) must be replaced by $(2r/3)$, and the conditions χ_{6a} and χ_{6b} must be adopted to cases A and B, discussed in the previous section. Also, the respective expressions for l_{\max_i} derived in each of these cases should be used in the inequalities χ_1 and χ_4 . Finally, the set of all conditions for spring design in the

case of R-joint is obtained to be:

$$\chi_a = \begin{cases} \chi_1 (l_{\max_i} \text{ in Eq. (5.25)}) \\ \chi_2 \\ \chi_3 \\ \chi_4 (l_{\max_i} \text{ in Eq. (5.25)}) \\ \chi_5 \\ \chi_{6a} := l_{0_i} \in]l_i(\overline{\alpha_{\max}}), 2h[\end{cases} \quad \chi_b = \begin{cases} \chi_1 (l_{\max_i} = l_{r_i}(\overline{\alpha_{\max}})) \\ \chi_2 \\ \chi_3 \\ \chi_4 (l_{\max_i} = l_{r_i}(\overline{\alpha_{\max}})) \\ \chi_5 \\ \chi_{6b} := l_{0_i} \in]0, l_i(\overline{\alpha_{\max}})] \end{cases} \quad (5.27)$$

Similar to the X-joint, the set of all feasible springs for the R-joint is obtained from $\chi_a \cup \chi_b$.

5.5.3 Cross-sections and masses of the bars of 2-R manipulator

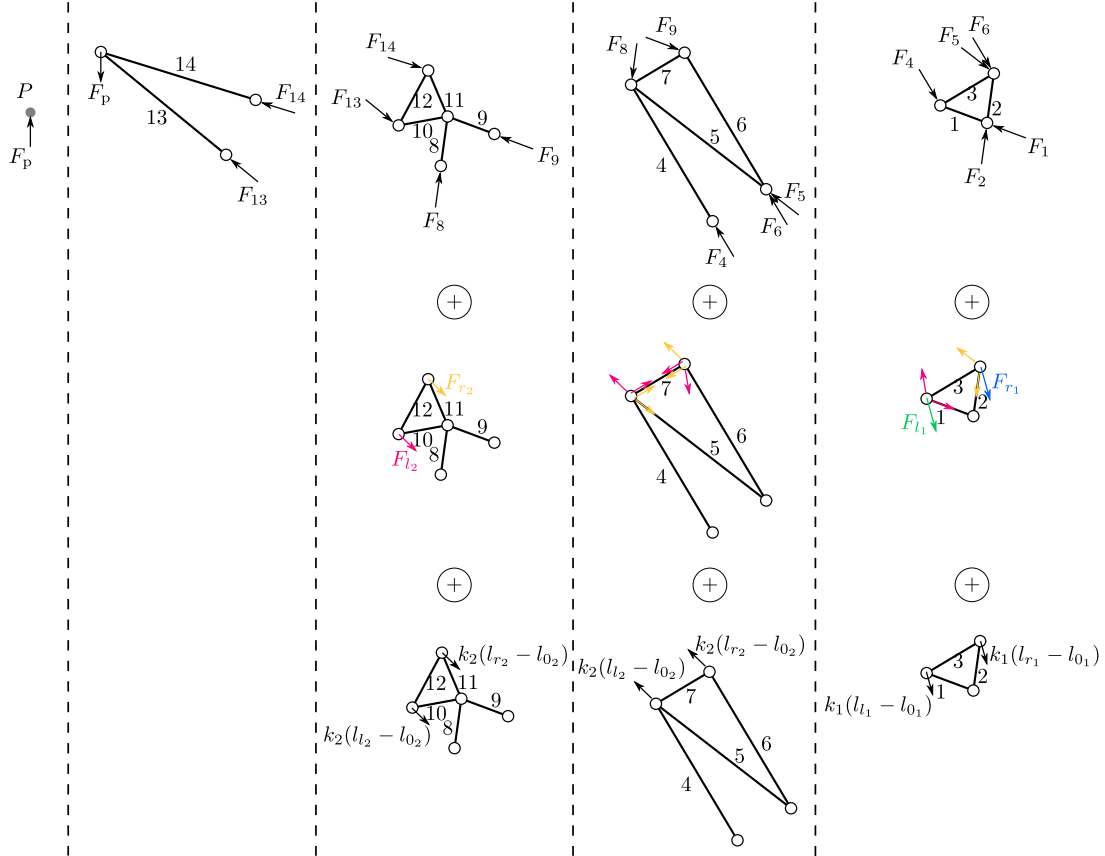


Figure 5.11 – Reaction forces at the ends of the bars.

There are 14 bars in the 2-R manipulator as shown in Fig 5.9a. They are all designed exactly like those in the 2-X manipulator in Section 5.4.3. The reaction forces at the ends of the bars due to the contacting bars, actuating cables, and springs are shown in Fig. 5.11. The expressions for forces in the bars are presented in Eqs. (5.28) and (5.29). Unlike in the case of 2-X manipulator, these coefficients involve only two varying angles (α_1, α_2) and three constant angles ($\beta_0, \beta_1, \beta_2$) in the offsets and joints (shown in Fig. 5.9a).

The forces due to payload, cables, and springs have the same bounds as in Eq. (5.22). On the other hand, the force coefficients belong to just two categories (I, IV) for this manipulator as presented in Table 5.3, and their bounds can be calculated as detailed in Section 5.4.3 and Appendix B. Finally, the bounds of forces in the bars can be overestimated, and their cross-section radii and masses can be computed in the same manner as illustrated for the 2-X manipulator. In this process, the symmetry of the manipulator is maintained about the configuration $(\alpha_1, \alpha_2) = (0, 0)$, by choosing identical radii for the bars (1, 2), (4, 6), (8, 9), (11, 12), (13, 14).

$$\left\{ \begin{array}{l}
 F_{14} = \Omega_p^{14} F_p \\
 F_{13} = \Omega_p^{13} F_p \\
 F_{12} = \Omega_{14}^{12} F_{14} + \Omega_{Fk_{r_2}}^{12} (F_{r_2} + k_2(l_{r_2} - l_{0_2})) \\
 F_{11} = \Omega_{14}^{11} F_{14} + \Omega_{Fk_{r_2}}^{11} (F_{r_2} + k_2(l_{r_2} - l_{0_2})) \\
 F_{10} = \Omega_{13}^{10} F_{13} + \Omega_{Fk_{l_2}}^{10} (F_{l_2} + k_2(l_{l_2} - l_{0_2})) \\
 F_9 = \Omega_{11}^9 F_{11} + \Omega_{10}^9 F_{10} \\
 F_8 = \Omega_{11}^8 F_{11} + \Omega_{10}^8 F_{10} \\
 F_7 = \Omega_9^7 F_9 + \Omega_{F_{l_2}}^7 F_{l_2} + \Omega_{F_{r_2}}^7 F_{r_2} + \Omega_{k_{r_2}}^7 k_2(l_{r_2} - l_{0_2}) \\
 F_6 = \Omega_9^6 F_9 + \Omega_{F_{l_2}}^6 F_{l_2} + \Omega_{Fk_{r_2}}^6 (F_{r_2} + k_2(l_{r_2} - l_{0_2})) \\
 F_5 = \Omega_8^5 F_8 + \Omega_7^5 F_7 + \Omega_{F_{l_2}}^5 F_{l_2} + \Omega_{F_{r_2}}^5 F_{r_2} + \Omega_{k_{l_2}}^5 k_2(l_{l_2} - l_{0_2}) \\
 F_4 = \Omega_8^4 F_8 + \Omega_7^4 F_7 + \Omega_{F_{l_2}}^4 F_{l_2} + \Omega_{F_{r_2}}^4 F_{r_2} + \Omega_{k_{l_2}}^4 k_2(l_{l_2} - l_{0_2}) \\
 F_3 = \Omega_6^3 F_6 + \Omega_5^3 F_5 + \Omega_{F_{r_2}}^3 F_{r_2} + \Omega_{Fk_{r_1}}^3 (F_{r_1} + k_1(l_{r_1} - l_{0_1})) \\
 F_2 = \Omega_6^2 F_6 + \Omega_5^2 F_5 + \Omega_{F_{r_2}}^2 F_{r_2} + \Omega_{Fk_{r_1}}^2 (F_{r_1} + k_1(l_{r_1} - l_{0_1})) \\
 F_1 = \Omega_4^1 F_4 + \Omega_{F_{l_2}}^1 F_{l_2} + \Omega_{Fk_{l_1}}^1 (F_{l_1} + k_1(l_{l_1} - l_{0_1}))
 \end{array} \right. \quad (5.28)$$

$$\left\{ \begin{array}{l}
 \Omega_p^{14} = \csc(2\beta_2) \cos(\beta_2 + \alpha_1 + \alpha_2); \Omega_p^{13} = \csc(2\beta_2) \cos(\beta_2 - \alpha_1 - \alpha_2); \\
 \Omega_{14}^{12} = -\sec(\beta_0) \cos(\beta_0 - \beta_2); \Omega_{Fk_{r_2}}^{12} = -\sec(\beta_2) \sin(\beta_0 - (\alpha_2/2)); \\
 \Omega_{14}^{11} = \sec(\beta_0) \sec(\beta_2); \Omega_{Fk_{r_2}}^{11} = \sec(\beta_0) \cos(\alpha_2/2); \\
 \Omega_{13}^{10} = \sec(\beta_0) \sin(\beta_2); \Omega_{Fk_{l_2}}^{10} = \sec(\beta_0) \cos(\alpha_2/2); \\
 \Omega_{11}^9 = \csc(2\beta_0) \sin(\alpha_2); \Omega_{10}^9 = \csc(2\beta_0) \sin(2\beta_0 + \alpha_2); \\
 \Omega_{11}^8 = \csc(2\beta_0) \sin(2\beta_0 - \alpha_2); \Omega_{10}^8 = -\csc(2\beta_0) \sin(\alpha_2); \\
 \Omega_9^7 = -\sin(\beta_0); \Omega_{F_{l_2}}^7 = 1 + \cos(\beta_1); \Omega_{F_{r_2}}^7 = 1 + \sin(\alpha_2/2); \Omega_{k_{r_2}}^7 = \sin(\alpha_2/2); \\
 \Omega_9^6 = \cos(\beta_0); \Omega_{F_{l_2}}^6 = \sin(\beta_1); \Omega_{Fk_{r_2}}^6 = -\cos(\alpha_2/2); \\
 \Omega_8^5 = -\sec(\beta_1) \sin(\beta_0); \Omega_7^5 = -\sec(\beta_1); \Omega_{F_{l_2}}^5 = -\sec(\beta_1) (-1 + \sin(\alpha_2/2)); \\
 \Omega_{F_{r_2}}^5 = 1 + \sec(\beta_1); \Omega_{k_{l_2}}^5 = -\sec(\beta_1) \sin(\alpha_2/2); \\
 \Omega_8^4 = \cos(\beta_0) + \sin(\beta_0) \tan(\beta_1); \Omega_7^4 = \tan(\beta_1); \\
 \Omega_{F_{l_2}}^4 = -\cos(\beta_1 + (\alpha_2/2)) \sec(\beta_1) - \tan(\beta_1); \\
 \Omega_{F_{r_2}}^4 = -\tan(\beta_1); \Omega_{k_{l_2}}^4 = -\sec(\beta_1) \cos(\beta_1 + (\alpha_2/2)); \\
 \Omega_6^3 = -\tan(\beta_0); \Omega_5^3 = -\cos(\beta_1) - \sin(\beta_1) \tan(\beta_0); \Omega_{F_{r_2}}^3 = \sec(\beta_0) \cos(\beta_0 - \beta_1); \\
 \Omega_{Fk_{r_1}}^3 = -\sec(\beta_0) \sin(\beta_0 - \alpha_1/2); \\
 \Omega_6^2 = -\sec(\beta_0); \Omega_5^2 = \sec(\beta_0) \sin(\beta_1); \Omega_{F_{r_2}}^2 = 1 - \sec(\beta_0) \sin(\beta_1); \\
 \Omega_{Fk_{r_1}}^2 = \sec(\beta_0) \cos(\alpha_1/2); \\
 \Omega_4^1 = \sec(\beta_0); \Omega_{F_{l_2}}^1 = 1 - \sec(\beta_0) \sin(\beta_1); \Omega_{Fk_{l_1}}^1 = \sec(\beta_0) \cos(\alpha_1/2);
 \end{array} \right. \quad (5.29)$$

Table 5.3 – Classification of the coefficients in Eq. (5.29) and computation of their bounds.

Category	Nature	Coefficients	Minimum	Maximum
I	Constant	$\Omega_{14}^{12}, \Omega_{14}^{11}, \Omega_{13}^{10}, \Omega_9^7, \Omega_{F_{l_2}}^7,$ $\Omega_9^6, \Omega_{F_{l_2}}^6, \Omega_8^5, \Omega_7^5, \Omega_{F_{r_2}}^5,$ $\Omega_8^4, \Omega_7^4, \Omega_{F_{r_2}}^4, \Omega_6^3, \Omega_5^3,$ $\Omega_{F_{r_2}}^3, \Omega_6^2, \Omega_5^2, \Omega_{F_{r_2}}^2, \Omega_4^1, \Omega_{F_{l_2}}^1$	Value of the constant	
IV	Possible extrema	$\Omega_p^{14}, \Omega_p^{13}, \Omega_{Fk_{r_2}}^{12}, \Omega_{Fk_{l_2}}^{10},$ $\Omega_{11}^9, \Omega_{10}^9, \Omega_{11}^8, \Omega_{10}^8, \Omega_{F_{r_2}}^7,$ $\Omega_{k_{r_2}}^7, \Omega_{Fk_{r_2}}^6, \Omega_{F_{l_2}}^5, \Omega_{k_{l_2}}^5, \Omega_{F_{l_2}}^4,$ $\Omega_{k_{l_2}}^4, \Omega_{Fk_{r_1}}^3, \Omega_{Fk_{r_1}}^2, \Omega_{Fk_{l_1}}^1$	Evaluate at stationary points, bounds; choose the minimum and maximum from them.	

5.5.4 Static model of 2-R manipulator

Following the same method as detailed in Section 3.5.1, the static equilibrium equations for the 2-R manipulator are also obtained in the form ($G_i = \Gamma_i$), $i = 1, 2$, where:

$$\begin{cases} G_1 = C_{1r} \sin \alpha_1 + C'_{1r} \sin(\alpha_1/2) - C_{3r} \sin(\alpha_1 + \alpha_2) \\ G_2 = C_{2r} \sin \alpha_1 + C'_{2r} \sin(\alpha_2/2) - C_{3r} \sin(\alpha_1 + \alpha_2) \\ \Gamma_1 = F_{l_1} (r \cos(\alpha_1/2) + h \sin(\alpha_1/2)) - F_{r_1} (r \cos(\alpha_1/2) - h \sin(\alpha_1/2)) \\ \Gamma_2 = F_{l_2} (r \cos(\alpha_2/2) + h \sin(\alpha_2/2)) - F_{r_2} (r \cos(\alpha_2/2) - h \sin(\alpha_2/2)) \end{cases} \quad (5.30)$$

with

$$\begin{cases} C_{1r} = -\frac{1}{2}ag(4m_{10} + 2m_{12} + 4m_{13} + 2m_4 + m_5 + 2m_7 + 4m_8 + 4m_{k_2} + 2m_p) \\ \quad -gh(m_1 + 4m_{10} + 2m_{12} + 4m_{13} + m_3 + 2m_4 + m_5 + m_7 + 3m_8 + m_{k_1} + 3m_{k_2} + 2m_p) \\ \quad + 2k_1 (r^2 - h^2) \\ C'_{1r} = 2hk_1 l_{0_1} \\ C_{2r} = 2k_2 (r^2 - h^2) \\ C'_{2r} = 2hk_2 l_{0_2} \\ C_{3r} = g(a(m_{13} + m_p) + h(m_{10} + m_{12} + 2m_{13} + m_{k_2} + m_p)) \end{cases} \quad (5.31)$$

The masses ($m_2, m_6, m_9, m_{11}, m_{14}$) have been replaced by ($m_1, m_4, m_8, m_{10}, m_{13}$) due to symmetry (see Fig. 5.9a and Section 5.5.3) of the manipulator. Similar to the 2-X manipulator, it can be shown that the coefficient of F_{l_i} (resp. F_{r_i}) is positive (resp. negative) in Eq. (5.30). Thus, the condition of equilibrium (α_1, α_2) can be satisfied only when $G_i \in [\Gamma_i, \bar{\Gamma}_i]$ for $i = 1, 2$.

The stiffness matrix can be computed for the 2-R manipulator similarly as illustrated for the 2-X manipulator in Section 3.5.1. Upon eliminating the forces (F_{l_1}, F_{l_2}) from the equilibrium equations, one obtains the stiffness matrix in terms of the redundant forces as:

$$\mathbf{K}_\alpha^{\text{rr}} = \begin{pmatrix} K_{11}^{\text{rr}} & K_{12} \\ K_{12} & K_{22}^{\text{rr}} \end{pmatrix} \text{ with } K_{11}^{\text{rr}} = \frac{K_{11}^{\text{rr}'}}{2(rc_1 + hs_1)} \text{ and } K_{22}^{\text{rr}} = \frac{K_{22}^{\text{rr}'}}{2(rc_2 + hs_2)} \quad (5.32)$$

where

$$\begin{cases} K_{11}^{\text{rr}'} = 2C_{1r} (c_1^3 r - hs_1^3) + C_{3r} \{h(c_1 s_{12} - 2c_{12} s_1) + r(-2c_1 c_{12} - s_1 s_{12})\} + C'_{1r} r - 2hrF_{r_1} \\ K_{22}^{\text{rr}'} = C_{3r} \{h(c_2 s_{12} - 2c_{12} s_2) + r(-2c_{12} c_2 - s_{12} s_2)\} + C_{2r} (2c_2^3 r - 2hs_2^3) + C'_{2r} r - 2hrF_{r_2} \\ K_{12} = -C_{3r} c_{12} \end{cases} \quad (5.33)$$

in which $c_1 = \cos(\alpha_1/2)$, $s_1 = \sin(\alpha_1/2)$, $c_2 = \cos(\alpha_2/2)$, $s_2 = \sin(\alpha_2/2)$, $c_{12} = \cos(\alpha_1 + \alpha_2)$, $s_{12} = \sin(\alpha_1 + \alpha_2)$. The coefficient of F_{r_i} in the stiffness matrix is found to be $\frac{-2hr}{2(rc_i + hs_i)}$, for $i = 1, 2$. It can be shown that this coefficient is negative for all values of (r, h) when α_i is within limits due to cable actuation, i.e., $\in]-\bar{\alpha}_{\text{max}}, \bar{\alpha}_{\text{max}}[$ as defined in Eq. (5.23). This indicates that unlike in the 2-X manipulator, the stiffness decreases with the increase in actuation forces for the 2-R manipulator. This result is consistent with the one obtained for a single R-joint in Section 2.5.1. In this case, the matrix corresponding to maximum stiffness must be obtained by setting two

actuation forces to their minimum bound of F_{\min} . For instance, from Eq. (5.32),(5.33), one obtains $\overline{\mathbf{K}}_{\alpha}^{\text{rr}} = \mathbf{K}_{\alpha}^{\text{rr}}(F_{r_1} = F_{\min}, F_{r_2} = F_{\min})$. Similarly, the other stiffness matrices ($\overline{\mathbf{K}}_{\alpha}^{\text{rl}}, \overline{\mathbf{K}}_{\alpha}^{\text{lr}}, \overline{\mathbf{K}}_{\alpha}^{\text{ll}}$) can also be obtained by setting the redundant forces to F_{\min} .

As in the case of the 2-X manipulator, the SWFJ for this manipulator is formed by all (α_1, α_2) configurations where the conditions of wrench-feasibility and stability are satisfied. Their mapping onto the task space is conducted using the kinematic model defined in the next section.

5.5.5 Kinematic model of 2-R manipulator

From Fig. 5.1b, the direct kinematics of 2-R manipulator can be expressed as:

$$\begin{cases} x = -(2h + a) \sin(\alpha_1) - (h + a) \sin(\alpha_1 + \alpha_2) \\ y = h + (2h + a) \cos(\alpha_1) + (h + a) \cos(\alpha_1 + \alpha_2) \end{cases} \quad (5.34)$$

Note that the kinematic model is independent of r .

It is well-known that the singularity of the 2-R manipulator occurs when $\alpha_2 = 0$ (fully stretched configuration) and $\alpha_2 = \pm\pi$ (folded back configuration). Recalling the joint limits $\alpha_i \in]-\frac{\pi}{2}, \frac{\pi}{2}[$, only the condition $\alpha_2 = 0$ is relevant for constructing the SWFW for this manipulator.

5.5.6 Stable wrench-feasible workspace of 2-R manipulator with a numerical example

The computation of SWFW for the 2-R manipulator follows the method described in Chapter 3. Notably, the discretization of α_1 and α_2 is performed within the joint limits of R-joint derived in Section 5.5.1.

As a numerical illustration, the following design is considered: $r = 0.1$ m, $h = 0.1732$ m, $a = 0.5$ m. These parameters ensure that the height and width for the joints and offsets of the 2-R manipulator are the same as those of the 2-X manipulator considered in Section 5.4.4. The other design parameters are assumed to be: $\sigma_{\alpha} = (9/10)$, $k_1 = 5000$ N/m, $\sigma_{k_1} = 0.7$, $k_2 = 2000$ N/m, $\sigma_{k_2} = 0.5$, $F_{\max} = 200$ N. The springs chosen are much stiffer than in the case of the 2-X manipulator, as those springs could not stabilize the 2-R manipulator at $(\alpha_1, \alpha_2) = (0, 0)$, in the absence of actuation forces. The main steps involved in computing the SWFJ and SWFW are listed in the following:

- **Section 4.2:** The computation of feasible design space for the springs of R-joint was performed in the same manner as illustrated for the X-joint in Section 5.4.4. The dependent parameters of spring 1 ($k_1 = 5000$ N/m, $\sigma_{k_1} = 0.7$), are: $d = 5.7$ mm, $D = 36.2069$ mm, $N_a = 45.3131$, $l_{0_1} = 0.3250$ m, $l_{\max_1} = 0.3644$ m, $m_{k_1} = 1.1008$ kg. The dependent parameters of spring 2 ($k_2 = 3000$ N/m, $\sigma_{k_2} = 0.5$) are: $d = 5.3$ mm, $D = 45.4872$ mm, $N_a = 42.7045$, $l_{0_2} = 0.3120$ m, $l_{\max_1} = 0.3728$ m, $m_{k_2} = 1.1311$ kg.
- **Section 4.1:** While $\sigma_{\alpha} = (9/10)$, $\overline{\alpha}_{\max} = 0.9425$ rad. From the free length of the springs, the actual maximum limit of movement for the two joints are found to be $\alpha_{\max_1} = 0.1976$ rad, $\alpha_{\max_2} = 0.3050$ rad, respectively, which shows that both springs belong to the set χ_a in the spring design space (i.e., case A in Fig. 5.4a).
- **Section 4.3:** The bounds estimated for the axial forces in the bars, their cross-section radii, and masses are presented in Table 5.4. The total moving mass is computed to be 5.5444 kg, with maximum contribution from the springs.

Table 5.4 – 2-R manipulator: Range of estimated buckling loads and the resulting safe cross-section radii for the bars along with their masses.

Bar index j	Estimated load [N]	Cross-section radius [mm]		Mass [kg] m_j
		Computed ($r_{b_j}^*$)	Corrected (r_{b_j})	
14	[-30.62, 65.65]	2.37	5.00	0.1081
13	[-30.62, 65.65]	2.37		
12	[-282.37, 23.34]	1.15	5.00	0.0424
11	[-34.67, 445.61]	2.39	5.00	0.0424
10	[-34.67, 445.61]	2.39		
9	[-193.60, 656.81]	2.64	5.00	0.0424
8	[-193.60, 656.81]	2.64		
7	[-346.87, 619.92]	2.60	5.00	0.0424
5	[-2603.15, 2603.15]	6.11	6.11	0.1704
6	[-489.19, 754.51]	4.32	6.07	0.1561
4	[-2716.72, 2939.62]	6.07		
3	[-3065.23, 2826.14]	3.80	5.00	0.0424
2	[-3370.15, 4120.78]	4.17	5.00	0.0424
1	[-3151.42, 3853.07]	4.11		
Total bar mass				1.0805
Mass of springs ($2(m_{k_1} + m_{k_2})$)				4.4639
Total moving mass of the manipulator				5.5444

- **Sections 4.4, 4.5, 4.6:** Using the static and kinematic models of the manipulator, its SWFJ and SWFW are constructed as shown in Figs. 5.12a and 5.12b, respectively. The opaque and transparent styles for the boundaries have the same meaning as described for the 2-X manipulator in Section 5.4.4.

From Fig. 5.12a, it is observed that the joint limits are much stronger for the 2-R manipulator when compared to its counterpart in Fig. 5.8a. This is mainly due to the geometry of the R-joint and the actuation scheme with cables, which limit the maximum amplitude of joint movement to $\frac{\pi}{2}$ (see Eq. (5.23)). Consequently, the 2-R manipulator has a much smaller SWFJ and SWFW than the 2-X manipulator. Therefore, the two maximally inscribed disks (radius = 0.0086 m) are much smaller than the ones found for the 2-X manipulator (radius = 0.0736 m) in Fig. 5.8b. The maximum vertical reach of the manipulator is nearly 200 times the radius of the maximal inscribed disk. Thus, the design is a very poor one. For this design, it takes about 7 ms (averaged over 100 runs) to compute the SWFW, which is over five times faster than that of the 2-X manipulator.

From Fig. 5.12, it is also observed that the stability boundary is very close to the home configuration $(\alpha_1, \alpha_2) = (0, 0)$, indicating that it is difficult to stabilize the 2-R manipulator, even with springs of large stiffness, unlike its counterpart.

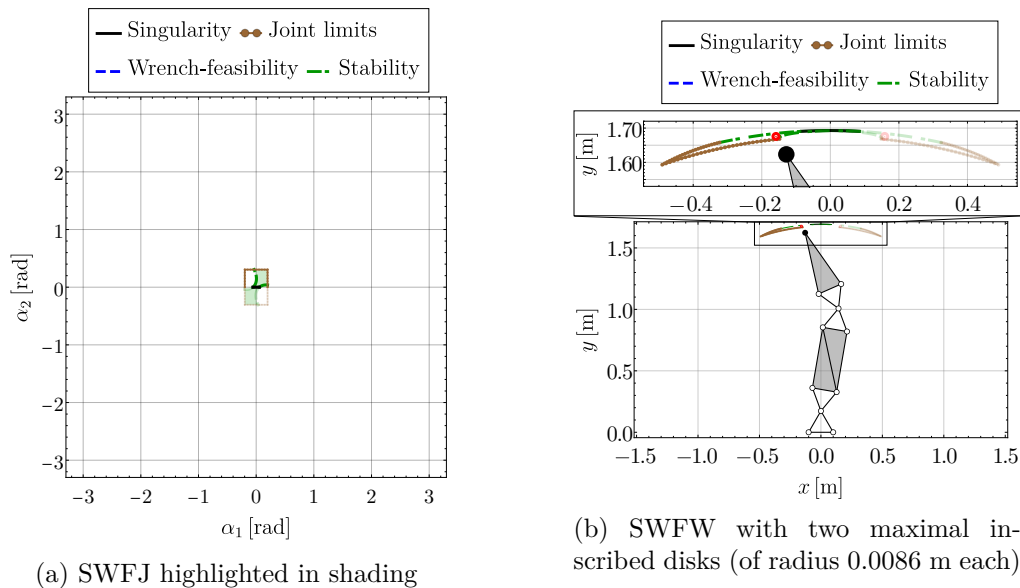


Figure 5.12 – The stable wrench-feasible joint space (SWFJ) and stable wrench-feasible workspace (SWFW) for the 2-R manipulator with: $r = 0.1$ m, $h = 0.1732$ m, $a = 0.5$ m, $\sigma_\alpha = (9/10)$, $k_1 = 5000$ N/m, $l_{0_1} = 0.3250$ m, $m_{k_1} = 1.1008$ kg, $k_2 = 2000$ N/m, $l_{0_2} = 0.3120$ m, $m_{k_2} = 1.1311$ kg, $F_{\max} = 200$ N/m. In the joint space (α_1, α_2) , the curves lying in the region $(\alpha_2 > 0)$ are shown in opaque style while those in the region $(\alpha_2 < 0)$ are shown in transparent style. The images of these curves in the task space are also shown in the same style for the sake of clarity.

5.6 Conclusions

Two planar cable-driven tensegrity-inspired manipulators composed of two anti-parallelogram (X) joints and two revolute (R) joints, respectively, were studied in this work. These joints are remotely actuated with two cables, each, by motors attached to the base. The joints also have springs on the two sides to stabilize the manipulator while it carries a payload at the end-effector in the presence of gravity. Globally, a method to compute the stable wrench-feasible workspace of these manipulators, which accounts for the mechanical feasibility of its constituent elements, was presented.

A systematic study of the joint limits due to the geometry and cable actuation was presented. The conditions responsible for the mechanical feasibility of the springs, namely, allowable shear stress, recommended spring index, standard wire diameters, minimum number of active coils, and safe helix angle, were used to construct the feasible design space for the springs. Two parameters are needed to access all the springs inside this space. The interdependence of the actual joint limits and the free length of the springs were explored on a case-by-case basis, covering all the possibilities exhaustively.

A method for finding safe cross-sections of the bars in these manipulators was proposed. Since all the bars in tensegrity-inspired manipulators are only loaded axially, a geometric approach has been used to compute the axial forces in the bars due to the payload, cable actuation, and springs. Using the limits on the movement of each joint and the range of forces achievable with

the cables and springs, upper limits for compressive loads in the bars were obtained. These limits were used to determine safe cross-sections for the bars. Further, it was ensured that the mass symmetry of the manipulators is preserved and the sections are large enough to avoid fabrication difficulties.

Subsequently, the static and models of the manipulators were formulated. It was found that contrary to the 2-X manipulator, the 2-R manipulator negative correlation between actuation forces and stiffness. By imposing realistic bounds on the cable forces, the stable wrench-feasible joint space (SWFJ) and stable wrench-feasible workspace (SWFW) were computed for the two manipulators. In order to quantify the size of SWFW, maximal disk(s) were inscribed inside it, and its radius was evaluated.

Numerical examples of 2-X and 2-R manipulators were presented, such that they have similar bar lengths and cable forces. The springs were chosen to ensure stability at the vertically straight configuration for both manipulators in the absence of actuation forces. While the two manipulators have a comparable moving mass, the size (as evaluated by the radius of the inscribed disk) of the SWFW for the 2-X manipulator is nearly 10 times larger than that of the 2-R manipulator. However, for both manipulators, the radius of the inscribed disk in SWFW itself is much smaller (0.005-0.05 times) compared to their maximum vertical reach. Due to a higher complexity of the model of the 2-X manipulator, the time taken to compute its SWFW with the inscribed disk (43 ms) is about six times that of the 2-R manipulator (7 ms). Nevertheless, the time taken is of the order of milliseconds for both manipulators, making the proposed computation scheme suitable for exploring several designs in an optimization framework.

It is noted that the observations reported on workspace sizing are specific to the examples considered and do not extend to all the designs of these manipulators. A more conclusive study must find *good* designs for the two tensegrity-inspired manipulators and study their properties. This problem will be addressed in the next chapter through design optimization of the 2-X and 2-R manipulators for the same inscribed disk in SWFW.

The overall design process illustrated for the two manipulators is generic and is, in principle, applicable to other architectures of planar tensegrity-inspired manipulators. It can also be adapted to different actuation schemes of the cables and different placements of the manipulator (e.g., ceiling-mounted systems like the Delta robot) by appropriately adjusting the direction of gravity.

OPTIMAL DESIGN AND COMPARISON OF 2-X AND 2-R MANIPULATORS

Abstract

This chapter conducts design optimization and comparison of two tensegrity-inspired manipulators composed of two anti-parallelogram (X) joints and two revolute (R) joints, respectively. These manipulators are equipped with springs and are actuated remotely with four cables each. Using the computation scheme developed in the previous chapter, we design the 2-X and 2-R manipulators to carry a given point mass payload over a disk of a specified radius while minimizing their maximal actuation forces, moving masses, and sizes. We present the Pareto optimal fronts for the two manipulators and compare several designs from them. Finally, we study the variation of the chosen objectives for different payload and disk radius specifications for the two manipulators to determine which one is better under what circumstances.

Contents

6.1	Introduction	146
6.2	Template of the SWFJ and SWFW for the two manipulators	147
6.3	Design variables and their bounds	148
6.4	Workspace optimization for a given payload	150
6.4.1	Problem formulation	150
6.4.2	Genetic algorithm based solver: NSGA-II	150
6.4.3	Results and discussion	151
6.5	Force, mass, and size optimization for a given payload and SWFW disk	152
6.5.1	Formulation and resolution of the design problem	152
6.5.2	Solution method and the Pareto optimal front	153
6.5.3	Extremal designs on the Pareto front	154
6.5.4	Exploration of the Pareto front	160
6.6	Effect of changing the payload and desired SWFW disk radius specifications	164
6.7	Possible applications and extensions	166
6.8	Conclusions	167

6.1 Introduction

Design optimization of robot manipulators has been attractive to the research community for nearly four decades [Li+23]. The development of new optimization techniques and advances in computational capabilities permit researchers to solve problems that were once intractable and conceive new ones that are more challenging. This chapter aims to perform the dimensional design of tensegrity-inspired manipulators for a prescribed workspace similar to conventional serial and parallel manipulators [GG91].

The current literature on the design of tensegrity-inspired manipulators is scanty. A piping inspection robot with 4-SPS-U tensegrity joints has been considered in [VCH21]. Each joint consists of a universal coupling between the base and top platforms and contains four springs on the sides, with a cable passing through each for actuation. A design optimization problem has been solved by considering the height of the joint and the free length of the springs as optimization variables to maximize the stiffness of the joint at the zero orientation (i.e., when the base and top platforms are parallel to each other). All the other parameters, such as the joint width and stiffness of the springs, were determined a priori based on other practical considerations. It must be noted that gravity effects were neglected in their work.

Another study concerns the design of tensegrity-based manipulators respecting the remote center of motion constraint for a medical application [BVR20]. Two variants of the X-shaped tensegrity mechanism inspired by the Snelson’s tensegrity structure (see [Sne65]) are considered. The first one contains two actuated crossed bars and springs on all four sides for stability. The second one, in contrast, has crossed bars of fixed length, springs on the top and bottom for stability, and two cables on the sides for actuation. In design approach 1, the first and second joints are stacked in series to form a tensegrity-based manipulator. On the other hand, in design approach 2, two of the second joints are stacked in series to form a different tensegrity-based manipulator. The orientation limits and distance from the remote center of motion are studied for the two manipulators for different ranges of movements of the actuators. This study helps select a suitable actuator for the two manipulators. But, there is still scope for optimization, considering the bar lengths (for the second joint) and the free length of the springs. This problem has been addressed in [Don+21], where the authors perform optimization of the first manipulator proposed in [BVR20] for compactness. They consider the lengths of the bars, the free length of springs, and the displacement bounds of the actuators as design variables to find the optimal manipulator design that reaches a prescribed workspace. However, we note that both of these works neglect the gravity effects and use actuators for fixing the position of some nodes. Consequently, the potential energy of the manipulator is only due to the elasticity of the springs (see Section 2.3, Eq. (2.7)). Further, since they use identical springs at all locations, the spring stiffness factors out in the expression of potential energy and only scales the stiffness of the manipulator without any influence on the equilibrium equations. Thus, the spring stiffness was not included as a design variable in [BVR20],[Don+21].

In contrast, this chapter conducts design optimization of remotely actuated tensegrity-inspired 2-X and 2-R manipulators shown in Fig. 5.1 to reach a prescribed workspace with a given point mass payload. Unlike in previous studies, gravity plays a significant role in the static model of these manipulators, making the design more challenging. The actuation scheme with four cables considered in the previous chapter is used in this study as well. The objectives of the design problem are to minimize the required actuation forces (consequently, the motor

size), moving mass, and size. A similar study has been conducted for single-DoF X and R joints equipped with zero free length springs and actuated antagonistically by two cables on the sides, in [MW21]. However, an extension of that study to 2-DoF manipulators is accompanied by several challenges. Primarily, realizing the zero free length assumption for the springs in joints that are not fixed to the ground is extremely difficult. The other design challenges have been addressed in Chapter 5.

The previous chapter presented a computational scheme that accounts for all the design issues and computes the SWFW. This chapter utilizes that scheme to perform design optimization of the 2-X and 2-R manipulators. The main contributions of this part may be summarized as follows:

- Two tensegrity-inspired manipulators with two anti-parallelogram and revolute joints, respectively, are optimized for their maximal actuation forces, mass, and size for a specified payload and workspace in the form of a disk.
- The Pareto optimal fronts are obtained using a genetic algorithm based optimizer for the two manipulators, and optimal designs are compared from them.
- Several payload and workspace disk specifications are considered to characterize the two manipulators in terms of (moving mass/payload) and (size/disk radius) metrics.

The rest of this chapter is organized as follows: a template of the SWFJ and SWFW for the two manipulators is presented in Section 6.2. The design variables and their bounds are defined for the two manipulators in Section 6.3. The maximum inscribed disk radii are obtained for different payloads in Section 6.4. The force, mass, and size optimization problem is posed and solved in Section 6.5. The same problem is solved for different payload and disk radius specifications in Section 6.6. Finally, the conclusions of this work are presented in Section 6.8.

6.2 Template of the SWFJ and SWFW for the two manipulators

A template of SWFJ and SWFW applicable to the two manipulators are shown in Figs. 6.1a (left) and 6.1b (right), respectively. From Fig. 6.1a, it is evident that there is a symmetry in its form, i.e., when (α_1, α_2) is a part of the SWFJ, $(-\alpha_1, -\alpha_2)$ is also part of the SWFJ. This feature is a consequence of the symmetry in the architectures of the two manipulators, their placement w.r.t. gravity, and their actuation schemes, about the home configuration $(\alpha_1, \alpha_2) = (0, 0)$.

Upon mapping the boundary of SWFJ and the singularities from the joint space onto the task space using the kinematic model, a template for SWFW is obtained, as shown in Fig. 6.1b. The SWFW is formed by two overlapping regions that are symmetric about the y -axis. Indeed, these are the images of the symmetric halves of the SWFJ (opaque and transparent styles) on either side of the singularity curve. Since the SWFJ is a single connected component, the manipulator can move between the two regions of the SWFW by changing its posture at a singular configuration, e.g., at $(\alpha_1, \alpha_2) = (0, 0)$, which is also the home configuration. This connectivity between the two parts of the SWFW is a desirable feature and will be guaranteed as long as the home cum singular configuration $(\alpha_1, \alpha_2) = (0, 0)$ remains part of the SWFJ.

The size of the SWFW is quantified by a maximal inscribed disk (\mathcal{D}) in one half of the workspace as shown in Fig. 6.1. The radius of this disk, denoted by r_d , is used as a measure of the size of the SWFW for these manipulators. This maximal inscribed disk will be referred as the ‘‘SWFW disk’’ in the following.

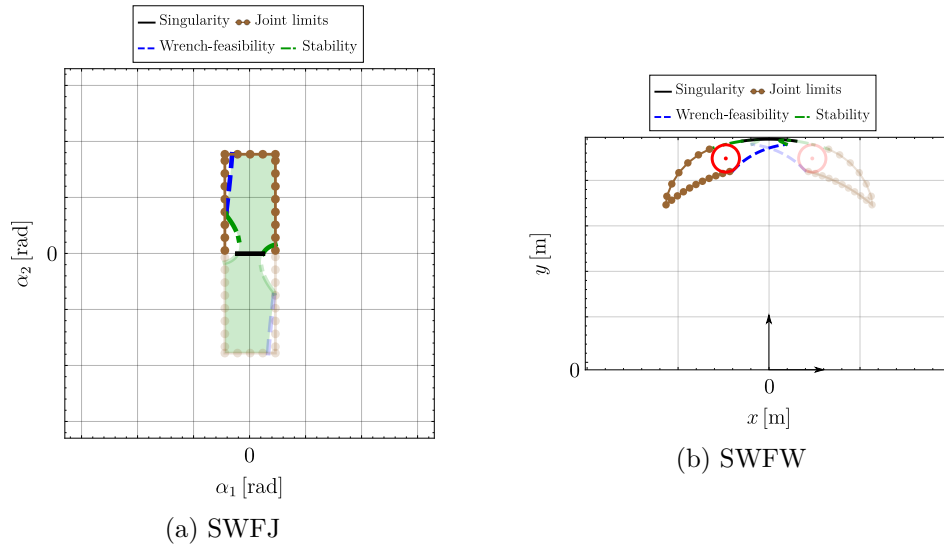


Figure 6.1 – Template of the stable wrench-feasible joint space (SWFJ) and stable-wrench feasible workspace (SWFW) for the 2-X and 2-R manipulators. In SWFJ (shaded portion), the curves lying above the singularity curve are shown in opaque style while those below are shown in transparent style. The images of these curves in the task space are also shown in the same style for the sake of clarity.

The eventual goal of this study is to conduct design optimization of the 2-X and 2-R manipulators, such that they contain the same SWFW disk ($\mathcal{D}(r_d)$) while carrying a point payload of mass m_p . In this regard, all the parameters that influence the SWFW of the two manipulators are identified and listed as design variables in the following section.

6.3 Design variables and their bounds

Table 6.1 – Design variables and their bounds for the 2-X and 2-R manipulators.

No.	2-X manipulator		2-R manipulator	
	Variable	Bounds	Variable	Bounds
1	b [m]	[0.05,1]	r [m]	[0.025,0.5]
2	$\lambda(l/b)$]1,10]	$\mu(h/r)$]0,5]
3	$\epsilon(a/b)$]0,10]	$\epsilon(a/(2r))$]0,10]
4	σ_α]0,1[σ_α]0,1[
5	k_1 [N/m]	[0,10000]	k_1 [N/m]	[0,10000]
6	σ_{k_1}	[0,1]	σ_{k_1}	[0,1]
7	k_2 [N/m]	[0,10000]	k_2 [N/m]	[0,10000]
8	σ_{k_2}	[0,1]	σ_{k_2}	[0,1]
9	F_{\max} [N]	[0,500]	F_{\max} [N]	[0,500]

A set of nine design variables $\mathbf{u} = [u_1, \dots, u_9]^\top$ have been presented for the two manipulators

in Table 6.1. The first three define the geometry of the manipulators; the next one specifies the safe joint limits; the next four define the springs in the two joints; the last variable specifies the maximum force in the actuation cables. More details on these variables are presented in the following:

- **Variables 1-3 (Geometry)**: For the 2-X manipulator (resp. 2-R manipulator), all the bar lengths are defined by the variables (b, l, a) (resp. (r, h, a)). However, only the first variable, which signifies the width of the manipulator, has been used as is. The other two lengths have been embedded as ratios relative to the base. Thus, the first variable scales the entire manipulator while the other two determine the relative lengths of the bars. The limiting values for the width have been specified as $[0.05, 1]$ m for both manipulators (note that r represents half the width of the 2-R manipulator). The lower bound is necessary to overcome fabrication issues associated with small bars, while the upper bound has been set at 1 m to avoid extremely large manipulators. The lower bound for $\lambda(l/b)$ is set as 1 to respect the assembly condition for X-joint, while all other limits for the ratios are set such that the geometry space of the two manipulators is almost the same.
- **Variable 4 (Safe joint limit)**: The movement of the X-joint and R-joint are limited by the flat-singularities and force-closure singularities, as explained in Sections 5.4.1 and 5.5.1, respectively. Suppose their occurrence are marked by $\alpha_i = \pm \overline{\alpha_{\max}}$, it is a practical necessity to remain *sufficiently* distant from these limiting configurations. But, the value for this distance is not an obvious one. Hence, a fraction (σ_α) is introduced as a design variable to define safe limits for joint movement. For X- and R-joints, a safe upper bound for their movements is given by $\overline{\alpha_{\max}} = \sigma_\alpha \overline{\alpha_{\max}}$. Note that the actual upper limit (α_{\max_i}) of movement for joint i can be less than or equal to its safe limit ($\overline{\alpha_{\max}}$) depending on the free length (l_{0_i}) of the springs installed on that joint (see Section 5.4.1). From the previous chapter, it is recalled that the springs that prevent the joints from reaching their safe limits belong to set χ_a , while those which allow them to reach their safe limits belong to set χ_b . The set of all feasible springs is formed by $\chi_a \cup \chi_b$.
- **Variables 5-8 (Springs)**: Using the geometry and safe joint limits, the complete feasible space ($\chi_a \cup \chi_b$) for the springs can be defined, as explained in Section 5.4.2. The choice of spring for each joint i depends on the stiffness (k_i) and the spring selection parameter (σ_{k_i}). Using (k_i, σ_{k_i}) , all the other parameters of the spring: wire diameter (d), coil diameter (D), number of active coils (N_a), free length (l_{0_i}), and mass (m_{k_i}) can be computed. Further, based on the free length and the safe joint limit ($\overline{\alpha_{\max}}$), the maximum operating length (l_{\max_i}) of the spring can also be computed. These computations have been illustrated in the previous chapter.
- **Variable 9 (Actuation force)**: The maximum actuation force (F_{\max}) of the cables is bounded inside $[0, 500]$ N for both the manipulators. The maximum bound is less than the rupture limit of commonly available synthetic cables, e.g., VECT070LE. This variable indicates the size of the motor required to actuate the manipulator.

In addition to the above variables, the SWFW is also affected by the mass of constituent bars of the manipulators. However, the cross-section and mass of the bars are not explicitly considered as design variables. Their values are determined from the limiting condition of buckling using the data of bar lengths, springs, and joint limits (see Section 5.4.3 for more details).

The bounds in Table 6.1 define the design space for the two manipulators. The next task

is to formulate design optimization problems for the two manipulators with a constraint that they contain a specified disk inscribed inside their SWFW. However, at this point, it is not clear what disk size suits both manipulators. Moreover, it can also change depending on the mass (m_p) of the payload loaded at the end-effector. Hence, firstly, a study should be conducted on the feasible disk sizes for a given payload for the two manipulators. This analysis is carried out in the next section by posing design optimization problems to maximize the SWFW disk radius.

6.4 Workspace optimization for a given payload

In this section, the 2-X and 2-R manipulators will be designed to maximize the radius of the SWFW disk, while ensuring that the home configuration $(\alpha_1, \alpha_2) = (0, 0)$ is stable in the absence of actuation forces. The problem formulation is discussed in Section 6.4.1, the solution method in 6.4.2, and the results in Section 6.4.3.

6.4.1 Problem formulation

The optimization problem for maximizing the SWFW disk radius (r_d) while the manipulator carries a payload of mass (m_p) is posed as follows:

$$\begin{aligned} & \underset{\mathbf{u}}{\text{Maximize}} && r_d \\ & \text{subject to} && \text{Stability at } (\alpha_1, \alpha_2) = (0, 0) \text{ with no actuation forces} \\ & && u_i \in [u_i, \bar{u}_i], \quad i = 1, \dots, 9, \end{aligned} \tag{6.1}$$

where u_i refers to the i^{th} design variable listed in Table 6.1, and $[u_i, \bar{u}_i]$ its lower and upper bounds, respectively, for both 2-X and 2-R manipulators. The stability at home configuration is imposed as a constraint for two reasons. Firstly, it is to ensure that the manipulators can stand on their own safely, without falling down, even when the motors are not powered. Secondly, it is to guarantee that the manipulator can move between the two symmetric regions of the SWFW as explained in Section 6.2.

Note that the payload mass (m_p) does not appear explicitly in the above formulation. But it is an implicit parameter that affects the SWFW directly through the static model and indirectly through the cross-sections of the bars (see Section 5.4.3).

The above problem is solved using an evolutionary optimization solver, as explained in the next section.

6.4.2 Genetic algorithm based solver: NSGA-II

In the optimization problem posed in Eq. (6.1), the computation of the objective function from a given set of design variables goes through several numerical steps, as detailed in Section 5.4.4. Hence, gradient-based optimization methods cannot be used for the problem at hand. Also, it is tough for the designer to come up with an initial guess which is firstly feasible and secondly good enough. This issue is evident from the arbitrarily chosen example designs in the previous chapter, where the size of the manipulator is 20-200 times larger than the radius of the SWFW disk. Hence, a possible solution is to use evolutionary optimization algorithms,

which require neither a good initial guess nor gradient information. Additionally, they explore the design space using heuristic operations that prevent stagnation around local optima. In this work, a genetic algorithm-based multi-objective evolutionary optimization tool, namely, *NSGA-II* (see [Deb+02]), will be used. The ability of this tool to handle multiple objectives has made it attractive for design optimization of mechanisms [AB17], parallel manipulators [BCG17], and robotic grippers [Sar+09], among others.

Table 6.2 – Internal parameters of the optimization solver *NSGA-II* along with their recommended and assumed values.

Parameter	Recommended values	Assumed value
Population size	Multiple of 4	5000
Number of generations	-	3000
Probability of crossover	[0.6, 1]	0.9
Probability of mutation	(1/no. of variables)	0.11
Distribution index for crossover	[5,20]	5
Distribution index for mutation	[5,50]	20
Seed for random number generator	[0,1]	0.3

There are a total of seven internal parameters in *NSGA-II* that the user must set to initiate an optimization run. They are listed along with their assumed values in Table 6.2. Large values have been chosen for the population size and the number of generations to enable a good exploration of the design space and a reasonably good convergence to the optimal solution. The probability of mutation is set to (1/number of design variables) as recommended in [Deb+02]. Most other parameters are adopted from another design problem presented in [Mur+20] with similar validations. However, the distribution index for mutation has been decreased from 35 in [Mur+20] to 20, to increase the variety designs in subsequent generations. It has been verified through various trial runs that the results are not significantly impacted even while the parameters are changed within their prescribed bounds.

The parameters presented in Table 6.2 are used for all the design problems presented in this work for both 2-X and 2-R manipulators. It takes about 25 hours¹ for a design run of the 2-X manipulator, and about 6 hours for a design run of the 2-R manipulator.

The optimal SWFW disk radii obtained for different payloads are presented for the two manipulators in the next section.

6.4.3 Results and discussion

The problem posed in Eq. (6.1) has been solved for four different payloads $m_p = \{0, 2, 5, 10\}$ kg at the end-effector, for the 2-X and 2-R manipulators. In the resulting optimal designs², it is observed that the design variable b (resp. r), which scales the 2-X manipulator (resp. 2-R manipulator), reaches its upper bound in most of the cases. In addition, the maximal actuation force (F_{\max}) also attains its upper bound of 500 N in all the cases. This shows that the optimal

1. All the computations reported in this chapter have been performed on a computer with an Intel® Core™ i7-6700 CPU running @ 3.40GHz processor, using a C++ code parallelized with OpenMP, employing eight threads.

2. In this chapter, the term “optimal design” is not used in the strict mathematical sense as the designs obtained through heuristic optimization algorithms cannot be proved for optimality.

designs are as large as possible with maximum actuation forces to produce the largest SWFW disk, which is logical.

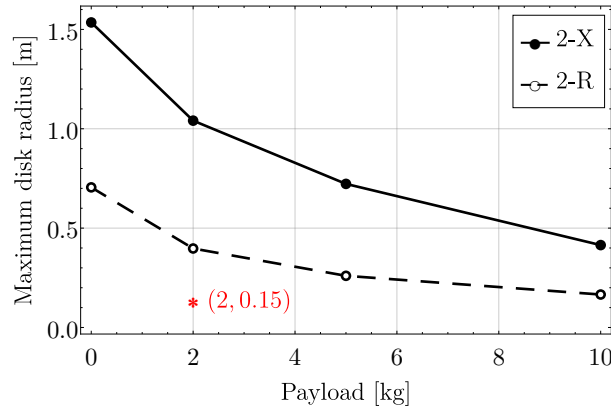


Figure 6.2 – Maximum SWFW disk radius for different payload at the end-effector.

The maximum SWFW disk radius (r_d) obtained for each payload is presented in Fig. 6.2. For both manipulators, it is found that the maximum disk radius decreases with the payload, which is logical. For all payloads, the SWFW disk radius for the 2-X manipulator is observed to be roughly two times greater than that of the 2-R manipulator. This result suggests that the 2-X manipulator should be preferred over its counterpart if the maximum SWFW disk size is the only criterion.

Additionally, the data in Fig. 6.2 can be used to find a feasible SWFW disk radius specification for a given payload, that is sufficiently far from the limiting value for both manipulators. For instance, while the end-effector carries a 2 kg payload, both manipulators can have an SWFW disk radius of 0.15 m, as highlighted in Fig. 6.2. This information will be useful for further optimizing these manipulators in terms of their actuation forces, moving masses, and sizes while fixing the same feasible payload and SWFW disk radius for them. The following section performs this optimization.

6.5 Force, mass, and size optimization for a given payload and SWFW disk

This section aims to find “good” designs for the 2-X and 2-R manipulators capable of carrying a payload of 2 kg while possessing an SWFW disk of radius 0.15 m.

6.5.1 Formulation and resolution of the design problem

Three properties have been chosen to assess and compare the global performance of a design: the maximal actuation force, total moving mass (without payload), and size of the manipulator.

Thus, a design optimization problem can be posed as follows:

$$\begin{aligned}
 & \text{Minimize } \mathbf{u} \quad \begin{cases} \text{Force: } F_{\max} \\ \text{Mass: } \sum_{j=1}^{n_b} m_j + 2(m_{k_1} + m_{k_2}) \\ \text{Size: } y(\alpha_1 = 0, \alpha_2 = 0) \end{cases} \\
 & \text{subject to} \quad \begin{cases} \text{Stability at } (\alpha_1, \alpha_2) = (0, 0) \text{ with no actuation forces} \\ \mathcal{D}(r_d) \in \text{SWFW}; \\ u_i \in [\underline{u}_i, \overline{u}_i], \quad i = 1, \dots, 9, \end{cases}
 \end{aligned} \tag{6.2}$$

where F_{\max} is the maximum actuation force, which is also a design variable listed in Table 6.1, m_j represents the mass of the j^{th} moving bar, n_b the total number of moving bars, m_{k_1}, m_{k_2} denote the mass of the springs installed in the first and second joints, respectively. The size of the two manipulators is quantified by their vertical reach at the home configuration, which is equivalent to the y -coordinate of the end-effector at the home configuration $(\alpha_1, \alpha_2) = (0, 0)$.

The stability of the home configuration in the absence of actuation forces is imposed as a constraint as in the previous problem (see Eq. (6.1)). In addition, the maximal inscribed disk (\mathcal{D}) in the SWFW is prescribed to have a radius greater than or equal to a user-specified value r_d . Using the data from the previous section, a payload mass of $m_p = 2$ kg and desired SWFW disk radius of $r_d = 0.15$ m and are set considering the feasibility for both the manipulators. Finally, the details on design variables u_i can be found in Table 6.1.

The above problem is solved in several stages using the NSGA-II solver, as explained in the following.

6.5.2 Solution method and the Pareto optimal front

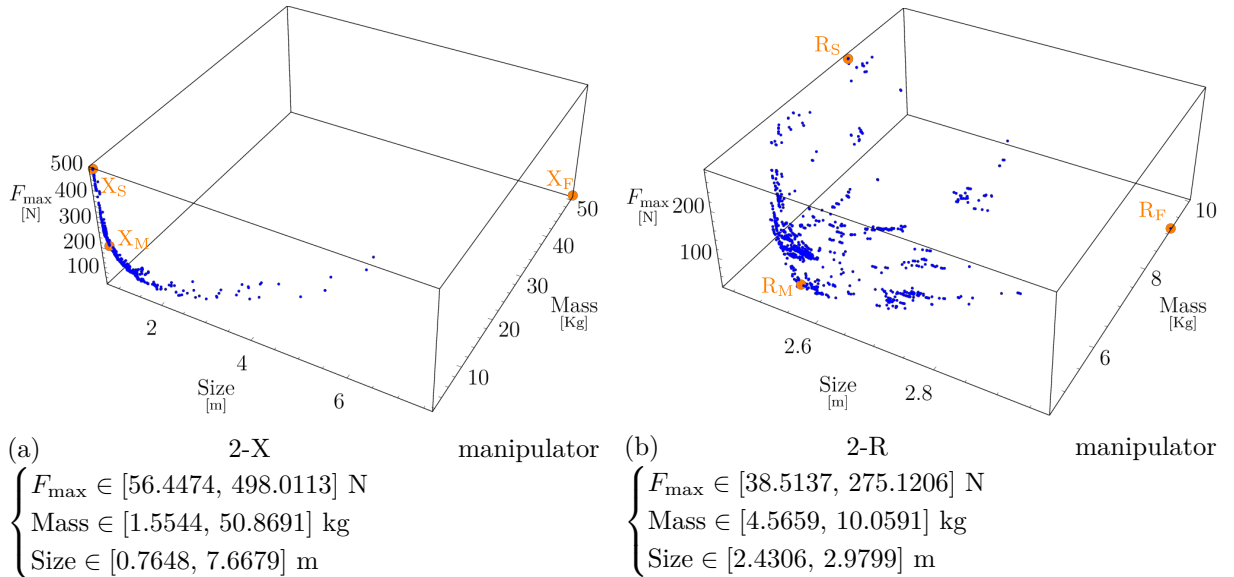


Figure 6.3 – Pareto fronts for the two manipulators obtained for a payload mass (m_p) of 2 kg and desired SWFW disk radius (r_d) of 0.15 m.

Since there are three objectives in the optimization problem posed in Eq. (6.2), its complete solution will be formed by a two-dimensional Pareto front in the objective space. The NSGA-II solver can handle multiple objectives to produce the desired solutions on the Pareto front. However, instead of using it directly on the above problem, it is used in two stages. The first one finds optimal designs for each objective, and the second one uses them to construct the Pareto front, as detailed in the following:

- Single objective optimization problems with force, mass, and size as objectives are solved separately. In these problems, the optimal design obtained while maximizing the SWFW disk size for a 2 kg payload (see Section 6.4.3) is added to the initial population since it is a known feasible design. This inclusion helps the solver to generate new feasible designs and better explore the feasible design space.
- A multi-objective optimization problem with force, mass, and size as three objectives is formulated. The three optimal designs obtained in the previous step are added to the initial population to aid the solver in producing a well-distributed Pareto front.

The Pareto fronts obtained for the 2-X and 2-R manipulators are shown in Figs. 6.3a and 6.3b, respectively. It is observed that the front of the 2-X manipulator is spread over a much wider range along all three axes than that of the 2-R manipulator, indicating that it has a better diversity of optimal designs. Both optimal fronts appear to have some discontinuities which may be attributed to the constraints in the problem. It is also observed that both plots are extremely sparse near the lower bounding values of F_{\max} .

The extremal designs in the Pareto front of the two manipulators marked in Fig. 6.3 are studied in the next section, and several other compromise designs are presented in the subsequent section.

6.5.3 Extremal designs on the Pareto front

The force, mass, and size optimal designs for the 2-X manipulator (resp. 2-R manipulator), denoted by X_F , X_M , X_S (resp. R_F , R_M , R_S), respectively, are presented in Table 6.3 (resp. Table 6.4). In addition to the values of the design variables, the dependent parameters are also presented below them in “{ }” for completeness. After the rows containing design variables, the actual limits of movement for the first and second joints are presented. This is followed by the six dependent spring parameters $(d, D, N_a, l_{0_i}, l_{\max_i}, m_{k_i})$ computed using the design variables k_i and σ_{k_i} for springs in the i^{th} joint. The designer can use these parameters directly for their fabrication. Then, the cross-section radii of the moving bars calculated implicitly using the other data are presented. Note that the bars are numbered from the bottom-left to the top-right (see Figs. 3.4 and 5.9a). Finally, the three objectives (force, mass, size) are presented for all the designs, and the minimum value for each objective is highlighted with a box.

The manipulators corresponding to optimal designs for each objective and their SWFW are presented for 2-X and 2-R architectures in Figs. 6.4, 6.5, 6.6 for a visual comparison. All the designs in this chapter are presented in the same scale to make such comparisons possible.

Using the data in Tables 6.3, 6.4, and Figs. 6.4, 6.5, 6.6, the following observations are made on the force, mass, and size optimal designs of the two manipulators:

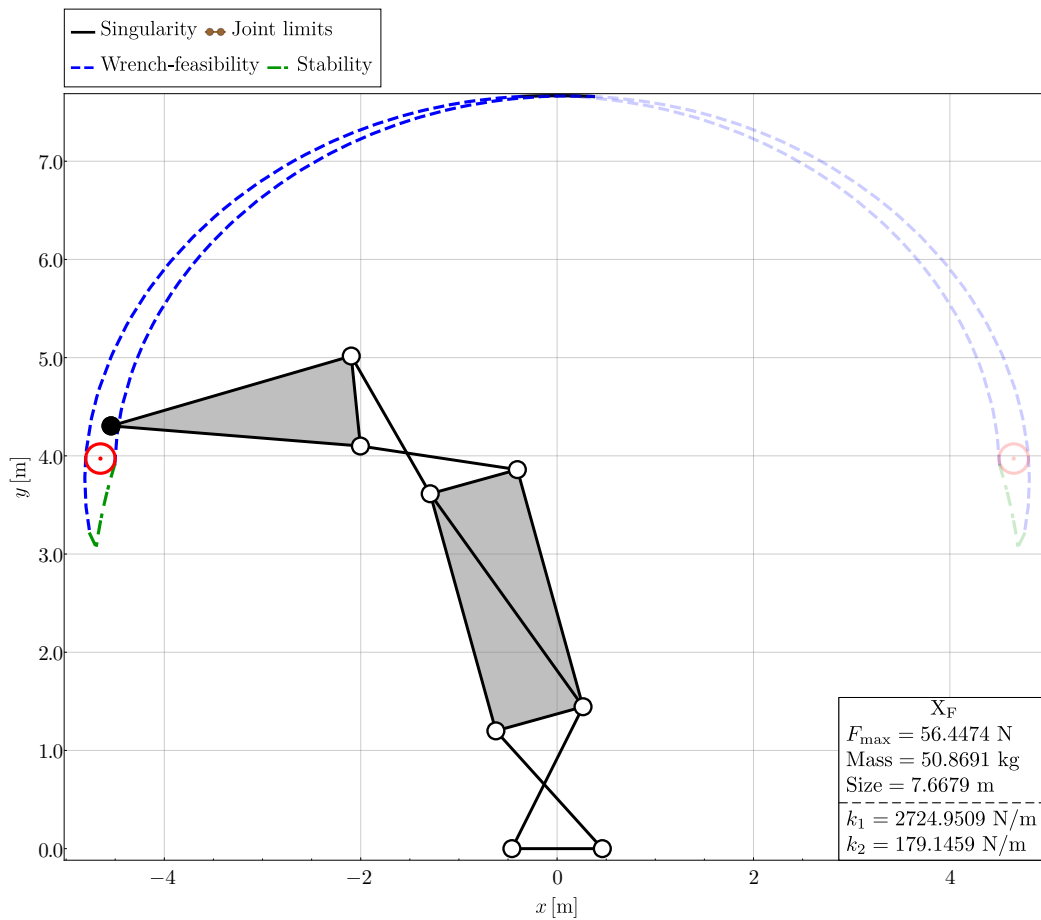
- **Objectives:** There is a strong compromise between the force and size values between the respective optimal designs for both manipulators. For the 2-X manipulator, between designs X_F and X_S , F_{\max} increases from 56.4474 N to 495.6961 N to achieve a reduction in

Table 6.3 – Force, mass, and size optimal designs for the 2-X manipulator for carrying a payload of mass 2 kg and inscribing an SWFW disk of radius 0.15 m.

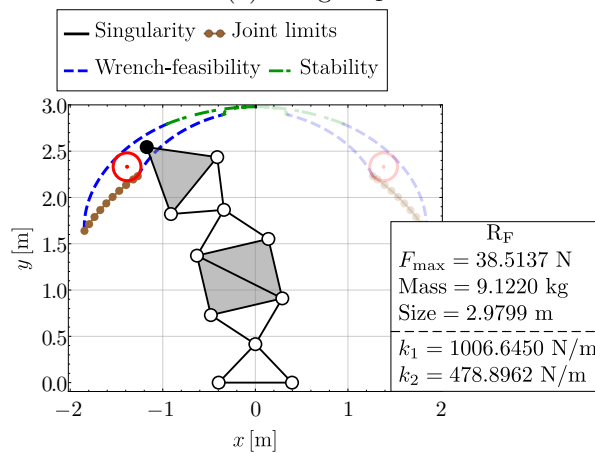
Variables	Limits	Optimal designs		
		X_F	X_M	X_S
b [m]	[0.05, 1.0]	0.9209	0.1341	0.1193
λ (l/b) { l [m]}]1, 10]	1.7553 {1.6165}	2.0275 {0.2720}	2.3865 {0.2846}
ϵ (a/b) { a [m]}]0, 10]	2.7205 {2.5054}	1.6574 {0.2223}	1.0392 {0.1239}
$\frac{\sigma_\alpha}{\{\alpha_{\max}\}}$ [rad]]0, 1[0.7271 {2.2842}	0.7060 {2.2179}	0.8054 {2.5304}
k_1 [N/m]	[0, 10000]	2724.9509	2432.2837	1917.3040
σ_{k_1}	[0, 1]	0.9704	0.2736	0.7956
k_2 [N/m]	[0, 10000]	179.1459	834.2743	1169.9118
σ_{k_2}	[0, 1]	0.9586	1.0000	0.9902
F_{\max} [N]	[0, 500]	56.4474	217.0522	495.6961
$\{\alpha_{\max_1}, \alpha_{\max_2}\}$ [rad]		{0.3586, 2.2842}	{1.1252, 2.2179}	{1.9170, 2.5304}
Spring 1: { d [mm], D [mm], N_a , l_{0_1} [m], l_{\max_1} [m], m_{k_1} [kg]}		{6.0, 29.60, 186.88, 1.17, 1.50, 3.92}	{3.4, 24.46, 38.27, 0.18, 0.32, 0.23}	{3.9, 34.90, 28.91, 0.18, 0.37, 0.33}
Spring 2: { d [mm], D [mm], N_a , l_{0_2} [m], l_{\max_2} [m], m_{k_2} [kg]}		{5.9, 111.73, 49.40, 0.51, 2.41, 3.95}	{3.2, 39.00, 21.59, 0.14, 0.39, 0.19}	{3.4, 33.56, 30.78, 0.17, 0.40, 0.25}
Bar cross-section radius r_{b_j} [mm] $j = 1, \dots, 12$		{16.73, 16.73, 10.68, 18.13, 18.92, 18.13, 7.11, 9.14, 9.14, 5.50, 6.03, 6.03}	{6.41, 6.41, 5.00, 5.00, 5.17, 5.00, 5.00, 5.00, 5.00, 5.00, 5.00, 5.00}	{7.59, 7.59, 5.00, 5.00, 5.00, 5.00, 5.00, 5.00, 5.00, 5.00, 5.00, 5.00}
Mass [kg]		50.8691	1.4744	1.7860
Size [m]		7.6679	0.9179	0.7648

Table 6.4 – Force, mass, and size optimal designs for the 2-R manipulator for carrying a payload of mass 2 kg and inscribing an SWFW disk of radius 0.15 m.

Variables	Limits	Optimal designs		
		R _F	R _M	R _S
r [m]	[0.025, 0.5]	0.3962	0.3347	0.3706
μ (h/r) { h [m]}	[0, 5]	1.0483 {0.4153}	1.0501 {0.3515}	1.1021 {0.4084}
ϵ ($a/(2r)$) { a [m]}]0, 10]	0.8322 {0.6594}	0.8739 {0.5851}	0.5375 {0.3984}
σ_α { α_{\max} [rad]}]0, 1[0.7040 {1.0726}	0.7054 {1.0735}	0.7666 {1.1297}
k_1 [N/m]	[0, 10000]	1006.6450	1081.0647	1776.7390
σ_{k_1}	[0, 1]	0.3156	0.0001	0.3437
k_2 [N/m]	[0, 10000]	478.8962	433.1571	424.6377
σ_{k_2}	[0, 1]	1.0000	1.0000	1.0000
F_{\max} [N]	[0, 500]	38.5137	103.5777	273.5630
$\{\alpha_{\max_1}, \alpha_{\max_2}\}$ [rad]		{0.6865, 1.0726}	{0.2873, 1.0735}	{0.5190, 1.1297}
Spring 1: { d [mm], D [mm], N_a , l_{0_1} [m], l_{\max_1} [m], m_{k_1} [kg]}		{4.7, 37.35, 94.78, 0.52, 1.05, 1.56}	{2.0, 8.01, 292.95, 0.60, 0.79, 0.18}	{4.8, 29.94, 113.39, 0.60, 0.98, 1.56}
Spring 2: { d [mm], D [mm], N_a , l_{0_2} [m], l_{\max_2} [m], m_{k_2} [kg]}		{5.3, 85.20, 27.14, 0.31, 1.12, 1.40}	{4.5, 70.09, 28.01, 0.26, 0.95, 0.85}	{4.9, 78.21, 28.91, 0.29, 1.09, 1.16}
Bar cross-section radius r_{b_j} [mm] $j = 1, \dots, 14$		{7.06, 7.06, 8.29, 6.47, 8.21, 6.47, 5.42, 5.20, 5.20, 5.00, 5.00, 5.00, 5.00, 5.00}	{6.41, 6.41, 7.70, 6.16, 7.71, 6.16, 5.20, 5.00, 5.00, 5.00, 5.00, 5.00, 5.00, 5.00}	{7.40, 7.40, 8.77, 5.31, 8.13, 5.31, 6.41, 5.52, 5.52, 5.00, 5.00, 5.00, 5.00, 5.00}
Mass [kg]		9.1220	4.5659	8.2551
Size [m]		2.9799	2.5761	2.4306



(a) Design X_F



(b) Design R_F

Figure 6.4 – Minimum force designs for the two manipulators.

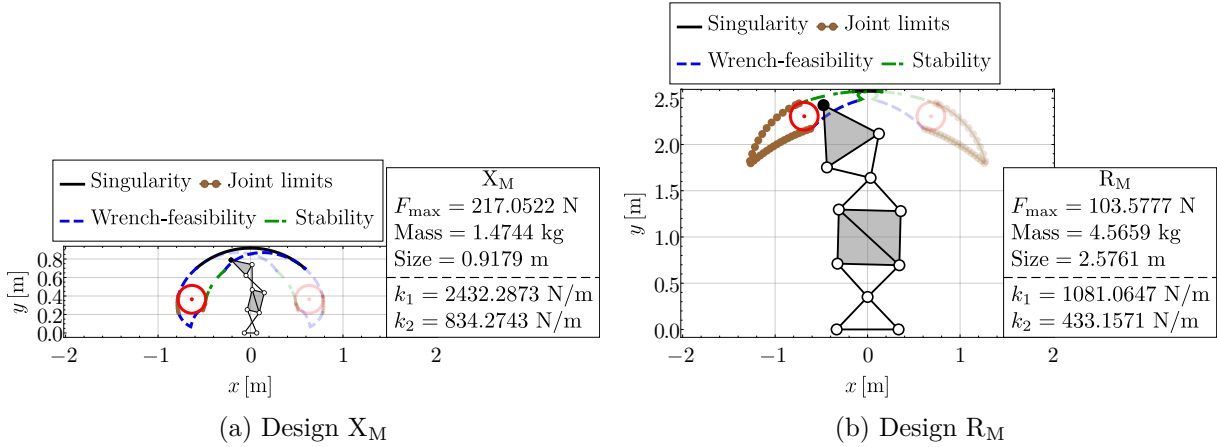


Figure 6.5 – Minimum mass designs.

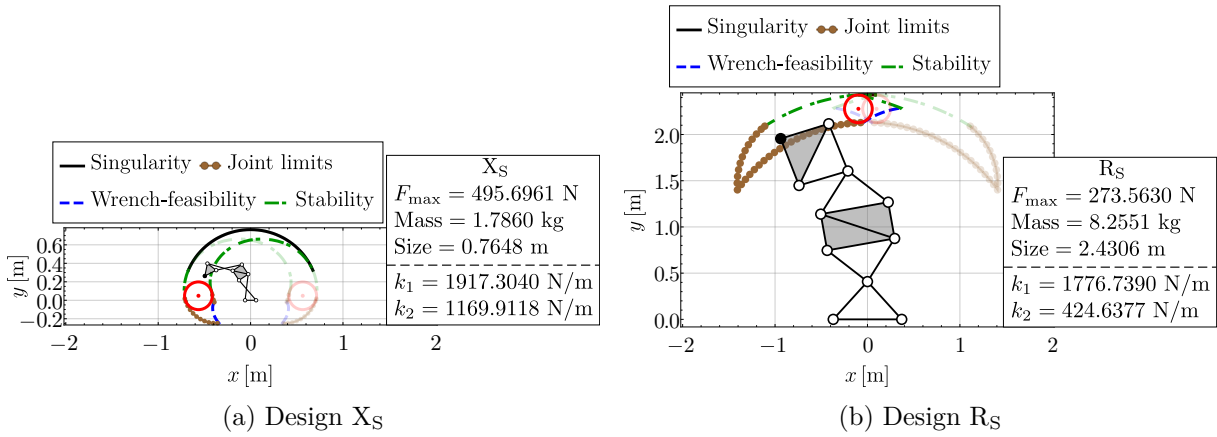


Figure 6.6 – Minimum size designs.

size from 7.6679 m to 0.7648 m. The mass optimal design X_M is placed in between with an F_{\max} of 217.0522 N and a size of 0.9179 m. On the other hand, for the 2-R manipulator, between the designs R_F and R_S , F_{\max} increases from 38.5137 N to 273.5630 N to achieve a reduction in size from 2.9799 m to 2.4306 m. The design R_M is placed between them with an F_{\max} of 103.5777 N and a size of 2.5761 m.

- **All designs:** Some features are common to all the extremal optimal designs of both manipulators. The inscribed SWFW disk has a radius that is marginally greater than the specified value of 0.15 m, as expected. The actual joint limit for the second joint is equal to the safe joint limit, i.e., $\alpha_{\max_2} = \pm\overline{\alpha_{\max}}$, while it is lesser for the first joint. Firstly, this indicates that the first joint, which supports a more significant mass (first offset and second joint with its springs), moves over a shorter range than the second joint, which supports a smaller mass. Secondly, it also shows that the springs chosen for the first joint belong to the set χ_a while those selected for the second joint belong to the set χ_b , which is interesting to note.

The springs in the first joint are stiffer and have a longer free length (l_{0_i}) than the ones

in the second joint. But, the springs in the second joint are wider (except in design X_M), i.e., have a larger coil diameter (D), and have longer operating length (l_{\max_i}) than their counterparts.

- **Designs X_F, X_M, X_S :** The design X_F is much taller (≈ 9 times), wider (≈ 7 times) and heavier (≈ 30 times) than X_M and X_S as presented in Fig. 6.4a. Hence, it may not be preferred despite its smaller actuation force ($\approx 1/7$ times). On the other hand, the designs X_M and X_S are compact and have a moving mass that is smaller than the payload mass ($m_p = 2$ kg) loaded at the end-effector, which makes them more attractive than X_F . Between X_M and X_S , the former would be a more reasonable choice owing to a smaller force requirement ($\approx 1/2$ times) and comparable mass and size values.
- **Designs R_F, R_M, R_S :** In all the optimal designs of 2-R manipulator, it is observed that the ratio (h/r) is close to unity, which indicates that the R-joint tends to have a geometry that keeps the joint limit ($\overline{\alpha_{\max}}$) due to actuation cables close to its maximum value of ($\pi/2$) (see Eq. (2.21)). Another point to be noted is that the ratio (h/r) is greater than one in all designs, contrary to what was observed for the optimal designs of a single R-joint in [MW21]. This difference is because of the free length (l_{0_i}) of the springs that was neglected in that study. It was proved in that work that ($r > h$) is necessary to stabilize the R-joint when springs are of zero free length. But, with a non-zero free length for springs, we find that it is possible to stabilize the R-joint for other geometries as well, and furthermore, all the optimal designs of the 2-R manipulator are such that h is slightly greater than r .

Unlike in the 2-X manipulator, the sizes of all three designs of the 2-R manipulator are comparable and are significantly larger than the specified SWFW disk radius. Despite the similarity in size, they have a significant difference in their forces and masses. The design R_S has a larger mass and higher force requirements for a marginally smaller size and is hence not a favorable one. However, between the designs R_F and R_M , there is no obvious choice. The former must be chosen if a smaller force is the priority, while the latter must be chosen if a smaller mass is the priority.

- **Designs X_F, R_F :** From Fig. 6.4, it is apparent that the design R_F has a smaller (≈ 1.5 times) F_{\max} and is significantly better than X_F in terms of other two the objectives, and is hence a preferred choice as the force optimal design.
- **Designs X_M, R_M :** From Fig. 6.5, it is observed that the design X_M has a smaller mass ($\approx 1/3$ times), smaller size ($\approx 1/3$ times) and a larger force requirement (≈ 2 times) when compared to the design R_M . Based on the mass value, it is clear that the design X_M should be preferred over R_M as the mass optimal design.
- **Designs X_S, R_S :** From Fig. 6.6, it is observed that the design X_S has a smaller mass ($\approx 1/5$ times), smaller size ($\approx 1/3$ times) and a larger force requirement (≈ 2 times) when compared to the design R_S . Based on the size value, it is clear that the design X_S should be preferred over R_S as the size optimal design.

It can be derived from the geometry and joint limits of the 2-R manipulator that its size must be at least $\frac{2\sqrt{2}}{\sqrt{2}-1} (\approx 6.8284)$ times the radius of the inscribed disk (see Appendix D). Thus, while considering other factors such as wrench-feasibility and stability, the size of the 2-R manipulator relative to the inscribed disk would be even larger. The large size is the primary reason for the large mass of the 2-R manipulators.

In summary, the 2-X manipulator is better in terms of mass and size, while the 2-R manipulator

is better in terms of the required actuation force. It would be interesting to study the other optimal designs in the Pareto front for the two manipulators that exhibit good compromise between the three objectives. This study is conducted in the next section.

6.5.4 Exploration of the Pareto front

The Pareto fronts for the 2-X and 2-R manipulators are enlarged in Figs. 6.7 and 6.8, respectively. The front of the 2-X manipulator has been trimmed by removing X_F and a few points close to it to present a better view of its central portion. Six designs have been chosen on the Pareto fronts of the two manipulators for study, and their complete data are presented in Appendix E. The following observations are made on the optimal designs and Pareto fronts of the two manipulators:

- **All designs:** The common properties for all the extremal designs (second item of the list in Section 6.5.3) are also exhibited by all the optimal designs of the two manipulators presented in Tables E.1 and E.2.
- **Pareto fronts:** From the front of the 2-X manipulator in Fig. 6.7, it is observed that for a given value F_{\max} , there is a spread of designs representing the compromise between the mass and size values. This spread is significant for small values of F_{\max} but becomes thinner with the increase of F_{\max} . On the other hand, in the front of the 2-R manipulator (see Fig. 6.8), visually, the spread of designs appears to be more uniform for all values of F_{\max} . However, it must be noted that the size of this front is smaller than its counterpart, as depicted by the ranges of the objectives. In particular, the variation in the size of the 2-R manipulator is extremely low ($\approx 23\%$) when compared to the other objectives ($\approx 614\%$ for F_{\max} and 120% for mass). Hence, size should not be a major criterion in selecting the best design for the 2-R manipulator.
- **Designs I, II, III:** The designs (X_I, X_{II}, X_{III}) and (R_I, R_{II}, R_{III}) have been chosen in the Pareto fronts of 2-X and 2-R manipulators, respectively, such that they have almost the same value for F_{\max} (120 N for 2-X and 43 N for 2-R). This choice is made to understand the compromise between mass and size values on the two fronts.

For the 2-X manipulator, the design X_I corresponds to the minimum mass and maximum size for the assumed F_{\max} . As one moves to the designs X_{II} and X_{III} , the mass increases by $\approx 22\%$ and $\approx 96\%$ respectively, while the size decreases by $\approx 4\%$ and 5% in the respective cases. Thus, it is apparent that the decrease in size is not as significant as the increase in mass in those designs. Thus, the design X_I will be favored over X_{II} and X_{III} . Another interesting feature is that the designs X_{II} and X_{III} are almost identical to one another except for the spring selection parameters σ_{k_i} . This difference causes them to have springs with different parameters, such as wire diameter (d) and coil diameter (D), even while their stiffness remains the same. Interestingly, the springs in design X_{III} turn out to be heavier than the ones in X_{II} . Specifically, each of the two springs in the first joint of X_{III} weighs ≈ 0.6 kg more than its counterpart in X_{II} , resulting in ≈ 1.2 kg increase in the overall mass of the manipulator. This shows that the selection of the spring parameters, even while its stiffness is fixed, can significantly affect the design of the tensegrity-inspired manipulators.

For the 2-R manipulator, the design R_I corresponds to the minimum mass and maximum size for the assumed F_{\max} . In comparison the designs R_{II} and R_{III} are $\approx 12\%$ and $\approx 65\%$

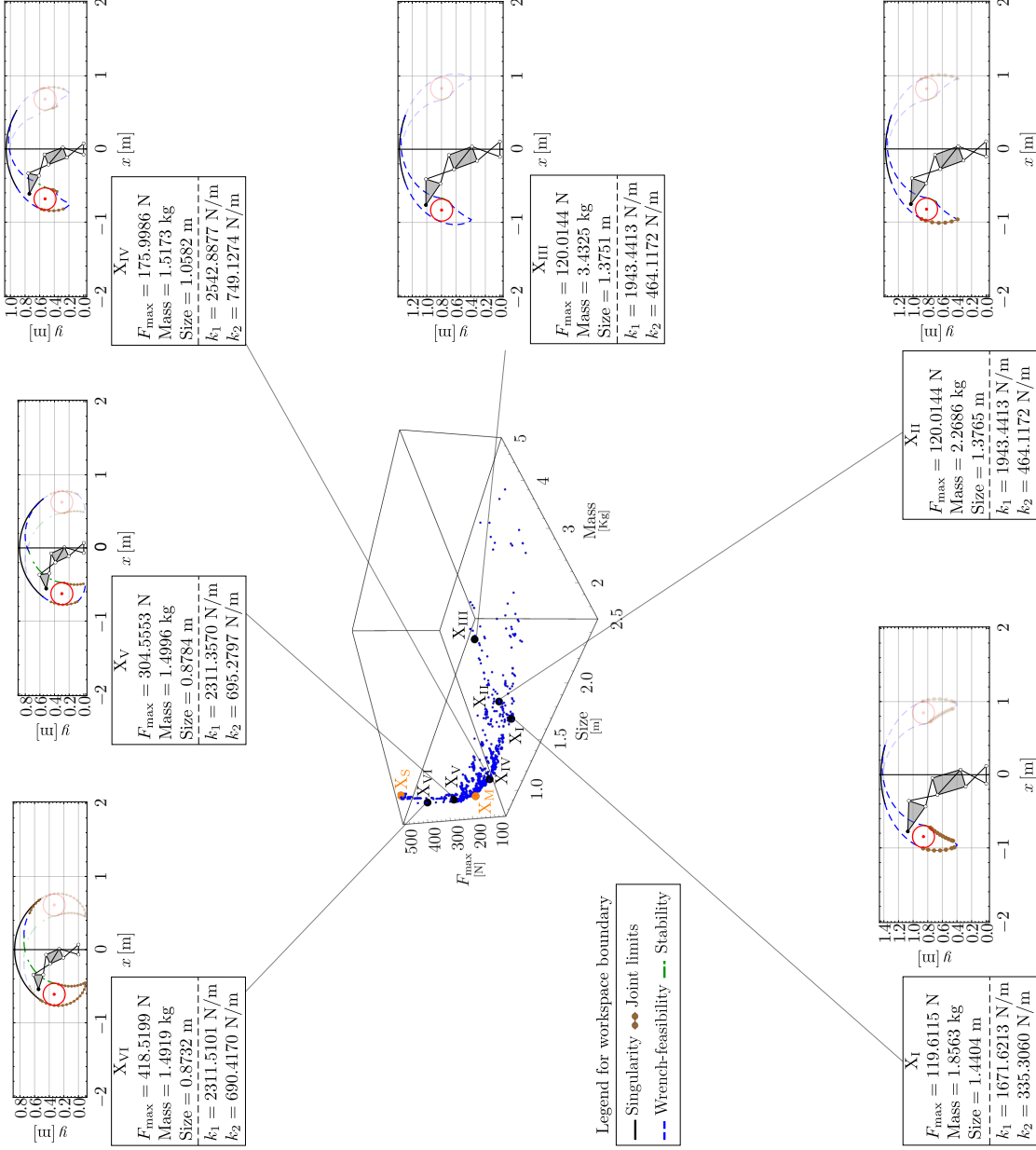


Figure 6.7 – Pareto front and six optimal designs (X_I, \dots, X_{VI}) of the 2-X manipulator obtained for a payload mass (m_p) of 2 kg and SWFW disk radius (r_d) of 0.15 m. The range of the objectives are $F_{\max} \in [56.4474, 498.0113]$ N, mass $\in [1.5544, 50.8691]$ kg, and size $\in [0.7648, 7.6679]$ m. The minimum force design and a few points closer to it have been deleted to present a better view of the major part of the front.

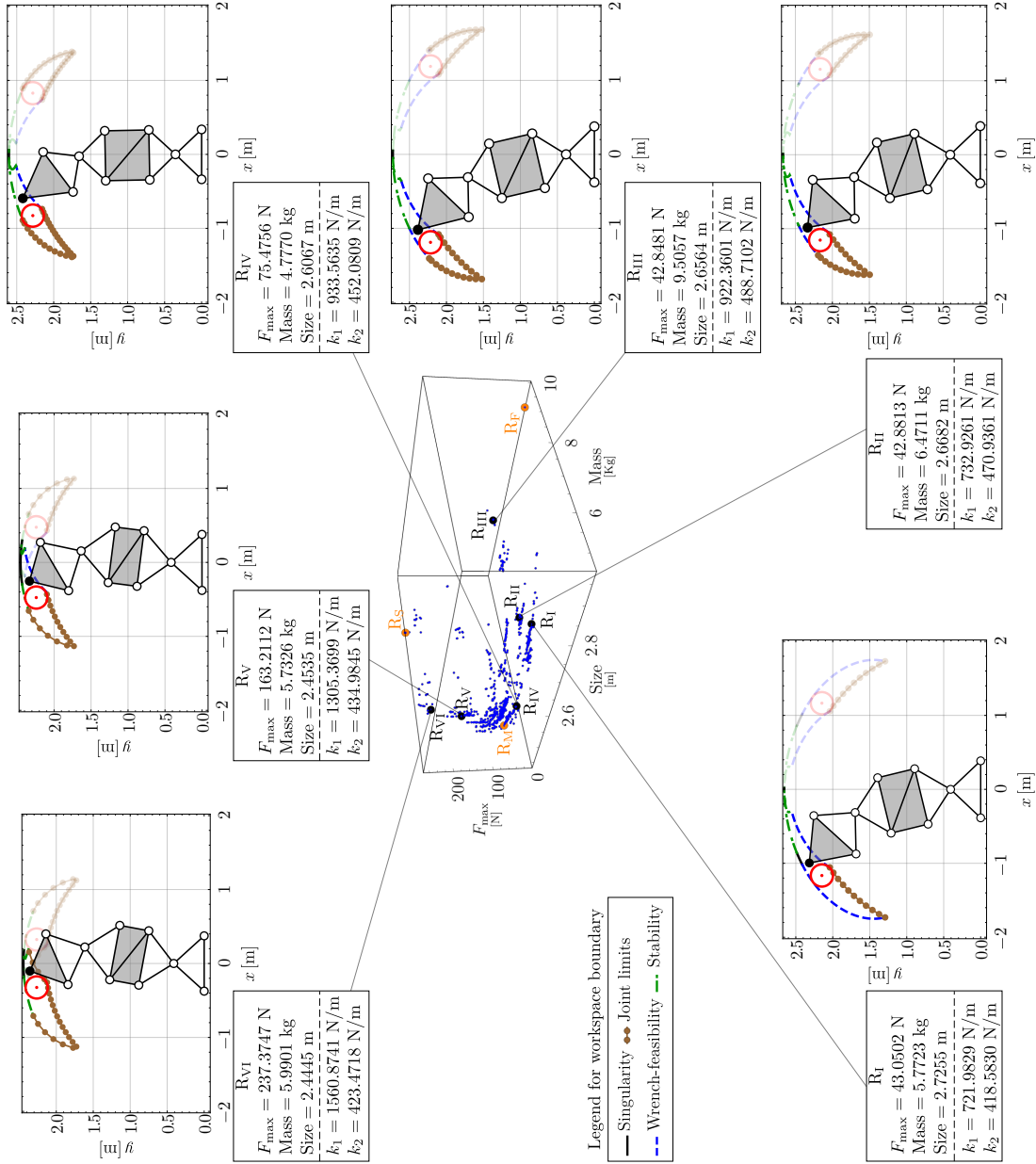


Figure 6.8 – Pareto front and six optimal designs (R_1, \dots, R_{VI}) of the 2-R manipulator obtained for a payload mass (m_p) of 2 kg and SWFW disk radius (r_d) of 0.15 m. The range of objectives are $F_{\max} \in [38.5137, 275.1206]$ N, mass $\in [4.5659, 10.0591]$ kg, size $\in [2.4306, 2.9799]$ m.

heavier respectively, while being $\approx 2\%$ and $\approx 3\%$ smaller in size. The significantly smaller mass makes the design R_I most favorable among the three.

Similar results have been found for different values of F_{\max} in the fronts of both manipulators. Hence, for any given value of force, the minimum mass design would be favored over the others.

- **Minimum mass designs:** Following the previous observation, new minimum mass designs for different values of F_{\max} have been chosen for the two manipulators. These are denoted by (X_{IV}, X_V, X_{VI}) and (R_{IV}, R_V, R_{VI}) on the fronts of the 2-X and 2-R manipulators, respectively.

On the front of the 2-X manipulator, all the chosen designs on the minimum mass curve, i.e., $(X_I, X_{IV}, X_M, X_V, X_{VI})$ are studied sequentially. In the part (X_I, X_{IV}, X_M) , F_{\max} increases while the mass and size decrease. On the other hand, in the part (X_M, X_V, X_{VI}) , F_{\max} increases while mass increases and size decreases. In addition to this trend, it is necessary to quantify the increase/decrease to choose the most favorable design. In this regard, as one moves from X_I to X_{IV} , force increases by $\approx 47\%$ while mass decreases by $\approx 18\%$ and size by 26% , which is a reasonable compromise. From X_{IV} to X_M , the force increases by $\approx 23\%$ while mass decreases by $\approx 3\%$ and size by $\approx 13\%$, which is a poor compromise. Further moving towards X_V and X_{VI} , the force increases by more than 35% with a small increase in mass and a reduction in size by less than 5% . This shows that the front rises steeply along the force axis without producing significant improvement in the mass and size values beyond the design X_{IV} . Hence, among the optimal designs that are presented, X_{IV} is the most favorable one.

On the front of the 2-R manipulator, the chosen designs on the minimum mass curve are $(R_I, R_{IV}, R_M, R_V, R_{VI})$. Similar to the front of the 2-X manipulator, as F_{\max} increases, the mass and size decrease till the design R_M , but beyond that, the mass increases while the size continues to decrease. However, the decrease in size between successive designs is small ($< 5\%$) and is hence not considered further. Between the designs R_I and R_{IV} , F_{\max} increases by $\approx 75\%$ while the mass decreases by $\approx 17\%$ which is a moderate compromise. Between R_{IV} and R_M , F_{\max} increases by $\approx 37\%$ while the mass decreases by $\approx 4\%$, which is a poor compromise. Succeeding designs are not studied since both force and mass increase in those cases. The compromise found on this front is not as good as that of the 2-X manipulator. However, it can be asserted that the favorable designs lie on the minimum mass curve between R_I and R_{IV} .

In summary, the favorable designs for both manipulators are on the minimum mass curves of the respective Pareto fronts. For the 2-X manipulator, the design X_{IV} seems to be the best among the ones considered. On the other hand, for the 2-R manipulator the best design is not very obvious, but, both R_I and R_{IV} are better than the others. Between the 2-X and 2-R manipulators, the choice once again depends on which objective is the critical one. If a smaller mass and/or size is more important, then design X_{IV} is the best choice. But, if smaller F_{\max} is more important, then R_I may be chosen.

In addition to studying the compromise, the Pareto fronts presented in Figs. 6.7 and 6.8 are helpful to the designer for finding favorable optimal designs in the presence of secondary constraints. For instance, if the goal is to build an optimal manipulator with existing actuators, then it amounts to slicing the front at the corresponding value of F_{\max} to obtain all the relevant optimal designs. Similarly, if there is a constraint on the mass/footprint of the manipulator, as

in space exploration missions, the range of mass and size objectives can be suitably adjusted to find the desired designs.

The following section presents the variation of force, mass, and size objectives for different payload and SWFW disk radius specifications.

6.6 Effect of changing the payload and desired SWFW disk radius specifications

This section aims to verify if the observations reported on the optimal designs of the 2-X and 2-R manipulators are valid even if the payload or disk radius specifications are altered. In this regard, four payloads $m_p = \{0, 2, 5, 10\}$ kg and four SWFW disk radii $r_d = \{0.05, 0.15, 0.25, 0.35\}$ m are considered. Design optimization problems have been posed and solved for all 16 combinations of specifications for both manipulators. Note that three of the combinations ($m_p = 5$ kg, $r_d = 0.35$ m), ($m_p = 10$ kg, $r_d = 0.25$ m), ($m_p = 10$ kg, $r_d = 0.35$ m) are not feasible for the 2-R manipulator (see Fig. 6.2) and are hence not considered for this manipulator.

The Pareto fronts have been obtained for all problems in the same manner as illustrated in Section 6.5.2. However, studying the compromise designs from the front in each case will be difficult. Hence, only the extremal designs, i.e., the ones optimal w.r.t. force, mass, and size objectives, are considered in the following.

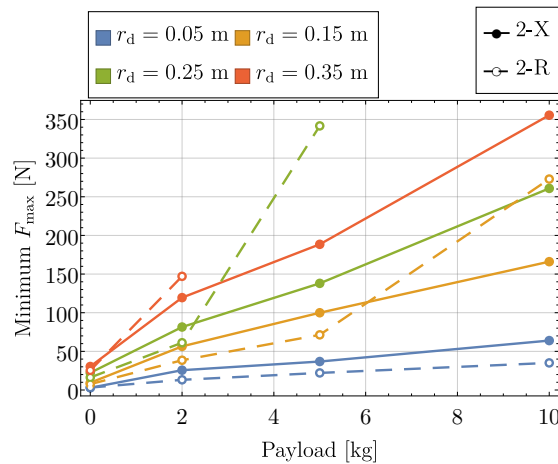


Figure 6.9 – Minimum F_{\max} values for different payload and disk specifications for the 2-X and 2-R manipulators.

The optimal F_{\max} values are plotted as a function of the payload mass (m_p) for various SWFW disk radius (r_d) specifications in Fig. 6.9. For the specification ($m_p = 0$ kg, $r_d = 0.05$ m), the resulting F_{\max} values are extremely small (< 5 N) for the two manipulators, with 2-X design having a slightly smaller value than the 2-R design. When $m_p = 0$ kg, for all other specified r_d , the 2-R manipulator has a smaller F_{\max} than 2-X manipulator. While for $m_p = 2$ kg (resp. 5 kg, 10 kg), 2-R manipulator has a smaller F_{\max} when $r_d \leq 0.25$ m (resp. 0.15 m, 0.05 m), but a greater F_{\max} otherwise.

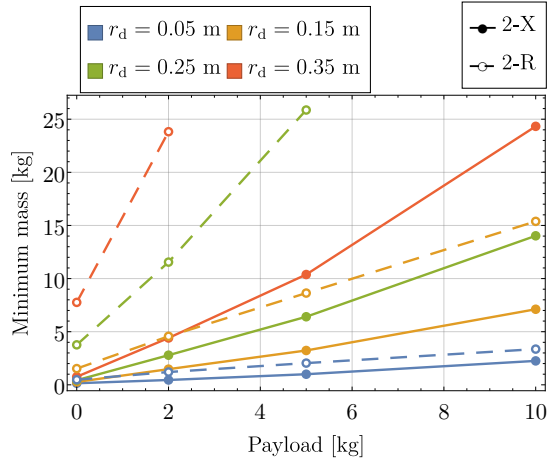


Figure 6.10 – Minimum moving mass values for different payload and disk specifications for the 2-X and 2-R manipulators.

The optimal moving mass values are plotted as a function of the payload mass (m_p) for various SWFW disk radius (r_d) specifications in Fig. 6.10. The optimal moving mass of the 2-X manipulator is smaller than that of the 2-R manipulator in all the scenarios. An interesting metric to study the mass optimality of manipulators is the moving mass to payload ratio (see [SB14]). It is apparent from the figure that this ratio is roughly the same for a given disk size, but it changes significantly as the disk size changes. While the SWFW disk radius (r_d) is specified as (0.05, 0.15, 0.25, 0.35) m, the moving mass to payload ratio (averaged over feasible payload specifications) for the 2-X manipulator is computed to be (0.22, 0.70, 1.36, 2.24), respectively, and for the 2-R manipulator it is found to be (0.45, 2.00, 5.47, 11.91), respectively. These data indicate that the 2-X manipulator should be preferred over the 2-R manipulator to have a good moving mass to payload ratio.

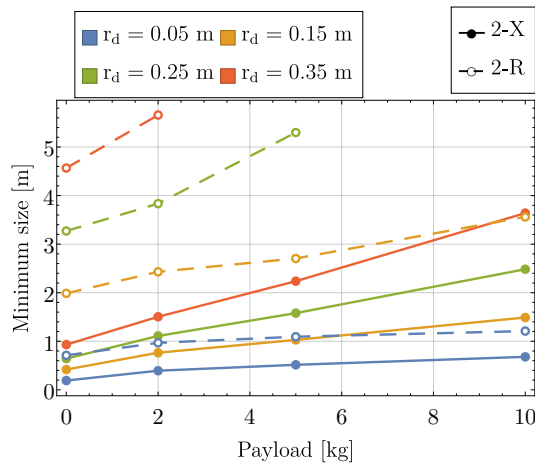


Figure 6.11 – Minimum size values for different payload and disk specifications for the 2-X and 2-R manipulators.

The optimal size values are plotted as a function of the SWFW disk radius (r_d) for various payload mass (m_p) specifications in Fig. 6.11, unlike in the previous two figures, as this presentation offers better insights into these data. All the size optimal designs of the 2-X manipulator are found to be smaller than those of the 2-R manipulator for a given SWFW disk radius specification, irrespective of the payload they carry. For instance, while the disk radius is specified to be 0.15 m, the size optimal design of the 2-X manipulator designed to carry a payload of 10 kg is smaller than that of the 2-R manipulator designed for no payload (i.e., 0 kg). A relevant metric to measure compactness is the ratio of manipulator size to SWFW disk radius (see [Rus23] for similar metrics). While the payload specification changes (0, 2, 5, 10) kg, for the 2-X manipulator, this metric (averaged over feasible disk radius specifications) is evaluated to be (2.96, 5.43, 7.47, 10.96), respectively, while for the 2-R manipulator it is (13.40, 16.77, 20.37, 23.97), respectively. This suggests that the 2-X manipulator must be preferred over its counterpart when a compact design is needed.

In summary, the 2-R manipulator has a smaller force requirement when the task is not challenging (i.e., light payload and small SWFW disk radius) but has a more significant force requirement when the task is challenging (i.e., heavy payload and/or large SWFW disk radius). On the other hand, the 2-X manipulator has a smaller moving mass and smaller size, irrespective of whether the task is challenging or not.

6.7 Possible applications and extensions

The optimal designs of the 2-X and 2-R manipulators obtained in the previous sections are suitable for inspection, welding, and painting applications, where the manipulator carries a constant payload inside its workspace.

Since the SWFW is dependent on the static model of the manipulator, it is susceptible to a change when the payload changes. We observed that the SWFW of a manipulator designed for carrying a payload of 2 kg reduces drastically while the payload is removed. The reason for this non-intuitive behavior is two-fold. Firstly, the manipulator is placed vertically upward against gravity. Secondly, stiff springs are used to stabilize the manipulator with the payload loaded at the end-effector. Thus, while the payload is removed, the stiffness of the manipulator increases and the actuation forces become insufficient to effect the same displacements that were possible with the payload. Thus, the vertically upward placement of the manipulator is unsuitable for an application involving varying payload, e.g., pick-and-place operations. In these cases, the manipulator must be mounted on the ceiling, vertically downward, similar to the Delta robot [Liu+04]. This arrangement makes it inherently stable with a payload and allows for reaching a larger workspace with the same actuation forces while the payload is unloaded. In order to find suitable designs for these applications, one can use the tools developed in the previous chapter and the design optimization problems formulated in this chapter as they are, just by reversing the sign of gravity. Design examples have been presented for the 2-X manipulator in Appendix F, neglecting stability in one scenario and suspending the manipulator along gravity in the other.

Another popular application of robot manipulators is machining. However, designing tensegrity-inspired manipulators for such tasks involves several challenges. Firstly, the direction and magnitude of forces required for machining should be taken into account. Then, the designer should find a good placement of the part inside the workspace. If there is more than one feasible configuration

for the manipulator at the chosen location, a suitable one must be chosen. Based on these data, the cross-sections of bars must be designed to avoid buckling failure. In this regard, analysis of force capabilities of tensegrity-inspired manipulators through polytopes [MWC22b] is a relevant work. The notions of available wrench set and prescribed wrench set (see, e.g., [REU04],[BGM09]) used in the context of cable-driven parallel manipulators can be applied to these manipulators as well.

6.8 Conclusions

Design optimization and comparison of 2-X and 2-R tensegrity-inspired manipulators, actuated by the 4-cable scheme, was conducted in this chapter. In these problems, the mechanical constraints associated with the springs (e.g., its maximum elongation) and the bars (safety from buckling failure) were accounted for implicitly, thereby ensuring physical feasibility for all the designs.

A set of nine design variables were composed for the 2-X and 2-R manipulators. This set contains three variables for defining the bar lengths, one for safe joint limits, four for springs, and one for maximal actuation force. Limits were set for these variables to define a design space that is realistic and similar for the two manipulators.

We found optimal designs for the two manipulators by maximizing the inscribed disk radius for four different payloads specified at the end-effector. For all specifications, the 2-X manipulator has a larger disk radius (about two times) than the 2-R manipulator. This result can be attributed to the large range of movement achievable with the X-joint compared to its counterpart.

Based on the optimal SWFW disk size, a combination of payload and SWFW disk radius viable for both manipulators were chosen. Design optimization problems were posed to minimize the maximal actuation force (F_{\max}), moving mass, and size (measured by maximal vertical reach) of the two manipulators while they respected the specifications on payload and SWFW disk radius. The optimal designs for the two manipulators were presented as Pareto fronts. The front of the 2-X manipulator has a larger range for all objectives, indicating a wider variety of optimal designs than its counterpart.

In most optimal designs of the two manipulators, the range of movement for the first joint (fixed to the base), which supports a more significant mass, is lesser than that of the second joint, which supports a smaller mass. The springs in the first joint are stiffer and have a longer free length, while the ones in the second joint are wider and have a longer operating length.

Among the optimal designs in the Pareto front, the extremal designs, i.e., the force, mass, and size optimal designs of the two manipulators were compared. It was found that the 2-R manipulator has a slightly smaller ($\approx 1/1.5$ times) actuation force requirement, while the 2-X manipulator has a much smaller ($\approx 1/3$ times) moving mass and size.

Then, several compromise designs from the Pareto fronts were presented. The compromise between mass and size was not very convincing for a given F_{\max} . The mass increased by (12 – 96)% to effect a reduction of (2 – 5)% in size for both manipulators. Thus, the minimum mass designs were favorable for all values of F_{\max} . Based on the compromise between F_{\max} and minimum mass and the associated change in size, a best design was proposed for the 2-X manipulator, while two good designs were proposed for the 2-R manipulator.

In order to verify if the above conclusions are valid for other specifications, four payloads

$\in [0, 10]$ kg and four SWFW disk radii $\in [0.05, 0.35]$ m were chosen. The design optimization was conducted for the two manipulators for all sixteen combinations of payload and SWFW disk radius specifications. It was found that the 2-R manipulator has a smaller F_{\max} when the specified disk radius is sufficiently small for a given payload, while the 2-X manipulator has a smaller F_{\max} in other cases. On the other hand, the 2-X manipulator has a smaller moving mass and much smaller size in all cases. The moving mass to payload ratio of the mass optimal 2-X (resp. 2-R) designs vary in the range (0.22 – 2.24) (resp. (0.45 – 11.91)) while the specified disk radii $\in [0.05, 0.35]$ m. Note that the ratio is less than one for smaller disks, which indicates that the resulting designs have a moving mass that is less than the payload they carry. This feature makes tensegrity-inspired manipulators interesting candidates for applications such as inspection, painting, etc. In addition, the ratio of manipulator size to SWFW disk radius for the size optimal 2-X (resp. 2-R) designs vary in the range (2.96 – 10.96) (resp. (13.40 – 23.97)), while the payload mass $\in [0, 10]$ kg. These results show that the size optimal designs of the 2-X manipulator are much more compact than their counterparts.

The proposed design method is generic and applies to all the tasks involving the manipulation of a payload. If the loading changes during the operation, as in a pick-and-place task, the manipulator must be mounted on the ceiling vertically downward. In such cases, the proposed design method can be used as it is just by reversing the sign of gravity.

In the future, this design method will be extended to consider the local performances of the manipulators, such as their velocities, force application capabilities, and variable stiffness.

SPATIAL 3-X MANIPULATOR

Abstract

This chapter proposes a modified design of the X-joint using only spherical joints. This joint, referred to as the modified X-joint, is suitable for building spatial tensegrity-inspired manipulators while being kinematically equivalent to a planar X-joint. We propose a 3-DoF spatial manipulator composed of three modified X-joints arranged in two perpendicular planes. We present the kinematics of this manipulator and show that the inverse problem admits up to thirty-two solutions. We derive the singularities of this manipulator and interpret them geometrically. We compute the workspace of this manipulator in the presence of joint limits and show several sections of it to acquire a global understanding. Finally, we present a prototype of the manipulator as a proof of concept and discuss several associated practical issues.

Contents

7.1	Introduction	170
7.2	Modified X-joint for spatial tensegrity systems	171
7.3	Kinematic model of 3-X manipulator	175
7.4	Inverse kinematic model	175
7.4.1	First sub-problem	175
7.4.2	Second sub-problem	177
7.4.3	Numerical example	177
7.5	Singularity analysis	178
7.6	Workspace of 3-X manipulator	181
7.6.1	Construction of the workspace	182
7.6.2	Cross-sections of the workspace	185
7.7	Proof of concept and practical issues	190
7.8	Conclusions	193

7.1 Introduction

Based on the promising results obtained with the X-joints in planar manipulators, this chapter ventures into the design of a spatial manipulator with this joint. In this regard, a simple approach is to place the planar 2-X manipulator on top of an X-joint whose plane is rotated by 90° as shown in Fig. 7.1. This spatial manipulator could be used for positioning tasks whose end-effector point P is controlled by the orientation of the three X-joints.

Another important feature while moving from a planar system to a spatial one concerns its loading. While a planar manipulator is expected to bear loads in its plane of movement, a spatial manipulator should withstand any arbitrary loading. Further, to qualify as a tensegrity-inspired system, there should be no transmission of bending/torsion/shearing loads between its constituent elements in any configuration. However, the manipulator proposed in Fig. 7.1 allows for the transmission of bending loads when it is subjected to a force parallel to the axis of a revolute joint. Hence, a tensegrity-inspired version of the 3-X manipulator should be devoid of revolute joints and be composed of spherical joints that cannot transmit any moments. This transformation requires a redesign of the X-joint and the offsets shown in Fig. 7.1. This chapter addresses this design problem and then studies the kinematics of the 3-X manipulator.

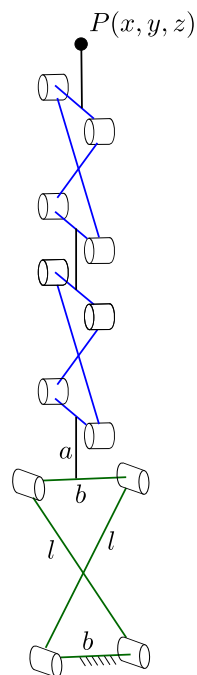


Figure 7.1 – A spatial manipulator with three X-joints arranged in two perpendicular planes.

The rest of this chapter is organized as follows: Section 7.2 designs a modified X-joint only using spherical joints and illustrates its utility in constructing the 3-X manipulator without compromising on the tensegrity properties. Sections 7.3 and 7.4 present the direct and inverse kinematic problems associated with the 3-X manipulator. Section 7.5 studies the singularities of this manipulator. Section 7.6 computes the workspace of the 3-X manipulator. Finally, Section 7.8 concludes this chapter.

7.2 Modified X-joint for spatial tensegrity systems

This section aims to synthesize a modified X-joint that is kinematically equivalent to a planar X-joint but comprising only spherical joints. The theory of screws (see, e.g., [Bal00],[Hun78]) is used to design the modified X-joint at one configuration. Then, the proposed design is shown to be equivalent to the X-joint over the entire range of movement. This claim is confirmed through a CAD simulation. The steps involved in this synthesis are detailed in the following:

1. As a first step, two rigid bodies designated as “fixed platform” and “moving platform” are considered as shown in Fig. 7.2. The task is to attach bars between them such that the relative movement between them is the same as between the base and top bars of a planar X-joint. The two platforms are placed next to an X-joint at its home configuration. Four lines designated as $\mathcal{L}_1, \dots, \mathcal{L}_4$ are marked along the pivot axes of the X-joint as shown in Fig. 7.2. From the construction of the X-joint, it is known that the four lines should always be parallel, and the distance between the lines ($\mathcal{L}_1, \mathcal{L}_3$) and ($\mathcal{L}_2, \mathcal{L}_4$) must be constant. In order to realize these constraints, four points (B_1, \dots, B_4) (resp. (P_1, \dots, P_4)) are chosen on the fixed (resp. moving) platform, such that (B_1, B_2, P_1, P_2) and (B_3, B_4, P_3, P_4) are on planes parallel to the plane of movement of the planar X-joint. Four bars are connected between the points (B_1, P_2), (B_2, P_1), (B_3, P_4), (B_4, P_3) with spherical joints as shown in Fig. 7.2. The distance between these two planes is set arbitrarily, as it does not alter the kinematics of the joint.

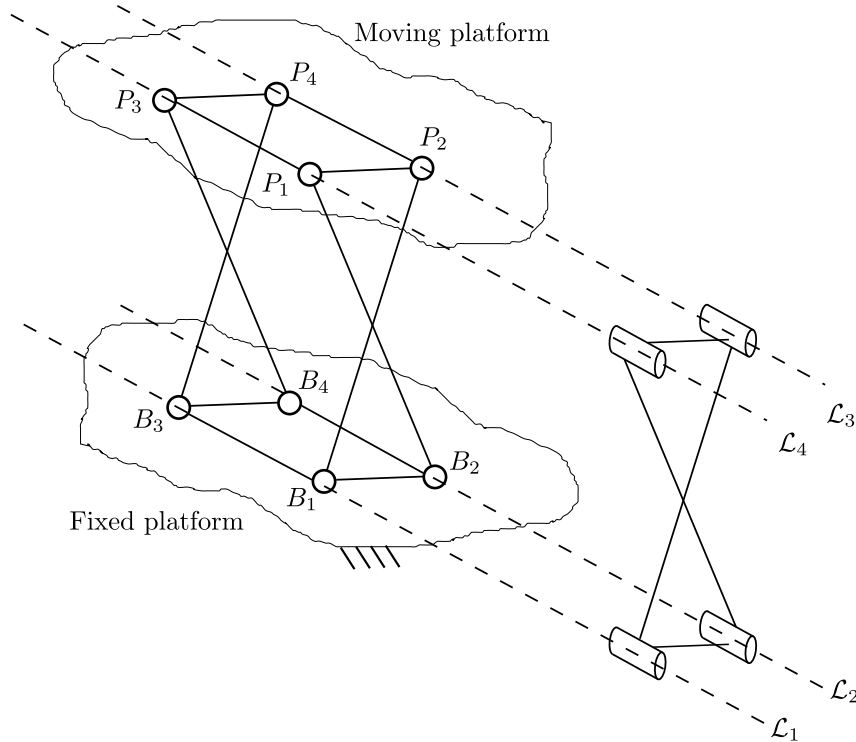


Figure 7.2 – Choosing attachment points for the bars on the fixed and moving platforms while designing the modified X-joint.

- It is well-known that a bar connecting two bodies with spherical joints on each side imposes a constraint force between them along the line joining the centers of the spheres. Since there are four such bars between the two platforms the set of all constraint wrenches between them is spanned by four forces (shown by red lines in Fig. 7.3), which are otherwise known as 0-pitch wrenches [KG07], and designated by $(\zeta_1^0, \zeta_2^0, \zeta_3^0, \zeta_4^0)$. The instantaneous relative movements between the two platforms are given by the twists that are reciprocal to the constraint wrenches. Given that there are four independent constraint wrenches, there should be two independent twists between the platforms. A possible basis for this twist system is shown in Fig. 7.3 (blue color), which indicates that the moving platform can rotate (ξ_1^0) about the axis passing through the intersection points of the crossed bars in the two planes, and also translate (ξ_2^∞) along the direction of this axis. Clearly, this translation changes the distance between the lines $(\mathcal{L}_1, \mathcal{L}_3)$ and $(\mathcal{L}_2, \mathcal{L}_4)$, unlike in a planar X-joint.

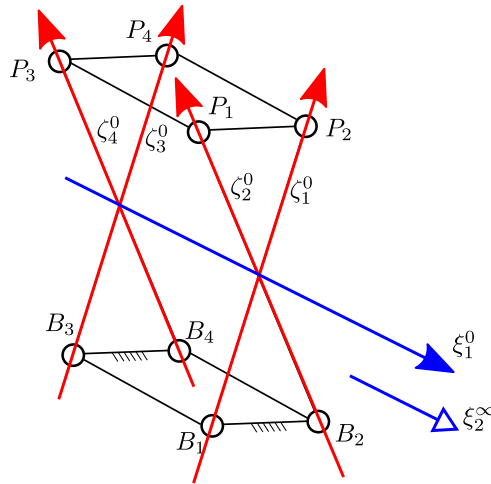


Figure 7.3 – Constraint wrenches (red) and twists (blue) between the fixed and moving platforms connected by four bars.

- In order to obtain the twist system that only belongs to that of the planar X-joint, one needs to introduce a new constraint force (ζ_5^0) passing through the instantaneous rotation axis, but not parallel to any of the existing forces, as shown in Fig. 7.4a. This can be achieved by adding a fifth bar along the indicated line connecting the points B_{13} and P_{24} as shown in Fig. 7.4b. This choice of attachment points additionally preserves the distance between the lines $(\mathcal{L}_1, \mathcal{L}_3)$ over the entire range of movement as in the planar X-joint. Thus, the resulting constraint wrenches form a 5-system with forces $(\zeta_1^0, \zeta_2^0, \zeta_3^0, \zeta_4^0, \zeta_5^0)$, and the only twist that remains is a pure rotation (ξ_1^0) as in the planar X-joint. This new joint will be referred to as the modified X-joint in this chapter.
- The synthesis of a modified X-joint starting from the planar X-joint at the home configuration ensures that the two systems are equivalent only at that configuration. Generally, this does not guarantee their equivalence at another configuration, let alone the entire range of movement. However, since the bars have been placed such that they conserve the distance between the lines $(\mathcal{L}_1, \mathcal{L}_3)$ and $(\mathcal{L}_2, \mathcal{L}_4)$, they are expected to be equivalent over

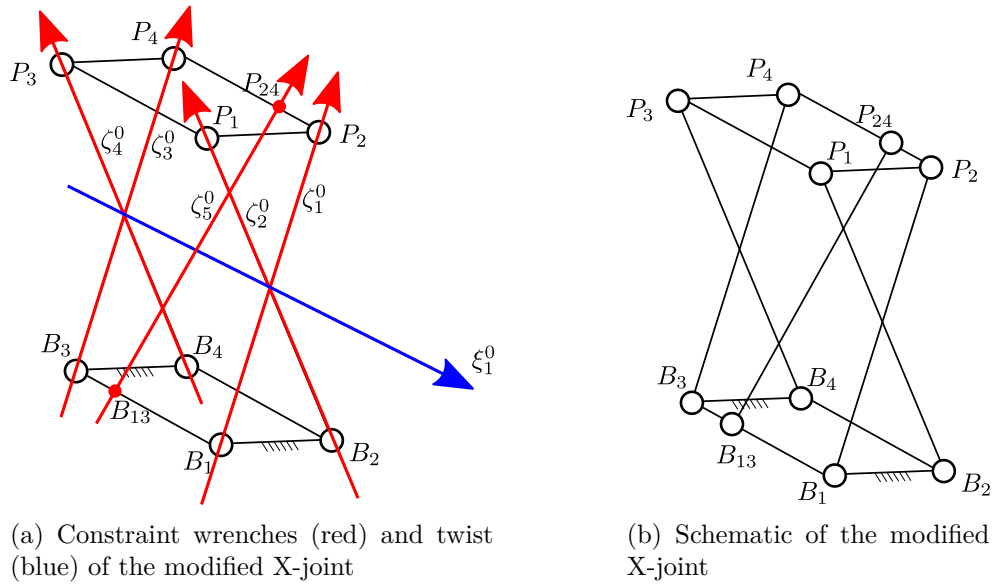


Figure 7.4 – Modified X-joint with five bars and spherical joints.

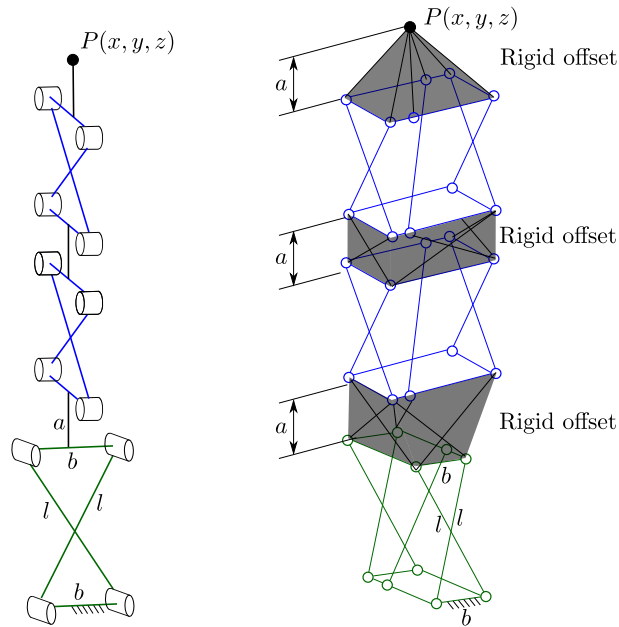


Figure 7.5 – Construction of the spatial tensegrity-inspired 3-X manipulator with modified X-joints.

the entire range of movement. This proposition is confirmed through a CAD simulation as shown in this link¹. It is observed that in one of the views, the modified X-joint looks exactly like a planar X-joint during the entire range of movement. Note that in the CAD model, the attachment points of the bars were moved along their respective lines \mathcal{L}_i to prevent interference between them. This change is similar to placing the bars of a planar X-joint in parallel planes, which does not alter the movement characteristics of the joint.

Thus, the modified X-joint can be used to construct spatial tensegrity-inspired manipulators, such as the 3-X manipulator as shown in Fig. 7.5, without compromising on the tensegrity property. However, it should be remarked that the platforms at the base and top of the modified X-joint will be subjected to a complex loading pattern, including bending, but they do not transmit these moments to the bars, thanks to the connections with spherical joints. The rigid offsets between two joints can also be realized within the tensegrity paradigm by appropriately adding a sixth bar to the modified X-joint as shown in Fig. 7.5.

The kinematic equivalence of the modified X-joint with its planar counterpart will permit us to study the kinematics of the 3-X manipulator by modeling the joint modules as planar X-joints, thereby simplifying the problem at hand. On the contrary, a few practical issues are associated with the modified X-joint, such as the collision between the top and base platforms and the limited range of movement offered by the spherical joints. These issues will be addressed in Section 7.7.

The remaining sections focus on the kinematic analysis of the spatial 3-X manipulator.

7.3 Kinematic model of 3-X manipulator

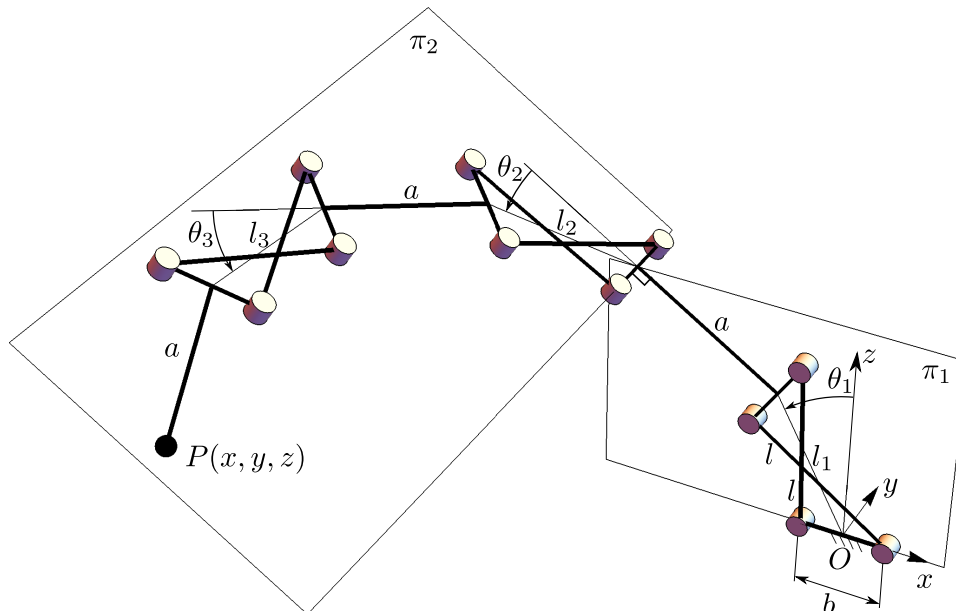


Figure 7.6 – Kinematic diagram of the spatial 3-X manipulator.

1. <https://youtu.be/ziyujL1sjiA>

The kinematic diagram of the 3-X spatial manipulator at an arbitrary configuration is shown in Fig. 7.6. It comprises three identical planar X-joints, whose base and top bars are of length b while the crossed bars are of length l . The first X-joint operates in the plane π_1 , the xz -plane in the global frame of reference. On the other hand, the second and third joints operate in the plane π_2 that is perpendicular to π_1 .

The movement of joint i is measured by the coordinate θ_i , which is the orientation of the line joining the mid-points of the base and top bars of the X-joint relative to a reference perpendicular to its base. There are three offsets of length a between successive joints and the last joint and the end-effector point P .

From Fig. 7.6, the direct kinematics of the manipulator, which involves expressing the position of the end-effector in terms of the joint angles, can be presented as follows:

$$\begin{cases} x = -\sin(2\theta_1) \{a \cos(2(\theta_2 + \theta_3)) + a \cos(2\theta_2) + a + l_3(\theta_3) \cos(2\theta_2 + \theta_3) + l_2(\theta_2) \cos(\theta_2)\} \\ \quad - l_1(\theta_1) \sin(\theta_1) \\ y = -a \sin(2(\theta_2 + \theta_3)) - a \sin(2\theta_2) - l_3(\theta_3) \sin(2\theta_2 + \theta_3) - l_2(\theta_2) \sin(\theta_2) \\ z = \cos(2\theta_1) \{a \cos(2(\theta_2 + \theta_3)) + a \cos(2\theta_2) + a + l_3(\theta_3) \cos(2\theta_2 + \theta_3) + l_2(\theta_2) \cos(\theta_2)\} \\ \quad + l_1(\theta_1) \cos(\theta_1) \\ \text{where } l_i(\theta_i) = \sqrt{l^2 - b^2 \cos^2(\theta_i)} \text{ for } i = 1, 2, 3 \end{cases} \quad (7.1)$$

The following section studies the inverse kinematic model of this manipulator.

7.4 Inverse kinematic model

The problem of inverse kinematics involves finding all possible joint angles $(\theta_1, \theta_2, \theta_3)$ for a given end-effector position (x, y, z) while the bar lengths are all known. This problem can be decomposed into two sub-problems for this manipulator. The first one involves finding all possible θ_1 values, and the second one involves computation of (θ_2, θ_3) for each value of θ_1 . These problems are described in the next two sections, followed by a numerical example.

7.4.1 First sub-problem

Since the first X-joint is in plane π_1 that is perpendicular to the plane π_2 of the other two joints, it is possible to compute the feasible values of θ_1 independent of the other two angles. From Fig. 7.6, it is apparent that θ_1 cannot alter the y -coordinate of the point P . Hence, the given end-effector point can be projected on the plane π_1 to obtain the point $P'(x, 0, z)$ as shown in Fig. 7.7. The plane π_2 has been suppressed, but its line of intersection with π_1 is indicated by the segment connecting X-joint to the point P' . A virtual prismatic joint with coordinate d_1 has been added along this line to locate the point P' from the first joint. Thus, we have an XP manipulator in the plane π_1 .

The first sub-problem consists of finding all possible θ_1 that can position the plane π_2 to meet the point P' (or point P). Equivalently, it involves finding the feasible coordinates (θ_1, d_1) for a given point P' .

It is possible to express the kinematics of this XP manipulator using $l_1 = \sqrt{l^2 - b^2 \cos^2 \theta_1}$ as in Eq. (7.1). However, the associated equations must be squared to eliminate the square

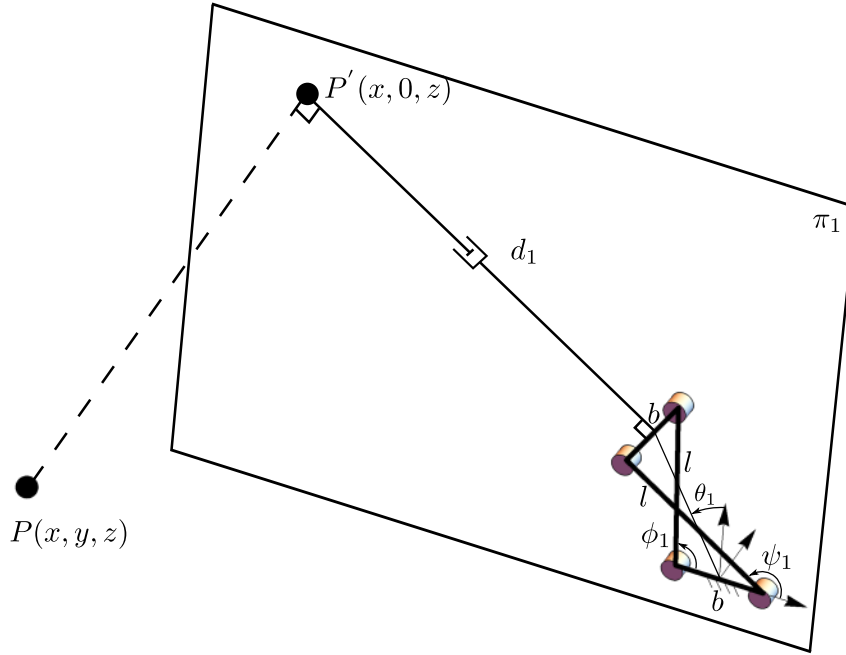


Figure 7.7 – First sub-problem in inverse kinematics.

roots, which would inject spurious solutions in the process. As an alternative, it is possible to express the direct kinematics in terms of the intermediate angle (ϕ_1) and include the associated loop-closure equation in the model, as carried out in [FW19],[WF21]. This process leads to the following equations:

$$\begin{cases} -(b/2) + l \cos(\phi_1) - (b/2) \cos(2\theta_1) - d_1 \sin(2\theta_1) - x = 0 \\ l \sin(\phi_1) - (b/2) \sin(2\theta_1) + d_1 \cos(2\theta_1) - z = 0 \\ b(1 + \cos(2\theta_1)) - l \{ \cos(\phi_1) + \cos(-2\theta_1 + \phi_1) \} = 0 \end{cases} \quad (7.2)$$

The above system contains three equations in three unknowns (θ_1, d_1, ϕ_1). Hence, it is possible to eliminate two of them and obtain a univariate polynomial involving only one of the variables. In order to simplify the elimination process, the equations are normalized by setting $l = 1$ without any loss of generality. Then, the `Projection` command from the `SIROPA` library of `Maple` was used to obtain the univariate polynomial in $t = \tan(\phi_1/2)$. More details on its implementation and applications can be found in [Cha+20]. The obtained univariate polynomial is presented below:

$$4(b+1)^2(x+1)t^4 - 16(b+1)zt^3 + 8(b^2-3)xt^2 - 16(b-1)zt + 4(b-1)^2(x-1) = 0 \quad (7.3)$$

It has a degree of 4, which indicates that there can be up to four real ϕ_1 for a given end-effector point P . For a feasible value of ϕ_1 , a unique combination of (θ_1, d_1) can be computed from the relations in Eq. (7.2).

Thus, the first sub-problem admits up to four solutions for θ_1 . The following section explores the second sub-problem.

7.4.2 Second sub-problem

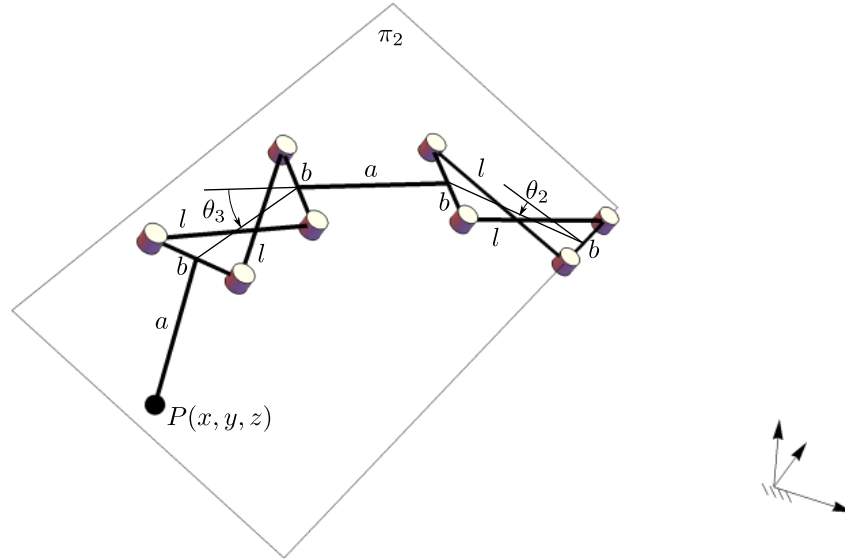


Figure 7.8 – Second sub-problem in inverse kinematics.

The second sub-problem in inverse kinematics involves computing the angles (θ_2, θ_3) for a given value of θ_1 . This sub-problem is confined to the plane π_2 and can be represented graphically as in Fig. 7.8. The plane π_2 and the base pivots of the first X-joint in this plane are known once θ_1 is given. Since the point P is also known, the computation of (θ_2, θ_3) is the same as computing the inverse kinematics of a planar 2-X manipulator with offsets. This problem has already been solved in [WF21], and it is known that there are up to eight solutions to this problem. Thus, combining the two sub-problems, there can be up to 32 (4×8) solutions for the inverse kinematic problem of the 3-X manipulator.

The following section presents a numerical example with thirty-two real solutions for this problem.

7.4.3 Numerical example

As a numerical illustration, consider the 3-X manipulator with the following geometry $b = 1$, $l = 2$, and $a = 6$. Note that all the lengths are normalized w.r.t. b , without any loss of generality. This setting obviates the need to specify the units of points and lengths of the bars. When the end-effector is positioned at the location $(x, y, z) = (3/2, 1, 3/2)$, thirty-two real inverse kinematic solutions are obtained as presented in Table 7.1. Note that these computations do not consider limits on the movement of the joints due to the flat-singularities. If one were to impose the bounds due to flat-singularities as $\theta_i \in]-\frac{\pi}{2}, \frac{\pi}{2}[$, $i = 1, 2, 3$, then, only six solutions are feasible.

The four configurations of the first joint are shown in different shades of gray in Fig. 7.9. The eight feasible configurations obtained for each value of θ_1 are presented in Fig. 7.10. All the thirty-two configurations are visualized in the same picture in Fig. 7.11.

Table 7.1 – Thirty-two inverse kinematic solutions for the 3-X manipulator with geometry $b = 1, l = 2, a = 6$ and the end-effector positioned at $(x, y, z) = (3/2, 1, 3/2)$. All the angular measures are presented in radians.

No.	θ_1	θ_2	θ_3	No.	θ_1	θ_2	θ_3
1	2.86	2.81	1.88	17	-0.68	2.30	2.19
2		2.97	-1.62	18		2.48	-1.34
3		-2.48	1.67	19		-2.30	1.37
4		-2.38	-1.82	20		-2.13	-2.15
5		-1.13	2.01	21		-1.23	2.33
6		-0.92	-1.45	22		-1.04	-1.17
7		1.27	1.40	23		1.21	1.14
8		1.48	-2.07	24		1.41	-2.36
9	-1.38	2.16	2.36	25	0.82	2.00	2.61
10		2.36	-1.20	26		2.24	-1.03
11		-2.22	1.22	27		-2.14	1.05
12		-2.04	-2.33	28		-1.91	-2.57
13		-1.31	2.50	29		-1.42	2.73
14		-1.10	-1.03	30		-1.18	-0.87
15		1.24	1.01	31		1.30	0.84
16		1.46	-2.53	32		1.55	-2.77

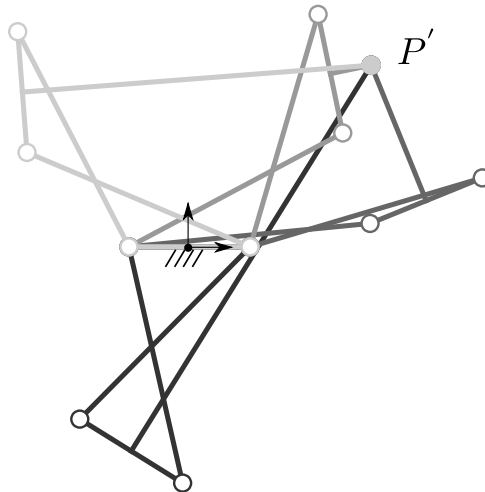


Figure 7.9 – Four feasible configurations of the first joint ($\theta_1 = \{2.86, -1.38, -0.68, 0.82\}$ rad) for a manipulator with geometry $b = 1, l = 2, a = 6$, when the end-effector is located at $(x, y, z) = (3/2, 1, 3/2)$.

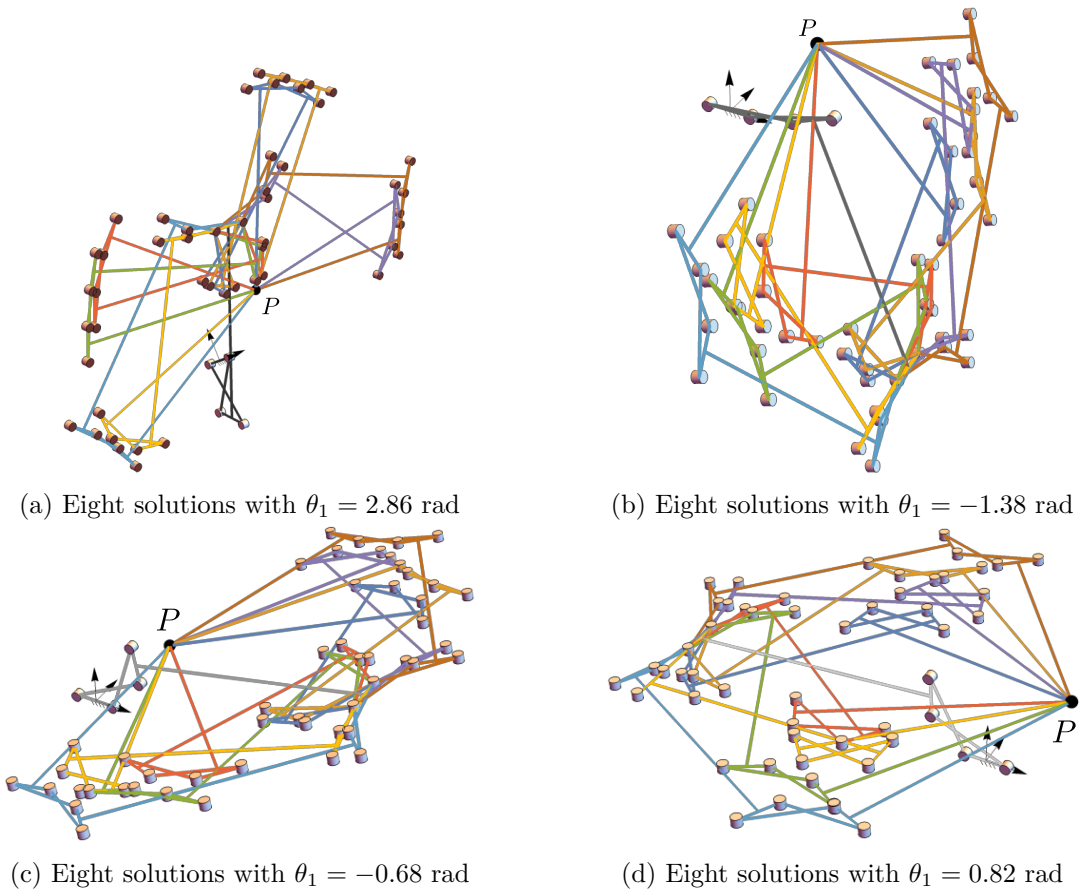


Figure 7.10 – Thirty-two inverse kinematic solutions of the manipulator (separated into four groups) with geometry $b = 1, l = 2, a = 6$, when the end-effector is located at $(x, y, z) = (3/2, 1, 3/2)$.

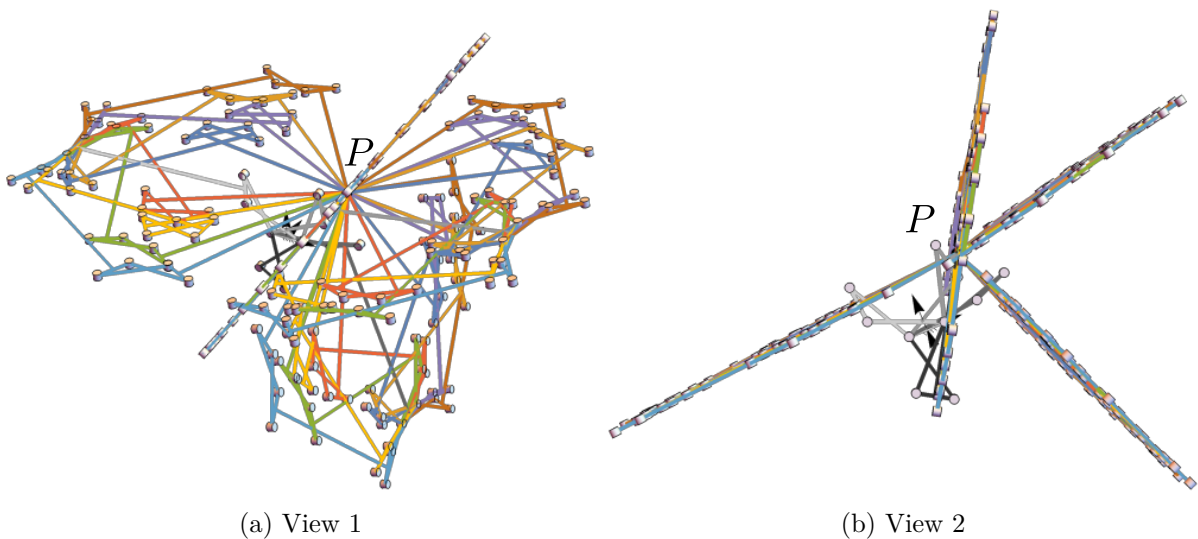


Figure 7.11 – Plot of all thirty-two inverse kinematic solutions of the manipulator together. The geometry of the manipulator is $b = 1, l = 2, a = 6$, and the end-effector is located at $(x, y, z) = (3/2, 1, 3/2)$.

7.5 Singularity analysis

The relation between end-effector velocity and the joint velocities can be obtained by differentiating the direct kinematic equations in Eq. (7.1) w.r.t. time. This yields:

$$\begin{bmatrix} \dot{x} \\ \dot{y} \\ \dot{z} \end{bmatrix} = \mathbf{J}_{3x} \begin{bmatrix} \dot{\theta}_1 \\ \dot{\theta}_2 \\ \dot{\theta}_3 \end{bmatrix} \quad (7.4)$$

where \mathbf{J}_{3x} is the Jacobian matrix of the position vector $[x, y, z]^\top$ w.r.t. the joint orientation vector $[\theta_1, \theta_2, \theta_3]^\top$. The singularity condition of the manipulator is obtained from the vanishing of the determinant of \mathbf{J}_{3x} , which, upon clearing the non-zero factors, leads to:

$$\det(\mathbf{J}_{3x}) = 0 \implies \sigma_1 \sigma_2 = 0 \quad (7.5)$$

where,

$$\begin{aligned} \sigma_1 = & -32a^2 \sin(\theta_3) \cos(\theta_3) \sqrt{l^2 - b^2 \cos^2(\theta_2)} \sqrt{l^2 - b^2 \cos^2(\theta_3)} - 4ab^2 \sin(\theta_2 - 2\theta_3) \sqrt{l^2 - b^2 \cos^2(\theta_3)} \\ & + 8ab^2 \sin(\theta_3) \sqrt{l^2 - b^2 \cos^2(\theta_2)} + 8ab^2 \sin(3\theta_3) \sqrt{l^2 - b^2 \cos^2(\theta_2)} \\ & + 4ab^2 \sin(\theta_2 + 2\theta_3) \sqrt{l^2 - b^2 \cos^2(\theta_3)} - 16al^2 \sin(\theta_3) \sqrt{l^2 - b^2 \cos^2(\theta_2)} \\ & - 8al^2 \sin(\theta_2 + 2\theta_3) \sqrt{l^2 - b^2 \cos^2(\theta_3)} + b^4 \sin(\theta_2 - \theta_3) - b^4 \sin(\theta_2 + \theta_3) - b^4 \sin(\theta_2 + 3\theta_3) \\ & + b^4 \sin(\theta_2 - 3\theta_3) - 2b^2 l^2 \sin(\theta_2 - \theta_3) + 4b^2 l^2 \sin(\theta_2 + \theta_3) + 2b^2 l^2 \sin(\theta_2 + 3\theta_3) \\ & + 8b^2 \sin(\theta_3) \cos(\theta_3) \sqrt{l^2 - b^2 \cos^2(\theta_2)} \sqrt{l^2 - b^2 \cos^2(\theta_3)} - 4l^4 \sin(\theta_2 + \theta_3) \end{aligned} \quad (7.6)$$

$$\begin{aligned} \sigma_2 = & 2\sqrt{l^2 - b^2 \cos^2(\theta_1)} \left\{ a \cos(2(\theta_2 + \theta_3)) + a \cos(2\theta_2) + a \right. \\ & \left. + \cos(2\theta_2 + \theta_3) \sqrt{l^2 - b^2 \cos^2(\theta_3)} + \cos(\theta_2) \sqrt{l^2 - b^2 \cos^2(\theta_2)} \right\} + (l^2 - b^2) \cos(\theta_1) \end{aligned} \quad (7.7)$$

The singularity of the 3-X manipulator occurs when $\sigma_1 = 0$ or $\sigma_2 = 0$. Interestingly, the factor σ_1 is only a function of θ_2 and θ_3 , while the factor σ_2 involves all three angles. Physically, the vanishing of σ_1 corresponds to the singularity of the planar 2-X manipulator in the plane π_2 , i.e., when the instantaneous centers of rotation of the two X-joints and the end-effector point become collinear as shown in Fig. 7.12.

In contrast, the geometric interpretation of the singularity due to $\sigma_2 = 0$ is more complicated. A special example of this singularity is presented in Fig. 7.13a, where the end-effector falls on the instantaneous axis of rotation of the first joint. In this configuration, the first joint cannot produce any velocity at the end-effector, and the manipulator is singular. A more general occurrence of $\sigma_2 = 0$ is presented in Fig. 7.13b, where the normal to plane π_2 dropped from the end-effector point intersects with the instantaneous axis of rotation of the first joint. In such a configuration, the velocity produced by the first joint at the end-effector lies in the plane π_2 , just as those produced by the second and third joints. Thus, the end-effector loses its ability to move out of the plane π_2 at this configuration, making the manipulator singular.

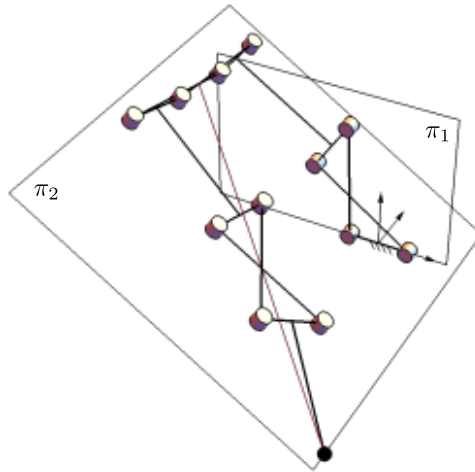
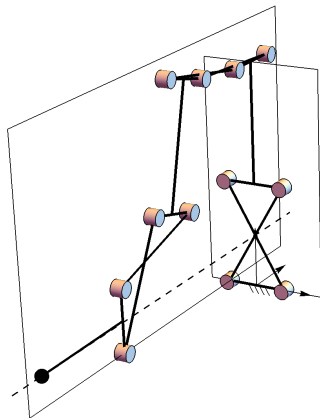
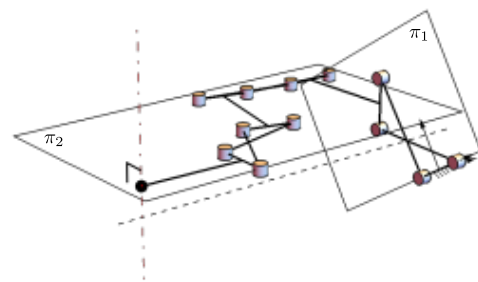


Figure 7.12 – Singular configuration of the 3-X manipulator with geometry $b = 1, l = 2, a = 2$, at $(\theta_1, \theta_2, \theta_3) = (0.5, 1.45, -0.26)$ rad corresponding to $\sigma_1(\theta_2, \theta_3) = 0$.



(a) $(\theta_1, \theta_2, \theta_3) = (0, 1.45, -0.66)$ rad



(b) $(\theta_1, \theta_2, \theta_3) = (0.5, 1.45, -0.68)$ rad

Figure 7.13 – Singular configurations of the 3-X manipulator with geometry $b = 1, l = 2, a = 2$, corresponding to $\sigma_2(\theta_1, \theta_2, \theta_3) = 0$.

7.6 Workspace of 3-X manipulator

This section presents a method to compute and visualize the workspace of the 3-X manipulator considering joint limits, but neglecting self-collisions in the manipulator. As an example, the geometry of the manipulator is chosen to be $b = 1, l = 2, a = 2$. The movements of the X-joints are limited between the flat-singularities as $\theta_i \in]-\frac{\pi}{2}, \frac{\pi}{2}[$, $i = 1, 2, 3$. A simple brute-force approach is to discretize the joint space into several grid points and plot their images in the task space to obtain a point cloud representing the workspace of the manipulator. Another possibility is to discretize the task space into uniform grid points and solve the inverse kinematic problem at each point to determine if it is inside the workspace or not [Gna23]. However, these approaches are computationally intensive, and the resulting point cloud is challenging to understand.

A better approach would be to obtain the workspace boundaries directly using the singularity conditions and joint limits, as illustrated for the planar 2-X manipulator in Chapter 3. This task is carried out in Section 7.6.1, and several planar cross-sections of the derived workspace are studied in Section 7.6.2.

7.6.1 Construction of the workspace

Since wrench-feasibility and stability are not considered in this study, the resulting workspace boundaries will be composed of images of the joint limits and the singularities within the joint limits. Following the same strategy presented in Chapter 3, the boundaries of the feasible regions are constructed in the joint space and then mapped to the task space using the direct kinematic model.

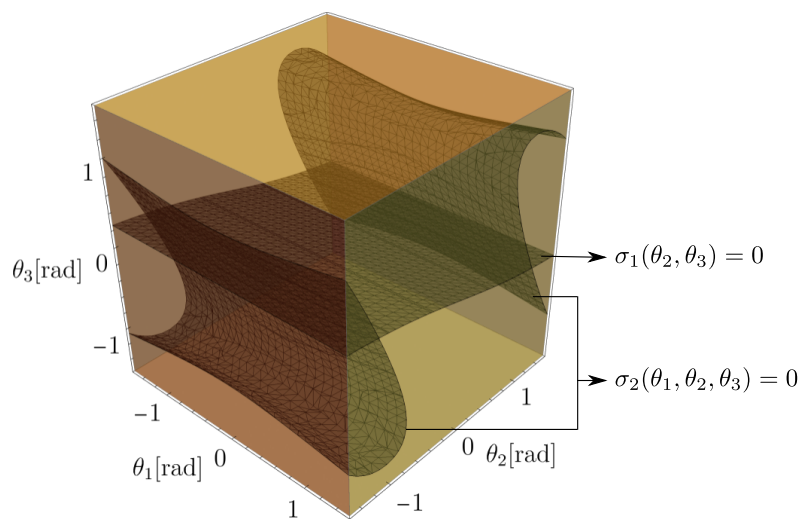


Figure 7.14 – Singularity surfaces ($\sigma_1 = 0, \sigma_2 = 0$) and joint limits ($\theta_1, \theta_2, \theta_3 = \pm\frac{\pi}{2}$) of a manipulator with geometry $b = 1, l = 2, a = 2$.

The joint limits form six faces of a cube in the joint space, as shown by the golden planes in Fig. 7.14. However, the representation of singularity contours is rather involved. The two singularity conditions $\sigma_1 = 0$ and $\sigma_2 = 0$ are treated separately. As per the computational scheme

in Section 3.6.2, the joint space is discretized into 900^2 equally spaced grid lines emerging from the faces (θ_1, θ_2) , (θ_2, θ_3) , and (θ_1, θ_3) . The singularity conditions $\sigma_1 = 0$ and $\sigma_2 = 0$ are rewritten as univariate polynomials in the tangent of half of one of the angles by suppressing the other two in the coefficients. These polynomials are solved appropriately to obtain all the singular points on the grid lines. Then, an interpolation is performed among these points with small triangular planes as a means for approximating the actual singularity surface. The resulting surfaces for $\sigma_1 = 0$ and $\sigma_2 = 0$ are plotted in black shade in Fig. 7.14.

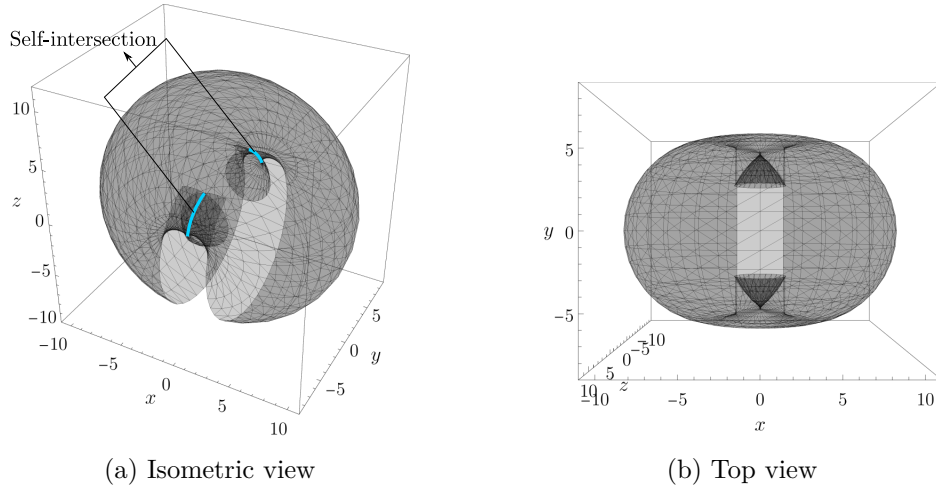


Figure 7.15 – Image of the singularity surface $\sigma_1(\theta_2, \theta_3) = 0$ for the manipulator $b = 1, l = 2, a = 2$.

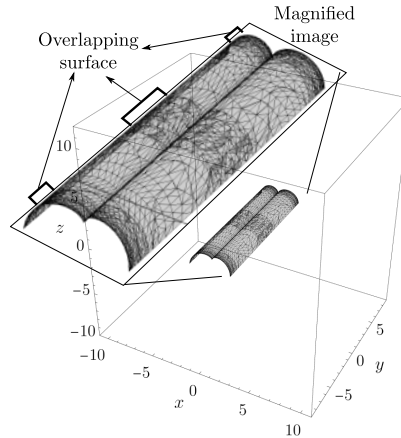


Figure 7.16 – Image of the singularity surface $\sigma_2(\theta_1, \theta_2, \theta_3) = 0$ for the manipulator $b = 1, l = 2, a = 2$.

In order to facilitate the plotting in the task space, the planes corresponding to joint limits are also split into small triangles. The vertices of the triangles on all the surfaces are mapped into the task space using the direct kinematic model in Eq. (7.1). The images of $\sigma_1 = 0$ and $\sigma_2 = 0$

2. The discretization can be made with any number of grid lines. The number 900 was chosen as a compromise between the accuracy of the depiction and the associated computation time.

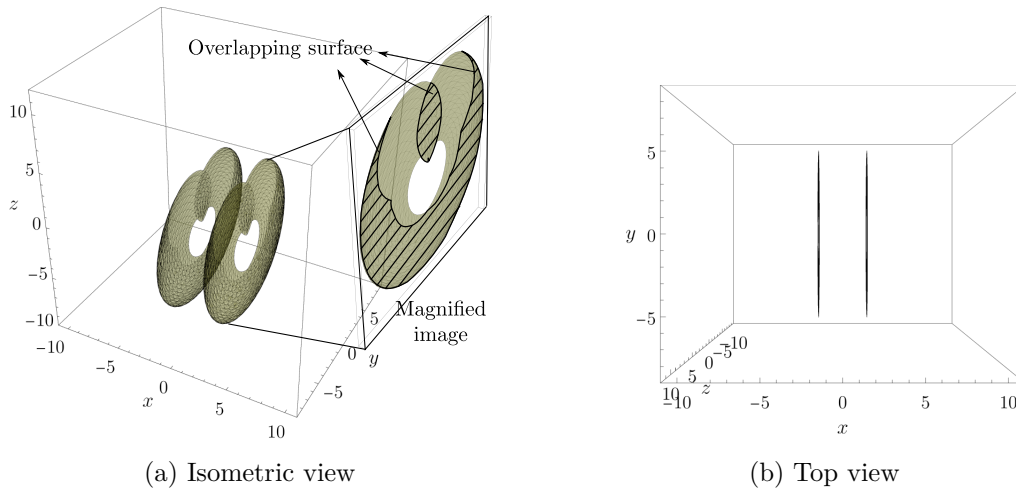


Figure 7.17 – Image of the joint limits $\theta_1 = \pm \frac{\pi}{2}$ for the manipulator $b = 1, l = 2, a = 2$.

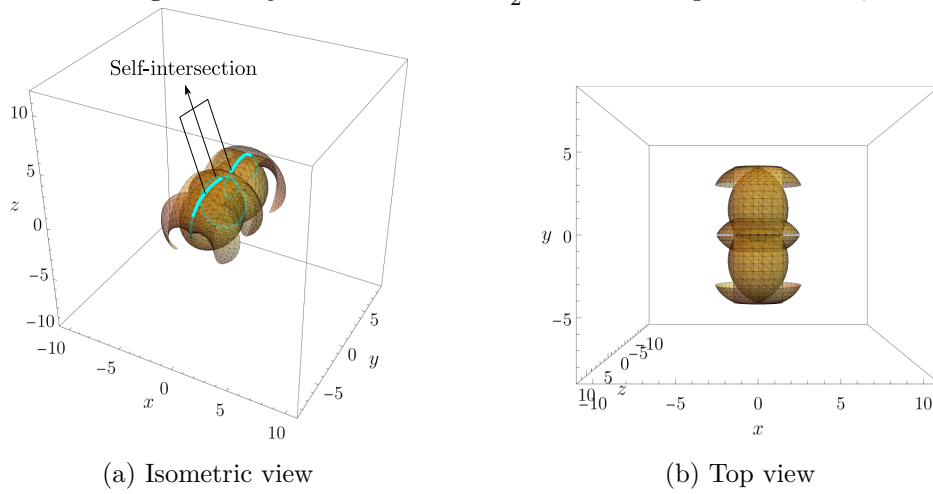


Figure 7.18 – Image of the joint limits $\theta_2 = \pm \frac{\pi}{2}$ for the manipulator $b = 1, l = 2, a = 2$.

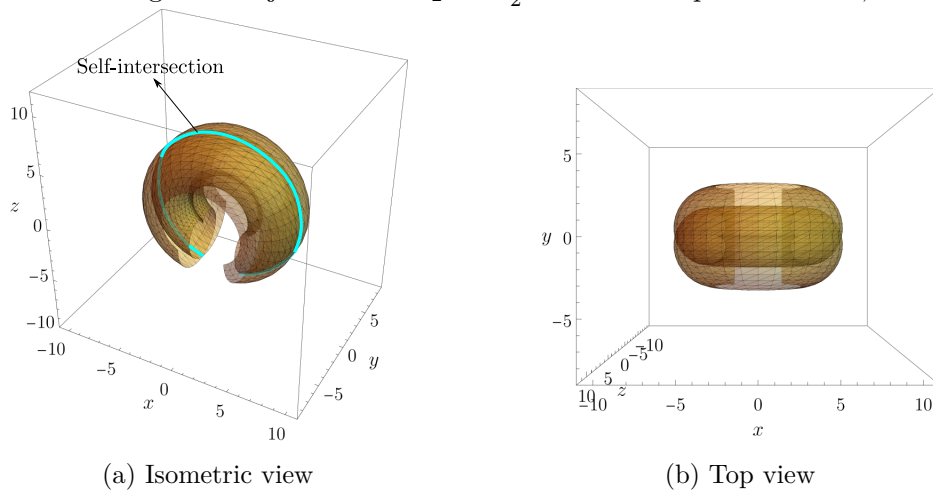


Figure 7.19 – Image of the joint limits $\theta_3 = \pm \frac{\pi}{2}$ for the manipulator $b = 1, l = 2, a = 2$.

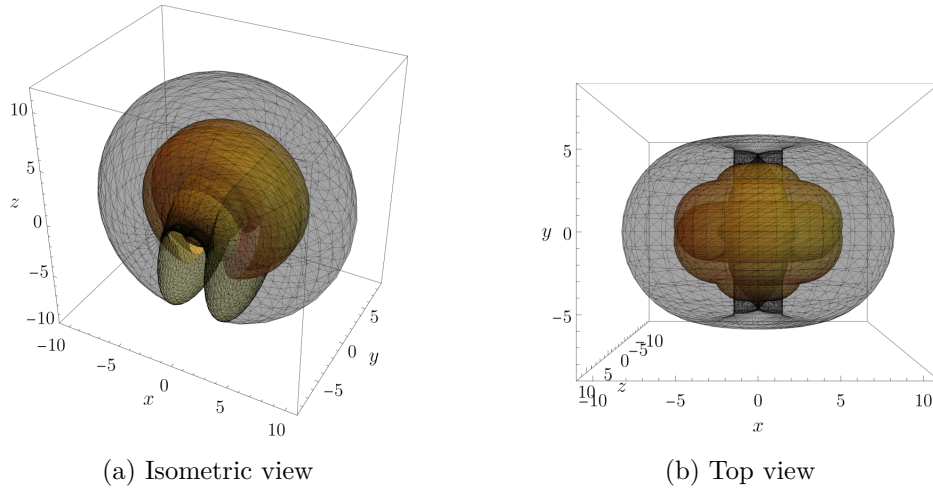


Figure 7.20 – Workspace boundaries of the 3-X manipulator with geometry $b = 1, l = 2, a = 2$, and joint limits $\theta_i = \pm \frac{\pi}{2}, i = 1, 2, 3$.

are presented in Figs. 7.15 and 7.16, respectively. It is observed that the surface corresponding to $\sigma_1 = 0$ looks like a part of a sphere with foldings on the inside, causing self-intersections at $x = 0$. On the other hand, the image of $\sigma_2 = 0$ appears to contain two semi-cylindrical surfaces touching one another at $x = 0$. Furthermore, certain portions on these surfaces have overlappings, as indicated in Fig. 7.16.

The images of joint limits of the first, second, and third joints are presented in Figs. 7.17, 7.18, and 7.19, respectively. It is observed that the limits of joint 1, $\theta_1 = \pm \frac{\pi}{2}$, have two identical planar images in the task space, which is logical since the end-effector remains in the plane π_2 while the first joint is fixed. However, these planes have overlapping regions, as highlighted in the magnified portion in Fig. 7.17a. The images of $\theta_2 = \pm \frac{\pi}{2}$ contain two symmetric parts, each of which looks like an ellipsoid with end caps. Notably, these surfaces intersect at $x = 0$ and $y = 0$, as indicated in Fig. 7.18a. The images of $\theta_3 = \pm \frac{\pi}{2}$ consist of two hollow tubes that intersect with each other at $y = 0$ as shown in Fig. 7.19a.

The complete workspace of the 3-X manipulator is obtained by combining all the boundaries together, as shown in Fig. 7.20. It is apparent that the workspace is symmetric about the planes $x = 0$ and $y = 0$. However, it is impossible to see the various regions it encompasses.

Hence, further study is conducted by visualizing several cross-sections of the workspace in the following.

7.6.2 Cross-sections of the workspace

The workspace of the 3-X manipulator shown in Fig. 7.20 is cut by the plane $x = 0$, and the resulting section is visualized in Fig. 7.21. Firstly, we observe that the section is symmetric about $y = 0$, which was expected. The boundaries due to singularities and joint limits split the workspace into regions with different numbers of inverse kinematic solutions, as indicated by the different colors in the figure. There is a large region close to the reachable boundary of the workspace with two inverse kinematic solutions. There are several small regions with the number of solutions ranging from zero to six around the origin.

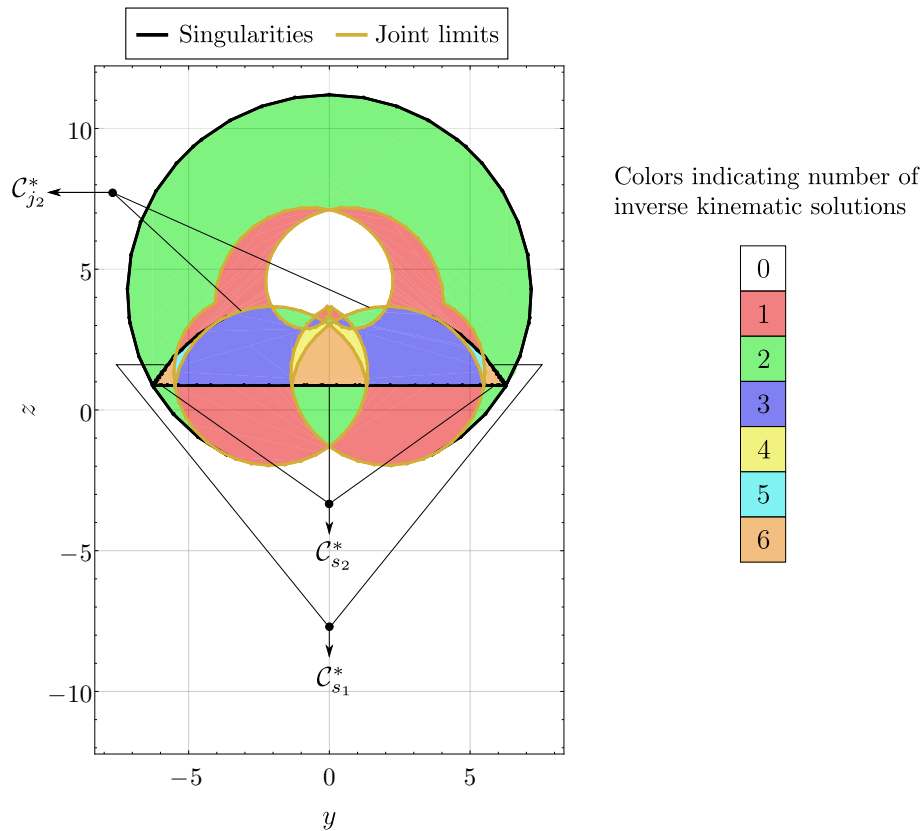


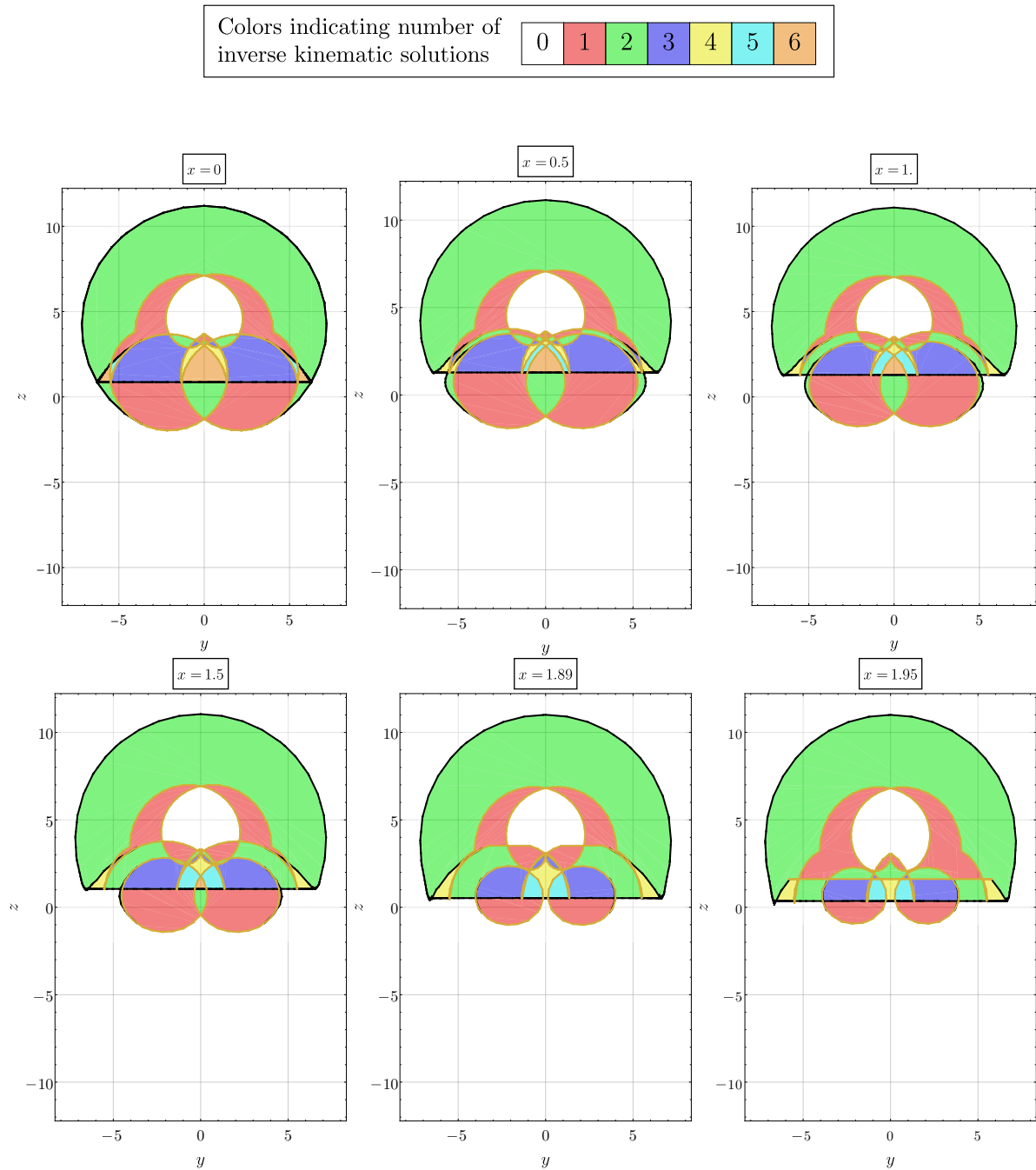
Figure 7.21 – Section of the workspace at $x = 0$ for the manipulator $b = 1, l = 2, a = 2$.

The number of solutions generally changes by one across a joint limit curve and by two across a singularity curve. However, there are certain special curves marked as $(\mathcal{C}_{s_1}^*, \mathcal{C}_{s_2}^*, \mathcal{C}_{j_2}^*)$ where this rule is not respected. It is because these curves lie on the self-intersections/overlapping surfaces of the singularity (see Figs. 7.15, 7.16) and joint limits (see Fig. 7.18). Thus, the number of solutions changes by four across the singularity curves $\mathcal{C}_{s_1}^*$ and $\mathcal{C}_{s_2}^*$, and by two across the joint limit curve $\mathcal{C}_{j_2}^*$. In effect, two pairs of inverse kinematic solutions become singular on the curves $\mathcal{C}_{s_1}^*$ and $\mathcal{C}_{s_2}^*$, while two solutions reach the limits of the second joint on the curve $\mathcal{C}_{j_2}^*$.

In order to understand the complete workspace, it is sliced at different values of $x \in [0, 10.5]$. The negative values of x are not considered as the workspace is symmetric about $x = 0$. The cross-sections of the workspace are displayed in Figs. 7.22, 7.23, and 7.24. Essential observations from these plots are listed in the following:

— **Sections of $x \in [0, 1.95]$** (Fig. 7.22):

As one moves from $x = 0$ to $x = 0.5$, the special curves $(\mathcal{C}_{s_1}^*, \mathcal{C}_{j_2}^*)$ are no longer present as the self-intersections in the respective surfaces occur only at $x = 0$. However, the special curve $\mathcal{C}_{s_2}^*$ still exists in all the sections when $x \in [0, 1.95]$, as the overlapping singularity surfaces in Fig. 7.16 is present throughout this range. The size of the region with six inverse kinematic solutions decreases as x increases and disappears beyond $x = 1.89$. It is observed that a new joint limit curve that is parallel to the y -axis appears when $x \geq 1.89$. It is cast by the limit $\theta_1 = \frac{\pi}{2}$, whose planar section intersects with the respective

Figure 7.22 – Sections of the workspace at $x \in [0, 1.95]$ for the manipulator $b = 1, l = 2, a = 2$.

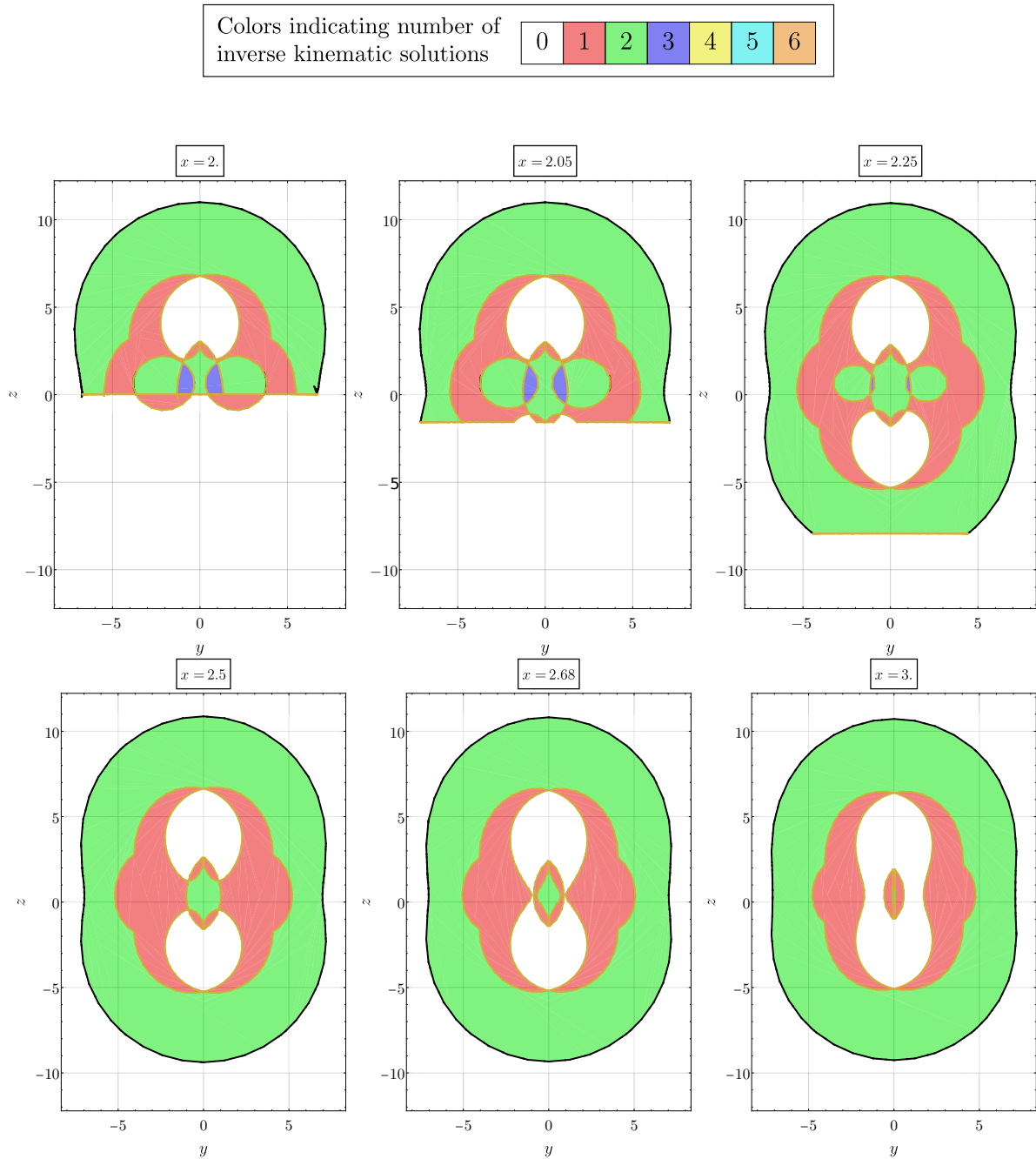
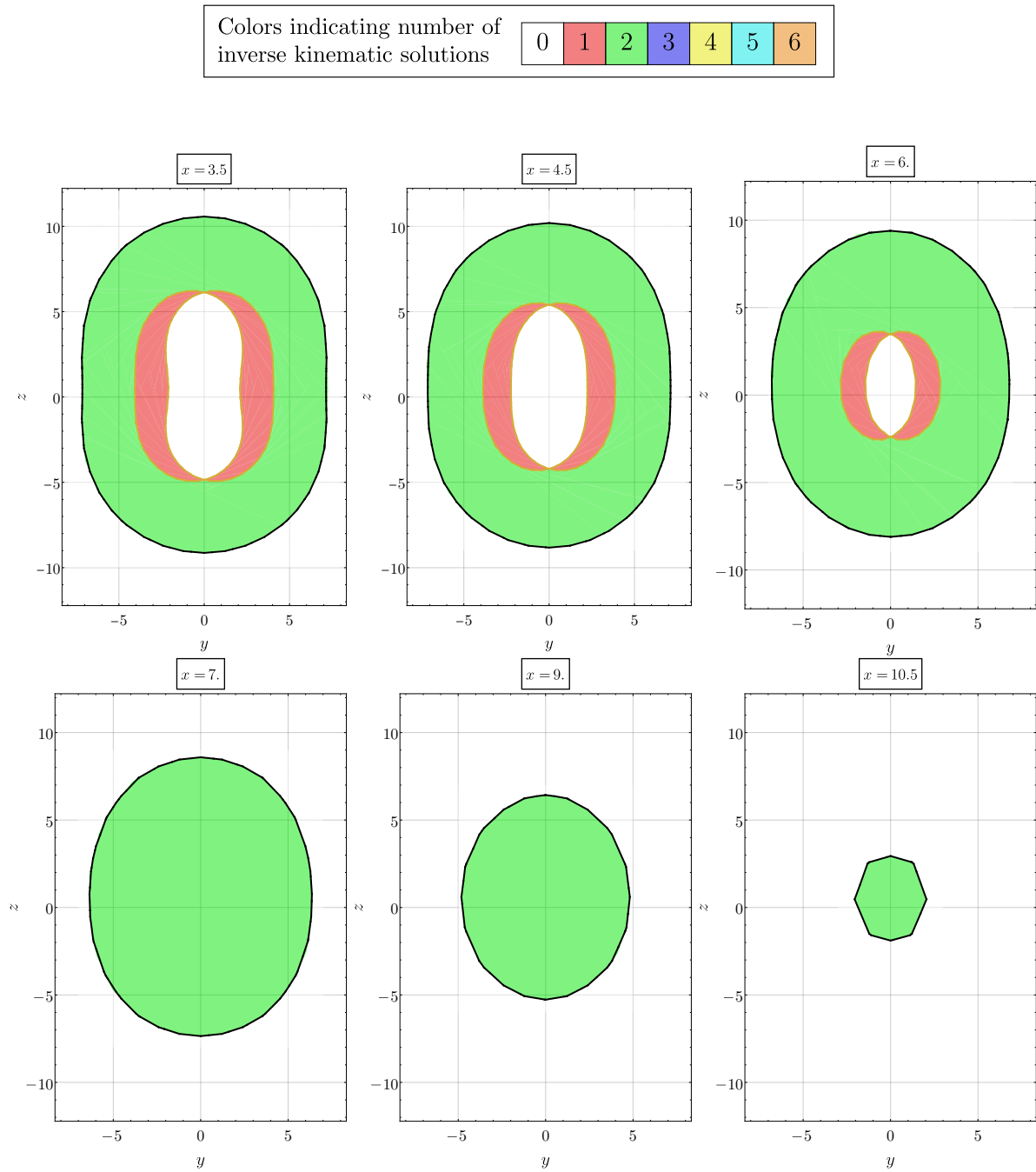


Figure 7.23 – Sections of the workspace at $x \in [2, 3]$ for the manipulator $b = 1, l = 2, a = 2$.

Figure 7.24 – Sections of the workspace at $x \in [3.5, 10.5]$ for the manipulator $b = 1, l = 2, a = 2$.

sectioning planes (see Fig. 7.17). Note that some parts of this limiting curve originate from overlapping surfaces and are hence special, i.e., they separate regions with a difference of two inverse kinematic solutions (see, e.g., section $x = 1.95$).

— **Sections of $x \in [2,3]$** (Fig. 7.23):

Beyond $x = 2$, the maximum number of inverse kinematic solutions reduces to three, and beyond $x = 2.5$, it further drops to two. However, the overall size of the workspace section nearly doubles from $x = 2$ to $x = 2.5$. We can understand this from the picture of the complete workspace in Fig. 7.20a, which shows that region $z < 0$ is not reachable around $x = 0$ but becomes accessible further from it. As x increases beyond 2.5, the voids in the middle grow and eventually merge into a single component, as seen in the section $x = 3$.

— **Sections of $x \in [3.5,10.5]$** (Fig. 7.24):

In the range $x \in [3.5, 6]$, the outer boundary of the workspace section, the regions with one solution, and the void decrease in size gradually. Whereas in the range $x \in [7, 10.5]$, the workspace sections contain only a single component with two solutions without any internal boundaries, and its size decreases significantly. The limit of the workspace occurs just after $x = 10.5$.

In summary, the sections of the workspace with $x \in [0, 2]$ contain a large region with two inverse kinematic solutions, a void at the center, and several small regions with up to six solutions. In the range $x \in [2, 3]$, the size of the workspace section increases two-fold, and the maximum number of inverse kinematic solutions is limited to three. Finally, when x increases from 3.5 to 10.5, the workspace section decreases in size globally, and beyond $x = 7$, it contains only one component with two inverse kinematic solutions.

The following section presents a prototype of the 3-X manipulator and discusses its practical issues.

7.7 Proof of concept and practical issues

In order to show the practical feasibility of the proposed 3-X manipulator, plastic prototypes of individual bars and spherical joints are printed and assembled, following the recommendations in [LGC01] for the spherical joints. Then, several practical problems, such as the limited range of movement of spherical joints, are discussed in the following.

Prototype

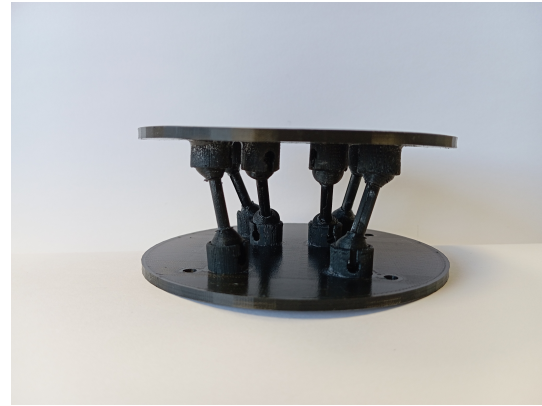
Plastic prototypes of the modified X-joint with five bars and rigid offsets with six bars are presented in Figs. 7.25a and 7.25b respectively. They are assembled in series to form the 3-X spatial tensegrity-inspired manipulator with geometry $b = 1, l = 2, a = 2$, as shown in Fig. 7.26 (right). A prototype of the same manipulator with planar X-joints is also presented in Fig. 7.26 (left) at the same configuration for a better visual understanding.

As a preliminary illustration of its movement, the end-effector of the 3-X manipulator was moved by hand. A video recording of this experiment can be found in this link³. Some of the issues encountered with this model are discussed in the following.

3. <https://youtu.be/yCPheEbnQ6M>



(a) Modified X-joint with five bars



(b) Rigid offset with six bars

Figure 7.25 – Plastic prototypes of modified X-joint (left) and rigid offset (right).



Figure 7.26 – Plastic prototypes of the 3-X spatial manipulator with planar X-joints (left) and modified X-joints (right).

Limited movement of spherical joints



Figure 7.27 – Commercially available rod-end bearing (Source: [Reb]).

Realizing a spherical joint with a ball and socket arrangement, as indicated in Fig. 7.25a, inevitably limits its range of movement to less than 120° (about an arbitrary axis) due to the collision between the bar and the socket. However, the desired range of movement is 180° (about one axis) to achieve the large orientations offered by the X-joint. Hence, a viable solution would be to use the rod-end bearing shown in Fig. 7.27, which offers an unlimited rotation about certain axes. Additionally, it is also possible to replace one of the two spherical joints in each bar with a universal joint to prevent the spinning of the bars about their axes.

Collision between the top and base platforms

Another limiting factor in the workspace of the spatial 3-X manipulator is the collision between its constituent elements. It is particularly pronounced with the modified X-joint due to its large top and base platforms (see Fig. 7.26). In the future, the collisions must be accounted for while computing the workspace of this manipulator.

Load distribution among the bars of a single joint

The proposed design of the modified X-joint contains four bars arranged parallel to the plane of movement and the fifth bar pointing in a different direction (see Figs. 7.4b, 7.25a). Hence, if a force is applied on the moving platform in the direction normal to the plane of movement, it will be balanced only by the fifth bar, which is not ideal. As an improvement, all the bars can be inclined like the fifth bar while maintaining their attachment points on the respective lines ($\mathcal{L}_1, \dots, \mathcal{L}_4$) shown in Figs. 7.2. This modification will preserve the kinematics of the joint while ensuring a better load distribution among the five bars.

Actuation scheme

Finally, we must address the actuation scheme of the 3-X manipulator with cables. This study should start by selecting a suitable number of cables, followed by the possible routing schemes. It would be interesting to study their stable wrench-feasible workspace as presented

in Section 3 for the planar 2-X manipulator. An important practical challenge will be finding a good arrangement of the pulleys to route the cables between joints that move in different planes. These problems should be addressed in the future.

7.8 Conclusions

In this chapter, the planar X-joint was redesigned with spherical joints to make it suitable for building spatial tensegrity-inspired systems. This joint is referred to as the modified X-joint. A 3-DoF spatial positioning manipulator was constructed with three modified X-joints arranged in two perpendicular planes. Due to the kinematic equivalence of the modified X-joint with its planar counterpart, the spatial manipulator was modeled with three planar X-joints for simplicity. The inverse kinematic problem was solved algebraically, and it was found that the manipulator can have up to thirty-two configurations for a given position of the end-effector. A numerical example with thirty-two configurations was presented as a validation. However, only six solutions could be found when the X-joint movement is limited to bounds imposed by the flat-singularities. The singularity conditions for this manipulator were derived and interpreted geometrically. Then, the workspace of the manipulator was studied with joint limits. All the fragments of the workspace boundaries were computed and visualized, for a numerical example. Due to the complex shape of the complete workspace, it was studied by slicing with several planes. The number of inverse kinematic solutions in all the connected regions was represented in each workspace section. Finally, a prototype of the proposed manipulator was presented, and several practical problems were discussed.

It would be interesting to study different cable actuation schemes for this manipulator in the future.

CONCLUSION AND FUTURE WORK

The following sections present a summary of this thesis, its contributions, and directions for future work.

Summary

This thesis studied tensegrity-inspired joints and manipulators antagonistically actuated by redundant cables. A notable difference from the existing literature on this subject is that the cables are not coupled with in-series springs to actuate the joints but are connected directly between two rigid bodies. We showed that it is possible to modulate the stiffness in such systems by changing the tension in the cables. The nature of stiffness modulation was primarily studied for two single-degree-of-freedom (1-DoF) symmetric tensegrity-inspired joints actuated by two cables. Firstly, a revolute joint made of two congruent triangular trusses, one inverted on the top of the other with actuating cables on the two sides, was considered. Secondly, several four-bar mechanisms with symmetric limbs actuated by cables linking the unconnected pivot pairs were considered. We found that the joint stiffness increases with an increase in actuation forces, similar to muscle coactivation in biological joints, only for the four-bar mechanisms with crossed limbs. In the other mechanisms and the revolute joints with congruent triangles, the stiffness decreases with increase in actuation forces. While both sets of joints can be used for stiffness modulation, the ones with coactivation are more energy efficient as they use low forces for low-stiffness tasks and increase them only on demand for high-stiffness tasks. However, we found that the coactivation feature can also be obtained in the other joints by changing their cable attachment points, albeit at the cost of decreasing the feasible range of movement. Among all the joints, the anti-parallelogram mechanism (X-joint) offers the maximum orientation range of $]-\pi, \pi[$ for its top bar relative to the base while exhibiting coactivation and is thus the most suited for developing bio-inspired systems.

Motivated by the above result, a planar positioning manipulator with two X-joints arranged in series with rigid offsets, referred to as the 2-X manipulator, was considered. A payload was placed at the end-effector, and the manipulator was arranged vertically against the direction of gravity. Hence, springs were added to the joints to stabilize the manipulator. Two actuation schemes with four and three cables, respectively, were considered with practical limits on the actuation forces. The 4-cable scheme uses two cables per joint independently, while the 3-cable scheme uses one cable on the right side for each joint and a common cable on the left side. The stable wrench-feasible workspace (SWFW) of the manipulator, which respects the conditions of reachability, wrench-feasibility, and stability, was computed for the two actuation schemes. The 4-cable scheme produces a more symmetric and larger SWFW than its counterpart. Further studies were conducted on the instantaneous velocity, forces, and stiffness performances of the manipulator for the two actuation schemes. It was found that the 4-cable scheme has a symmetric performance on the two halves of its workspace, applies larger forces on the environment, and modulates stiffness over a wider range. On the other hand, the 3-cable scheme offers larger end-effector velocities in certain directions on the right part of the workspace.

Owing to the symmetric and better performance obtained with the 4-cable scheme, subsequent studies were conducted with this scheme. The design issues associated with the 2-X manipulator and another manipulator composed of two R-joints, termed the 2-R manipulator, were addressed. The first issue concerns the joint limits that arise due to the geometry of the joint, cable attachments, and free length of the springs. The second issue is the mechanical feasibility of the springs installed in the joints. The third issue is the safety of the constituent bars from buckling failure. A computational scheme that accounts for all these issues and computes the SWFW for any given bar lengths, spring stiffnesses, and maximal actuation forces was presented and illustrated for 2-X and 2-R manipulators with examples. It was found that an arbitrary choice of design parameters leads to a very small SWFW for the manipulators.

The above scheme was used in an optimization framework to find good designs for the two manipulators by imposing equivalent bounds on their respective design parameters. The maximal actuation force, total moving mass, and size (maximum vertical reach) of the manipulators were set as objectives while they were constrained to possess a disk of a given radius inside their SWFW with a specified payload at the end-effector. The Pareto optimal front was presented for the two manipulators. It was found that the 2-X manipulator has a much smaller mass and size than the 2-R manipulator for all specified payloads and disk radii. In contrast, the 2-R manipulator has a smaller force requirement than its counterpart when the payload is light, and the disk specified is small but has a significantly larger force requirement otherwise.

Due to the promising results obtained with the X-joint in planar manipulators, a modified X-joint for application in spatial tensegrity-inspired manipulators was designed. This version contains five bars connected between fixed and moving platforms using only spherical joints. Such an arrangement ensures no transmission of bending or twisting moments between any components even while the moving platform is subjected to loads perpendicular to the plane of movement, thereby retaining an essential feature of tensegrity systems. Using the modified X-joint, a 3-X spatial positioning manipulator was considered. The inverse kinematic problem for this manipulator was solved algebraically, resulting in a maximum of thirty-two solutions. The singularities of this manipulator and its workspace were studied with numerical examples. Finally, a plastic prototype was presented as a proof of concept and practical issues associated with it were discussed.

Contributions of this thesis

The contributions of this work are listed in the following:

1. **Study of stiffness modulation through force coefficients:**

Chapter 2 presented a simple formula for the force coefficients in the stiffness expression of a general 1-DoF joint, which involves only the first- and second-order derivatives of the cable lengths. It was shown that the correlation between actuation forces and joint stiffness is purely characterized by the signs of these coefficients, which are kinematic quantities. Additionally, it was shown that one obtains the same coefficients in the stiffness expression even if linear springs are introduced in series with the actuating cables and the actuators fix the distal ends of these springs as considered in [Boe+17b],[CCJ18]. This shows that the study of force coefficients is relevant even for designing other tensegrity-inspired systems as well as series elastic actuators. Furthermore, it was illustrated through

several examples that the nature of stiffness modulation can be changed for a given joint by modifying the attachment points of the cables.

2. Fast and robust tool for computing stable-wrench feasible workspace:

Chapter 3 presented a novel method for computing the bounding points of the SWFW accurately and interpolating them with linear segments to obtain a polygonal approximation of the workspace. An existing `c++` library `polylabel`⁴ was used to find the maximally inscribed disk inside the polygon. The entire process is quite generic and can be used to compute the workspace and maximal disk of any planar non-redundant manipulator whose governing conditions (e.g., wrench-feasibility) are available as inequalities. For the 2-X and 2-R manipulators, computation time is in the order of milliseconds for a given design, which enabled the exploration of millions of designs in an optimization framework.

3. Integration of mechanical feasibility of springs in the design process:

As part of the design considerations of a tensegrity-inspired manipulator, the mechanical feasibility conditions associated with the springs, namely, the allowable shear stress, recommended spring index, standard wire diameters, minimum number of active coils, and safe helix angle, were accounted for. Additionally, constraints on the free length and maximum elongation limit derived from the joint range of movement were also incorporated. We showed that the set of all feasible springs defines a two-dimensional design space that can be accessed with two parameters, chosen as the spring stiffness and a selection parameter $\in [0, 1]$. This formulation ensures that the resulting springs are physically feasible. Also, all the dependent parameters, namely, wire diameter, coil diameter, number of coils, spring free length, mass, etc. can be found from the chosen combination of stiffness and the selection parameter.

In the literature, papers that include springs in the design optimization typically consider the spring stiffness and free length as optimization variables [MKA04],[DVA15]. However, this approach assumes that springs of any stiffness can possess any free length independently of each other, and the springs can elongate as much as the application demands. However, these assumptions are not valid physically. Thus, real springs may not exist corresponding to the parameters obtained from the optimizer. Alternatively, it is possible to incorporate the two-parameter representation of the feasible spring space proposed in this thesis to ensure that all the springs considered in the design are physically feasible. Note that this retains the same number of design variables (two) for the springs as the former. The proposed parametrization is relevant for the optimal design of all mechanical systems using springs, e.g., gravity-balancing systems [AB15], variable stiffness joints [CCLCC21], collaborative robots [Jea+20].

4. Design optimization of tensegrity-inspired manipulators considering gravity:

Chapter 6 conducted design optimization of 2-X and 2-R tensegrity-inspired manipulators for carrying a given payload over a specified workspace while accounting for gravity. In the literature on tensegrity systems, gravity effects are usually neglected. However, this work showed that it could significantly influence the design of such manipulators while accounting for their stability. It was also found that in many designs, the total mass of springs is more than the total mass of the moving bars, indicating that the spring mass

4. <https://github.com/mapbox/polylabel>

along with its free length, play a significant part in the static model of such manipulators. A discussion on the placement of the manipulator relative to gravity was also presented, which indicated that for tasks such as pick-and-place, where the payload keeps changing in a cycle, it is best to suspend the manipulator from the ceiling as the increased payload will not destabilize it.

5. **Proposition of spatial tensegrity-inspired manipulators with modified X-joints:** Chapter 7 proposed a method to modify the design of planar X-joint with spherical joints without affecting its kinematics. This modification allowed for its application in spatial tensegrity systems while retaining its planar mathematical model. We proposed a 3-X spatial manipulator with three modified X-joints arranged in two perpendicular planes. We showed that the inherent planar character of each joint facilitates the study of the kinematics and singularities of the manipulator.

Directions for future work

Using the analysis and results of this thesis, we conceive the following directions of work for the future:

1. **Conception of multi-DoF joints:**

This thesis was focused on 1-DoF joints and manipulators constructed out of such joints. However, studying joints with multiple DoF antagonistically actuated by cables could also be interesting. The motivation for this study stems from biological joints where contact between bone surfaces typically permits more than one-DoF. They could be used as remotely actuated wrists in serial/parallel/cable-driven manipulators or for developing bio-inspired systems. These joints have several possible architectures, e.g., universal/spherical joint with three/four cables [Ven+19] or a 2-DoF parallel manipulator [JMW23]. Additionally, for each architecture, there are various possible cable actuation schemes.

Another interesting possibility to realize multi-DoF joints is to fabricate the contacting surfaces of bones and connect them with springs and antagonistic cables following the anatomy of a biological joint as closely as possible [Xu+12]. Modeling the kinematics of such joints and realizing the desired movement between them can pose interesting problems to the mechanisms community.

2. **Coactivation in multi-DoF joints:**

For 1-DoF joints, the force coefficients in the expression for stiffness turned out to be a scalar. Hence, the study of their signs was sufficient to understand the nature of stiffness modulation induced by the actuation forces. For an n -DoF joint, its stiffness will be characterized by an $(n \times n)$ matrix, whose positive definiteness ensures the stability of the system. When the joint is actuated by $n + 1$ cables, n of the actuation forces can be solved for from the equilibrium equations, and the remaining redundant force, say (F_1) , will feature in the stiffness matrix (\mathbf{K}). It is possible to decompose this matrix into two parts as follows: $\mathbf{K} = \mathbf{K}_g + \Upsilon_1 F_1$, where \mathbf{K}_g accounts for the effects of gravity and springs, and Υ_1 forms the force coefficient matrix in the stiffness. While we neglect \mathbf{K}_g it is evident that the condition for F_1 to have a positive influence on the stiffness is the positive definiteness of Υ_1 . It would be interesting to study which joints/mechanisms

and cable arrangements can offer coactivation and investigate if the nature of stiffness modulation remains the same within its feasible range of movement.

3. **Cable actuation schemes for manipulators with three or more DoF:**

Unlike in the case of 2-DoF manipulators discussed in this work, there are various possibilities for cable routing in a manipulator composed of three or more joints. It would be interesting to study the manipulator performance for different schemes, e.g., [TCW23].

4. **Prototyping of tensegrity-inspired manipulators and comparison with serial counterparts:**

Practical validation of the designs of tensegrity-inspired manipulators proposed in this thesis must be carried out in the future. Further, it would be interesting to compare the performance of tensegrity-inspired manipulators with equivalent serial manipulators theoretically and experimentally to find which one is preferable under what circumstances.

RELEVANT PERSONAL PUBLICATIONS

Journal publications

1. **V. Muralidharan** and P. Wenger, “Optimal design and comparative study of two antagonistically actuated tensegrity joints”, *Mechanism and Machine Theory*, 159, 2021. doi:10.1016/j.mechmachtheory.2021.104249
2. **V. Muralidharan**, N. Testard, C. Chevallereau, A. Abourachid, and P. Wenger, “Variable stiffness and antagonist actuation for cable-driven Manipulators inspired by the bird neck”, *ASME Journal of Mechanisms and Robotics*, 15(3), 2023. doi:10.1115/1.4062302
3. **V. Muralidharan**, P. Wenger, and C. Chevallereau, “Design Considerations and Workspace Computation of 2-X and 2-R Planar Cable-Driven Tensegrity-Inspired Manipulators”, in review, *Mechanism and Machine Theory*, 2024.
4. **V. Muralidharan**, C. Chevallereau, and P. Wenger, “Coactivation in symmetric four-bar mechanisms antagonistically actuated by cables”, in review, *ASME Journal of Mechanisms and Robotics*, 2024.
5. **V. Muralidharan**, P. Wenger, and C. Chevallereau, “Design optimization and comparison of 2-X and 2-R Planar Cable-Driven Tensegrity-Inspired Manipulators”, to be submitted, *Mechanism and Machine Theory*, 2024.

Conference publications

1. **V. Muralidharan**, P. Wenger, and M. Furet, “Static analysis and design strategy of two antagonistically actuated joints”, in proceedings of 8th European Conference on Mechanism Science, EuCoMeS 2020. *Mechanisms and Machine Science*, vol 89. Springer, Cham 2020.
2. **V. Muralidharan**, P. Wenger, and C. Chevallereau, “Kinematic and static analysis of a cable-driven 2-X tensegrity manipulator for two actuation strategies”, in proceedings of Advances in Robot Kinematics 2022, Bilbao, Spain, 2022.
3. **V. Muralidharan**, P. Wenger, and C. Chevallereau, “Computation of stable wrench-feasible workspace of cable-driven n-X tensegrity manipulators”, in proceedings of 25^{ème} Congrès Français de Mécanique, Nantes, France, 2022.
4. **V. Muralidharan**, C. Chevallereau, P. Wenger, and N. J. S. Testard, “Effect of antagonistic cable actuation on the stiffness of symmetric four-bar mechanisms”, in proceedings of Cable-Driven Parallel Robots. CableCon 2023. *Mechanisms and Machine Science*, vol 132. Springer, Nantes, France, 2023.
5. **V. Muralidharan**, C. Chevallereau, and P. Wenger, “Kinematics and workspace of a spatial 3-DoF manipulator with anti-parallelogram joints”, in review, *Advances in Robot Kinematics 2024*, Ljubljana, Slovenia, 2024.

DERIVATION OF EQUIVALENT POLYNOMIAL EQUATIONS FOR ${}^4f_1 = 0$

Using the expressions in Eqs. (3.7),(3.8),(3.9), the equation ${}^4f_1 = 0$ in Eq. (3.19) can be expanded into:

$$\begin{aligned}
& b \cos\left(\frac{\alpha_1}{2}\right) (F_{\max} - F_{\min}) + C_{1x} \sin \alpha_1 - C'_{3x} \sin(\alpha_1 + \alpha_2) \\
& + \frac{\sin\left(\frac{\alpha_1}{2}\right) \left(b^2 C''_{1x} (\cos(\alpha_1) - \lambda^2 + 1) + \cos\left(\frac{\alpha_1}{2}\right) (-C'_{1x} + b^2 (F_{\max} + F_{\min}))\right)}{\sqrt{l^2 - b^2 \cos^2\left(\frac{\alpha_1}{2}\right)}} \quad (\text{A.1}) \\
& - 2bC_{3x} \sin\left(\alpha_1 + \frac{\alpha_2}{2}\right) \sqrt{\lambda^2 - \cos^2\left(\frac{\alpha_2}{2}\right)} = 0
\end{aligned}$$

The intermediate substitutions $\theta_1 = \alpha_1/2$ and $\theta_2 = \alpha_2/2$ have been reversed to identify the occurrence of α_1, α_2 in different parts of the equation explicitly. The above condition would be processed differently to obtain polynomials in $t_1 = \tan(\alpha_1/4)$ and $t_2 = \tan(\alpha_2/4)$, respectively, in the following sections.

A.1 Polynomial in $t_1 = \tan(\alpha_1/4)$

The objective is to rewrite ${}^4f_1 = 0$ as a polynomial in $t_1 = \tan(\alpha_1/4)$. In this case, α_2 and all other parameters are assumed to be known. Starting from Eq. (A.1), the trigonometric terms with compound angles are expanded and the substitutions $\lambda = (l/b)$, $c_2 = \cos(\alpha_2/2)$, $s_2 = \sin(\alpha_2/2)$ are carried out. The next step is to eliminate the square root involving α_1 . Hence, this equation is rewritten in terms of intermediate variables (for simplicity and fast computations) as follows:

$$\begin{aligned}
& -\sin(\alpha_1/2) (aa_6 + \cos(\alpha_1/2)(aa_4 + aa_5 \cos(\alpha_1/2))) \frac{1}{\sqrt{\lambda^2 - \cos^2(\alpha_1/2)}} \quad (\text{A.2}) \\
& = b \cos(\alpha_1/2)(aa_1 \sin(\alpha_1/2) + aa_3) + aa_2 \cos \alpha_1
\end{aligned}$$

where

$$\begin{cases} aa_1 = -4bc_2C_{3x}\sqrt{\lambda^2 - c_2^2} + 2C_{1x} - 2c_2^2C'_{3x} + 2C'_{3x}s_2^2 \\ aa_2 = -2s_2 \left(bC_{3x}\sqrt{\lambda^2 - c_2^2} + c_2C'_{3x} \right) \\ aa_3 = b(F_{\max} - F_{\min}) \\ aa_4 = -C'_{1x} + b^2(F_{\max} + F_{\min}) \\ aa_5 = 2b^2C''_{1x} \\ aa_6 = -b^2C''_{1x}\lambda^2 \end{cases} \quad (\text{A.3})$$

Squaring both sides of Eq. (A.2) and clearing the denominator ($\neq 0$) results in:

$$\begin{aligned} & \sin^2(\alpha_1/2) (aa_6 + \cos(\alpha_1/2)(aa_4 + aa_5 \cos(\alpha_1/2)))^2 \\ & - (\lambda^2 - \cos^2(\alpha_1/2))(b \cos(\alpha_1/2)(aa_1 \sin(\alpha_1/2) + aa_3) + aa_2 \cos \alpha_1)^2 = 0 \end{aligned} \quad (\text{A.4})$$

Introducing the variable $t_1 = \tan(\alpha_1/4)$, and replacing $\cos(\alpha_1/2) = \frac{1-t_1^2}{1+t_1^2}$ and $\sin(\alpha_1/2) = \frac{2t_1}{1+t_1^2}$, results in a rational equation. After clearing the non-zero denominator $(1+t_1^2)^6$, one obtains a degree-12 polynomial as follows:

$$\sigma_0 + \sigma_1 t_1 + \sigma_2 t_1^2 + \sigma_3 t_1^3 + \sigma_4 t_1^4 + \sigma_5 t_1^5 + \sigma_6 t_1^6 + \sigma_7 t_1^7 + \sigma_8 t_1^8 + \sigma_9 t_1^9 + \sigma_{10} t_1^{10} + \sigma_{11} t_1^{11} + \sigma_{12} t_1^{12} = 0 \quad (\text{A.5})$$

where

$$\begin{cases} \sigma_0 = -b^2(\lambda^2 - 1)(aa_2 + aa_3)^2 \\ \sigma_1 = -4b^2aa_1(\lambda^2 - 1)(aa_2 + aa_3) \\ \sigma_2 = 4(aa_4 + aa_5 + aa_6)^2 + 2b^2(-2aa_1^2(\lambda^2 - 1) + (aa_2 + aa_3)(aa_2(5\lambda^2 - 7) - aa_3(\lambda^2 + 1))) \\ \sigma_3 = -4aa_1b^2(9aa_2 + 3aa_3 + \lambda^2(aa_3 - 5aa_2)) \\ \sigma_4 = -16(aa_5 - aa_6)(aa_4 + aa_5 + aa_6) + b^2(-16aa_1^2 + aa_2^2(63 - 15\lambda^2) + aa_3^2(\lambda^2 - 1) \\ \quad + 2aa_2aa_3(13 + 11\lambda^2)) \\ \sigma_5 = 8aa_1b^2(11aa_2 + aa_3 + (3aa_2 + aa_3)\lambda^2) \\ \sigma_6 = 4\{-2aa_4^2 + 6aa_5^2 - 4aa_5aa_6 + 6aa_6^2 + b^2(aa_3^2(1 + \lambda^2) + 2aa_1^2(3 + \lambda^2) - aa_2^2(25 + 13\lambda^2))\} \\ \sigma_7 = 8aa_1b^2(-11aa_2 + aa_3 + (aa_3 - 3aa_2)\lambda^2) \\ \sigma_8 = 16(aa_4 - aa_5 - aa_6)(aa_5 - aa_6) - b^2\{16aa_1^2 - 63aa_2^2 + 26aa_2aa_3 + aa_3^2 \\ \quad + \lambda^2(15aa_2^2 + 22aa_2aa_3 - aa_3^2)\} \\ \sigma_9 = -4aa_1b^2\{-9aa_2 + 3aa_3 + \lambda^2(5aa_2 + aa_3)\} \\ \sigma_{10} = 4(-aa_4 + aa_5 + aa_6)^2 + 2b^2\{(aa_2 - aa_3)(-7aa_2 + aa_3 + \lambda^2(5aa_2 + aa_3)) \\ \quad - 2aa_1^2(\lambda^2 - 1)\} \\ \sigma_{11} = 4aa_1b^2(aa_2 - aa_3)(\lambda^2 - 1) \\ \sigma_{12} = -b^2(aa_2 - aa_3)^2(\lambda^2 - 1) \end{cases} \quad (\text{A.6})$$

The above coefficients will be known as numbers when the manipulator parameters and α_2 are given.

A.2 Polynomial in $t_2 = \tan(\alpha_2/4)$

Incorporating the substitutions $c_1 = \cos(\alpha_1/2)$, $s_1 = \sin(\alpha_1/2)$ into Eq. (A.1), and rearranging it, results in:

$$(ba_1 \cos(\alpha_2/2) + ba_2 \sin(\alpha_2/2)) \sqrt{\lambda^2 - \cos^2(\alpha_2/2)} = ba_3 + ba_4 \cos(\alpha_2) + ba_5 \sin(\alpha_2) \quad (\text{A.7})$$

where

$$\begin{cases} ba_1 = -4c_1 s_1 C_{3x} \\ ba_2 = 2C_{3x}(s_1^2 - c_1^2) \\ ba_3 = -\frac{2C'_{1x}c_1s_1 + b^2C''_{1x}s_1(-3c_1^2 + 2\lambda^2 + s_1^2 - 1)}{2b\sqrt{\lambda^2 - c_1^2}} + 2C_{1x}c_1s_1 \\ \quad + bc_1 \left\{ F_{\max} \left(\frac{s_1}{\sqrt{\lambda^2 - c_1^2}} - 1 \right) + F_{\min} \left(\frac{s_1}{\sqrt{\lambda^2 - c_1^2}} + 1 \right) \right\} \\ ba_4 = -2C'_{3x}c_1s_1 \\ ba_5 = C'_{3x}(s_1^2 - c_1^2) \end{cases} \quad (\text{A.8})$$

Squaring both sides of Eq. (A.7) to eliminate the square root leads to:

$$(ba_1 \cos(\alpha_2/2) + ba_2 \sin(\alpha_2/2))^2 (\lambda^2 - \cos^2(\alpha_2/2)) - (ba_3 + ba_4 \cos(\alpha_2) + ba_5 \sin(\alpha_2))^2 = 0 \quad (\text{A.9})$$

Introducing the variable $t_2 = \tan(\alpha_2/4)$, replacing $\cos(\alpha_2/2) = \frac{1-t_2^2}{1+t_2^2}$ and $\sin(\alpha_2/2) = \frac{2t_2}{1+t_2^2}$, and clearing the non-zero denominator $(1+t_2^2)^4$, one obtains:

$$\sigma_0 + \sigma_1 t_2 + \sigma_2 t_2^2 + \sigma_3 t_2^3 + \sigma_4 t_2^4 + \sigma_5 t_2^5 + \sigma_6 t_2^6 + \sigma_7 t_2^7 + \sigma_8 t_2^8 = 0 \quad (\text{A.10})$$

$$\begin{cases} \sigma_0 = b^2 ba_1^2 (\lambda^2 - 1) - (ba_3 + ba_4)^2 \\ \sigma_1 = 4b^2 ba_1 ba_2 (\lambda^2 - 1) - 8ba_5 (ba_3 + ba_4) \\ \sigma_2 = 4 [b^2 \{ba_1^2 + ba_2^2 (\lambda^2 - 1)\} - ba_3^2 + 2ba_3 ba_4 + 3ba_4^2 - 4ba_5^2] \\ \sigma_3 = 4b^2 ba_1 ba_2 (\lambda^2 + 3) - 8ba_5 (ba_3 - 7ba_4) \\ \sigma_4 = b^2 \{8ba_2^2 (\lambda^2 + 1) - 2ba_1^2 (\lambda^2 + 3)\} - 6ba_3^2 + 20ba_3 ba_4 - 38ba_4^2 + 32ba_5^2 \\ \sigma_5 = 8ba_5 (ba_3 - 7ba_4) - 4b^2 ba_1 ba_2 (\lambda^2 + 3) \\ \sigma_6 = 4 [b^2 \{ba_1^2 + ba_2^2 (\lambda^2 - 1)\} - ba_3^2 + 2ba_3 ba_4 + 3ba_4^2 - 4ba_5^2] \\ \sigma_7 = 8ba_5 (ba_3 + ba_4) - 4b^2 ba_1 ba_2 (\lambda^2 - 1) \\ \sigma_8 = b^2 ba_1^2 (\lambda^2 - 1) - (ba_3 + ba_4)^2 \end{cases} \quad (\text{A.11})$$

Similar to the previous case, all of these coefficients will be known as numbers when the manipulator parameters and α_1 are given.

ILLUSTRATIONS ON THE CATEGORIZATION OF THE FORCE COEFFICIENTS IN THE DESIGN OF BARS OF 2-X MANIPULATOR

This section illustrates the algebraic steps involved in categorizing the force coefficients in Table 5.1 with one example each. The coefficients in category I need no processing. Hence, one coefficient from the remaining categories is chosen and studied in the following:

- **Category II:** From Eq. (5.21), $\Omega_{11}^{10} = \csc(\psi_2 - \alpha_2) \sin(\beta_2 + \alpha_2 - \psi_2)$. Substituting for ψ_2 in terms of α_2 using the loop-closure equation (see [Fur+19]) and recalling that $\alpha_2 = 2\theta_2$, the above coefficient can be rewritten solely in terms of θ_2 as:

$$\Omega_{11}^{10} = -\frac{\sec \theta_2 \cos(\beta_2 + \theta_2) \sqrt{\lambda^2 - \cos^2 \theta_2} + \sin(\beta_2 + \theta_2)}{\sqrt{\lambda^2 - \cos^2 \theta_2} + \sin \theta_2} \quad (\text{B.1})$$

where $\lambda = (l/b)$. Differentiation w.r.t. θ_2 results in:

$$\frac{d\Omega_{11}^{10}}{d\theta_2} = \frac{\lambda^2 \sin(\beta_2) \sec^2 \theta_2}{\sqrt{\lambda^2 - \cos^2 \theta_2} (\sqrt{\lambda^2 - \cos^2 \theta_2} + \sin \theta_2)} \quad (\text{B.2})$$

Recalling that $\lambda > 1$ (see Section 2.6.3), it can be shown that the denominator is strictly positive when $\theta_2 \in [-\frac{\pi}{2}, \frac{\pi}{2}]$ (see [MW21]). Additionally, since $\beta_2 \in [0, \frac{\pi}{2}]$ (see Fig. 3.4), it follows that $\frac{d\Omega_{11}^{10}}{d\theta_2} > 0$. Thus, Ω_{11}^{10} increases monotonically with $\theta_2 \in [-\frac{\pi}{2}, \frac{\pi}{2}]$, or, equivalently with $\alpha_2 \in [-\pi, \pi]$.

- **Category III:** From Eq. (5.21), $\Omega_{Fk_{l_2}}^9 = \csc(\psi_2 - \alpha_2) \cos(\theta_2 - \psi_2)$. As in the previous case, the force coefficient and its first derivative can be written as:

$$\Omega_{Fk_{l_2}}^9 = \frac{\lambda}{\sqrt{\lambda^2 - \cos^2 \theta_2} + \sin \theta_2} \quad (\text{B.3})$$

$$\frac{d\Omega_{Fk_{l_2}}^9}{d\theta_2} = -\frac{\lambda \cos \theta_2}{\sqrt{\lambda^2 - \cos^2 \theta_2} (\sqrt{\lambda^2 - \cos^2 \theta_2} + \sin \theta_2)} \quad (\text{B.4})$$

Clearly, $\frac{d\Omega_{Fk_{l_2}}^9}{d\theta_2} < 0$ while $\theta_2 \in [-\frac{\pi}{2}, \frac{\pi}{2}]$, or $\alpha_2 \in [-\pi, \pi]$. This implies that $\Omega_{Fk_{l_2}}^9$ monotonically decreases in the specified domain.

— **Category IV:** From Eq. (5.21), $\Omega_{11}^9 = \csc(\psi_2 - \alpha_2) \sin(\beta_2)$. It can be rewritten as:

$$\Omega_{11}^9 = \frac{\lambda \sec \theta_2 \sin \beta_2}{\sqrt{\lambda^2 - \cos^2 \theta_2} + \sin \theta_2} \quad (\text{B.5})$$

Differentiating w.r.t. θ_2 yields:

$$\frac{d\Omega_{11}^9}{d\theta_2} = \frac{\lambda \sin \beta_2 (\sqrt{\lambda^2 - \cos^2 \theta_2} \tan \theta_2 \sec \theta_2 - 1)}{\sqrt{\lambda^2 - \cos^2 \theta_2} (\sin \theta_2 + \sqrt{\lambda^2 - \cos^2 \theta_2})} \quad (\text{B.6})$$

Unlike in the previous cases, the above expression is not provably positive or negative. Hence, there is a possible extrema for Ω_{11}^9 within the domain of interest. The associated stationary points can be found from the zeros of the function in Eq. (B.6). Since the denominator and the first two factors in the numerator are positive, only the remaining factor must be considered for finding the zeros. This results in:

$$\sqrt{\lambda^2 - \cos^2 \theta_2} \tan \theta_2 \sec \theta_2 - 1 = 0 \quad (\text{B.7})$$

$$\implies \sqrt{\lambda^2 - \cos^2 \theta_2} = \frac{1}{\tan \theta_2 \sec \theta_2} \quad (\text{B.8})$$

Squaring both sides and incorporating the tangent half-angle substitutions: $\sin \theta_2 = \frac{2t_2}{1+t_2^2}$ and $\cos \theta_2 = \frac{1-t_2^2}{1+t_2^2}$, with $t_2 = \tan\left(\frac{\theta_2}{2}\right)$, one obtains:

$$\frac{(1+t_2^2)^2 (t_2^4 - 2(2\lambda^2 + 1)t_2^2 + 1)}{(1+t_2^2)^2} = 0 \quad (\text{B.9})$$

Clearing the non-zero factors in the numerator and denominator yields:

$$t_2^4 - 2(2\lambda^2 + 1)t_2^2 + 1 = 0 \quad (\text{B.10})$$

The zeros of this polynomial contain the stationary points (if any) and possibly some spurious solutions to $\frac{d\Omega_{11}^9}{d\theta_2} = 0$ (introduced due to squaring of Eq. (B.8)). Note that these roots depend only on the ratio $\lambda = (l/b)$, and only the real roots within the bounds of θ_2 (equivalent to those of α_2) are of interest. The function Ω_{11}^9 can be evaluated at these roots as well as the bounds of θ_2 to form a set. Then, the lower and upper bounds of Ω_{11}^9 can be found as the minimum and maximum values, respectively, in this set.

COMPUTATION OF ACTUAL COMPRESSIVE LOADS IN THE BARS AND VALIDATION OF 2-X AND 2-R DESIGNS

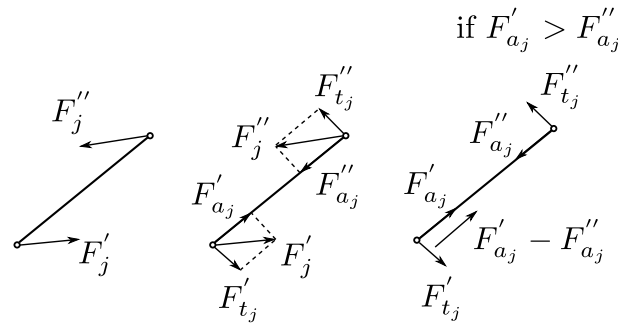


Figure C.1 – Computation of the buckling load in the bar j subjected to forces F'_j and F''_j at the two ends.

This section aims to show that the critical values for buckling load assumed in the design process (see Tables 5.2 and 5.4) are larger than the actual loads experienced by the bars in 2-X and 2-R manipulators.

This study is conducted inside the SWFJ at equilibrium configurations for both manipulators. Since four cables redundantly actuate these manipulators, it is necessary to specify the two redundant forces along with the configuration while defining their static models. As a first step, the Newton-Euler equations were developed for each of the bars in the two manipulators. The masses of the bars, as well as the springs (see Sections 5.4.4 and 5.5.6), are included in this model to determine the reaction forces accurately.

Then, the joint space (α_1, α_2) is discretized into 900 equally spaced grid points within the joint limits. Of these, the points inside the SWFJ are selected as feasible configurations. At each point, 100 combinations of redundant forces $\in [F_{\min}, F_{\max}]$ are considered to cover the actuation force space sufficiently. Finally, the static model is solved at the chosen configuration for the assumed combination of redundant forces to determine the reaction forces at the ends of the bars.

For a bar j , the forces acting at the two ends are shown in Fig. C.1(left). Note that these forces are not directed along the axis of the bar as assumed in the design process (see Sections 5.4.3 and 5.5.3). This is to balance the forces and moments induced by the self-weight of the bar, which were neglected during the design process.

Next, the reaction forces at the two ends of the bar are resolved into the axial and transverse

directions, as shown in Fig. C.1(center). Since only the axial component of reactions is responsible for buckling, only F'_{a_j} and F''_{a_j} are considered in further computations. When both these forces point in the same direction, no axial stresses are induced in the bar. When their directions are opposite but directed away from the center of the bars, they induce tensile stresses in the bar, which cannot cause buckling failure. However, when the forces are directed toward the center of the bar, buckling is possible. The difference in the magnitude of these forces balances the self-weight component, while $\min(F'_{a_j}, F''_{a_j})$ induces a buckling load in the bar. Hence, the numerical value of $\min(F'_{a_j}, F''_{a_j})$ is quantified as the actual buckling load faced by this bar (see Fig. C.1(right)).

The above computation is performed for all the bars at each grid point inside the SWFJ and the chosen levels of redundant forces. The minimum and maximum values of the axial loads for each of the bars are presented along with their assumed values in Table C.1 (resp. C.2) for the 2-X manipulator (resp. 2-R manipulator).

It is observed that the range of actual load lies within the range of estimated load for the bars in both manipulators. This validates the manipulator designs as safe and free from buckling failure.

Table C.1 – Ranges of the estimated load and the actual load in the bars of the 2-X manipulator. The positive sign indicates compressive loading while the negative sign indicates tensile loading.

Bar index (j)	Estimated load [N]	Actual load [N]
12	[-101.92, 101.92]	[-53.50, 53.51]
11	[-101.92, 101.92]	[-53.50, 53.51]
10	[-461.71, 162.19]	[-174.79, -42.30]
9	[-173.81, 772.84]	[87.79, 361.38]
8	[-173.81, 772.84]	[87.79, 361.38]
7	[-726.05, 807.06]	[-57.25, 328.22]
6	[-567.46, 958.53]	[-72.66, 283.76]
5	[-4128.03, 4128.03]	[-218.52, 218.00]
4	[-4091.47, 4107.72]	[-158.60, 377.77]
3	[-8434.49, 8240.10]	[-311.62, 278.13]
2	[-9041.49, 10451.80]	[384.62, 831.61]
1	[-9694.20, 11896.80]	[384.62, 831.61]

Table C.2 – Ranges of the estimated load and the actual load in the bars of the 2-R manipulator. The positive sign indicates compressive loading while the negative sign indicates tensile loading.

Bar index (j)	Estimated load [N]	Actual load [N]
14	[-30.62, 65.65]	[-15.73, 34.10]
13	[-30.62, 65.65]	[-15.73, 34.10]
12	[-282.37, 23.34]	[-166.97, -38.64]
11	[-34.67, 445.61]	[55.05, 369.02]
10	[-34.67, 445.61]	[55.05, 369.02]
9	[-193.60, 656.81]	[80.42, 361.92]
8	[-193.60, 656.81]	[80.42, 361.92]
7	[-346.87, 619.92]	[-49.71, 309.58]
6	[-489.19, 754.51]	[-15.55, 253.20]
5	[-2603.15, 2603.15]	[-51.87, 51.85]
4	[-2716.72, 2939.62]	[-43.63, 221.51]
3	[-3065.23, 2826.14]	[-195.39, 3.56]
2	[-3370.15, 4120.78]	[122.71, 635.37]
1	[-3151.42, 3853.07]	[122.71, 635.37]

SIZE OF THE 2-R MANIPULATOR RELATIVE TO THE MAXIMAL INSCRIBED DISK

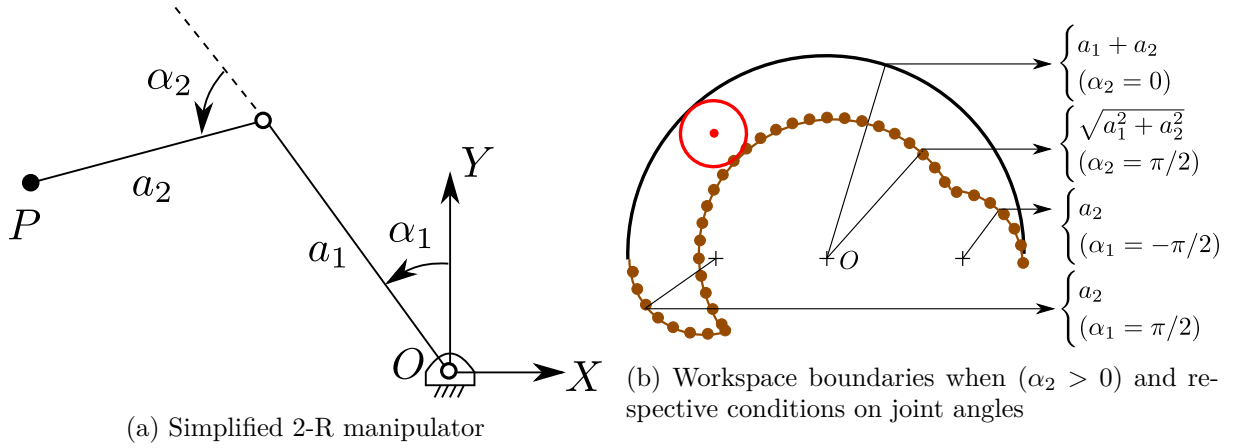


Figure D.1 – Simplified sketch of the 2-R manipulator and one half of its workspace in the presence of joint limits $\alpha_1, \alpha_2 \in]-\pi/2, \pi/2[$.

A simplified sketch of the 2-R manipulator composed of two bars with lengths a_1 and a_2 is presented in Fig. D.1a. The maximal reach or size of the manipulator is fixed at $S := a_1 + a_2$. Let the R-joints reach their maximum possible range of movement $\alpha_1, \alpha_2 \in]-\pi/2, \pi/2[$ (see Eq. (2.21)). The workspace of this manipulator would be bounded by several circular arcs whose centers and radii are shown in Fig. D.1b (only one half is shown since the other half is symmetric about the y -axis).

Clearly, the maximal inscribed disk must be tangential to the two arcs formed by $(\alpha_2 = 0)$ and $(\alpha_2 = \pi/2)$. This disk has several possible placements, one of which is shown in Fig. D.1b. It has a radius of $r_d = \left((a_1 + a_2) - \sqrt{a_1^2 + a_2^2} \right) / 2$, which can be rewritten in terms of the size (S) as: $r_d = (S - \sqrt{S^2 - 2a_1a_2}) / 2$.

For a fixed size S , the inscribed disk radius can be maximized by maximizing the product (a_1a_2) subject to the condition: $a_1 + a_2 = S$. This leads to the optimal solution $a_1 = a_2 = S/2$. Substituting this result into the above expression of r_d results in: $r_d = \frac{\sqrt{2}-1}{2\sqrt{2}} S \left(\approx \frac{S}{6.8284} \right)$.

Thus, the maximal reach (or size) of the 2-R manipulator must be at least $\frac{2\sqrt{2}}{\sqrt{2}-1} (\approx 6.8284)$ times the radius of the inscribed disk.

DESIGNS ON THE PARETO FRONTS OF THE 2-X AND 2-R MANIPULATORS

All the parameters of the optimal designs chosen on the Pareto front of the 2-X manipulator are presented in Table E.1, and those of the 2-R manipulator are presented in Table E.2.

Table E.1 – Optimal designs on the Pareto front of the 2-X manipulator for carrying a payload of mass 2 kg and inscribing an SWFW disk of radius 0.15 m.

Variables	Limits	Optimal designs					
		X _I	X _{II}	X _{III}	X _{IV}	X _V	X _{VI}
b [m]	[0.05, 1.0]	0.2415	0.2082	0.2082	0.1492	0.1362	0.1362
λ (l/b) { l [m]}]1, 10]	1.6535 {0.3992}	1.9562 {0.4074}	1.9571 {0.4075}	2.0077 {0.2996}	2.0213 {0.2753}	2.0214 {0.2753}
ϵ (a/b) { a [m]}]0, 10]	1.6660 {0.4022}	1.6238 {0.3381}	1.6196 {0.3373}	1.8052 {0.2693}	1.4687 {0.2000}	1.4490 {0.1973}
σ_α { σ_{\max} [rad]}]0, 1[0.6038 {1.8968}	0.7228 {2.2707}	0.7233 {2.2724}	0.6773 {2.1279}	0.7280 {2.2870}	0.7278 {2.2863}
k_1 [N/m]	[0, 10000]	1671.6213	1943.4413	1943.4413	2542.8877	2311.3570	2311.5101
σ_{k_1}	[0, 1]	0.0175	0.0429	0.3610	0.0988	0.4074	0.3583
k_2 [N/m]	[0, 10000]	335.3060	464.1172	464.1172	749.1274	695.2797	690.4170
σ_{k_2}	[0, 1]	0.9530	0.8545	0.8708	0.9432	0.9697	0.9663
F_{\max} [N]	[0, 500]	119.6115	120.0144	120.0144	175.9986	304.5553	418.5199
{ $\alpha_{\max_1}, \alpha_{\max_2}$ } [rad]		{0.5976, 1.8968}	{0.6881, 2.2707}	{0.7406, 2.2724}	{0.8818, 2.1279}	{1.2575, 2.2870}	{1.2310, 2.2863}
Spring 1: { d [mm], D [mm], N_a , l_{0_1} [m], l_{\max_1} [m], m_{k_1} [kg]}		{2.5, 13.73, 91.90, 0.25, 0.40, 0.16}	{3.0, 17.08, 85.23, 0.29, 0.43, 0.26}	{4.8, 40.07, 43.26, 0.28, 0.43, 0.83}	{3.0, 17.85, 57.02, 0.20, 0.33, 0.19}	{3.7, 29.72, 31.47, 0.17, 0.33, 0.27}	{3.6, 28.05, 33.53, 0.17, 0.33, 0.26}
Spring 2: { d [mm], D [mm], N_a , l_{0_2} [m], l_{\max_2} [m], m_{k_2} [kg]}		{2.5, 29.24, 47.49, 0.17, 0.57, 0.18}	{3.3, 42.54, 33.82, 0.19, 0.59, 0.33}	{3.4, 45.60, 30.93, 0.19, 0.59, 0.35}	{3.0, 32.60, 31.80, 0.16, 0.42, 0.20}	{2.8, 30.78, 30.89, 0.15, 0.39, 0.16}	{2.8, 30.88, 30.80, 0.15, 0.39, 0.16}
Bar cross-section radius r_{b_j} [mm] $j = 1, \dots, 12$		{6.81, 6.81, 5.00, 5.61, 6.20, 5.61, 5.00, 5.00, 5.00, 5.00, 5.00, 5.00}	{7.01, 7.01, 5.00, 5.39, 6.00, 5.39, 5.00, 5.00, 5.00, 5.00, 5.00, 5.00}	{7.06, 7.06, 5.00, 5.38, 5.99, 5.38, 5.00, 5.00, 5.00, 5.00, 5.00, 5.00}	{6.44, 6.44, 5.00, 5.06, 5.53, 5.06, 5.00, 5.00, 5.00, 5.00, 5.00, 5.00}	{6.69, 6.69, 5.00, 5.00, 5.08, 5.00, 5.00, 5.00, 5.00, 5.00, 5.00, 5.00}	{6.98, 6.98, 5.00, 5.00, 5.30, 5.00, 5.00, 5.00, 5.00, 5.00, 5.00, 5.00}
Mass [kg]		1.8563	2.2686	3.4325	1.5173	1.4996	1.4919
Size [m]		1.4404	1.3765	1.3751	1.0582	0.8785	0.8732

Table E.2 – Optimal designs on the Pareto front of the 2-R manipulator for carrying a payload of mass 2 kg and inscribing an SWFW disk of radius 0.15 m.

Variables	Limits	R_I	R_{II}	R_{III}	R_{IV}	R_V	R_{VI}
r [m]	[0.025, 0.5]	0.3781	0.3862	0.3857	0.3373	0.3787	0.3739
μ (h/r) { h [m]}	[0, 5]	1.0112 {0.3824}	1.0527 {0.4066}	1.0546 {0.4067}	1.0486 {0.3537}	1.1015 {0.4171}	1.1013 {0.4117}
ϵ ($a/(2r)$) { a [m]}	[0, 10]	0.7908 {0.5980}	0.6745 {0.5210}	0.6674 {0.5148}	0.8832 {0.5959}	0.5183 {0.3925}	0.5333 {0.3988}
σ_α { σ_{\max} [rad]}	[0, 1]	0.6745 {1.0520}	0.7075 {1.0750}	0.7072 {1.0733}	0.6995 {1.0657}	0.7659 {1.1292}	0.7666 {1.1304}
k_1 [N/m]	[0, 10000]	721.9829	732.9261	922.3601	933.5635	1305.3699	1560.8741
σ_{k_1}	[0, 1]	0.0321	0.0378	0.5411	0.0055	0.0001	0.0072
k_2 [N/m]	[0, 10000]	418.5830	470.9361	488.7102	452.0809	434.9845	423.4718
σ_{k_2}	[0, 1]	1.0000	1.0000	1.0000	1.0000	1.0000	1.0000
F_{\max} [N]	[0, 500]	43.0502	42.8813	42.8481	75.4756	163.2112	237.3947
{ $\alpha_{\max_1}, \alpha_{\max_2}$ } [rad]		{0.5450, 1.0520}	{0.5492, 1.0750}	{0.7332, 1.0733}	{0.3571, 1.0657}	{0.2871, 1.1292}	{0.2931, 1.1304}
Spring 1: { d [mm], D [mm], N_a , l_{0_1} [m], l_{\max_1} [m], m_{k_1} [kg]}		{2.9, 17.96, 172.40, 0.53, 0.94, 0.51}	{3.0, 18.43, 179.79, 0.57, 0.99, 0.59}	{5.3, 49.11, 73.59, 0.48, 1.04, 2.05}	{2.2, 10.02, 253.88, 0.58, 0.82, 0.24}	{2.4, 9.61, 291.86, 0.72, 0.93, 0.32}	{2.8, 11.79, 244.52, 0.71, 0.92, 0.44}
Spring 2: { d [mm], D [mm], N_a , l_{0_2} [m], l_{\max_2} [m], m_{k_2} [kg]}		{4.7, 73.97, 29.35, 0.28, 1.04, 1.02}	{5.2, 83.74, 26.94, 0.30, 1.09, 1.31}	{5.3, 85.65, 26.18, 0.30, 1.09, 1.36}	{4.6, 71.17, 27.99, 0.27, 0.95, 0.90}	{5.0, 79.58, 29.04, 0.30, 1.11, 1.23}	{4.9, 77.85, 29.39, 0.29, 1.10, 1.17}
Bar cross-section radius r_{b_j} [mm] $j = 1, \dots, 14$		{6.48, 6.48, 7.84, 5.92, 7.65, 5.92, 5.16, 5.00, 5.00, 5.00, 5.00, 5.00, 5.00, 5.00}	{6.61, 6.61, 7.98, 5.54, 7.60, 5.54, 5.33, 5.10, 5.10, 5.00, 5.00, 5.00, 5.00, 5.00}	{6.77, 6.77, 8.02, 5.53, 7.62, 5.53, 5.36, 5.13, 5.13, 5.00, 5.00, 5.00, 5.00, 5.00}	{6.34, 6.34, 7.61, 6.14, 7.64, 6.14, 5.07, 5.00, 5.00, 5.00, 5.00, 5.00, 5.00, 5.00}	{6.87, 6.87, 8.35, 5.00, 7.71, 5.00, 5.98, 5.35, 5.35, 5.00, 5.00, 5.00, 5.00, 5.00}	{7.14, 7.14, 8.64, 5.21, 8.01, 5.21, 6.28, 5.47, 5.47, 5.00, 5.00, 5.00, 5.00, 5.00}
Mass [kg]		5.7723	6.4711	9.5057	4.7770	5.7326	5.9901
Size [m]		2.7255	2.6682	2.6564	2.6067	2.4535	2.4445

OPTIMAL DESIGNS OF 2-X MANIPULATOR FOR DIFFERENT SCENARIOS

In this section, design optimization of the 2-X manipulator is conducted under two scenarios. In the first scenario, the manipulator is placed against gravity, and stability is not imposed (i.e., only wrench-feasibility is considered). This choice is inspired by the existing serial manipulators in the industries, which are stabilized electronically by control laws. The second design scenario involves suspending the 2-X manipulator along gravity, similar to the Delta parallel robot used in pick-and-place tasks. In this case, gravity itself aids in the stabilization of the manipulator, thereby obviating the need for any sophisticated control laws.

Design optimization problems were posed and solved for the two scenarios, following the same process illustrated in Chapter 6. The Pareto optimal fronts representing the compromise between the objectives, namely, maximal actuation force, moving mass, and size of the manipulator, are presented in Figs. F.1 and F.2. The following remarks are made from these plots:

- **WFW (against gravity) in Fig. F.1:** The Pareto front has two surfaces, one with designs requiring low forces $F_{\max} < 60$ N and the other with designs requiring large F_{\max} . As one moves along the first surface from X_F towards X_{III} , the force increases from 7.68 N to 53.48 N while the mass decreases from 4.27 kg to 0.72 kg, and the size decreases from 3.77 m to 0.97 m. Clearly, this compromise is in favor of X_{III} . However, as one moves from X_{III} to X_{IV} on the other surface, the force and mass increase by $\approx 3\%$ and $\approx 7\%$, but the size decreases by $\approx 26\%$, indicating that X_{IV} is better among the two. The further ascent on the second surface causes an increase in F_{\max} and a decrease in mass and size up to X_M , and an increase in F_{\max} and mass beyond X_M . The numerical values indicate that good compromise designs lie between X_{IV} and X_M . From the presented examples, X_V seems to be the best choice.
- **SWFW (along gravity) in Fig. F.2:** The Pareto front is composed of a thin strip running from X_F to X_M/X_S . The compromise between force and (mass/size) is significant, while the compromise between mass and size itself is negligible. From the figure, it is apparent that the ascent of F_{\max} is small between designs X_F and X_{III} , relatively large between X_{III} and X_V , and significantly large beyond X_V . From the data presented on other objectives, X_V seems to be the best choice.

As a notable difference from the designs presented in scenario SWFW (against gravity) in Chapter 6, the stiffnesses of the springs are negligible in many optimal designs of the scenarios WFW (against gravity) and SWFW (along gravity). This indicates that springs can be eliminated from the manipulators if mechanical stability is not essential or if they are suspended along gravity.

Table F.1 – Optimal designs of the 2-X manipulator for carrying a payload of mass 2 kg and inscribing an SWFW disk of radius 0.15 m in different scenarios.

Variables	Limits	Optimal designs		
		SWFW (against gravity)	WFW (against gravity)	SWFW (along gravity)
b [m]	[0.05, 1.0]	0.1492	0.1117	0.2519
λ (l/b) { l [m]}]1, 10]	2.0077 {0.2996}	1.3733 {0.1534}	2.0005 {0.5040}
ϵ (a/b) { a [m]}]0, 10]	1.8052 {0.2693}	1.3114 {0.1465}	1.3459 {0.3391}
σ_α { α_{\max} [rad]}]0, 1[0.6773 {2.1279}	0.9407 {2.9552}	0.6831 {2.1461}
k_1 [N/m]	[0, 10000]	2542.8877	13.9352	0.2137
σ_{k_1}	[0, 1]	0.0988	0.4278	0.5379
k_2 [N/m]	[0, 10000]	749.1274	2.0425	0.4486
σ_{k_2}	[0, 1]	0.9432	1.0000	0.9909
F_{\max} [N]	[0, 500]	175.9986	145.7323	131.7583
$\{\alpha_{\max_1}, \alpha_{\max_2}\}$ [rad]		{0.8818, 2.1279}	{1.7273, 2.9552}	{1.2148, 2.1461}
Spring 1: { d [mm], D [mm], N_a , l_{0_1} [m], l_{\max_1} [m], m_{k_1} [kg]}		{3.0, 17.85, 57.02, 0.20, 0.33, 0.19}	{0.5, 8.99, 65.50, 0.05, 0.22, $3e-3$ }	{0.2, 3.67, 1543.35, 0.32, 0.60, $4e-3$ }
Spring 2: { d [mm], D [mm], N_a , l_{0_2} [m], l_{\max_2} [m], m_{k_2} [kg]}		{3.0, 32.60, 31.80, 0.16, 0.42, 0.20}	{0.2, 3.58, 173.65, 0.04, 0.26, $5e-4$ }	{0.2, 3.99, 574.04, 0.12, 0.71, $2e-3$ }
Bar cross-section radius r_{b_j} [mm] $j = 1, \dots, 12$		{6.44, 6.44, 5.00, 5.06, 5.53, 5.06, 5.00, 5.00, 5.00, 5.00, 5.00, 5.00}	{6.83, 6.83, 5.38, 5.00, 5.00, 5.00, 5.00, 5.00, 5.00, 5.00, 5.00, 5.00}	{6.87, 6.87, 5.00, 5.00, 5.00, 5.13, 5.00, 5.00, 5.00, 5.00, 5.00, 5.00}
Mass [kg]		1.5173	0.4358	1.1816
Size [m]		1.0582	0.5032	1.5513

For the sake of comparison, the designs chosen from the Pareto fronts of the three design scenarios are presented in Table F.1. The respective plots of their workspace are presented in Figs. F.3. It is observed that in comparison to the design X_{IV} (SWFW (against gravity)), the design X_V (WFW (against gravity)) has a smaller F_{\max} , mass, and size. On the other hand, the design X_{IV} (WFW (along gravity)) has a smaller F_{\max} and mass but a larger size.

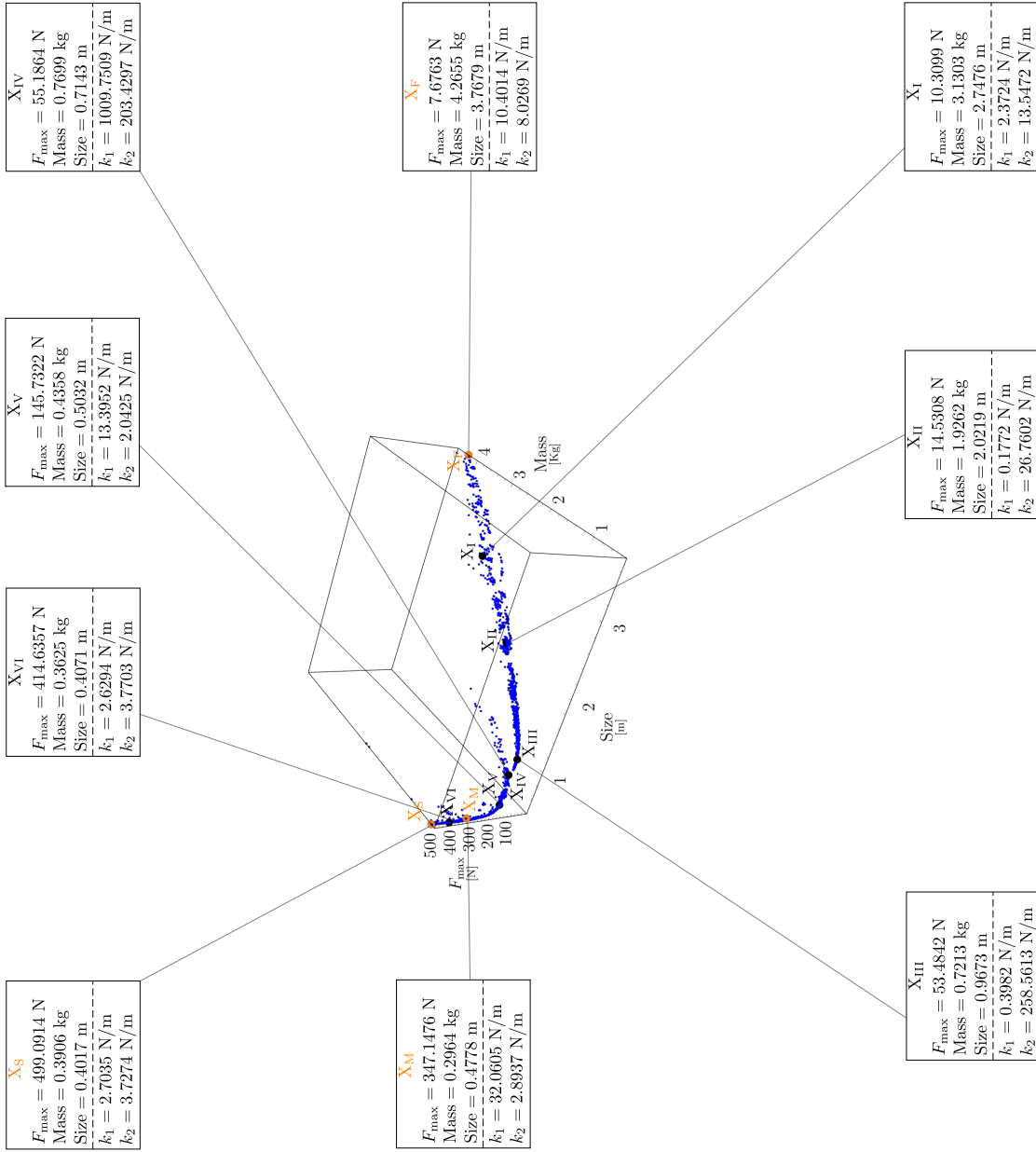


Figure F.1 – Wrench-feasible workspace without stability: Pareto front and some optimal designs (X_I, \dots, X_{VI}) of the 2-X manipulator obtained for a payload (m_p) of 2 kg and WFW disk radius (r_d) of 0.15 m. The range of the objectives are $F_{\max} \in [7.6763, 499.0914]$ N, mass $\in [0.2964, 4.5853]$ kg, size $\in [0.4017, 3.7679]$ m.

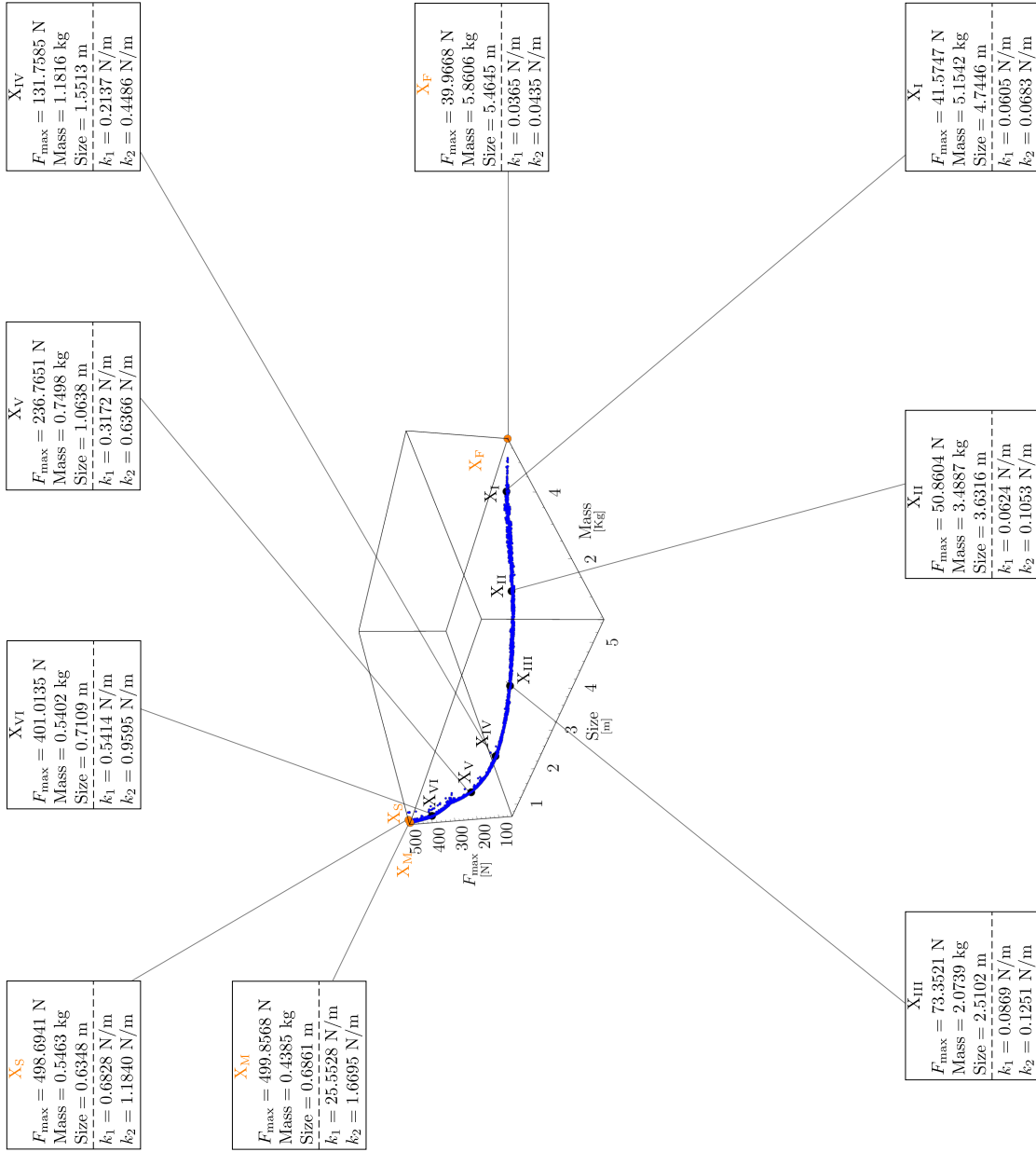


Figure F.2 – Manipulator suspended along gravity: Pareto front and some optimal designs (X_1, \dots, X_{VI}) of the 2-X manipulator obtained for a payload (m_p) of 2 kg and SWFW disk radius (r_d) of 0.15 m. The range of the objectives are $F_{\max} \in [39.9668, 499.8568]$ N, mass $\in [0.4385, 5.8606]$ kg, size $\in [0.6348, 5.4645]$ m.

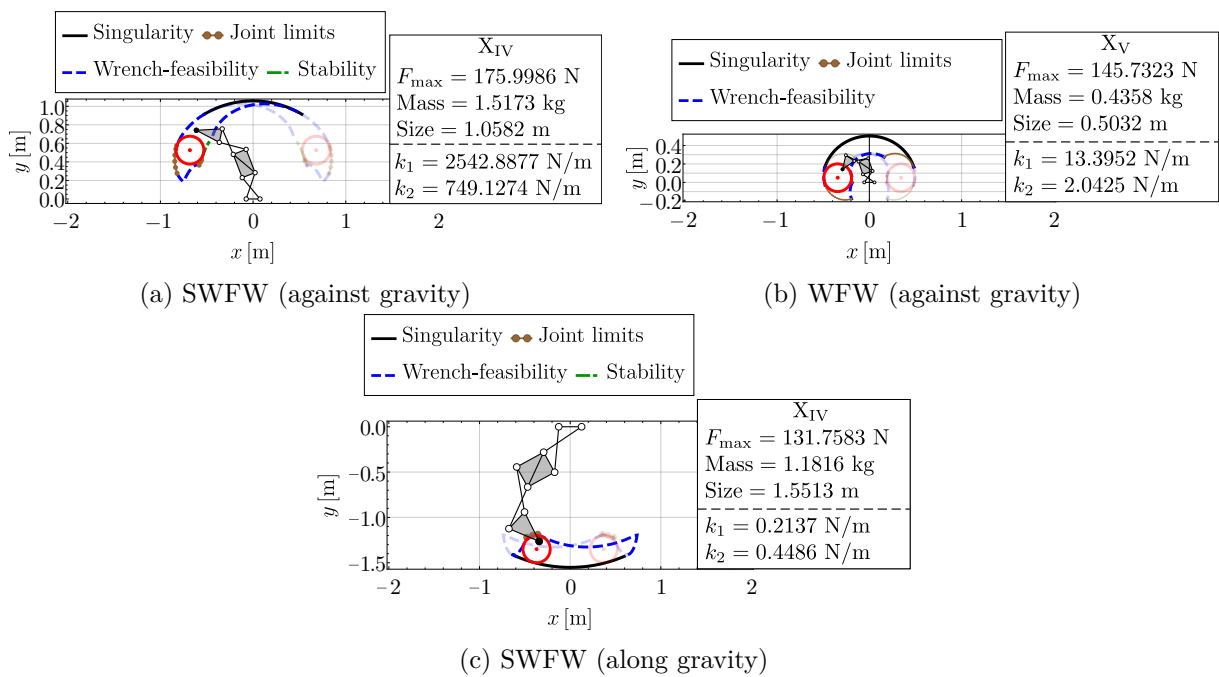


Figure F.3 – Optimal designs of 2-X manipulator chosen from the Pareto fronts obtained for different design scenarios.

BIBLIOGRAPHY

- [AB15] Vigen Arakelian and Sébastien Briot. *Balancing of Linkages and Robot Manipulators: Advanced Methods with Illustrative Examples*. Vol. 27. Mechanism and Machine Science. Switzerland: Springer International Publishing, 2015. DOI: 10.1007/978-3-319-12490-2.
- [AB17] Saurav Agarwal and Sandipan Bandyopadhyay. « Design of six-bar function generators using dual-order structural error and analytical mobility criteria ». In: *Mechanism and Machine Theory* 116 (2017), pp. 326–351. DOI: 10.1016/j.mechmachtheory.2017.04.016.
- [Abo+19] Anick Abourachid, Christine Böhmer, Philippe Wenger, Damien Chablat, Christine Chevallereau, Benjamin Fasquelle, and Matthieu Furet. « Modelling, design and control of a bird neck using tensegrity mechanisms ». In: *ICRA'2019 Workshop on Tensegrity*. Montréal, Canada, 2019.
- [AG06] Marc Arsenault and Clément M. Gosselin. « Kinematic, static and dynamic analysis of a planar 2-DOF tensegrity mechanism ». In: *Mechanism and Machine Theory* 41.9 (2006), pp. 1072–1089. DOI: 10.1016/j.mechmachtheory.2005.10.014.
- [AG08] Marc Arsenault and Clément M. Gosselin. « Kinematic and Static Analysis of a Three-degree-of-freedom Spatial Modular Tensegrity Mechanism ». In: *The International Journal of Robotics Research* 27.8 (2008), pp. 951–966. DOI: 10.1177/0278364908091152.
- [Ake+99] Prasad Akella, Michael Peshkin, Ed Colgate, Witaya Wannasuphoprasit, Nidamaluri Nagesh, Jim Wells, Steve Holland, Tom Pearson, and Brian Peacock. « Cobots for the automobile assembly line ». In: *Proceedings 1999 IEEE International Conference on Robotics and Automation*. Vol. 1. 1999, pp. 728–733. DOI: 10.1109/ROBOT.1999.770061.
- [Ars01] Marc Arsenault. « Développement et analyse de mécanismes de tésegrité ». PhD thesis. Université Laval, 2001.
- [Ars11] Marc Arsenault. « Stiffness Analysis of a 2DOF Planar Tensegrity Mechanism ». In: *Journal of Mechanisms and Robotics* 3.2 (2011), p. 021011. DOI: 10.1115/1.4003849.
- [ATB17] Arash Ajoudani, Nikos G. Tsagarakis, and Antonio Bicchi. « Choosing Poses for Force and Stiffness Control ». In: *IEEE Transactions on Robotics* 33.6 (2017), pp. 1483–1490. DOI: 10.1109/TR0.2017.2708087.
- [Bad+18] Nicolas Badeau, Clément Gosselin, Simon Foucault, Thierry Laliberté, and Muhammad E. Abdallah. « Intuitive Physical Human-Robot Interaction: Using a Passive Parallel Mechanism ». In: *IEEE Robotics & Automation Magazine* 25.2 (2018), pp. 28–38. DOI: 10.1109/MRA.2018.2800520.
- [Bal00] Robert Stawell Ball. *A Treatise on the Theory of Screws*. Cambridge: Cambridge University Press, 1900.

-
- [Ban09] R. K. Bansal. *A textbook of strength of materials*. 4th ed. New Delhi, India: Laxmi Publications, 2009.
- [Bar+19] Paolo Barattini, Federico Vicentini, Gurvinder Singh Virk, and Tamás Haidegger. *Human-Robot Interaction: Safety, Standardization, and Benchmarking*. Florida, USA: CRC Press, 2019.
- [BCG17] Sébastien Briot, Stéphane Caro, and Coralie Germain. « Design Procedure for a Fast and Accurate Parallel Manipulator ». In: *Journal of Mechanisms and Robotics* 9.6 (2017), p. 061012. DOI: 10.1115/1.4038009.
- [BGM09] Samuel Bouchard, Clément Gosselin, and Brian Moore. « On the Ability of a Cable-Driven Robot to Generate a Prescribed Set of Wrenches ». In: *Journal of Mechanisms and Robotics* 2.1 (2009), p. 011010. DOI: 10.1115/1.4000558.
- [BLG21] Gabriel Boucher, Thierry Laliberté, and Clément Gosselin. « Mechanical Design of a Low-Impedance 6-Degree-of-Freedom Displacement Sensor for Intuitive Physical Human–Robot Interaction ». In: *Journal of Mechanisms and Robotics* 13.2 (2021). DOI: 10.1115/1.4049191.
- [Boe+15] Quentin Boehler, Isabelle Charpentier, Marc S. Vedrines, and Pierre Renaud. « Definition and Computation of Tensegrity Mechanism Workspace ». In: *Journal of Mechanisms and Robotics* 7.4 (2015), p. 044502. DOI: 10.1115/1.4029809.
- [Boe+17a] Quentin Boehler, Salih Abdelaziz, Marc Vedrines, Philippe Poignet, and Pierre Renaud. « From modeling to control of a variable stiffness device based on a cable-driven tensegrity mechanism ». In: *Mechanism and Machine Theory* 107 (2017), pp. 1–12. DOI: 10.1016/j.mechmachtheory.2016.09.015.
- [Boe+17b] Quentin Boehler, Salih Abdelaziz, Marc Vedrines, Philippe Poignet, and Pierre Renaud. « Towards the Control of Tensegrity Mechanisms for Variable Stiffness Applications: A Case Study ». In: *New Trends in Mechanism and Machine Science*. Ed. by Philippe Wenger and Paulo Flores. Cham: Springer International Publishing, 2017, pp. 163–171.
- [Bor+23] Daniele Borzelli, Stefano Pastorelli, Andrea d’Avella, and Laura Gastaldi. « Virtual Stiffness: A Novel Biomechanical Approach to Estimate Limb Stiffness of a Multi-Muscle and Multi-Joint System ». In: *Sensors* 23.2 (2023). DOI: 10.3390/s23020673.
- [BREU06] Paul Bosscher, Andrew T. Riechel, and Imme Ebert-Uphoff. « Wrench-feasible workspace generation for cable-driven robots ». In: *IEEE Transactions on Robotics* 22.5 (2006), pp. 890–902. DOI: 10.1109/TR0.2006.878967.
- [Bur21] Stuart Burgess. « A review of linkage mechanisms in animal joints and related bioinspired designs ». In: *Bioinspiration & Biomimetics* 16.4 (2021), p. 041001. DOI: 10.1088/1748-3190/abf744.
- [BVR20] Jeremy Begey, Marc Vedrines, and Pierre Renaud. « Design of Tensegrity-Based Manipulators: Comparison of Two Approaches to Respect a Remote Center of Motion Constraint ». In: *IEEE Robotics and Automation Letters* 5.2 (2020), pp. 1788–1795. DOI: 10.1109/LRA.2020.2969190.

-
- [Böh+17] Valter Böhm, Tobias Kaufhold, Igor Zeidis, and Klau Zimmermann. « Dynamic analysis of a spherical mobile robot based on a tensegrity structure with two curved compressed members ». In: *Archive of Applied Mechanics* 87.5 (2017), pp. 853–864. DOI: 10.1007/s00419-016-1183-z.
- [CBG10] Philippe Cardou, Samuel Bouchard, and Clément Gosselin. « Kinematic-Sensitivity Indices for Dimensionally Nonhomogeneous Jacobian Matrices ». In: *IEEE Transactions on Robotics* 26.1 (2010), pp. 166–173. DOI: 10.1109/TR0.2009.2037252.
- [CCJ18] Bingxing Chen, Zuo Cui, and Hongzhou Jiang. « Producing negative active stiffness in redundantly actuated planar rotational parallel mechanisms ». In: *Mechanism and Machine Theory* 128 (2018), pp. 336–348. DOI: 10.1016/j.mechmachtheory.2018.06.002.
- [CCLCC21] María Guadalupe Contreras-Calderón, Med Amine Laribi, and Eduardo Castillo-Castañeda. « New Variable Stiffness Joint (VSJ): Study and Simulation ». In: *Mechanism Design for Robotics*. Ed. by Saïd Zegloul, Med Amine Laribi, and Marc Arsicault. Cham: Springer International Publishing, 2021, pp. 284–293.
- [CDM09] Eric Courteille, Dominique Deblaise, and Patrick Maurine. « Design optimization of a Delta-like parallel robot through global stiffness performance evaluation ». In: *2009 IEEE/RSJ International Conference on Intelligent Robots and Systems*. 2009, pp. 5159–5166. DOI: 10.1109/IR0S.2009.5353906.
- [Cha+20] Damien Chablat, Guillaume Moroz, Fabrice Rouillier, and Philippe Wenger. « Using Maple to Analyse Parallel Robots ». In: *Maple in Mathematics Education and Research*. Ed. by Jürgen Gerhard and Ilias Kotsireas. Cham: Springer International Publishing, 2020, pp. 50–64.
- [Chi21] Peter R. N. Childs. *Mechanical Design: Theory and Applications*. 3rd ed. Butterworth-Heinemann, 2021. DOI: 10.1016/B978-0-12-821102-1.00015-9.
- [CJ21] Bingxing Chen and Hongzhou Jiang. « Body Stiffness Variation of a Tensegrity Robotic Fish Using Antagonistic Stiffness in a Kinematically Singular Configuration ». In: *IEEE Transactions on Robotics* 37.5 (2021), pp. 1712–1727. DOI: 10.1109/TR0.2021.3049430.
- [CWA23] Christine Chevallereau, Philippe Wenger, and Anick Abourachid. « A New Bio-Inspired Joint with Variable Stiffness ». In: *New Trends in Medical and Service Robotics*. Ed. by Daniela Tarnita, Nicolae Dumitru, Doina Pisla, Giuseppe Carbone, and Ionut Geonea. Cham: Springer Nature Switzerland, 2023, pp. 220–227.
- [Deb+02] Kalyanmoy Deb, Amrit Pratap, Sameer Agrawal, and T. Meyarivan. « A fast and elitist multiobjective genetic algorithm: NSGA-II ». In: *IEEE Transactions on Evolutionary Computation* 6.2 (2002), pp. 182–197. DOI: 10.1109/4235.996017.
- [DML08] Xiumin Diao, Ou Ma, and Qi Lu. « Singularity Analysis of Planar Cable-Driven Parallel Robots ». In: *2008 IEEE Conference on Robotics, Automation and Mechatronics*. 2008, pp. 272–277. DOI: 10.1109/RAMECH.2008.4681507.

-
- [DN19] Apurba Das and Mashuq un Nabi. « A review on Soft Robotics: Modeling, Control and Applications in Human-Robot interaction ». In: *2019 International Conference on Computing, Communication, and Intelligent Systems (ICCCIS)*. 2019, pp. 306–311. DOI: 10.1109/ICCCIS48478.2019.8974461.
- [Don+21] Yang Dong, Jianzhong Ding, Chunjie Wang, and Xueao Liu. « Kinematics Analysis and Optimization of a 3-DOF Planar Tensegrity Manipulator under Workspace Constraint ». In: *Machines* 9.11 (2021). DOI: 10.3390/machines9110256.
- [DVA15] Qingjuan Duan, Vineet Vashista, and Sunil K. Agrawal. « Effect on wrench-feasible workspace of cable-driven parallel robots by adding springs ». In: *Mechanism and Machine Theory* 86 (2015), pp. 201–210. DOI: 10.1016/j.mechmachtheory.2014.12.009.
- [EJ+22] Hamza El El Jjouaoui, Giorgio Mackenzie Cruz-Martinez, Juan-Carlos Avila Vilchis, Adriana Vilchis González, Salih Abdelaziz, and Philippe Poinet. « Modeling of a Remote Center of Motion Spherical Parallel Tensegrity Mechanism for Percutaneous Interventions ». In: *Advances in Robot Kinematics 2022*. Ed. by Oscar Altuzarra and Andrés Kecskeméthy. Cham: Springer International Publishing, 2022, pp. 332–339.
- [Emm64] David Georges Emmerich. *Construction de réseaux autotendants*. French patent No. 1377290. 1964.
- [ER99] Chad English and Donald L. Russell. « Mechanics and stiffness limitations of a variable stiffness actuator for use in prosthetic limbs ». In: *Mechanism and Machine Theory* 34.1 (1999), pp. 7–25. DOI: 10.1016/S0094-114X(98)00026-3.
- [Fas+20] Benjamin Fasquelle, Matthieu Furet, Parag Khanna, Damien Chablat, Christine Chevallereau, and Philippe Wenger. « A bio-inspired 3-DOF light-weight manipulator with tensegrity X-joints ». In: *Proceedings of 2020 IEEE International Conference on Robotics and Automation (ICRA 2020)*. Paris, France, 2020.
- [Fas+21] Benjamin Fasquelle, Parag Khanna, Christine Chevallereau, Damien Chablat, Denis Creusot, Stéphane Jolivet, Philippe Lemoine, and Philippe Wenger. « Identification and Control of a 3-X Cable-Driven Manipulator Inspired From the Bird’s Neck ». In: *Journal of Mechanisms and Robotics* 14.1 (2021), p. 011005. DOI: 10.1115/1.4051521.
- [FMI90] Tamar Flash and Ferdinando Mussa-Ivaldi. « Human arm stiffness characteristics during the maintenance of posture ». In: *Experimental Brain Research* 82.2 (1990), pp. 315–326. DOI: 10.1007/BF00231251.
- [Ful62] Richard Buckminster Fuller. *Tensile-integrity structures*. United States patent No. US3063521A. 1962.
- [Fur+19] Matthieu Furet, Anders van Riesen, Christine Chevallereau, and Philippe Wenger. « Optimal Design of Tensegrity Mechanisms Used in a Bird Neck Model ». In: *EuCoMeS 2018*. Ed. by Burkhard Corves, Philippe Wenger, and Mathias Hüsing. Vol. 59. Cham: Springer International Publishing, 2019, pp. 365–375. DOI: 10.1007/978-3-319-98020-1_43.

-
- [Fur+22] Matthieu Furet, Anick Abourachid, Christine Böhmer, Valentine Chummun, Christine Chevallereau, Raphaël Cornette, Xavier De La Bernardie, and Philippe Wenger. « Estimating motion between avian vertebrae by contact modeling of joint surfaces ». In: *Computer Methods in Biomechanics and Biomedical Engineering* 25.2 (2022), pp. 123–131. DOI: 10.1080/10255842.2021.1934676.
- [FW19] Matthieu Furet and Philippe Wenger. « Kinetostatic Analysis and Actuation Strategy of a Planar Tensegrity 2-X Manipulator ». In: *Journal of Mechanisms and Robotics* 11.6 (2019), p. 060904. DOI: 10.1115/1.4044209.
- [GG10] Weizhong Guo and Feng Gao. « Solution space atlases, workspace characteristics charts and joint space maps for the design of planar serial manipulators ». In: *Mechanism and Machine Theory* 45.3 (2010), pp. 392–407. DOI: 10.1016/j.mechmachtheory.2009.09.012.
- [GG91] Clément M. Gosselin and Michel Guillot. « The Synthesis of Manipulators with Prescribed Workspace ». In: *Journal of Mechanical Design* 113.4 (1991), pp. 451–455. DOI: {10.1115/1.2912804}.
- [GM98] Amitabha Ghosh and Asok Kumar Mallik. *Theory of Mechanisms and Machines*. 3rd ed. New Delhi: Affiliated East-West Press Private Limited, 1998.
- [Gna23] Barath Gnanamoorthy. « Design and prototyping of a spatial 3-DoF tensegrity light-weight manipulator ». Master’s Thesis. École Centrale de Nantes, 2023.
- [GS19] Alessandro Gasparetto and Lorenzo Scalera. « A Brief History of Industrial Robotics in the 20th Century ». In: *Advances in Historical Studies* 8.1 (2019), pp. 24–35.
- [GT15] Jishu Guo and Guohui Tian. « Conceptual Design and Analysis of Four Types of Variable Stiffness Actuators Based on Spring Pretension ». In: *International Journal of Advanced Robotic Systems* 12.5 (2015), p. 62. DOI: 10.5772/60580.
- [Gue10] Simon D. Guest. « The stiffness of tensegrity structures ». In: *IMA Journal of Applied Mathematics* 76.1 (2010), pp. 57–66. DOI: 10.1093/imamat/hxq065.
- [HAC14] Arnaud Hamon, Yannick Aoustin, and Stéphane Caro. « Two walking gaits for a planar bipedal robot equipped with a four-bar mechanism for the knee joint ». In: *Multibody System Dynamics* 31.3 (2014), pp. 283–307. DOI: 10.1007/s11044-013-9382-7.
- [Had+08] Sami Haddadin, Alin Albu-Schaffer, Mirko Frommberger, and Gerd Hirzinger. « The role of the robot mass and velocity in physical human-robot interaction - Part II: Constrained blunt impacts ». In: *2008 IEEE International Conference on Robotics and Automation*. 2008, pp. 1339–1345. DOI: 10.1109/ROBOT.2008.4543389.
- [Ham+07] Ronald Van Ham, Bram Vanderborght, Michaël Van Damme, Björn Verrelst, and Dirk Lefeber. « MACCEPA, the mechanically adjustable compliance and controllable equilibrium position actuator: Design and implementation in a biped robot ». In: *Robotics and Autonomous Systems* 55.10 (2007), pp. 761–768. DOI: 10.1016/j.robot.2007.03.001.
- [Hex] *Motion Simulator*. https://en.wikipedia.org/wiki/Motion_simulator. {Last accessed: 25/10/2023}.

-
- [HNP08] Martin Hägele, Klas Nilsson, and J. Norberto Pires. « Industrial Robotics ». In: *Springer Handbook of Robotics*. Ed. by Bruno Siciliano and Oussama Khatib. Berlin, Heidelberg: Springer, 2008, pp. 963–986. DOI: 10.1007/978-3-540-30301-5_43.
- [Hua+22] Long Huang, Bei Liu, Leiyu Zhang, and Lairong Yin. « Equilibrium Conformation of a Novel Cable-Driven Snake-Arm Robot under External Loads ». In: *Micromachines* 13.7 (2022). DOI: 10.3390/mi13071149.
- [Hun78] Kenneth Henderson Hunt. *Kinematic Geometry of Mechanisms*. Oxford: Clarendon Press, 1978.
- [HZ03] Jochen Heinzmann and Alexander Zelinsky. « Quantitative Safety Guarantees for Physical Human-Robot Interaction ». In: *The International Journal of Robotics Research* 22.7-8 (2003), pp. 479–504. DOI: 10.1177/02783649030227004.
- [IVC16] Joshua M Inouye and Francisco Valero-Cuevas. « Muscle Synergies Heavily Influence the Neural Control of Arm Endpoint Stiffness and Energy Consumption ». In: *PLoS computational biology* 12.2 (2016), e1004737. DOI: 10.1371/journal.pcbi.1004737.
- [Jea+20] Guillaume Jeanneau, Vincent Bégoc, Sébastien Briot, and Alexandre Goldsztejn. « R-Min: a Fast Collaborative Underactuated Parallel Robot for Pick-and-Place Operations ». In: *2020 IEEE International Conference on Robotics and Automation (ICRA)*. 2020, pp. 10365–10371. DOI: 10.1109/ICRA40945.2020.9196990.
- [JMW23] Isaac John, Santhakumar Mohan, and Philippe Wenger. « Kinematic and Static Modelling of a New Two-Degree-of-Freedom Cable Operated Joint ». In: *New Advances in Mechanisms, Transmissions and Applications*. Ed. by Med Amine Laribi, Carl A. Nelson, Marco Ceccarelli, and Saïd Zeghloul. Cham: Springer Nature Switzerland, 2023, pp. 111–123.
- [KCP04] Sébastien Krut, Olivier Company, and François Pierrot. « Velocity performance indices for parallel mechanisms with actuation redundancy ». In: *Robotica* 22.2 (2004), pp. 129–139. DOI: 10.1017/S0263574703005411.
- [KG07] Xianwen Kong and Clément M. Gosselin. *Type Synthesis of Parallel Mechanisms*. Berlin: Springer, 2007.
- [Kur] *Kurilpa bridge*. https://en.wikipedia.org/wiki/Kurilpa_Bridge. {Last accessed: 25/10/2023}.
- [Lat18] Mark L. Latash. « Muscle coactivation: definitions, mechanisms, and functions ». In: *Journal of Neurophysiology* 120.1 (2018), pp. 88–104. DOI: 10.1152/jn.00084.2018.
- [Lee97] Jihong Lee. « A study on the manipulability measures for robot manipulators ». In: *Proceedings of the 1997 IEEE/RSJ International Conference on Intelligent Robot and Systems. Innovative Robotics for Real-World Applications. IROS '97*. Vol. 3. 1997, pp. 1458–1465. DOI: 10.1109/IROS.1997.656551.

-
- [Les+18] Saman Lessanibahri, Marc Gouttefarde, Stéphane Caro, and Philippe Cardou. « Twist Feasibility Analysis of Cable-Driven Parallel Robots ». In: *Cable-Driven Parallel Robots*. Ed. by Clément Gosselin, Philippe Cardou, Tobias Bruckmann, and Andreas Pott. Cham: Springer International Publishing, 2018, pp. 128–139. DOI: 10.1007/978-3-319-61431-1_12.
- [LGC01] Thierry Laliberte, Clément M. Gosselin, and Gabriel Côté. « Practical prototyping ». In: *IEEE Robotics & Automation Magazine* 8.3 (2001), pp. 43–52. DOI: 10.1109/100.956813.
- [Li+22] Zhongyi Li, Weihai Chen, Jianbin Zhang, Qihang Li, Jianhua Wang, Zaojun Fang, and Guilin Yang. « A novel cable-driven antagonistic joint designed with variable stiffness mechanisms ». In: *Mechanism and Machine Theory* 171 (2022), p. 104716. DOI: 10.1016/j.mechmachtheory.2021.104716.
- [Li+23] Qinchuan Li, Chao Yang, Lingmin Xu, and Wei Ye. *Performance Analysis and Optimization of Parallel Manipulators*. Singapore: Springer Nature, 2023. DOI: 10.1007/978-981-99-0542-3.
- [Liu+04] Xin-Jun Liu, Jinsong Wang, Kun-Ku Oh, and Jongwon Kim. « A New Approach to the Design of a DELTA Robot with a Desired Workspace ». In: *Journal of Intelligent and Robotic Systems* 39.2 (2004), pp. 209–225. DOI: 10.1023/B:JINT.0000015403.67717.68.
- [Liu+19a] Fei Liu, Wenfu Xu, Hailin Huang, Yinghao Ning, and Bing Li. « Design and Analysis of a High-Payload Manipulator Based on a Cable-Driven Serial-Parallel Mechanism ». In: *Journal of Mechanisms and Robotics* 11.5 (2019). DOI: 10.1115/1.4044113.
- [Liu+19b] Yuwang Liu, Zhuang Ge, Shangkuai Yang, Ian D. Walker, and Zhaojie Ju. « Elephant’s Trunk Robot: An Extremely Versatile Under-Actuated Continuum Robot Driven by a Single Motor ». In: *Journal of Mechanisms and Robotics* 11.5 (2019). DOI: 10.1115/1.4043923.
- [Liu+22] Yixiang Liu, Qing Bi, Xiaoming Yue, Jiang Wu, Bin Yang, and Yibin Li. « A review on tensegrity structures-based robots ». In: *Mechanism and Machine Theory* 168 (2022), p. 104571. DOI: 10.1016/j.mechmachtheory.2021.104571.
- [LLD22] Zishuai Zou Li Liu Fu Guo and Vincent G. Duffy. « Application, Development and Future Opportunities of Collaborative Robots (Cobots) in Manufacturing: A Literature Review ». In: *International Journal of Human–Computer Interaction* (2022), pp. 1–18. DOI: 10.1080/10447318.2022.2041907.
- [LOH13] Darwin Lau, Denny Oetomo, and Saman K. Halgamuge. « Generalized Modeling of Multilink Cable-Driven Manipulators With Arbitrary Routing Using the Cable-Routing Matrix ». In: *IEEE Transactions on Robotics* 29.5 (2013), pp. 1102–1113. DOI: 10.1109/TR0.2013.2264866.
- [LSS17] Stephen Levin, Susan Lowell de Solórzano, and Graham Scarr. « The significance of closed kinematic chains to biological movement and dynamic stability ». In: *Journal of Bodywork and Movement Therapies* 21.3 (2017), pp. 664–672. DOI: 10.1016/j.jbmt.2017.03.012.

-
- [MA12] Shabbir Kurbanhusen Mustafa and Sunil Kumar Agrawal. « On the Force-Closure Analysis of n-DOF Cable-Driven Open Chains Based on Reciprocal Screw Theory ». In: *IEEE Transactions on Robotics* 28.1 (2012), pp. 22–31. DOI: 10.1109/TR0.2011.2168170.
- [MCW23] Vimallesh Muralidharan, Christine Chevallereau, and Philippe Wenger. « Coactivation in symmetric four-bar mechanisms antagonistically actuated by cables ». In: (2023). , submitted to the ASME Journal of Mechanisms and Robotics.
- [MKA04] Rajkiran Madangopal, Zaeem A. Khan, and Sunil K. Agrawal. « Biologically Inspired Design Of Small Flapping Wing Air Vehicles Using Four-Bar Mechanisms And Quasi-steady Aerodynamics ». In: *Journal of Mechanical Design* 127.4 (2004), pp. 809–816. DOI: 10.1115/1.1899690.
- [MM17] David A. Madsen and David P. Madsen. *Engineering Drawing and Design*. 6th ed. Cengage Learning, 2017.
- [Moh20] Abolfazl Mohebbi. « Human-Robot Interaction in Rehabilitation and Assistance: a Review ». In: *Current Robotics Reports* 1.3 (2020), pp. 131–144. DOI: 10.1007/s43154-020-00015-4.
- [Mot03] René Motro. *Tensegrity: Structural Systems for the Future*. London, United Kingdom: Hermes Science Publishing Limited, 2003.
- [MPG22] Andrea Micheletti and Paolo Podio-Guidugli. « Seventy years of tensegrities (and counting) ». In: *Archive of Applied Mechanics* 92.9 (2022), pp. 2525–2548. DOI: 10.1007/s00419-022-02192-4.
- [MS10] John Michael McCarthy and Gim Song Soh. *Geometric Design of Linkages*. 2nd ed. New York: Springer-Verlag, 2010.
- [Mur+20] Vimallesh Muralidharan, Ashwin Bose, Kishen Chatra, and Sandipan Bandyopadhyay. « Methods for dimensional design of parallel manipulators for optimal dynamic performance over a given safe working zone ». In: *Mechanism and Machine Theory* 147 (2020), p. 103721. DOI: 10.1016/j.mechmachtheory.2019.103721.
- [Mur+23a] Vimallesh Muralidharan, Christine Chevallereau, Philippe Wenger, and Nicolas J. S. Testard. « Effect of Antagonistic Cable Actuation on the Stiffness of Symmetric Four-Bar Mechanisms ». In: *Cable-Driven Parallel Robots*. Ed. by Stéphane Caro, Andreas Pott, and Tobias Bruckmann. Cham: Springer Nature Switzerland, 2023, pp. 332–343.
- [Mur+23b] Vimallesh Muralidharan, Nicolas Testard, Christine Chevallereau, Anick Abourachid, and Philippe Wenger. « Variable stiffness and antagonist actuation for cable-driven manipulators inspired by the bird neck ». In: *Journal of Mechanisms and Robotics* 15.3 (2023). DOI: 10.1115/1.4062302.
- [Mur22] Vimallesh Muralidharan. « Computation of the feasible design space for helical extension springs and its parametric representation ». Technical Report. LS2N, École Centrale de Nantes, 2022.

-
- [MW21] Vimallesh Muralidharan and Philippe Wenger. « Optimal design and comparative study of two antagonistically actuated tensegrity joints ». In: *Mechanism and Machine Theory* 159 (2021), p. 104249. DOI: 10.1016/j.mechmachtheory.2021.104249.
- [MWC22a] Vimallesh Muralidharan, Philippe Wenger, and Christine Chevallereau. « Computation of stable wrench-feasible workspace of cable driven n-X manipulator ». In: *Proceedings of the 25ème Congrès Français de Mécanique*. Nantes, France, 2022.
- [MWC22b] Vimallesh Muralidharan, Philippe Wenger, and Christine Chevallereau. « Kinematic and Static Analysis of a Cable-Driven 2-X Tensegrity Manipulator for Two Actuation Strategies ». In: *Advances in Robot Kinematics 2022*. Ed. by Oscar Altuzarra and Andrés Kecskeméthy. Cham: Springer International Publishing, 2022, pp. 149–159.
- [Nii+22] Atsuhiko Niikura, Hiroyuki Nabae, Gen Endo, Megu Gunji, Kent Mori, Ryuma Niyama, and Koichi Suzumori. « Giraffe Neck Robot: First Step Toward a Powerful and Flexible Robot Prototyping Based on Giraffe Anatomy ». In: *IEEE Robotics and Automation Letters* 7.2 (2022), pp. 3539–3546. DOI: 10.1109/LRA.2022.3146611.
- [Pan+21] Gaoyang Pang, Geng Yang, Wenzheng Heng, Zhiqiu Ye, Xiaoyan Huang, Huayong Yang, and Zhibo Pang. « CoboSkin: Soft Robot Skin With Variable Stiffness for Safer Human-Robot Collaboration ». In: *IEEE Transactions on Industrial Electronics* 68.4 (2021), pp. 3303–3314. DOI: 10.1109/TIE.2020.2978728.
- [Par] Marcelo Pars. <http://www.tensegriteit.nl/>. {Last accessed: 25/10/2023}.
- [Par01] Manuel Paredes. « Développement d’outils d’assistance à la conception optimale des liaisons élastiques par ressorts ». PhD thesis. INSA, 2001.
- [PCS13] Vincenzo Parenti-Castelli and Nicola Sancisi. « Synthesis of Spatial Mechanisms to Model Human Joints ». In: *21st Century Kinematics*. Ed. by J. Michael McCarthy. London: Springer London, 2013, pp. 49–84.
- [Pie+17] Nico Pietroni, Marco Tarini, Amir Vaxman, Daniele Panozzo, and Paolo Cignoni. « Position-based tensegrity design ». In: *ACM Transactions on Graphics* 36.6 (2017), pp. 1–14. DOI: {10.1145/3130800.3130809}.
- [Pla] *Estadio Único Diego Armando Maradona*. https://en.wikipedia.org/wiki/Estadio_Único_Diego_Armando_Maradona. {Last accessed: 25/10/2023}.
- [PMM22] Pierpaolo Palmieri, Matteo Melchiorre, and Stefano Mauro. « Design of a Lightweight and Deployable Soft Robotic Arm ». In: *Robotics* 11.5 (2022), p. 88. DOI: 10.3390/robotics11050088.
- [PW95] G.A. Pratt and M.M. Williamson. « Series elastic actuators ». In: *Proceedings 1995 IEEE/RSJ International Conference on Intelligent Robots and Systems. Human Robot Interaction and Cooperative Robots*. Vol. 1. 1995, pp. 399–406. DOI: 10.1109/IR0S.1995.525827.

-
- [QG08] Cyril Quennouelle and Clément M. Gosselin. « Stiffness Matrix of Compliant Parallel Mechanisms ». In: *Advances in Robot Kinematics: Analysis and Design*. Ed. by Jadran Lenarčič and Philippe Wenger. Dordrecht: Springer Netherlands, 2008, pp. 331–341. DOI: 10.1007/978-1-4020-8600-7_35.
- [Ram+20] Vishal Ramadoss, Darwin Lau, Dimiter Zlatanov, and Matteo Zoppi. « Analysis of Planar Multilink Cable Driven Robots Using Internal Routing Scheme ». In: vol. Volume 10: 44th Mechanisms and Robotics Conference (MR). International Design Engineering Technical Conferences and Computers and Information in Engineering Conference. 2020, V010T10A029. DOI: 10.1115/DETC2020-22502.
- [Reb] *Rod end bearing*. <https://chassisparts.com/>. {Last accessed: 25/10/2023}.
- [REU04] Andrew T. Riechel and Imme Ebert-Uphoff. « Force-feasible workspace analysis for underconstrained, point-mass cable robots ». In: *Proceedings of IEEE International Conference on Robotics and Automation (ICRA 04)*. Vol. 5. 2004, pp. 4956–4962. DOI: 10.1109/ROBOT.2004.1302503.
- [Rus23] Matteo Russo. « Measuring Performance: Metrics for Manipulator Design, Control, and Optimization ». In: *Robotics* 12.1 (2023). DOI: 10.3390/robotics12010004.
- [RZZ19] Vishal Ramadoss, Dimiter Zlatanov, and Matteo Zoppi. « Kinematic And Workspace Analysis Of Minimally Routed Cable Driven Open Chains ». In: *Advances in Mechanism and Machine Science, IFToMM WC 2019*. Ed. by Tadeusz Uhl. Vol. 73. Cham: Springer, 2019, pp. 2841–2851. DOI: 10.1007/978-3-030-20131-9_281.
- [Sab+15] Andrew P. Sabelhaus, Jonathan Bruce, Ken Caluwaerts, Pavlo Manovi, Roya Fallah Firoozi, Sarah Dobi, Alice M. Agogino, and Vytas SunSpiral. « System design and locomotion of SUPERball, an untethered tensegrity robot ». In: *2015 IEEE International Conference on Robotics and Automation (ICRA)*. 2015, pp. 2867–2873. DOI: 10.1109/ICRA.2015.7139590.
- [Sal80] J. Kenneth Salisbury. « Active stiffness control of a manipulator in cartesian coordinates ». In: *1980 19th IEEE Conference on Decision and Control including the Symposium on Adaptive Processes*. 1980, pp. 95–100. DOI: 10.1109/CDC.1980.272026.
- [Sar+09] R. Saravanan, S. Ramabalan, N. Godwin Raja Ebenezer, and C. Dharmaraja. « Evolutionary multi criteria design optimization of robot grippers ». In: *Applied Soft Computing* 9.1 (2009), pp. 159–172. DOI: 10.1016/j.asoc.2008.04.001.
- [SB14] Stuart Shepherd and Alois Buchstab. « KUKA Robots On-Site ». In: *Robotic Fabrication in Architecture, Art and Design 2014*. Ed. by Wes McGee and Monica Ponce de Leon. Cham: Springer International Publishing, 2014, pp. 373–380. DOI: 10.1007/978-3-319-04663-1_26.
- [Sca] *SCARA*. <https://en.wikipedia.org/wiki/SCARA>. {Last accessed: 25/10/2023}.
- [SH13] Kenneth Snelson and Eleanor Heartney. « Kenneth Snelson, Art and Ideas ». In: *Kenneth Snelson, Marlborough Gallery, NY* (2013).
- [SMBJ04] Joseph E. Shigley, Charles R. Mischke, and Thomas Hunter Brown Jr. *Standard handbook of machine design*. 3rd ed. McGraw-Hill Education, 2004.

-
- [Sne65] Kenneth D. Snelson. *Continuous tension, discontinuous compression structures*. United States patent No. US3169611A. 1965.
- [Sne96] Kenneth Snelson. « Snelson On The Tensegrity Invention ». In: *International Journal of Space Structures* 11.1–2 (1996), pp. 43–48. DOI: 10.1177/026635119601–207.
- [SO09] Robert E. Skelton and Mauricio de Oliveira. *Tensegrity Systems*. United States: Springer, 2009. DOI: 10.1007/978-0-387-74242-7.
- [SR95] J.R. Singh and J. Rastegar. « Optimal synthesis of robot manipulators based on global kinematic parameters ». In: *Mechanism and Machine Theory* 30.4 (1995), pp. 569–580. DOI: 10.1016/0094-114X(94)00051-L.
- [Str06] Gilbert Strang. *Linear Algebra and its Applications*. 4th ed. New Delhi: Cengage Learning India Pvt. Ltd., 2006.
- [Sul09] Cornel Sultan. « Tensegrity: 60 Years of Art, Science, and Engineering ». In: *Advances in Applied Mechanics*. Vol. 43. Advances in Applied Mechanics. Elsevier, 2009, pp. 69–145. DOI: 10.1016/S0065-2156(09)43002-3.
- [TCW23] Nicolas J. S. Testard, Christine Chevallereau, and Philippe Wenger. « Comparison Analysis of Tendon-Driven Manipulators Based on Their Wrench Feasible Workspace ». In: (2023). in review, ASME Journal of Mechanisms and Robotics.
- [Tib02] Gunnar Tibert. « Deployable tensegrity structures for space applications ». PhD thesis. KTH, 2002.
- [UPS04] John J. Uicker, Gordon R. Pennock, and Joseph E. Shigley. *Theory of Machines and Mechanisms*. New Delhi: Oxford University Press, 2004.
- [Van+13] Bram Vanderborght, Alin Albu-Schäeffler, Antonio Bicchi, Etienne Burdet, Darwin G. Caldwell, Raffaella Carloni, Manuel G. Catalano, Oliver Eiberger, Werner Friedl, Gowrishankar Ganesh, Manolo Garabini, Markus Grebenstein, Giorgio Grioli, Sami Haddadin, Hannes Höppner, Amir Jafari, Matteo Laffranchi, Dirk Lefeber, Florian Petit, Stefano Stramigioli, Nikos G. Tsagarakis, Michael Van Damme, Ronald Van Ham, Ludo C. Visser, and Sebastian Wolf. « Variable impedance actuators: A review ». In: *Robotics and Autonomous Systems* 61.12 (2013), pp. 1601–1614. DOI: 10.1016/j.robot.2013.06.009.
- [VCH21] Swaminath Venkateswaran, Damien Chablat, and Pol Hamon. « An Optimal Design of a Flexible Piping Inspection Robot ». In: *Journal of Mechanisms and Robotics* 13.3 (2021), p. 035002. DOI: 10.1115/1.4049948.
- [Ven+19] Swaminath Venkateswaran, Matthieu Furet, Damien Chablat, and Philippe Wenger. « Design and Analysis of a Tensegrity Mechanism for a Bio-Inspired Robot ». In: vol. 5A: 43rd Mechanisms and Robotics Conference. International Design Engineering Technical Conferences and Computers and Information in Engineering Conference. 2019. DOI: 10.1115/DETC2019-97544.
- [Wah44] Arthur M. Wahl. *Mechanical Springs*. 1st ed. Penton Publishing Company, 1944.

-
- [Wen+21] Kefei Wen, Tan Sy Nguyen, David Harton, Thierry Laliberté, and Clément Gosselin. « A Backdrivable Kinematically Redundant (6+3)-Degree-of-Freedom Hybrid Parallel Robot for Intuitive Sensorless Physical Human–Robot Interaction ». In: *IEEE Transactions on Robotics* 37.4 (2021), pp. 1222–1238. DOI: 10.1109/TR0.2020.3043723.
- [WF21] Philippe Wenger and Matthieu Furet. « Kinematic Analysis of a Planar Manipulator with Anti-parallellogram Joints and Offsets ». In: *Advances in Robot Kinematics 2020*. Ed. by Jadran Lenarčič and Bruno Siciliano. Cham: Springer International Publishing, 2021, pp. 319–326.
- [Wil+16] Bauer Wilhelm, Bender Manfred, Martin Braun, Peter Rally, and Oliver Scholtz. « Lightweight robots in manual assembly - best to start simply! Examining companies' initial experiences with lightweight robots ». Technical Report. Fraunhofer Institute for Industrial Engineering, 2016.
- [Wol+16] Sebastien Wolf, Giorgio Grioli, Oliver Eiberger, Werner Friedl, Markus Grebenstein, Hannes Höppner, Etienne Burdet, Darwin G. Caldwell, Rafaella Carloni, Manuel G. Catalano, Dirk Lefebvre, Stefano Stramigioli, Nikos G. Tsagarakis, Michael Van Damme, Ronald Van Ham, Bram Vanderborght, Ludo C. Visser, Antonio Bicchi, and Alin Albu-Schäafer. « Variable Stiffness Actuators: Review on Design and Components ». In: *IEEE/ASME Transactions on Mechatronics* 21.5 (2016), pp. 2418–2430. DOI: 10.1109/TMECH.2015.2501019.
- [Xio+22] Xiaoyu Xiong, Xiantao Sun, Wenjie Chen, Yali Zhi, and Xiaohan Fang. « Design of a Variable Stiffness Actuator Based on Variable Radius Mechanisms ». In: *2022 IEEE/ASME International Conference on Advanced Intelligent Mechatronics (AIM)*. 2022, pp. 1567–1572. DOI: 10.1109/AIM52237.2022.9863246.
- [Xu+12] Zhe Xu, Vikash Kumar, Yokyo Matsuoka, and Emanuel Todorov. « Design of an anthropomorphic robotic finger system with biomimetic artificial joints ». In: *2012 4th IEEE RAS & EMBS International Conference on Biomedical Robotics and Biomechatronics (BioRob)*. 2012, pp. 568–574. DOI: 10.1109/BioRob.2012.6290710.
- [Yos85] Tsuneo Yoshikawa. « Manipulability of robotic mechanisms ». In: *International Journal of Robotics Research* 4.2 (1985), pp. 3–9.
- [Yu+15] Haoyong Yu, Sunan Huang, Gong Chen, Yongping Pan, and Zhao Guo. « Human-Robot Interaction Control of Rehabilitation Robots With Series Elastic Actuators ». In: *IEEE Transactions on Robotics* 31.5 (2015), pp. 1089–1100. DOI: 10.1109/TR0.2015.2457314.
- [YYL22] Chao Yang, Wei Ye, and Qinchuan Li. « Review of the performance optimization of parallel manipulators ». In: *Mechanism and Machine Theory* 170 (2022), p. 104725. DOI: 10.1016/j.mechmachtheory.2022.104725.
- [ZBG02] Dimiter Zlatanov, Ilian A. Bonev, and Clement M. Gosselin. « Constraint singularities of parallel mechanisms ». In: *Proceedings of the 2002 IEEE International Conference on Robotics and Automation*. Washington, DC, May 2002, pp. 496–502.

-
- [Zha+21] Wanda Zhao, Anatol Pashkevich, Alexandr Klimchik, and Damien Chablat. « Elastostatic Modeling of Multi-Link Flexible Manipulator Based on Two-Dimensional Dual-Triangle Tensegrity Mechanism ». In: *Journal of Mechanisms and Robotics* 14.2 (2021), p. 021002. DOI: 10.1115/1.4051789.
- [Eur14] European Standard. *EN 13906-2:2014 - Cylindrical helical springs made from round wire and bar - Calculation and design - Part 2: Extension springs*. 2014.
- [Eur22] European Standard. *EN 10270-1:2022 - Steel wire for mechanical springs - Part 1: Patented cold drawn unalloyed spring steel wire*. 2022.

Titre : Conception et analyse de manipulateurs inspirés par la tensegrité

Mot clés : Tensegrité, conception bio-inspirée, anti-parallélogramme, actionnement antagoniste, espace de travail, conception optimale

Résumé : Cette thèse étudie les articulations et les manipulateurs inspirés de la tensegrité, équipés de ressorts et actionnés de manière redondante par des câbles antagonistes. La redondance de l'actionnement est exploitée pour moduler leur rigidité dans une configuration donnée. La condition pour obtenir une corrélation positive entre les forces d'actionnement et la rigidité est obtenue pour une articulation générale à un seul degré de liberté (1-DDL). Ce phénomène, appelé coactivation dans les articulations biologiques, permet d'améliorer l'efficacité énergétique. Parmi les articulations à pivot (R) et les mécanismes symétriques à quatre barres, l'antiparallélogramme (X) offre la plus grande amplitude de mouvement avec coactivation. C'est pourquoi un manipulateur planaire 2-DDL avec deux ar-

ticulations X est conçu. Deux schémas d'actionnement avec quatre et trois câbles, respectivement, sont examinés pour ce manipulateur. Les performances en termes d'espace de travail, de vitesse, de force et de rigidité sont comparées pour les deux schémas. Les considérations de conception de tels manipulateurs, à savoir les limites des articulations, la faisabilité mécanique des ressorts et la résistance des barres, sont abordées. L'optimisation de la conception et la comparaison des manipulateurs 2-X et 2-R sont effectuées avec des spécifications identiques en matière de charge utile et d'espace de travail. Enfin, une articulation X modifiée est développée avec seulement des articulations sphériques, et un manipulateur spatial 3-X inspiré de la tensegrité est construit et étudié.

Title: Design and analysis of tensegrity-inspired manipulators

Keywords: Tensegrity, bio-inspired design, anti-parallelogram, antagonistic actuation, workspace, optimal design

Abstract: This thesis studies tensegrity-inspired joints and manipulators equipped with springs and redundantly actuated by antagonistic cables. The actuation redundancy is leveraged to modulate their stiffness at a given configuration. The condition to achieve a positive correlation between actuation forces and stiffness is derived for a general single-degree-of-freedom (1-DoF) joint. This phenomenon is called coactivation in biological joints, which leads to energy efficiency. Among the revolute joint (R-joint) and symmetric four-bar mechanisms, the anti-parallelogram (X-joint) offers the maximum range of movement with coactivation. Hence, a planar 2-DoF ma-

nipulator with two X-joints is conceived. Two actuation schemes with four and three cables, respectively, are examined for this manipulator. The workspace, velocity, force, and stiffness performances are compared for the two schemes. The design considerations for such manipulators, namely, the joint limits, mechanical feasibility of springs, and safety of bars, are addressed. Design optimization and comparison of 2-X and 2-R manipulators are performed with identical payload and workspace specifications. Finally, a modified X-joint is developed with only spherical joints, and a spatial 3-X tensegrity-inspired manipulator is constructed and studied.
